Development of a targeted nanoscale drug delivery system using pH-responsive DNA-nanoparticle conjugate

Lei Song

Submitted in accordance with the requirements for the degree of
Doctor of Philosophy

The University of Leeds
School of Chemistry

May, 2013

The candidate confirms that the work submitted is his own, except where work which has formed part of jointly authored publications has been included. The contribution of the candidate and the other authors to this work has been explicitly indicated below. The candidate confirms that appropriate credit has been given within the thesis where reference has been made to the work of others.

Acknowledgements

First and foremost, I would like to express my sincere gratitude to my PhD supervisor, Dr. Dejian Zhou, for his tremendous support and guidance throughout this research. I very much appreciate all his contributions of time, knowledge, experience and patience to make my PhD venture productive and valuable. It has been a great honour to be one of his PhD students.

I would also like to thank my co-supervisors, Dr. Patrick McGowan and Dr. Rongjun Chen, for their help and advice; and my former project supervisors, Dr. Zheng-liang Zhi, Prof. John Pickup, Prof. Shengrong Guo, Prof. Xiaoling Fang and Dr. Qingshan Huang for their support at all times.

I want to thank all of my colleagues for their help, especially Dr. Yuan Guo, Ms Haiyan Zhang, Ms Yue Zhang, Mr Yifei Kong, Ms Deborah Roebuck, Mr Girish Malhotra, Dr. Vincent Ho, Dr. Zhenglian Ling, Dr. Beihui Liu, Mr Martin Huscroft, Mr Dave Fogarty, Dr. Lin Wu and Miss Yibo Liu.

I also want to thank the research groups of Dr. Sarah Calaghan, Dr. Julie Fisher, Dr. Bruce Turnbull, Prof. Dongsheng Liu, Prof. Peter Stockly, Dr. Jim Thomas and Dr. Michael Webb for their support; and the University of Leeds for offering me the FIRS scholarship.

Last but not least, I would like to extend my deepest gratitude to my family and friends for their extraordinary support, encouragement and love. Without them, I could never have finished this thesis. Big thanks to my parents, my sister and my grandparents for their unconditional love and continued support; warmest thanks to my dear wife, Tang, who has always encouraged me, believed in me

and helped me to overcome difficulties without complaining, and to my lovely daughter, Linlin, for being part of my life and bringing me so much happiness. Very special thanks to my family friend, Ms Amy Fletcher, for the time and effort she has put into proofreading; and to my best friend, Mr Ron Barnes, for always being so kind to me and 100% behind me in all I do.

Abstract

Cancer is one of the most devastating diseases facing society, accounting for some 8 millions deaths worldwide in 2008 alone, and, more alarmingly, the number is predicted to increase to 13.1 million in 2030. Although conventional cancer treatments, such as radiotherapy and chemotherapy, have provided profound beneficial effects for millions of cancer patients, serious side effects cannot be avoided, mostly due to the lack of specific targeting of these treatments. A long-term goal for the pharmaceutical and healthcare industries is to develop intelligent drug delivery systems that can selectively target and deliver drugs specifically to tumour region, to maximize their therapeutic index and reduce side-effects.

Nanotechnology, the "next Industrial Revolution", offers the possibility of developing new materials, structures, devices and systems at the atomic and molecular levels that have significantly improved physicochemical properties. One of the most exciting developments in nanotechnology is that of nanoscale drug delivery systems, which are expected to change the landscape of pharmaceutics in the near future. These innovative nanoscale drug delivery systems are capable of improving transcytosis of drugs across tight epithelial and endothelial barriers, targeting drugs to cell- or tissue-specific sites and delivering macromolecule drugs to intracellular sites of action.

Inspired by such promise, this project aims to combine a pH-responsive DNA nanomachine with a biocompatible gold nanoparticle (GNP) to develop a new nanoscale tumour-targeting drug delivery system. Doxrubicin (DOX), a model anticancer drug, can bind to the system quickly and efficiently, and be released in a pH-responsive manner. This system is further modified by polyethylene glycol (PEG) for improved stability and stealth effect. Thus it has the potential to act as an excellent drug carrier. Preliminary cellular studies reveal that this system is able to deliver DOX to model (HeLa) cancer cells through the endocytic pathway, and that its cell-killing efficiency is comparable to that of the drug on its own. Furthermore, targeting ligands can be attached to this type of system for active targeting, and other functioning inorganic nanoparticles (*i.e.* gold nanorods and gold-coated magnetic nanoparticles) can also be used to replace the GNP as scaffold. This should allow the development of a multifunctional drug delivery system with the potential to offer more effective multi-modal therapeutic and imaging modalities.

Table of Contents

List of Tables

List of Figures

List of Abbreviations

BPY	$[(bpy)_2$ Ru (tpphz) Ru $(bpy)_2]^{4+}$
$BS(PEG)_5$	Bis-*N*-succinimidyl-(pentaethylene glycol) ester
C-quadruplex	cytosine-quadruplex
CTAB	hexadecyltrimethyl ammonium bromide
DCC	dicyclohexylcarbodiimide
DCU	dicyclohexylurea
DLS	dynamic light scattering
DMEM	Dulbecco's Modified Eagle's Medium
DMSO	anhydrous dimethylsulfoxide
DOX	doxorubicin hydrochloride
dsDNA	double stranded DNA
EPR	enhanced permeability and retention
FA	folic acid
FBS	fetal bovine serum
Fe@Au NPs	gold-coated magnetic nanoparticles
GNP	gold nanoparticle
GNR	gold nanorod
HD	hydrodynamic diameter
MES	monohydrate [2-(N-Morpholino) ethanesulfonic Acid]
MNP	magnetic nanoparticle

MRI	magnetic resonance imaging
MSA	mercaptosuccinic acid
NDDS	nanoscale drug delivery system
NHS	N-hydroxysuccinimide
NIR	near-infrared region
nm	nanometre
NP	nanoparticle
PEG	polyethylene glycol
PI	propidium iodide
SDD	surface density of DNA
ssDNA	single stranded DNA
SPIO	superparamagnetic iron oxide
TEA	triethylamine
TEM	transmission electron microscope
THPC	tetrakis (hydroxymethyl) phosphonium chloride
Tm	melting temperature
TMM	(methyl-PEG12)$_3$-PEG4-Maleimide
VSM	vibrating sample magnetometry
RGD	Arginine-Glycine-Aspartic

1 Chapter 1: Introduction

1.1 Nanotechnology and nanomedicine

Nanotechnology

Nanotechnology is widely regarded as being the spearhead of the next Industrial Revolution, in terms of the profound impact it will have on current science and technology. The prefix *nano*, derived from the Greek word for dwarf, means one-billionth. The U.S. National Nanotechnology Initiative defines nanotechnology as "science, engineering, and technology conducted at the nanoscale, which is about 1 to 100 nanometers" (Figure 1.1), although it commonly refers to structures of up to several hundred nm in size, developed by either top-down or bottom-up techniques[1, 2].

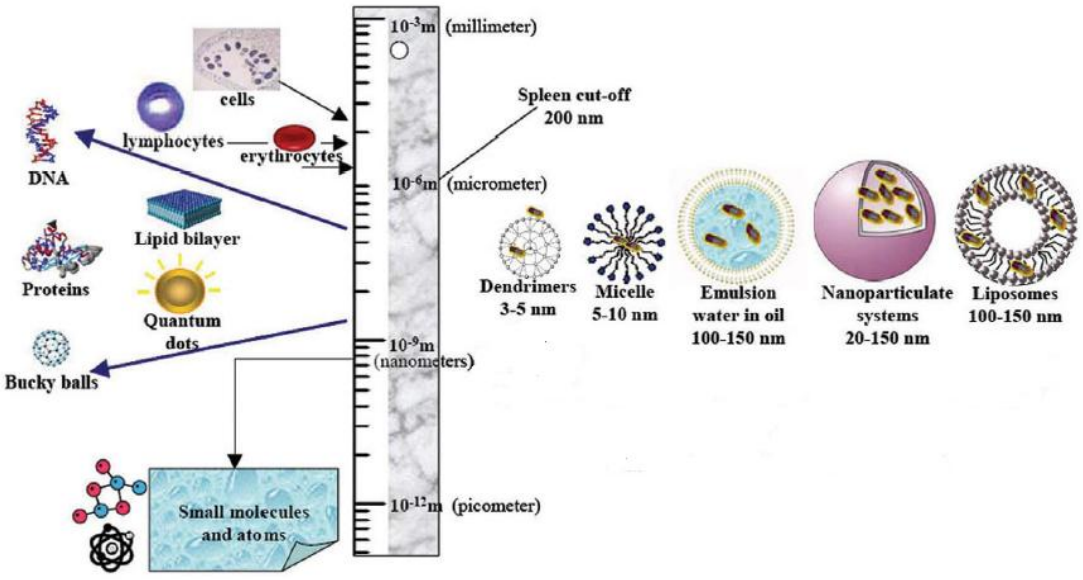

Figure 1.1. Schematics of some nanoscale materials, adapted from ref [3].

Nanotechnology also means the ability to work at the atomic, molecular and supramolecular levels, allowing the design and development of materials,

structures, devices and systems with new and significantly improved physical and chemical properties. Many of these are due to the large surface area to volume ratio of nanoparticles, and to the dominant quantum effects associated with their very small sizes[4].

The development of nanotechnology has made available a wide range of nanoscale products, such as nanotubes, fullerene derivatives, inorganic metal nanoparticles and fluorescent semiconductor nanocrystals, or quantum dots (QDs). These innovative tools have been used in a vast variety of disciplines, ranging from basic materials science, chemistry and biology, to personal healthcare applications.

Nanotechnology-based medicine (Nanomedicine)

There is no doubt that one of the most important applications of nanotechnology will be the development of new and effective medical treatments. The concept of nanotechnology-based medicine is known as nanomedicine[5-7], and it refers to highly specific medical interventions at the molecular scale for the diagnosis, prevention and treatment of disease. Thus nanomedicine covers a very large field, ranging from *in vitro* diagnostics and *in vivo* imaging, to therapeutic treatments such as targeted delivery and regenerative medicine.

The new ideas and tools of nanomedicine will have significant impact on existing medical practices[8, 9]. For example, nanoparticles and nanomaterials have unique, size-dependent biophysicochemical properties[10] which do not exist on the macroscale. These can be used for attaching therapeutic components, thus overcoming many of the problems associated with conventional diagnosis and treatment. Although nanomedicine is still in the early

stages of development, it has already offered tremendous promise and the development of ingenious nanodevices is well on the way to revolutionising therapeutics and diagnostics. It is predicted that nanomedicine will expand to an over US$160 billion industry by 2015 [11].

1.2 Drug delivery and targeting

1.2.1 Nanoscale drug delivery systems (NDDSs)

A significant part of nanomedicine is the development of nanoscale drug delivery systems (Figure 1.2), which are expected to change the landscape of the pharmaceutical industry in the foreseeable future[12-17]. Compared to conventional drug delivery systems, a NDDS can significantly improve the delivery of poorly water-soluble drugs due to its higher surface-to-volume ratio. The surface properties of the NDDS, or drug nanocarrier, are known to play a key role in the way they interact with cells, significantly affecting the drug's bioavailability. Nanocarriers can function at the cellular level and be endocytosed, resulting in efficient internalization by target cells. So NDDSs can help transcytosis of drugs across tight epithelial and endothelial barriers, targeting drugs to cell- or tissue-specific sites; they can deliver macromolecular drugs to intracellular sites of action and at the same time visualize drug delivery sites by combining therapeutic and targeting agents with imaging modalities[2, 18].

Several types of NDDSs have been developed, such as polymer–drug

conjugates, polymeric nanoparticles, liposomes, micelles, dendrimers and carbon nanotubes, and these are in various stages of laboratory or clinical research[19]. They use various materials with unique architectures to serve as drug nanocarriers for the treatment of some particularly devastating diseases, including cancer, HIV, cardiovascular disease, and diabetes. The use of nanocarriers to deliver drugs safely and effectively to infected regions has shown great promise in treating these diseases. To date, there are quite a few NDDSs which have been approved for clinical use (Table 1.1)[19]. Among these, liposomes and polymer-drug conjugates are two of the most often-used carriers that have been shown to improve drug bio-availability. Although advances in nano systems are very promising, many challenges still remain.

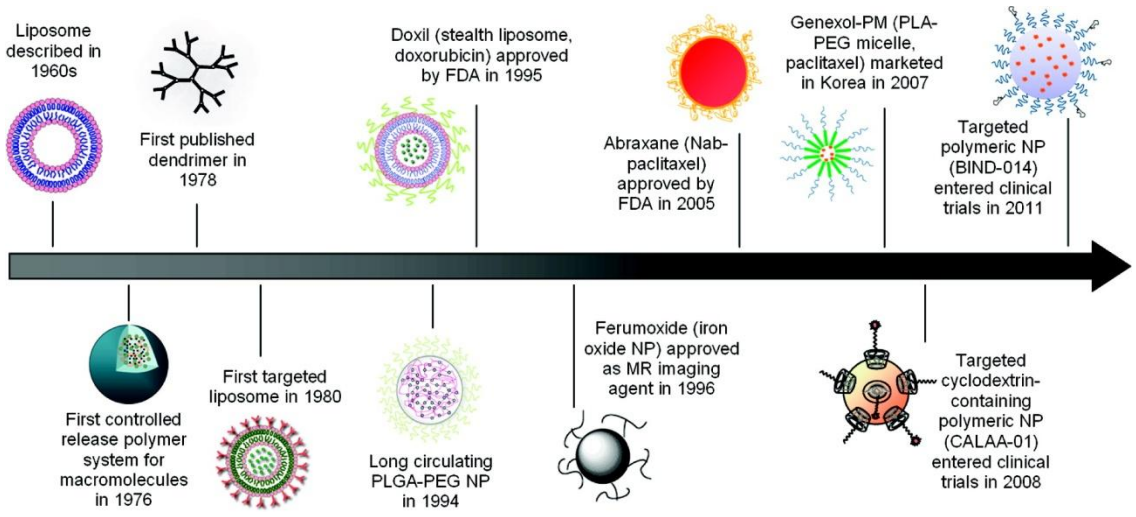

Figure 1.2. Development of clinical-stage NDDSs. Figure adapted from ref.[20].

Table 1.1. Examples of NDDSs currently on the market[19].

Compound	Commercial name	Nanocarrier	Indications
Styrene maleic anhydride-neocarzinostatin	Zinostatin/Stimalmer	Polymer–protein conjugate	Hepatocellular carcinoma
PEG -L-asparaginase	Oncaspar	Polymer–protein conjugate	Acute lymphoblastic leukemia
PEG -granulocyte colony-stimulating factor	Neulasta/PEG filgrastim	Polymer–protein conjugate	Prevention of chemotherapy-associated neutropenia
IL 2 fused to diphtheria toxin	Ontak(Denilelukindiftitox)	Immunotoxin (fusion protein)	Cutaneous T-cell lymphoma
Anti-CD33 antibody conjugated to calicheamicin	Mylotarg	Chemo-immunoconjugate	Acute myelogenous leukemia
Anti-CD20 conjugated to yttrium-90 or Indium-111	Zevalin	Radio-immunoconjugate	Relapsed or refractory, low-grade, follicular, or transformed non-Hodgkin's lymphoma
Anti-CD20 conjugated to iodine-131	Bexxar	Radio-immunoconjugate	Relapsed or refractory, low-grade, follicular, or transformed non-Hodgkin's lymphoma
Daunorubicin	DaunoXome	Liposomes	Kaposi's sarcoma
Doxorubicin	Myocet	Liposomes	Combinational therapy of recurrent breast cancer, ovarian cancer, Kaposi's sarcoma
Doxorubicin	Doxil/Caelyx	PEG -liposomes	Refractory Kaposi's sarcoma, recurrent breastcancer, ovarian cancer
Vincristine	Onco TCS	Liposomes	Relapsed aggressive non-Hodgkin's lymphoma (NHL)
Paclitaxel	Abraxane	Albumin-bound paclitaxel nanoparticles	Metastatic breast cancer

Polymer-based NDDSs, consisting mainly of polymer-drug conjugates and polymer nanoparticles, are among the most widely-studied vehicles for drug delivery. Polymer-drug conjugates, in which polymers are chemically conjugated with drugs, are regarded as entirely new chemical entities, as their pharmacokinetic profiles are distinct from those of the parent drugs[21, 22]. However, only a few drugs and polymers have been repeatedly used for developing polymer-drug conjugates; most studies have focused on

biodegradable polymers[23, 24]. Polymers used for making nanoparticles for drug delivery applications come either from synthetic polymers, of which the classic ones are poly(lactic acid) (PLA) and poly-(lactic-co-glycolic acid) (PLGA)[25, 26], or from natural polymers such as chitosan[27, 28] and collagen[29, 30]. These systems have been tested for drug delivery for several decades. They can be fabricated in a wide range of different-sized particles which can encapsulate drugs without chemical modification. Encapsulated drugs can be released in a controlled manner through surface or bulk erosion, or diffusion through the polymer matrix. However, the inherent structural heterogeneity of polymers, such as their high poly-dispersity index, may lead to variations between batches, which are often difficult to control and can cause concerns on robust formulation [31, 32].

Lipid-based NDDSs have attractive biological properties, such as excellent biocompatibility, biodegradability and the ability to carry both hydrophilic and hydrophobic drugs. They form the other major category of nanoscale drug delivery carriers. Most lipid-based carriers are based on liposomes and micelles.

Liposomes are self-closed, spherical bilayer particles, prepared from cholesterol and non-toxic natural phospholipids. Because they are composed of natural materials, liposomes have the advantage of being harmless drug delivery carriers that can circulate in the blood for a long time when modified with polyethylene glycol (PEG) functional groups[33-35]. Micelles are self-assembled, closed lipid monolayer particles with a hydrophobic inner core and a hydrophilic outer shell, which can be used to carry water-insoluble drugs[36]. Liposome-based drug nanocarriers are the first NDDSs to have successfully completed clinical trials for cancer treatment [37, 38]. Despite these

developments, significant problems remain, most notably the following: relatively low carrier stability, difficulty (and sometimes impossiblility) of achieving a controlled release of chemotherapeutic drugs (most of which display a burst-releasing character), low drug-encapsulation efficiency, and non-specific uptake by the mononuclear phagocytic system[39-41].

Dendrimers belong to a special class of polymeric NDDS. They are repeatedly branched to form a tree-like structure[42], and unlike ordinary polymers, they are prepared in a step-by-step, or generation-by-generation, fashion from monomers. Dendrimers of different generations are produced in precisely controlled shapes and sizes, and without polydispersity. Drug molecules can be connected for delivery either to the interior or the outer surface groups of the dendrimers [43]. Although dendrimer-based systems are very attractive as drug carriers, their use is limited by their synthetic capability, since a higher generation dendrimer has to be prepared by a number of repeated coupling reactions which must be highly efficient and produced on a large scale. Compared with conventional polymer or inorganic NDDSs, they are more complicated to prepare and hence more expensive[44, 45].

Carbon nanotubes are nanoscale tubes formed from either a single-layer (single- walled) or multi-layer (multi-walled) graphene sheet. Both single- and multi-walled carbon nanotubes have been explored as drug carriers[46, 47]. However, the toxicity and cytotoxicity of carbon nanotubes is a major concern if they are to be used at preclinical and clinical levels [48, 49].

1.2.2 Targeting approaches: an emerging platform for cancer therapy

Cancer

Cancer is one of the most devastating diseases worldwide, accounting for about 7 million deaths each year. Despite research efforts spanning the last 40 years,

no significant progress has been achieved in reducing its mortality rate. More alarmingly, according to the World Cancer Report, cancer rates could increase by 50%, to 15 million new cases by the year 2020 [50]. Therefore action needs to be taken urgently to face this, one of our most challenging healthcare problems. Current cancer treatments - surgical intervention, radiotherapy, and chemotherapies based mainly on small-molecule-based anti-cancer drugs - provide not only beneficial effects but also adverse effects such as killing healthy cells and causing toxicity. One of the long-term goals for the pharmaceutical industry is to develop an intelligent drug delivery system that can deliver active ingredients selectively to specific parts of the body, maximising the therapeutic index by reducing toxicity.

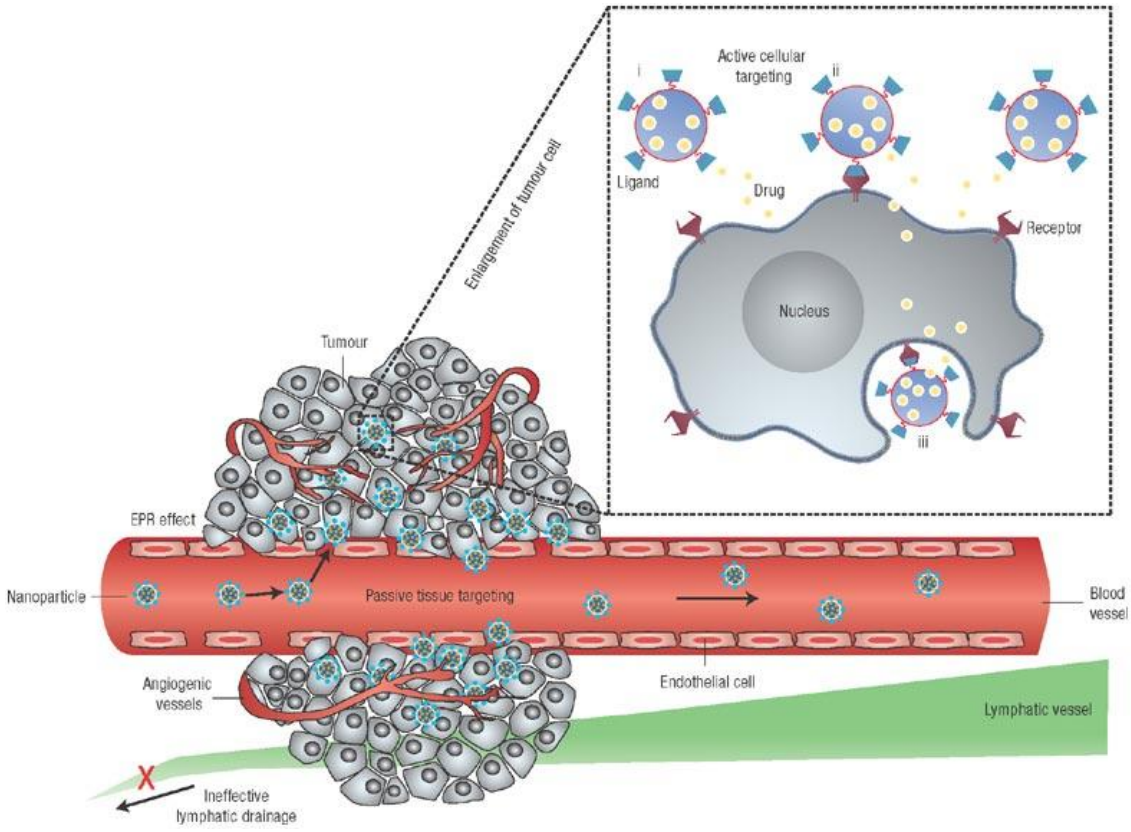

Figure 1.3. Schematic representation of different mechanisms by which nanocarriers can deliver drugs to tumours. Passive tissue targeting is achieved by EPR effect. Active cellular targeting (inset) can be achieved by functionalizing the surface of nanoparticles with ligands that promote cell-specific recognition and binding. Figure adapted from ref. [19].

Targeting strategies

In 1891, Paul Ehrlich introduced the “magic bullet” concept, the first description of targeted drug delivery. The magic bullet would be able to deliver drugs to the diseased part exclusively, at the right concentration and for the right period of time. Unlike traditional drug delivery systems, in which drugs are distributed systemically throughout the whole body *via* blood circulation, targeted drug delivery can concentrate drugs preferentially in specific parts of the body, thus improving drug efficacy and greatly reducing side effects. Targeted drug delivery systems can be used to treat many diseases, such as HIV, cardiovascular disease, etc. However, their most important application would be to treat cancer. There are two ways in which drug nanocarriers can achieve targeted drug delivery: passive targeting and active targeting (Figure 1.3).

Passive targeting. Passive targeting for cancer therapy is based on the enhanced permeability and retention (EPR) effect, a characteristic property of tumours [51]. Because tumour cells develop very fast and require a greater supply of nutrients and oxygen, blood vessel walls suffer rapid and defective angiogenesis and become leaky. Unlike free drugs which diffuse nonspecifically around the whole body, nanocarriers can extravasate into tumours through the leaky vessels. At the same time, because lymphatic clearance is dysfunctional these nanocarriers can accumulate inside the tumours and release their encapsulated drugs. The EPR effect is an essential characteristic of solid tumours but not of normal healthy tissues. It provides a good opportunity for the passive targeting of tumours by nanocarriers and has become accepted as a “gold standard” in the design of passive targeted drug delivery.

Active targeting. Active targeting strategy is based on the exclusive expression

of various epitopes or receptors on the surface of cancer cells. Active targeting carriers can interact with antigens or receptors on target cells after extravasation through targeting agents (ligands), which are capable of binding to specific receptors on the cell surface with high specificity, stability and efficiency. There are several different types of ligand that can be used for active targeting, such as proteins (mostly antibodies and their fragments[52-54]), nucleic acids (aptamers), peptides, vitamins, and carbohydrates (galactose, lactose). They can be conjugated to drug carriers to enhance the specific interactions of drug delivery systems to cancer cells. This leads to significantly improved cellular uptake (internalization) via receptor-mediated endocytosis before the loaded drugs are released. The active targeting strategy has great potential to improve the bioavailability of drugs, and to greatly reduce the side effects of therapeutic drugs.

With the development of nanotechnology and the discovery of new targeting agents, targeted delivery of therapeutic drugs at the cell- or tissue-specific level is becoming possible. Combining NDDSs with targeting approaches can offer much more effective therapeutic options with significantly reduced side effects for a myriad of serious disease treatments, particularly cancer therapy[55, 56]. In the case of cancer-specific drug delivery, NDDSs can be engineered through the attachment of targeting ligands that recognize and bind specifically to the over-expressed receptors or ligands on cancer cells (Figure 1.4).

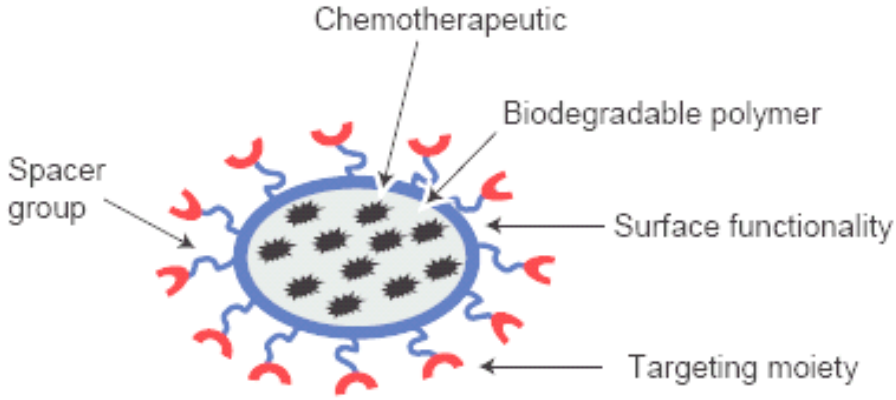

Figure 1.4. Schematic representation of a nanoscale targeted drug delivery vehicle, composed of polymeric nanoparticles whose surface has been modified with targeting agents. Adapted from ref.[14].

1.2.3 Poly(ethylene glycol) (PEG) and its role in drug delivery

Poly(ethylene glycol) (PEG), is a polyether whose structure is shown in Figure 1.5. PEGs are prepared by polymerization of ethylene oxide, and their molecular weights can range from 300 to 10,000,000 with differing physical properties (*e.g*. viscosity). As their molecular weight increases, PEGs change from viscous, colourless liquids to waxy solids. Due to their amphiphilic nature, PEGs are soluble in common non-polar organic solvents, such as benzene and dichloro-methane, and in polar solvents such as methanol and water, and the end-group modifications are relatively easy. Compared with other polymers, PEGs have the lowest protein or cellular adsorption *in vitro* or *in vivo*, making them one of the most valuable polymers in the biomedical field, and particularly in drug delivery systems. PEGs can be used directly to modify small molecule drugs and proteins[57], as well as drug carriers such as polymeric carriers[58-60] and liposomes[61-63]. The process of PEG modification is called PEGylation, and was first introduced by Davis and Abuchowski in the late 1970s [64-66]. Since the first PEGylated protein drug was approved in the early 1990s, a large number of PEGylated drugs and drug delivery systems have been developed and approved by regulators in the USA and the EU[67, 68]

(Table1.2).

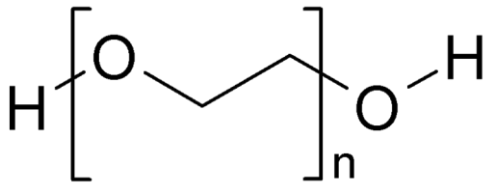

Figure 1.5. Molecular structure of poly(ethylene glycol).

Table 1.2. Drug-delivery systems stabilized with PEG that have received regulatory approval in the USA and/or the EU[67].*

PEG drug description	Company	Indication	Year of approval
Adagen (11–17×5 kDa mPEG per adenosine deaminase)	Enzon Inc. (USA & Europe)	severe combined immunodeficiency	1990 (USA)
Oncospar (5 kDa mPEG-L-asparaginase)	Enzon Inc. (USA)/ Rhône–Poulenc Rorer (Europe)	acute lymphoblastic leukemia	1994 (USA)
Doxil/Caelyx (SSL formulation of doxorubicin)	Alza Corp. (USA)/ Schering-Plough Corp. (Europe)	Kaposi's sarcoma, ovarian cancer, breast cancer, multiple myeloma	1995 (USA) 1999 (USA) all 1996 (EU)
PEG-Intron (2×20 kDa mPEG-interferon-α-2a)	Schering- Plough Corp. (USA & EU)	chronic hepatitis C	2000 (EU) 2001 (USA)
Pegasys (12 kDa mPEG-interferon-α-2b)	Hoffmann-La Roche (USA & EU)	chronic hepatitis C	2002 (USA & EU)
Neulasta (20 kDa mPEG-G-CSF)	Amgen Inc. (USA & EU)	febrile neutropenia	2002 (USA & EU)
Somavert (4–6×5 kDa mPEG per structurally modified HG receptor antagonist)	Pfizer (USA & EU)	acromegaly	2002 (EU) 2003 (USA)
Macugen (2×20 kDa mPEG- anti-VEGF- aptamer)	Pfizer (EU)/OSI Pharm. Inc. and Pfizer (USA)	age-related macular degeneration	2004 (USA) 2006 (EU)
Cimzia (2×40 kDa mPEG- anti-TNFα)	UCB S. A. (USA & EU)	Crohn's disease, rheumatoid arthritis	2008 (USA) 2009 (USA) 2009 (EU)

* mPEG: methoxypoly(ethylene glycol), SSL: sterically stabilized liposome, G-CSF: granulocyte-colony stimulating factor, HG: human growth, VEGF: vascular endothelial growth factor, TNF: tumor necrosis factor.

The most widely used polymer in the field of drug delivery, PEG is able to influence the pharmacokinetic properties of drugs and drug delivery systems[67, 69, 70] (Figure 1.6). For example, by attaching PEGs to hydrophobic drugs and drug carriers, their solubility in aqueous media is increased by the hydrophilicity of the PEG moieties . In addition, PEGylation can also increase the size of small

molecule drugs or drug carriers above the renal clearance threshold, and thus avoid fast renal clearance. For instance, small molecule drugs, oligonucleotides and siRNAs can be conjugated with high molecular weight PEGs (20 kDa-50kDa), and some macromolecules like antibodies with low molecular weight PEGs (1 kDa-5kDa)[67]. PEGs have highly flexible polymer chains with a large number of possible conformations which change constantly, resulting in a "conformational cloud"[71]. The steric hindrance of this "conformational cloud" makes drugs and drug carriers more stable, reducing aggregation during storage and preventing interactions with blood components and proteins *in vivo*. In addition, steric hindrance can mask the charges in charged carriers and decrease charge-induced interactions *in vivo*. Therefore, PEGylated drugs and drug carriers can avoid fast recognition by the immune system and subsequent rapid blood clearance, thereby reducing enzymatic degradation, immunogenicity and antigenicity. These beneficial properties that PEGylation can achieve in pharmacokinetics are termed the "Stealth effect"[67] (by reference to stealth planes) and they result in prolonged blood circulation which allows drug delivery systems more time to accumulate in specific sites, thus improving drug efficacy.

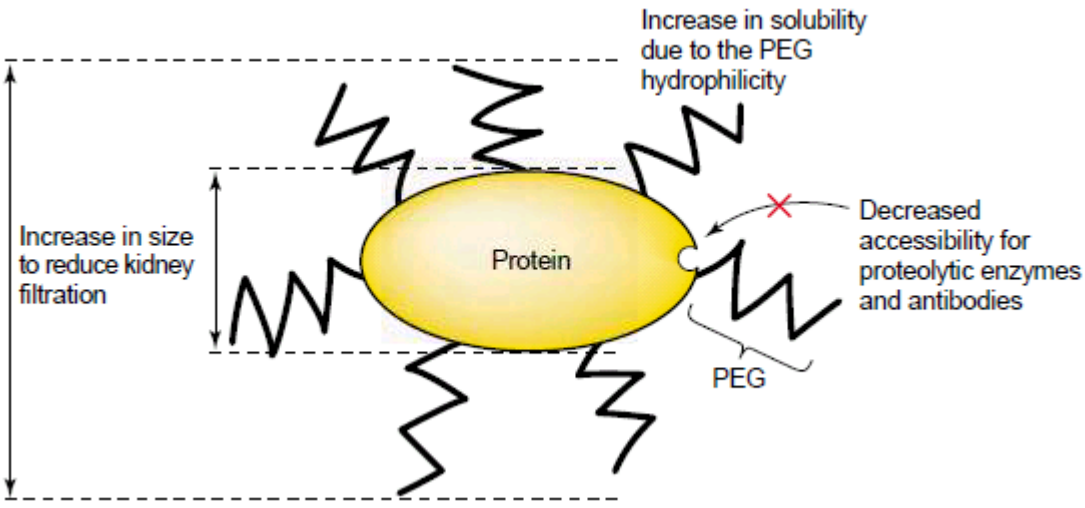

Figure 1.6. Schematic showing the main advantages of PEGylated protein, adapted from ref.[69].

The limitations of PEGs include non-biodegradability and relatively easy degradation when exposed to oxygen. PEGs may also cause hypersensitivity due to unpredictable complement activation[67]. Despite these limitations, PEG is the most popular polymer in pharmaceutical and biomedical applications, with many favourable properties, and is in fact the gold standard in the biomedical field as a number of PEGylated pharmaceutical products have already been approved and commercialized.

1.3 Background of the project

1.3.1 Metallic nanoparticles

Even though for over three decades most studies of NDDSs have been focused on two classical nanomaterials, liposomes and polymeric nanoparticles, and a number of such systems have already been FDA approved for clinical applications, nonetheless they still do not meet all the requirements for an ideal cancer therapy drug nanocarrier (Table 1.3).

Table 1.3. Ideal design of nanocarriers for cancer therapy[19].

Nanocarriers can offer many advantages over free drugs. They can:	**For rapid and effective clinical translation, the nanocarrier should:**
protect drugs from premature degradation;	be made from a material that is biocompatible, well characterized, and easily functionalized;
prevent drugs from interacting prematurely with the biological environment;	exhibit higher differential uptake efficiency in the target cells over normal cells (or tissue);
enhance absorption of drugs into a selected tissue (*e.g.* solid tumour);	be either soluble or colloidal under aqueous conditions for increased effectiveness;
control the pharmacokinetic and drug tissue distribution profile;	have an extended circulating half-life, a low rate of aggregation, and a long shelf life.
improve intracellular penetration.	be biodegradable and/or able to be efficiently cleared from the body after drug release

Metallic nanoparticles are beginning to emerge as promising candidates for nanoscale drug delivery. They belong to another important class of nanomaterials that have specific size-dependent physico-chemical features such as unique magnetic and electronic properties, and they represent a new platform in the development of nanoparticle-based tumour-targeting drug delivery systems[72-76].

Table 1.4. Various metal and semiconductor nanomaterials[77].

Core particle	*Characteristics*	*Ligand*
Au	Absorption, fluorescence quenching, stability	Thiol, disulfide, phosphine
Ag	Surface-enhanced fluorescence	Thiol, amine
Pt	Catalytic property	Thiol, phosphine, amine, isocyanide
CdSe	Luminescence, photostability	Thiol, phosphine, pyridine
Fe_2O_3	Magnetic property	Diol, dopamine derivative, amine
SiO_2	Biocompatibility	Alkoxysilane

Many inorganic nanoparticles have been developed, such as Au, Ag and Fe_3O_4; these have unique size-dependent properties that are distinct and unavailable from the bulk (Table 1.4). They can be synthesized with particularly uniform small sizes (<50 nm) and their large surface areas allow them not only to carry drugs in high doses, but also to be functionalised through ligand attachments on the surfaces (Table 1.4). For example, targeting ligands (*e.g.* antibodies and aptamers) and reporter molecules can also be incorporated into inorganic nanoparticle-based drug or gene delivery systems to achieve simultaneous targeting and tracking/imaging functions (Figure 1.7)[78]. In addition, it has been proven that some metallic nanoparticle-based systems are non-toxic and biocompatible[79-81]. Many new targeted drug delivery systems using metal

nanoparticles as carriers are currently being developed for cancer treatment[80, 82].

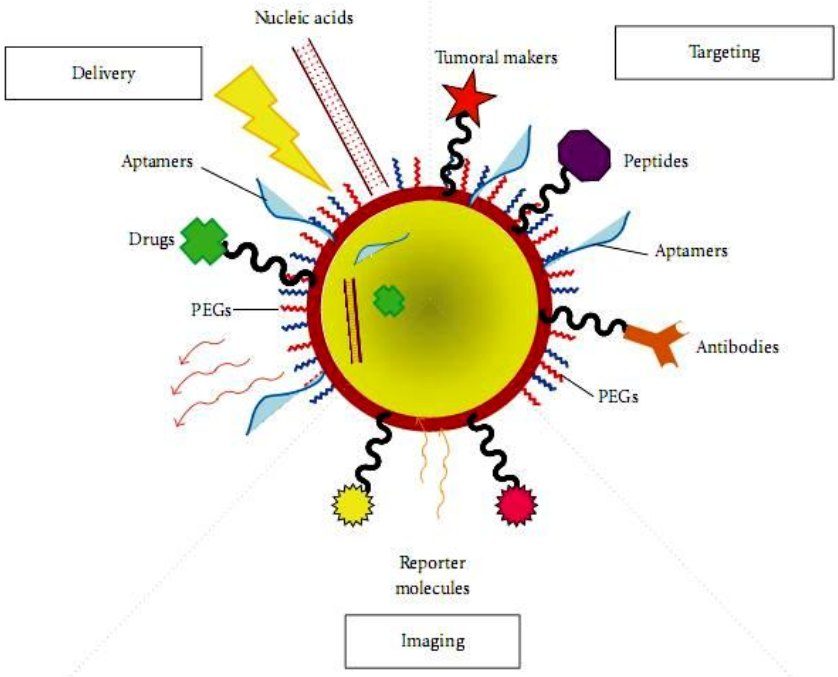

Figure 1.7. Representation of a metallic nanoparticle-based system for tumour targeting, delivery and imaging. Figure adapted from ref.[78].

A distinct advantage of metallic nanoparticles as compared with polymer- or liposome-based drug nanocarriers is that they can act not only as drug carriers, but also provide a unique function in cancer diagnosis and treatments by virtue of their electronic, magnetic and optical properties(Figure 1.8)[79, 83-86]. This makes it possible to develop multifunctional NDDSs that combine simultaneous diagnosis and treatment modalities. For example, the strong magnetic properties of metallic nanoparticles such as Fe_3O_4 can be exploited for cancer imaging (magnetic resonance imaging, MRI) and hyperthermia cancer treatment, as well as being drug nanocarriers[87-89], while gold nanorods can be used for photothermal therapy as they have extremely strong absorption in the near-infrared (NIR) region (optimal range for light penetration into tissues)[90-92]. These nanoparticle systems offer a promising platform for

developing ‘ideal’ drug carriers with their own anticancer functions.

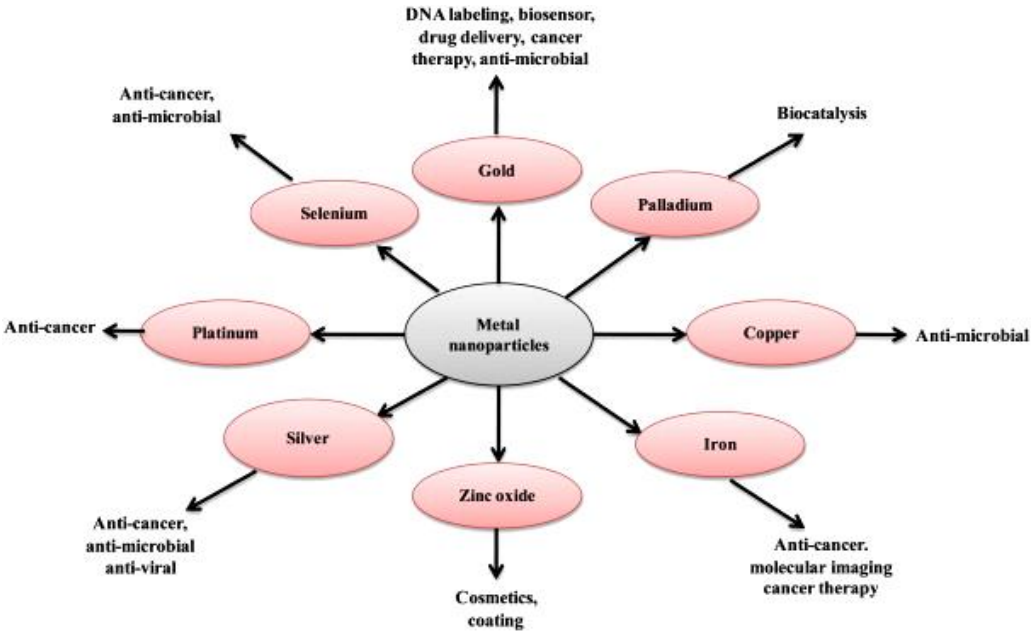

Figure 1.8. Types of metal nanoparticles and their applications in biotechnology. Figure adapted from ref.[83].

Gold Nanoparticles (GNPs)

One of the most promising nanoscale metallic structures, gold nanoparticles (GNPs), have attracted considerable attention because of their extremely strong plasmon absorption which can be manipulated by varying nanoparticle size, shape and state of aggregation. They have shown great potential in a wide range of biomedical applications, particularly in photothermal therapy, biosensing, and bioimaging [92-96].

To date, many different approaches have been developed for synthesizing GNPs in various shapes (*e.g.* nanospheres and nanorods), and sizes ranging from one nanometer to a few micrometers. The most common method for GNP synthesis, introduced by Turkevich et al[97, 98] and developed by Frens[99, 100], is based on the citrate reduction of $HAuCl_4$ in an aqueous solution. This method is capable of producing GNPs with sizes ranging from ~12 nm to over

100 nm by varying the initial molar ratio of $HAuCl_4$ and trisodium citrate[99]. In this reaction, citrate firstly acts as the reducing agent (to reduce $HAuCl_4$ to Au^0) and then as a stabilizing capping agent by adsorption *in situ* onto the formed GNPs, to give the particle surface negative charges which repel each other and prevent aggregation. The usual method of producing smaller sized GNPs, developed by Brust et al[101], is *via* a borohydride reduction of gold salt in the presence of thiol capping ligands in a two-phase (aqueous/organic phase) system, with a phase transfer reagent or a single-phase solvent. Figure 1.9 shows a schematic of the preparation of GNPs through citrate and borohydride reduction, and their subsequent modification[102-108].

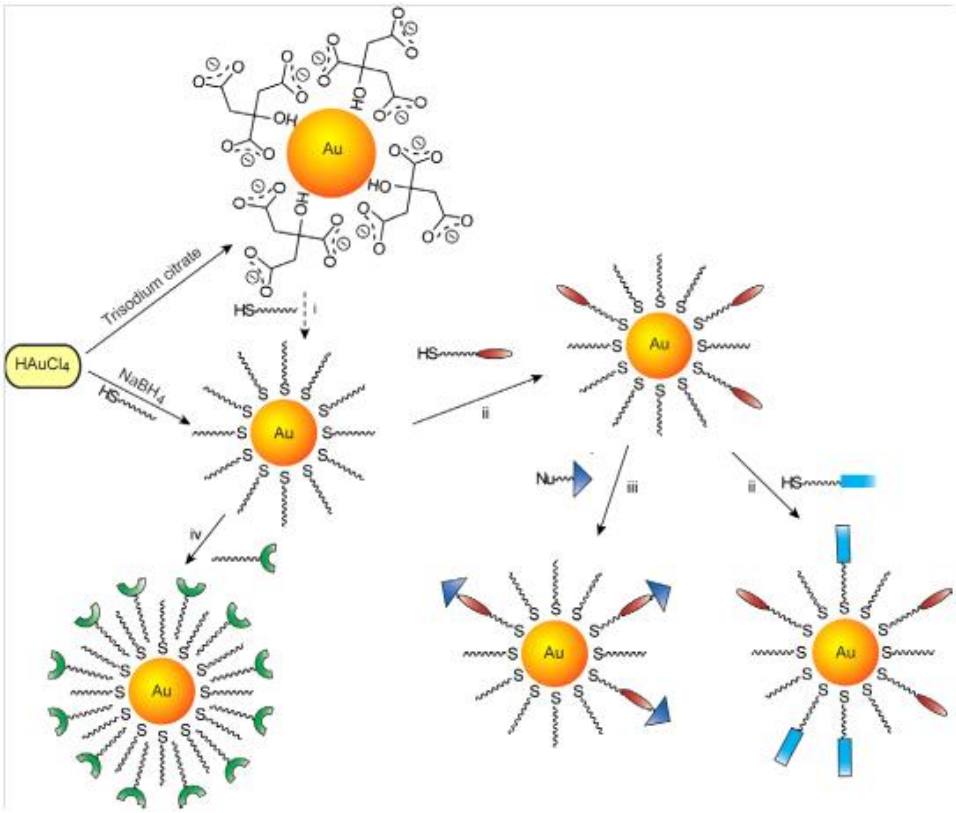

Figure 1.9. Construction of colloidal gold nanoparticles through citrate or Brust reduction and subsequent modification such as digestive ripening (i), Murray place-exchange reaction (ii)[102-104], nucleophilic reaction (iii), and encapsulation of hydrophobic clusters into surfactant micelles (iv)[107, 108].

There are also various ways of preparing gold nanoparticles in rod shapes (using bottom-up and top-down methods)[109, 110]. Among these, the 'seed-mediated' growth method, developed independently by the Murphy and El-Sayed groups, is the most widely used (Figure 1.10), and can produce gold nanorods of great uniformity in high yields.

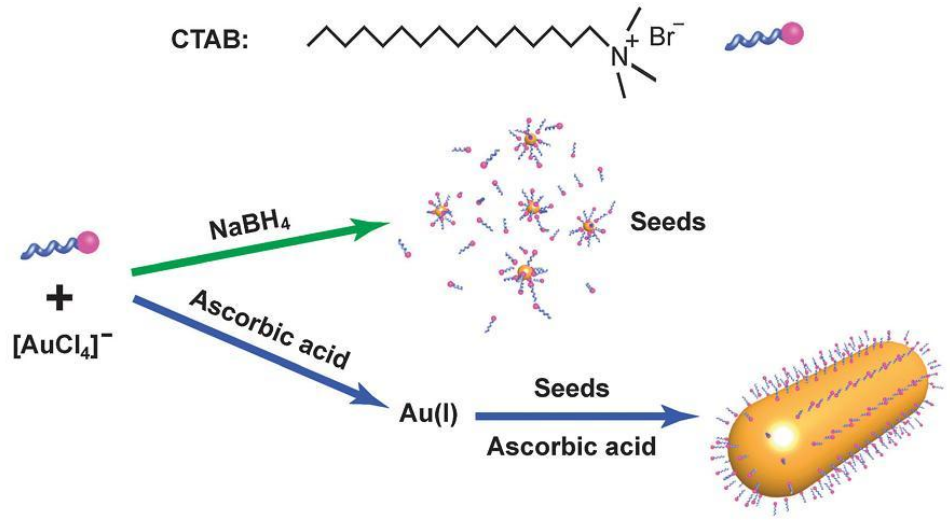

Figure 1.10. Schematic of the 'seed-mediated' growth method of preparing gold nanorods. Small gold seeds are first synthesized through the reduction of chloroauric acid with borohydride in the presence of CTAB, then mixed with a growth solution containing chloroauric acid and ascorbic aid to produce CTAB-stabilised gold nanorods. Figure adapted from ref.[110].

GNPs have been considered as potential drug delivery carriers for cancer treatment because of their unique properties[111, 112]. Besides the high loading efficiency provided by their large surface areas, GNPs are chemically stable and inert in aqueous media, and have proved biocompatible with low toxicity and cytotoxicity in *in vitro* and *in vivo* experiments. They can be easily synthesized with uniform, small sizes and easily characterised by their strong surface plasmon absorption. Another useful feature of GNPs is their ability to strongly attach functional biomolecules such as peptides, antibodies and aptamers onto their surfaces through various affinity interactions, such as the strong gold-thiol

bond[113].

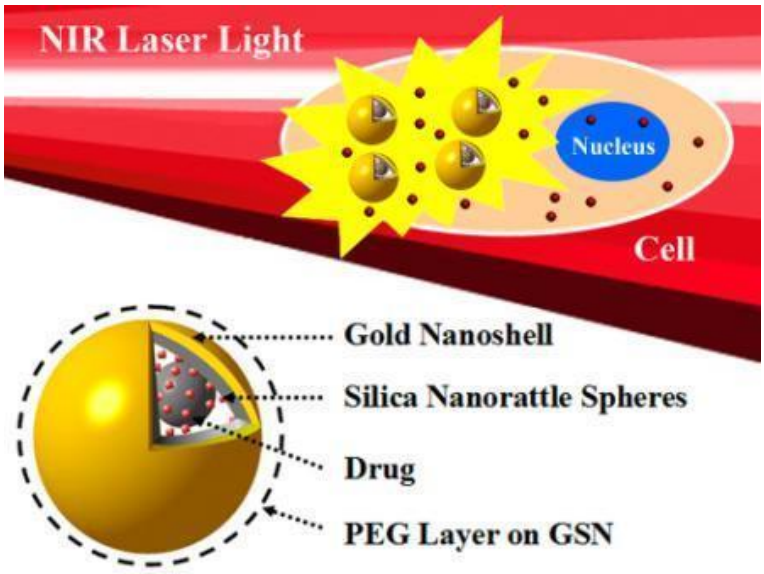

Figure 1.11. Schematic representing a gold-coated silica NDDS for chemotherapy and hyperthermia cancer treatment under exposure to NIR laser light. An anticancer drug is loaded inside the silica core which is covered with a gold nanoshell, and thiolated PEG is then attached to the surface of nanoshell to achieve the stealth effect. Figure adapted from ref.[114].

These advantages also prompt the use of gold as ultrathin nanoshells in core-shell nanocomposites (such as gold-coated silica nanoparticles[115-117] and gold-coated magnetic nanoparticles[118, 119]), to achieve optimum tunable optical properties, improve chemical stability and biocompatibility of the core, and favour surface functionalisation (*i.e.* chemical conjugation)[120-122]. Gold nanoshells have attracted enormous scientific attention and have been intensively studied for their biomedical applications. For example, by tuning gold nanoshell thickness and core size, gold-coated silica nanoparticles (*i.e.* AuroShell^{TM}, currently in the early stages of clinical trial [123]) can be designed to possess strong absorption in the near infrared region and generate heat to kill cancer cells[114, 124, 125]. Anticancer drugs can also be incorporated into gold-coated silica nanoparticles, which can be carried either on the surface

through conjugation or inside the cores *via* adsorption to the mesoporous and hollow structure of the cores(Figure 1.11)[114, 126]. GNPs (in the form of nanospheres, nanorods and nanoshells) therefore appear to offer a highly attractive nanoparticle-based platform for developing multifunctional targeted drug delivery systems for cancer treatment.

1.3.2 DNA: from biology to materials

Deoxyribose nucleic acid (DNA) is one of the most important molecules for life due to its ability to store and transmit the genetic information of all living organisms to subsequent generations. Well-characterized as a biological polymer, its non-biological functions have recently been extensively explored. DNA can be engineered as a building block of nanoscale materials with unique characteristics and defined architecture[127]. Various DNA-based nano-sized topologies have been developed through self-assembly, exploiting the high specificity of hydrogen-bonding interactions between DNA base pairs, such as adenine-thymine and guanine-cytosine[128]. DNA also has many advantages over traditional polymers[129]. DNA with monodispersity can be synthesized by an automated phosphoramidite chemistry, making it more cost-effective. Functional groups can be attached covalently to the middle or the end of the DNA by simple attaching chemistry. The structure of a DNA-based system can be precisely designed to be either rigid or flexible, by altering its length and topology. Other polymers cannot easily attain the unique structure of double-stranded (ds)DNA, around 2 nm diameter with a high degree of length tunability. Furthermore, DNA can be precisely manipulated by certain DNA enzymes, offering a very valuable molecular toolbox not only for DNA structure confirmation, but also for DNA structure modification.

Although DNA is chemically stable, it is easily degraded by DNA degrading enzymes (DNases), which exist in biological fluids such as serum and extracellular fluid, and in cytosolic compartments. To solve the problem of biological instability, chemical modifications can be employed to impair recognition and cleavage by nucleases[130]. Figure 1.12 shows various chemical modification strategies that have been applied to increase DNA stability and resistance to DNase digestions: phosphorothioate DNA, 2-O-methyl DNA, morpholino DNA, methylphosphonate, phosphoramidate DNA and locked nucleic acid. A few other modifications have also been reported to increase DNA stability, such as covalent linkage of cholesterol[131, 132] and conjugation with nanoparticles[133, 134].

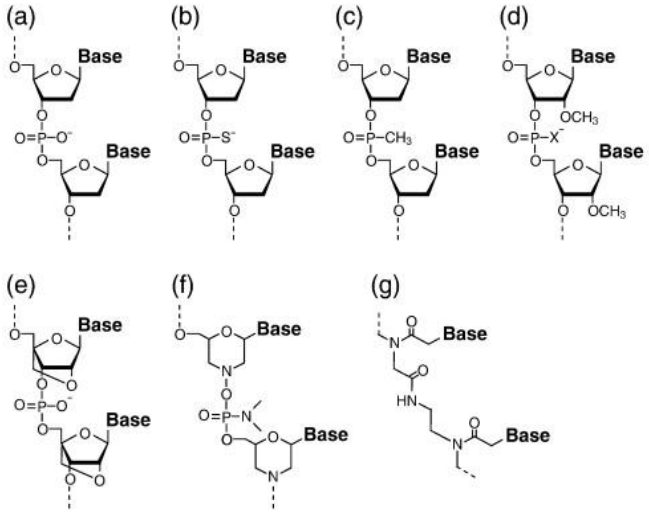

Figure 1.12. Structures of natural (phosphodiester) DNA and various DNA derivatives. Most DNA derivatives are more resistant to degradation by DNases than phosphodiesters. (a) phosphodiester DNA, (b) phosphothioate DNA, (c) methylphosphonate DNA, (d) 2'-O-methyl RNA (X = O or S), (e) locked nucleic acid, (f) morpholino and (g) PNA. Figure adapted from ref. [130].

DNA has attracted attention due to its functionality and versatility. The specificity of DNA hybridization has been exploited to develop DNA nanoscale systems with unique molecular recognition functions, which can be applied for

biomedical applications such as gene regulation[133], drug delivery[135-137] and diagnostic detection[136, 138]. A promising new era has begun, with more DNA-based systems being studied and applied in the field of nanomedicine.

1.3.2.1 DNA nanotechnology

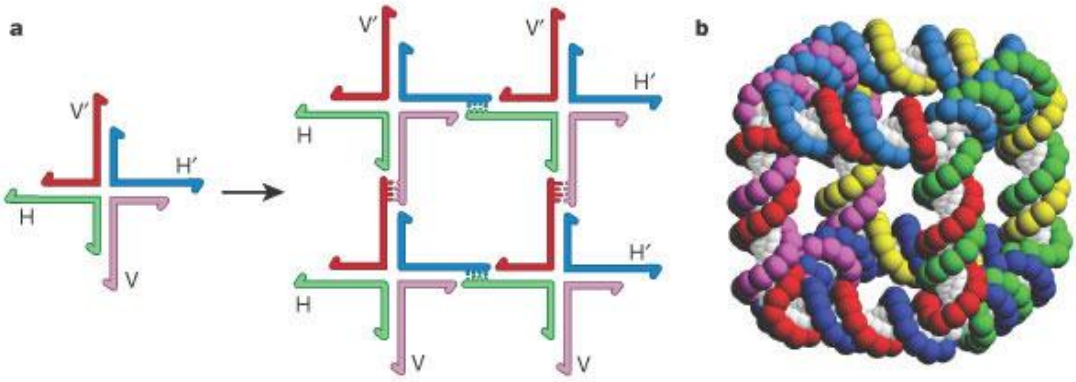

Figure 1.13. Assembly of a DNA branch, a two dimensional DNA network and a cube-like DNA nanostructure. (a) a DNA branched junction formed by four DNA strands with sticky-end overhangs (V, V', H and H', of which V' is complementary to V and H' is complementary to H), and a square-like unit formed by four DNA branched junctions, which can further form a two-dimensional network. (b) A more complex cube-like DNA nanostructure created by interconnected DNA rings in the presence of sticky ends[139]. Figure adapted from ref.[140].

DNA self-assembly offers a very attractive 'bottom up' strategy for designing complex nanostructures, as dsDNA has certain features, such as a diameter of 2 nm, a repeatable unit (helical pitch) of around 3.5 nm and stiffness at a persistence length of up to 50 nm, which fulfill the requirement for building well-defined structures[140]. As well as linear double-stranded DNA formed *via* base pair recognition, more complex DNA structures can be generated by introducing sticky ends, which are short single-stranded overhangs at the end of double stranded DNAs. These structures can be DNA branches,

two-dimensional DNA networks, and even three-dimensional nanostructures (Figure 1.13). The first artificial DNA fabrication, a sticky cube made entirely of DNA, was constructed more than a decade ago (Figure 1.13b)[139]. Since then, several simple yet versatile self-assembly techniques have been developed to construct more complex DNA nanostructures[141-143].

DNA nanomachines

As well as these complex two- and three-dimensional static DNA nanostructures, DNA-based nanomechanical devices (DNA nanomachines) have also been generated which can perform nanoscale movements responding to specific stimuli. Bernard Yurke and his colleagues developed a DNA nanomachine known as molecular tweezers (Figure 1.14)[144]. This was formed by hybridising three DNA strands, A, B and C, and made to open and close by the alternate addition of “fuel” strands F (closing strand) and F’ (opening strand). DNA F can hybridize with the overhangs of B and C to make the tweezers close and F’ can separate F from the tweezers *via* thermo-dynamically favoured hybridization to leave them open. The motion of the DNA molecular tweezer can be monitored by measuring the changes in fluorescence intensity as a function of the separation between dye TET and dye TAMRA, which were attached to the 5’ and 3’ ends of DNA A, respectively. When the tweezers are pulled closed by F, fluorescence intensity is reduced due to Fluorescence Resonant Energy Transfer (FRET) from Dye TET to Dye TAMRA.

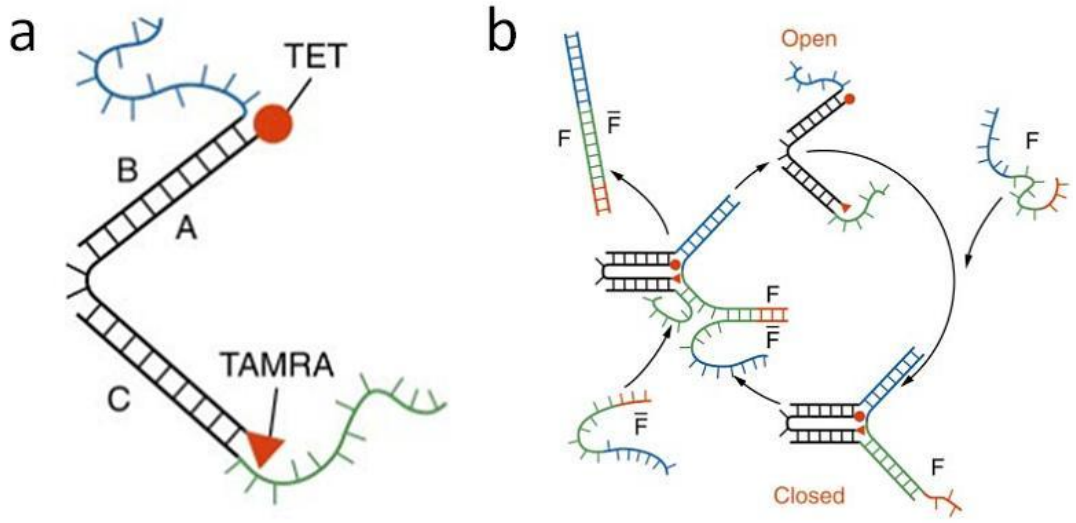

Figure 1.14. DNA-fuelled tweezers. (a) Structure of DNA tweezers created by hybridisation of DNA strands A, B and C. (b) Performance of DNA tweezers between open and closed states *via* alternative addition of closing strand and opening strand. Figure adapted from ref.[144].

1.3.2.2 *i*-motif DNA nanomachine

Although the DNA molecular tweezers described above can perform precisely controlled motions powered by DNA fuels, they do however suffer from some drawbacks, such as relatively slow operational speed and gradually decreasing performance due to system poisoning by waste DNA produced in the cycle. Nevertheless, they inspired researchers to design new DNA nanomachines such as the *i*-motif DNA nanomachine. *i*-motif DNA contains stretches of two or more cytosines (C-rich domains), and at acidic pH the cytosines in the C-rich domains are partially protonated, which leads to the formation of triple hydrogen bonds between pairs of protonated (CH^+) and nonprotonated (C) cytosines. As a result, *i*-motif DNA can adopt a non-B tetrameric structure (C-quadruplex), denoted as '*i*-DNA motif' or '*i*-motif', from the formation of hemiprotonated cytosine base pairs (Figure 1.15), instead of classic Watson-Crick base pairs.

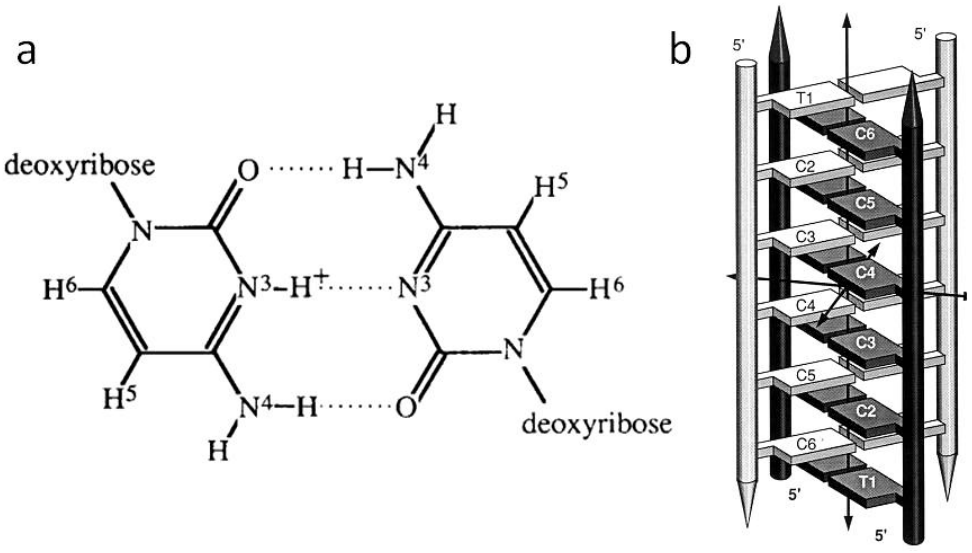

Figure 1.15. (**a**) Scheme of the triple hydrogen bonding between cytosine and protonated cytosine ($C{\cdot}C^+$) base pairs; (**b**) Schematic representation of the *i*-motif structure formed by four DNA oligomers (5-d(TCCCCC)). Figure adapted from ref.[145] .

Cytosine base pairs were first observed decades ago in acetylcytosine crystals [146], then later found in polydeoxyribonucleotides[147] and polyribo-nucleotides[148, 149]. Oligodeoxynucleotides with hemi-protonated cytosine base pairs formed at slightly acidic pH had been thought of as a double stranded DNA structure until 1993, when Kalle Gehring and colleagues used NMR spectroscopy to investigate the structure formed by DNA oligomers 5-d(TCCCCC) at acidic pH. and confirmed it to be a complex four-stranded structure (Figure 1.15b)[145].

In this pH-dependent tetrameric conformation, two parallel strands form a duplex *via* $C \bullet C^+$ base pairs. One parallel-stranded duplex is linked with the other duplex in an orthogonal, anti-parallel orientation, through intercalation of the cytosine base pairs. As well as the *i*-motif in form of a tetramer, *i*-motif dimmers and *i*-motif monomers (intramolecular *i*-motifs) can also be formed by DNA strands with two and four stretches of cytosines, respectively (Figure 1.16)[150]. Strictly speaking, the structure of an *i*-motif is a not true quadruplex,

like the G-quadruplex based on quartet formation, but a double-duplex based on cytosine base pairs and intercalation.

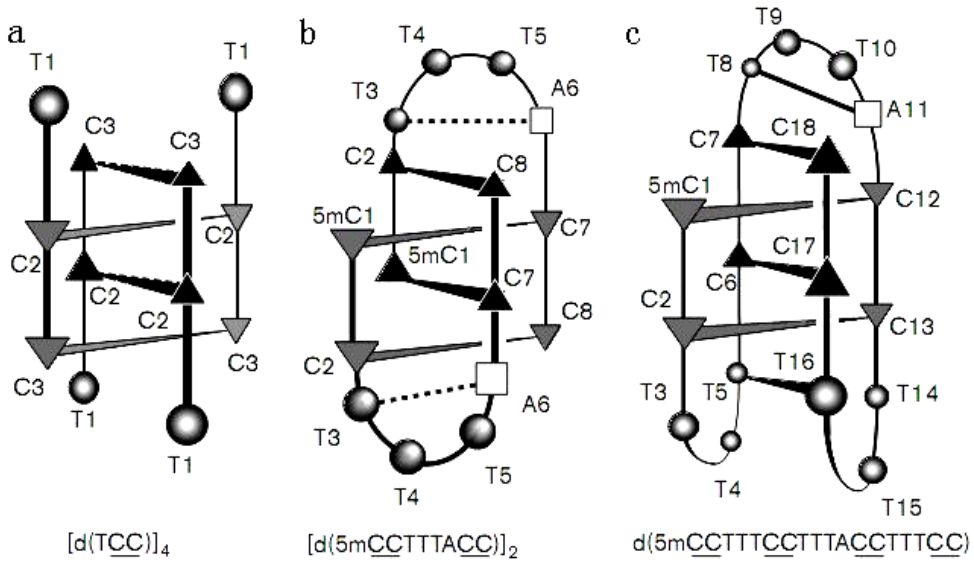

Figure 1.16. Representation of *i*-motif structures formed by four monomers (**a**), two dimers (**b**) and a tetramer (**c**), respectively. Figure adapted from ref.[150].

Although the formation of *i*-motif is mainly driven by the triple-hydrogen bond formed between hemi-protonated C≡CH+ pairs at weakly acidic pH, other favourable interactions are also involved and contributed to its overall stability[150, 151]. For example, the C·CH+ base pairs are stacked nearly orthogonally within the *i*-motif structure, which form two wide grooves and two narrow grooves. The short distance between deoxyriboses in the narrow grooves can lead to the formation of relatively weak CH···O hydrogen bonds that are energetically favourable for *i*-motif formation. Also the parallel flat base pairs in the two intercalated duplexes within the *i*-motif structure allow for π–π stacking and hydrophobic interactions, reducing the exposure of relatively hydrophobic bases to the aqueous environment which is also favourable. And finally, in the case of our specific *i*-motif designs, the possible formation of A=T base pairs in the three TAA loops at the ends of *i*-motif structure can further contribute to the overall thermodynamic stability.

An *i*-motif structure can also unfold into a random coil, or form a duplex DNA

with a complementary DNA as a result of external stimuli such as pH changes. It has been reported that *i*-motif based nanomachines (molecular motors) can perform a two-stroke movement (contraction and extension), responding to *i*-motif structures (closed state) and random coils or duplex DNAs (open state) [152-156].

One possible way of fuelling this kind of *i*-motif nanomachine to repeatedly perform such movements is by adding DNA fuel strands (Figure 1.17a)[153]. The *i*-motif structure (core sequence) can be unfolded into a duplex DNA, which is driven by the addition of a complementary DNA fuel strand (red/black). To refold into an *i*-motif, the other DNA fuel strand (blue/green) is added to replace the core sequence, then hybridised with the red/black fuel strand, which allows the core sequence to be dispatched and to self-assemble into a compact *i*-motif structure. However, a byproduct, duplex DNA waste, is produced during each cycle in the system. This can impact on the cycling ability of this type of DNA nanomachine as more and more DNA waste accumulates in the system, and poisons it, leading to gradually decreased performance like that reported for the DNA tweezers above.

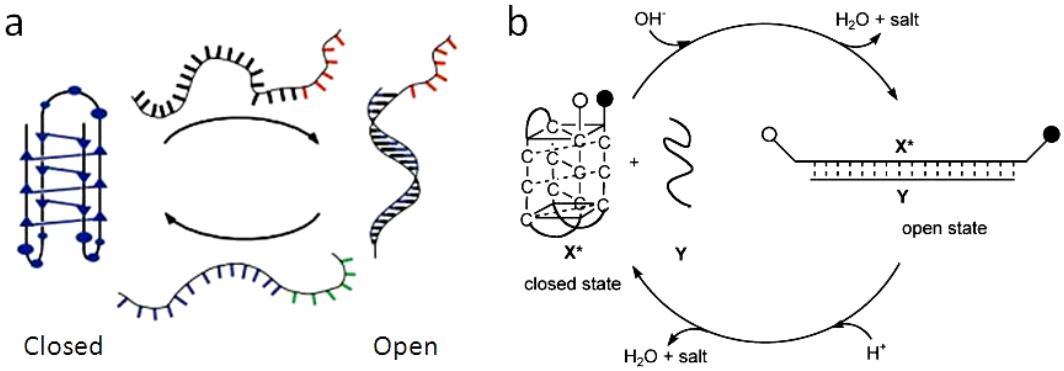

Figure 1.17. *i*-motif based nanomachines fuelled by DNA strands (**a**) and proton (pH changes) (**b**). Figure adapted from refs[153, 157].

The other stimulus for fuelling the *i*-motif based nanomachine is proton (or pH changes), first proposed by Liu and Balasubramanian in 2003 (Figure

1.17b)[157]. A 21 mer single strand DNA X with four stretches of cytosines (5-d[$(CCCTAA)_3$ CCC] and a complementary DNA Y with two mismatches were used to construct this pH-driven DNA nanomachine. To monitor the two-stroke movements of the *i*-motif machine, DNA X was labelled with a rhodamine green fluorophore at the 5' end and a dabcyl quencher at the 3' end, named X*. When the system pH was 5.0, DNA X (X*) folded into a compact *i*-motif structure and the fluorescence of rhodamine green was strongly quenched by the dabcyl. When the system pH was changed to 8.0, the *i*-motif unfolded into a random coil and hybridised to DNA Y to form a rigid duplex. Fluorescence recovery then became strong, because the fluorophore and quencher were widely separated and quenching was thus greatly reduced. This *i*-motif based DNA nanomachine was highly reversible; its operating performance showed no signs of degradation even after 30 full cycles, with the alternate addition of HCl and NaOH changing the system pH between 5.0 and 8.0. In fact it showed a very rapid response: the conformation changes between contraction and extension happened in seconds following each environmental pH change. Compared to the DNA-fuelled *i*-motif nanomachine, the proton-fuelled *i*-motif nanomachine system is more robust and displays a faster response. It is also cleaner than most other DNA nanomachines; the waste byproducts H_2O and NaCl which result from the addition of HCl and NaOH seem to have no impact on the nanomachine's performance, even after 30 cycles.

As well as manual adjustment of the system pH, this proton-fuelled *i*-motif nanomachine can also be driven by an oscillatory chemical reaction [158, 159], or UV light radiation both of which can lead to the system pH being cycled automatically, *i.e.* without direct contact. This would make the *i*-motif based DNA nanomachine system highly desirable for the construction of a wide range of pH-responsive DNA nanostructures and devices.

For practical applications, DNA nanomachines should ideally be stable, robust and simple to operate, without generating harmful byproducts and they should conjugate easily to the relevant objects[155]. In these respects, the proton-fuelled *i*-motif DNA nanomachine appears to be highly attractive, and indeed several functioning DNA nanodevices have been successfully constructed using the proton-fuelled *i*-motif nanomachine. Some examples of these include: a DNA-based optical on/off nanoswitch[160], a pH-responsive surface that can switch between hydrophilic and hydrophobic in response to environmental pH [161], a controllable way of assembling nanoscale objects (*i.e.* GNPs)[162], a device for bending microscale objects(*i.e.* a micromechanical cantilever array covered with gold-film)[163], colorimetric and electrochemical pH sensors[164, 165] and a synthetic nanopore that can mimic functions of ion channels[166].

Proton-fuelled *i*-motif nanomachine applied inside endosomes of living cells

Endosomes are membrane-bound vesicles inside eukaryotic cells, formed through the endocytic process (endocytosis). They are used for transporting various internalized substances from plasma membrane to lysosomes for digestion[167] (Figure 1.18). Three different types of endosome (early endosomes, late endosomes and lysosomes) can be found inside the cells. They exhibit different morphologies and respond to different development stages of endosome maturation, with initial forms of early endosomes maturing into late endosomes and then fusing into lysosomes[168]. Due to the activity of the V-ATPase, endosomes at different stages have different characteristic pH values, which are typically in the range of 6-6.2 in early endosomes, 5.5 in late endosomes and 4.3-5 in lysosomes[169]. In other words, the pH value becomes

progressively more acidic during the process of endosome maturation.

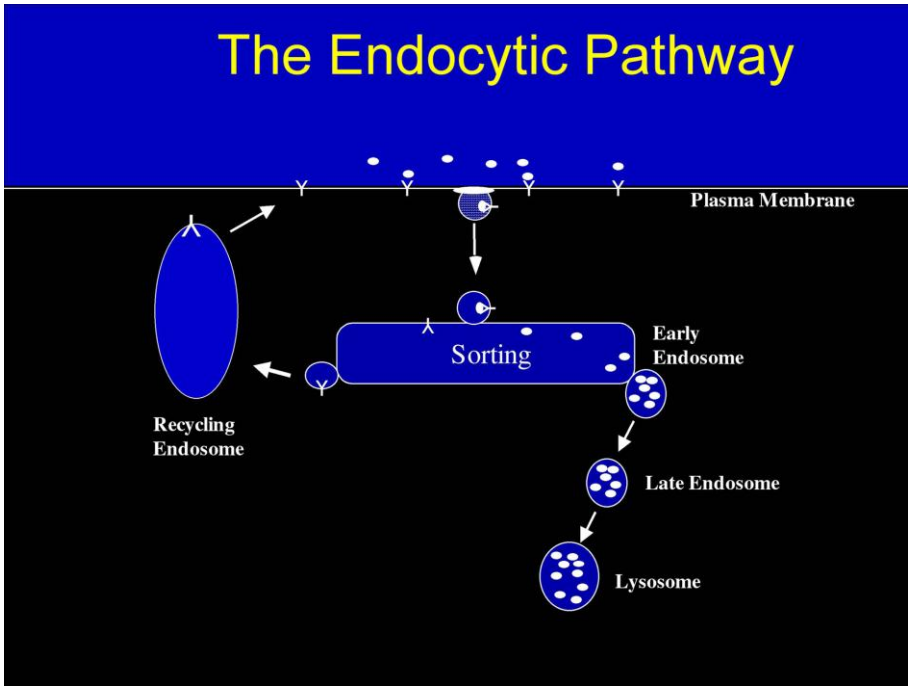

Figure 1.18. A schematic representation of the endocytic pathway. Substances outside cells are internalised from the plasma membrane, then are sorted and either recycled back to the plasma membrane through the recycling pathway or transported to lysosomes through late endosomes. Figure adapted from ref.[170].

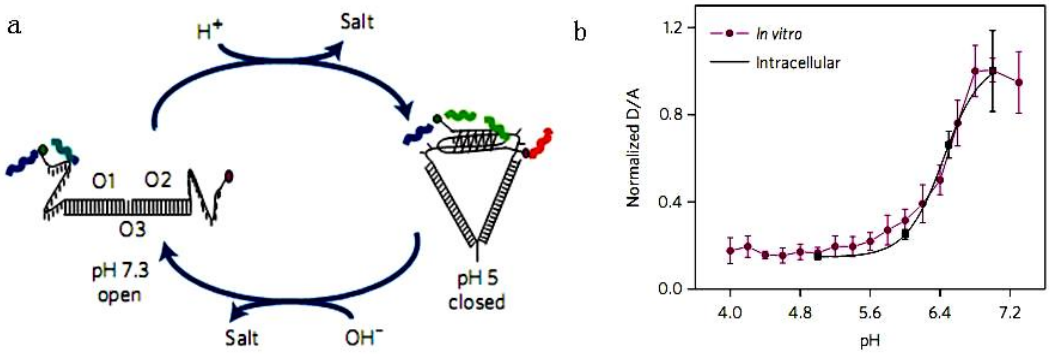

Figure 1.19. (**a**) Working principle of an *i*-motif DNA nanomachine for mapping pH changes during endosome maturation: at pH 7.3, it is in an 'open' state, leading to low FRET and at pH 5, it is in a 'closed' state, resulting in high FRET; (**b**) Plots of normalised donor/acceptor (D/A) intensity ratios *in vitro* and inside cells (endosomes) as a function of pH, indicating that the intracellular pH calibration curve is overlapped with the *in vitro* pH profile. Figure adapted from ref.[171].

In 2009, Krishnan and co-workers demonstrated an *i*-motif nanomachine that would work inside living cells[171]. This was used to map spatial and temporal pH changes related to the endosome maturation process (Figure 1.19). As *i*-motif DNAs have conformational transitions in a similar pH range, they can be employed to monitor and capture spatio-temporal pH changes during endocytosis. To do this three DNA strands, O1, O2 and O3, were designed, and both O1 and O2 hybridised to O3 with a one-base gap between the O1 and O2 duplex regions. O1 and O2 both contained one single stranded overhang with two stretches of five cytosines, and at acidic pH the two overhangs were able to form an *i*-motif structure. By attaching an Alexa-488/ Alexa-647 FRET pair at the end of each overhang, an *i*-motif DNA system was developed as a pH sensor based on FRET. A intracellular pH calibration curve was obtained by measuring the ratio of fluorescence intensity in the donor (Alexa-488) to that of the acceptor (Alexa-647) (D/A) as a function of pH in endosomes, which matched well with that *in vitro*. This curve was subsequently used to monitor the endosomal maturation process. With time, the D/A ratios in the endosomes changed and pH values were determined to be 5.9 at 5 min, 5.45 at 60 min and 5.0 at 120 min, corresponding to the different stages of endosome maturation. This is the first example of a DNA nanomachine that works inside living cells, and it may inspire researchers to develop further DNA nanomachine systems for *in vivo* applications such as diagnostics and targeted drug delivery.

_i_-motif nanomachines functioning as potential drug carriers

The *i*-motif nanomachine system (*i.e. i*-motif hydrogel and *i*-motif nanocontainer) has also been employed as a potential drug carrier to entrap and release drugs in response to pH-induced conformational changes.

_i_-motif hydrogel

Liu and Zhou designed a Y-shaped DNA building block with three arms (Y-unit), which was able to form an *i*-motif DNA hydrogel by interacting with others, forming intermolecular *i*-motifs (Figure 1.20). This pH-responsive *i*-motif hydrogel can potentially be applied to entrap drugs at low pH and release them at high pH[172].

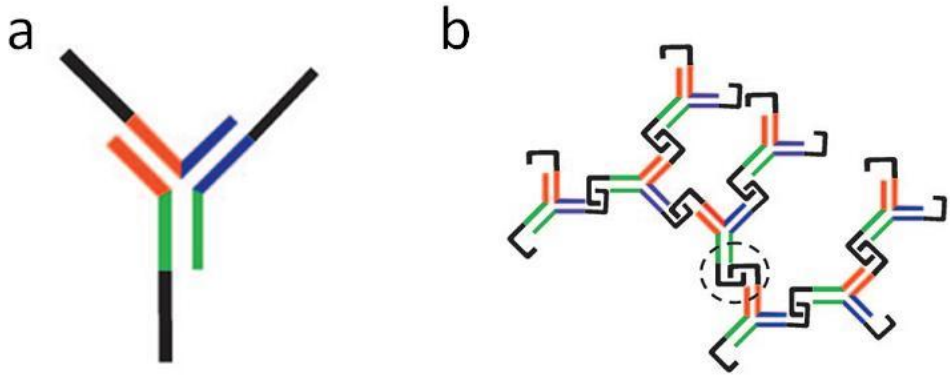

Figure 1.20. Working principle of the DNA hydrogel. (**a**) A Y-shaped DNA (Y unit) with three overhanging C-rich domains (two stretches of four cytosines) for interlocking; (**b**) Three-dimensional DNA hydrogel created through formation of *i*-motifs (*i.e.* the circled region) between adjacent Y units. Figure adapted from ref.[172].

Y-shaped DNA comprises three single-stranded DNAs, each containing two functional domains, a Y-shape domain (two DNA sequences half-complementary to the other two DNAs) and an *i*-motif domain (two stretches of four cytosines). GNPs were employed as a drug model for observing the gel-non-gel transition process, and dispersed in the system. At pH 5.0, the three *i*-motif domains from each Y unit formed inter-unit *i*-motifs with their neighbouring Y units. As a result, the system turned into an unrestricted three-dimensional DNA assembly, a hydrogel made of entirely from DNA where GNPs are trapped, resulting in a red-color gel which cannot escape. At pH 8.0, the *i*-motif domains unfold into random coils and the Y-units can no longer interact with each other, turning the system into a solution (non-gel) state and releasing GNPs. This *i*-motif hydrogel can respond very quickly to

environmental pH changes, the transition between gel state and non-gel state taking place in one minute. However, its pH-responsiveness happens on the wrong side of the pH range for cancer treatment.

i-motif nanocontainer

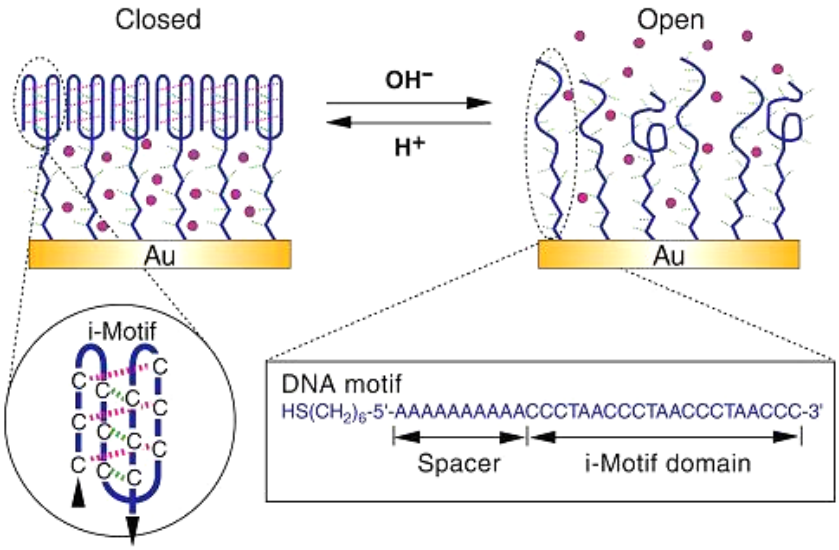

Figure 1.21. A nanocontainer formed by attaching *i*-motif DNAs (also containing a spacer sequence) to a gold surface, where small molecules can be entrapped in the 'closed' state at low pH, and released in the 'open' state at high pH. Figure adapted from ref.[173].

Using a surface-based 'bottom-up' technique, an *i*-motif nanocontainer (nanocarrier) with the ability to catch and release small molecules was reported by Liu and co-workers[173]. 5'-thiol modified *i*-motif DNAs containing both a single-stranded poly-$(dA)_n$ spacer (n=10-35) and an *i*-motif domain (d[$(CCCTAA)_3CCC$]) was designed and these *i*-motif DNAs were attached to the gold surface at pH 4.5 (Figure 1.21). The four-stranded *i*-motif domains are tightly packed, while single stranded spacers are packed with low density to allow space for storing small target molecules. The *i*-motif DNAs with these packing patterns cooperate with one another on the gold surface, forming a smart nanocontainer between the tightly packed *i*-motif layer and the gold surface. This can close or open to catch or release non-specific small molecules

in response to environmental pH stimuli. This nanocontainer can be designed to be impermeable in the closed state, and reversible transition between the closed and open states is rapid.

Although *i*-motifs have been demonstrated to form hydrogels and nanocontainers, their loading and releasing mechanisms mean that they are still far from being practical as drug carriers. Unlike healthy tissues which have a normal pH of ~7.4, diseased regions such as tumours and intracellular endosomal/lysosomal compartments often exhibit abnormally high local acidities [169, 174]. Therefore any pH-responsive drug nanocarrier to be used for cancer targeting should be stable without release at physiological pH, and only release the loaded drugs as the environmental pH becomes weakly acidic; not vice versa. Therefore, *i*-motif based hydrogels and nanocontainers cannot be used for cancer targeting.

1.3.3 Doxorubicin: from old drug to new form of chemotherapy

Doxorubicin (DOX, trade name: Adriamycin®), an anthracycline family of antibiotics derived from a strain of Streptomyces, is one of the most widely-used active chemotherapeutic agents. It has a wide spectrum of activity against different types of cancer, such as bladder, breast, stomach, lung, ovaries, thyroid, soft tissue sarcoma and multiple myeloma [175, 176] *etc*. DOX consists of an aglycone with a tetracyclic ring and a sugar moiety (daunosamine). DOX is sensitive to light and degrades relatively quickly at alkaline pH while it is relatively stable between pH values of 2 and 7[177]. Although developed nearly half a century ago, the mechanism of action of DOX remains unclear currently. A number of mechanisms have been proposed[178, 179], including: 1) intercalation into the dsDNA gene to inhibit gene transcription; 2) formation of free radicals, resulting in gene damage and/or lipid peroxidation; 3) DNA binding

and alkylation; 4) DNA cross-linking; 5) intervention in DNA unwinding and helicase activity, and 6) inhibition of topoisomerase II activity. To date, there has been no unambiguous conclusion on which is the main mechanism of action yet. It is highly possible that DOX may exert one or more modes of action, which may also be dependent on its concentration. However, the uncertainty of action mechanism has certainly not prevented it being widely used as a model chemotherapy drug for cancer research studies, where the numbers of published papers and citations have shown an exponential increase over the past 10 years (Figure 1.22).

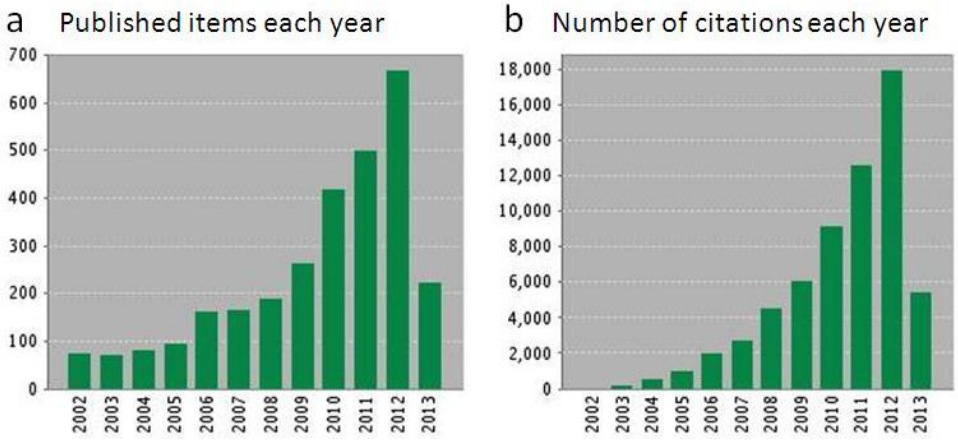

Figure 1.22. Growing number of published papers (**a**) and citations (**b**) over the past 10 years which refer to DOX as the model chemotherapy drug. These data were obtained from the Web of Science using the search term: **topic = 'doxorubicin' and 'drug delivery' and 'cancer'** on 7th May 2013.

Despite extensive clinical use for several decades, its serious side effects, particularly irreversible cardiac damage, have significantly limited its clinical dosage and hence therapeutic efficacy [180, 181]. To improve cardiac safety and efficacy, two different approaches have been explored[179]. One is to develop new analogs by introducing chemical modifications, substitutions or conjugations in the aromatic ring and/or the sugar moiety of anthracyclines. In this regard, more than 2000 analogs have been developed, however, only a few DOX analogs, *e.g.* epirubicin and pirarubicin, have shown slightly better

therapeutic improvements and subsequently been approved as new anti-cancer drugs, The other more effective approach has been to improve its chemotherapeutical index and favourable clinical use by employing targeted drug nanocarriers to deliver DOX specifically into the tumour region. This can also reduce the risk of inducing multidrug resistance[182, 183]. To date, several different targeted DOX delivery systems have been developed (*e.g.* liposomes, polymer-based and inorganic nanoparticle-based nanocarriers), many of which have shown significant improvements in terms of both therapeutic efficacy and reduced side effects, some of which has already been approved for clinical use. In addition, a variety of DOX loading mechanisms have been successfully employed, such as encapsulation[184, 185], electrostatic binding[186, 187], physical adsorption[188] and chemical conjugation[189, 190].

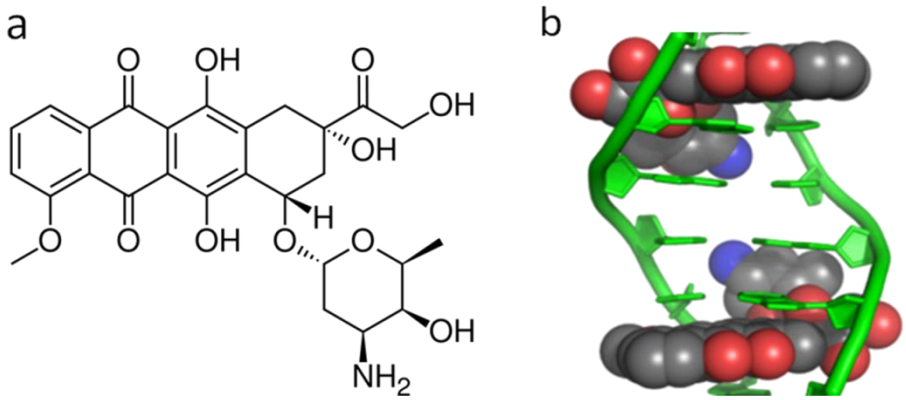

Figure 1.23. (**a**): Molecular structure of DOX; (**b**): structural model of DOX intercalated duplex DNA[191].

Besides the loading mechanisms mentioned above, DOX can also be carried by dsDNAs in a form of physical conjugate dsDNA-DOX through intercalation. Due to the presence of flat aromatic rings in its structure and its appropriate size, the DOX molecule can fit itself in between two base pairs of a dsDNA with the daunosamine moiety locating in the minor groove and interacting with flanking base pairs (Figure 1.24). Such conjugate is stabilised by π-π stacking between

the aromatic ring of DOX and DNA bases and hydrogen bond interaction assisted by water molecules. dsDNA-DOX conjugate was first studied for DOX delivery in the1970s[192-194] and has been incorporated into nanoscale tumour-targeting systems in recent years, benefiting from nanotechnology development[195-200]. Intercalating DOX into dsDNA offers a very simple, direct DOX loading in native format without involving any chemical modifications or conjugation that may interfere with DOX activity and cytotoxicity. However, DOX release from such literature systems is mainly through passive dissociation, lacking of stimulus-responsive release. As a result, it tends to be a slow process, for example, only 28%[198] or 50%[200] of the loaded DOX was released over 24 h. Also, these systems exhibit limited stability in biological fluids, which can seriously limit their potential for in vivo application. Therefore the development of a dsDNA-DOX conjugate that can offer efficient environmental stimuli-triggered DOX release and good stability in biological relevant media is an urgent unresolved issue which is also essential to realising its application in vivo.

1.4 Aims of the project

In this project, we aim to develop a new pH-responsive targeted drug delivery system by combining the pH-responsiveness of the *i*-motif DNA nanomachine with the excellent biocompatibility and stability of metal nanoparticles (Figure 1.24). We hope that this system will prove to be an effective anticancer treatment, combining efficient delivery with a pH-responsive release of drug load.

Firstly, *i*-motif DNA strands (containing one, two or three *i*-motif domains to increase their drug loading capacity) are to be designed as the pH-responsive strands. The specific *i*-motif sequence used in this project is the C-rich strand

sequence of the human telomere structure, which, together with its complementary G-rich strand, is critical for maintaining the gene stability and cell division, and hence has high biological significance. C-rich sequences capable of forming *i*-motif structures can also be found in centromeres and gene promoters regions, although their specific biological functions are still not very clear currently. These pH-responsive strands will further be used to form dsDNAs with complementary DNAs, acting as drug carriers where DOX can be readily loaded in native format through intercalation. These dsDNA-DOX conjugates will be studied to evaluate the feasibility of using an *i*-motif DNA nanomachine to control drug loading/releasing in a pH-responsive manner (*i.e.* loading in physiological pH and releasing in slightly acidic pH).

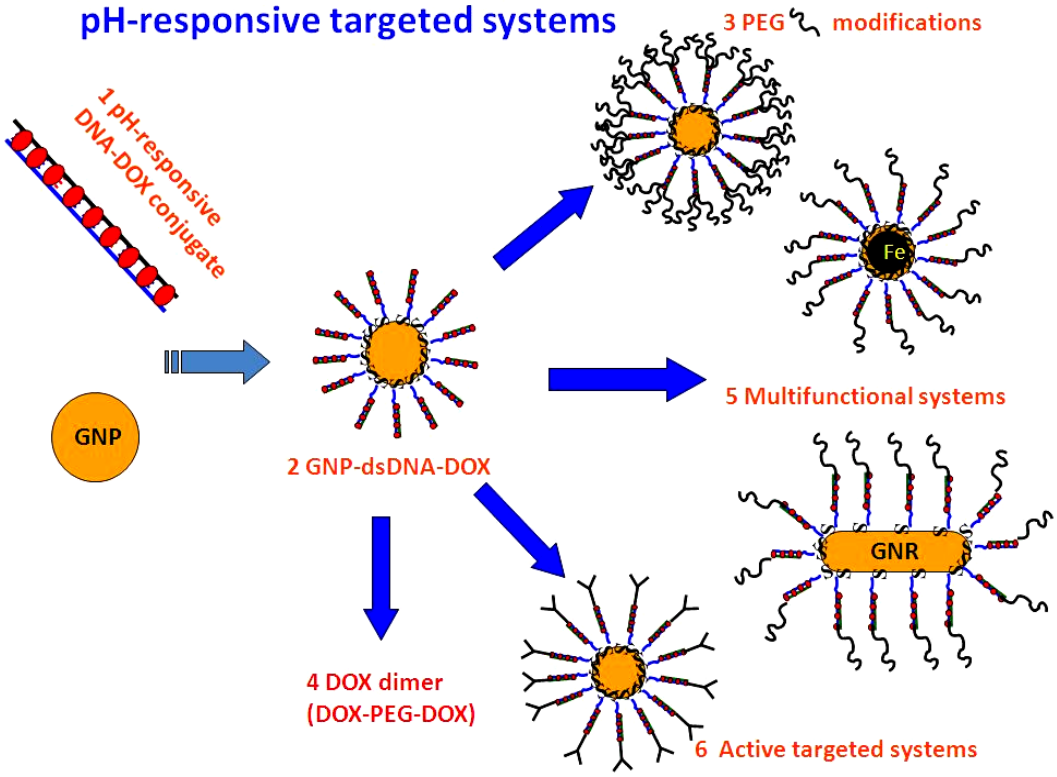

Figure 1.24. Schematic of aims of the project: **1** to employ *i*-motif DNA-formed dsDNA to carry DOX *via* intercalation; **2** to attach a dsDNA-DOX conjugate to GNPs to prepare a pH-responsive GNP-dsDNA-DOX system; **3** to incorporate PEGs into the surface of the GNP-dsDNA-DOX system; **4** to synthesize a DOX dimer; **5** to prepare GNR-dsDNA-DOX and Fe@Au-dsDNA-DOX systems; **6** to attach targeting ligands to the surface of the GNP-dsDNA-DOX system for active targeting.

Secondly, the dsDNA-DOX conjugates are to be attached to GNPs to prepare a passive targeted NDDS (GNP-dsDNA-DOX conjugate), which can exploit the EPR effect characteristic for solid tumours and accumulate inside them. Relevant cellular studies are to be performed to confirm that this NDDS can be taken in by cells through the endocytic pathway, so that local acidic pH in intracellular endosomes/lysosomes will trigger DOX release inside cells, resulting in high cytotoxicity.

Finally, several modifications based on this GNP-dsDNA-DOX system are to be performed, to further enhance therapeutic efficacy as follows (Figure 1.24):

1. PEG will be incorporated into the surface of the system to enhance its stability and resistance to non-specific adsorption of biomolecules
2. Gold nanorods and gold-coated magnetic nanoparticles are to be synthesized to replace the GNP when preparing GNR-dsDNA-DOX and Fe@Au-dsDNA-DOX, with the aim of constructing multifunctional NDDSs that can provide multiple therapeutic modalities with imaging capability
3. A DOX dimer will be synthesized to investigate whether its therapeutic index can be enhanced and DNA binding affinity improved compared to the DOX monomer
4. Targeting ligands (*i.e.* an RGD peptide and folic acid) will be attached to the surface of the system to explore the possibility of further developing this system into an active targeted drug delivery system, with improved cancer targeting ability and therapeutic efficacy.

2 Chapter 2: pH-responsive dsDNA-DOX conjugates

The principle to prepare pH-responsive dsDNA-DOX conjugate is based on the following facts: (1) A single-stranded (ss) DNA motor containing 4-stretches of cytosine (C) rich sequences can reversibly switch its conformation between a random coil and an *i*-motif structure following environmental pH changes *via* the non-Watson-Crick DNA base pairings between hemiprotonated cytosines[145]. (2) Some well-known anticancer drugs (*e.g.* DOX) can intercalate with specific sequences within double-stranded DNA[135, 200, 201], but not with single-stranded or *i*-motif structures.

Here we designed a series of single-stranded (ss) DNA motors, M1, M2 and M3, containing one, two and three *i*-motif domains respectively, where each domain contains four stretches of C-rich sequences, and acts as a pH responsive unit. These DNA motors are used to form double-stranded (ds) DNA structures with a complementary strand, MC2 (MC3 or MC4) which has two (three or four) base mismatches to the *i*-motif domain. PEG-modified complementary DNAs (MC2 (PEG250) and MC2 (PEG750)) were also used to form dsDNAs with M1 in order to evaluate PEG effects on *i*-motif conformation switch.

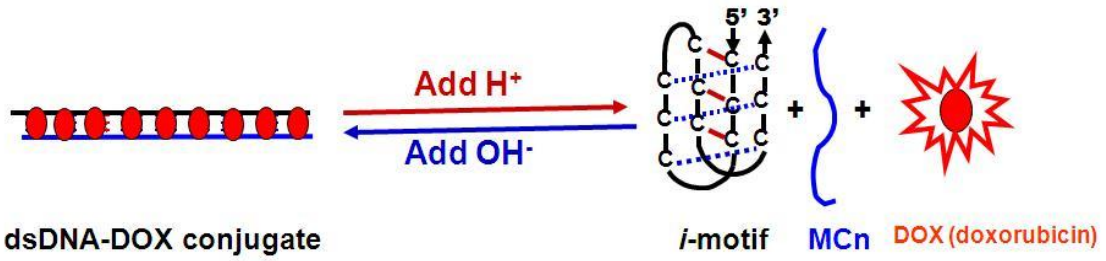

Figure 2.1. Schematic procedures of the proposed pH-responsive DNA switch system for reversible DOX binding and release. The fluorescence of DOX intercalated within the DNA duplex is quenched but becomes strongly fluorescent after release (MCn: n=2-4).

DOX is used as the model intercalating drug. The system design is shown schematically in Figure 2.1. At neutral pH or above, the DNA exists as a dsDNA structure such that DOX can intercalate to produce a dsDNA-DOX conjugate, whereas as the solution pH is changed to weakly-acidic, the *i*-motif domain(s) in M1 (M2 or M3) will fold into one (two or three) C-quadruplex (*i*-motif) structure, detaching its complementary strand so that DOX is released from the DNA system. We would like to study the formation of the dsDNA-DOX conjugate, the kinetic information about the conformation switch between the dsDNA-DOX conjugate and C-quadruplex + free DOX + complementary DNA states, and whether this switch is reversible as the solution pH is cycled between neutral and weakly acidic pHs.

2.1 Materials and Methods

2.1.1 Materials

MES (2-(*N*-morpholino)ethane sulfonic acid monohydrate) (98%) was purchased from Alfa Aesar. HCl (36%), NaOH, NaCl (99.99%), and doxorubicin hydrochloride were purchased from Fisher Scientific. Millipore water (resistance >18.2 MΩ.cm), purified by ELGA Purelab classic UVF system, was used for making buffers in all experiments. All buffers were filtered through a Whatman syringe filter (0.20 μm pore size, Whatman Plc.) before use. HPLC purified oligonucleotides (except for MC2(PEG750), which was synthesized by Prof. Dongsheng Liu's Group, Tsinghua University, China) were all purchased from IBA GmbH, Germany, and their sequences and abbreviations are given in Table 2.1.

Table 2.1. DNA abbreviations and their sequences (5'→3') used in this thesis.

DNA name	Sequence (5' → 3')
M1	(thiol)TTT TTT TTT TCC CTA ACC CTA ACC CTA ACC C
M2	(thiol)TTT TTT TTT TCC CTA ACC CTA ACC CTA ACC CTA ACC CTA ACC CTA ACC CTA ACC C
M3	(thiol)TTT TTT TTT TCC CTA ACC CTA ACC CTA ACC CTA ACC CTA ACC CTA ACC CTA ACC CTA ACC CTA ACC CTA ACC C
MC2	G**T**G TTA GG**T** TTA GGG TTA GGG
MC3	G**T**G TTA GG**T** TTA GGG TTA G**T**G
MC4	G**T**G TTA GG**T** TTA GGG **A**TA G**T**G
MC2(PEG250)	PEG_{250}-G**T**G TTA GG**T** TTA GGG TTA GGG
MC2(PEG750)	PEG_{750}-G**T**G TTA GG**T** TTA GGG TTA GGG

*MC2: two mismatches; MC3: three mismatches; MC4: four mismatches, and the mismatch sequences are shown in red.

2.1.2 DNA hybridisation

5 nmol M1, M2 or M3 was mixed with 5 (10 or 15) nmol of MC2 (MC3, MC4, MC2 (PEG250) or MC2 (PEG750)), in 150 µL of MES buffer (pH 7.4, 50 mM MES, 0.15 M NaCl) and allowed to hybridize for 3 h to make the M1/MC3, M2/MC3, M3/MC3, M1/MC2, M1/MC4, M1/MC2(PEG250), and M1/MC2(PEG750) dsDNAs, which were then used to prepare the DOX-dsDNA physical conjugates.

2.1.3 Preparation of DOX and dsDNA conjugates (dsDNA-DOX conjugates)

2.5 nmol dsDNA was gradually added to 500 µL of 10 µM DOX MES buffer solution to form dsDNA-DOX conjugates, during which the fluorescence spectra of DOX were recorded on a Spex Fluoro Max-3 Spectrofluorometer (0.75 mL

quartz cuvette, excitation wavelength: 480 nm, with an emission scanning range of 500-720 nm).

2.1.4 pH responsiveness and reversibility of dsDNA-DOX conjugates

The pH of the dsDNA-DOX conjugates was then gradually adjusted from 7.4 to 4 using 1 M HCl (in total 27.6 μL), and the pH value at each stage was obtained through the pH calibration curve (Figure 2.2). The resulting fluorescence spectra were recorded. Then the solution pH was cycled between 4 and 7.4 by alternate additions of 1M NaOH or 1M HCl, and the resulting fluorescence spectra were recorded 3 min after each solution pH change.

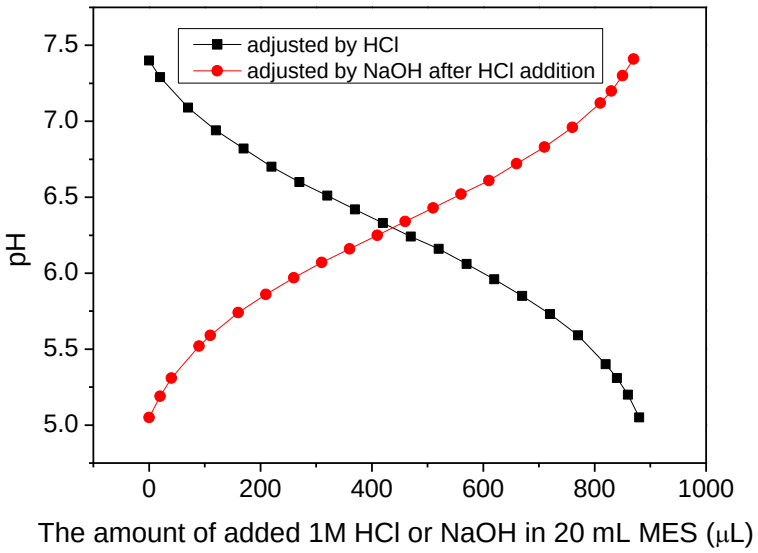

Figure 2.2. pH calibration curve.

2.1.5 Melting temperature measurement

dsDNAs (1 μM for M1-formed dsDNAs; 0.5 μM for M2/MC3 and 0.375 μM for M3/MC3) and dsDNA-DOX conjugates (where the dsDNA concentrations were the same as their corresponding dsDNA-only samples, with a fixed DOX concentration of 5 μM) were prepared in the MES buffer solution (50 mM MES, 0.15 M NaCl, pH 7.4). Their temperature-dependent absorbances at 260 nm (*i.e.*

UV-melting curve, mainly resulting from DNA absorption) were obtained on a HP 8452A Diode Array Spectrophotometer (temperature ramp: 0.1; holding time: 2 min, and temperature range from 20 to 80 °C). The corresponding absorbances at 360 and 480 nm were monitored at the same time. The MES buffer-only solution was used as a blank.

2.1.6 Circular Dichroism (CD) measurement

CD spectra of M1/MC2 (10 μM), M2/MC2 (10 μM) and M3/MC2 (10 μM) were obtained on a Jasco J715 spectropolarimeter. All DNAs were dissolved in the MES buffer (pH 7.4, 50 mM MES, 0.15 M NaCl). After the measurements at pH 7.4, the pHs of DNAs were then adjusted to 5 by addition of 1 M HCl to get the CD spectra at pH 5.

2.2 Results and discussion

DOX possesses fluorescence properties and when it intercalates with a double-stranded DNA structure to form conjugate, its fluorescence is heavily quenched upon intercalation[202]. Therefore, its fluorescence can be used as a convenient way to monitor the binding and release of DOX from the dsDNA.

2.2.1 dsDNA-DOX conjugates with a different number of *i*-motif unit (Comparison between M1, M2 and M3)

2.2.1.1 The formation of dsDNA-DOX conjugates (M1/MC3-DOX, M2/MC3-DOX and M3/MC3-DOX)

Figure 2.3 shows fluorescence spectra of DOX in the presence of different concentrations of added dsDNAs (M1/MC3, M2/MC3 and M3/MC3). It is clear that as increasing amount of dsDNA are added DOX fluorescence is significantly quenched, which indicates that DOX can indeed intercalate with

dsDNAs to form dsDNA-DOX conjugates (M1/MC3-DOX, M2/MC3-DOX and M3/MC3-DOX). Maximal fluorescence quenching happens at approximately 0.35:1 molar equivalence of M1/MC3 to DOX (0.17:1 for M2/MC3; 0.12:1 for M3/MC3). Therefore, the dsDNA molar equivalence required for maximum fluorescence quenching decreases in the order of M1/MC3, M2/MC3 and M3/MC3, at a ratio which is inversely proportional to the number of the *i*-motif units (M1, M2 and M3 contain 1, 2, and 3 *i*-motif units respectively).

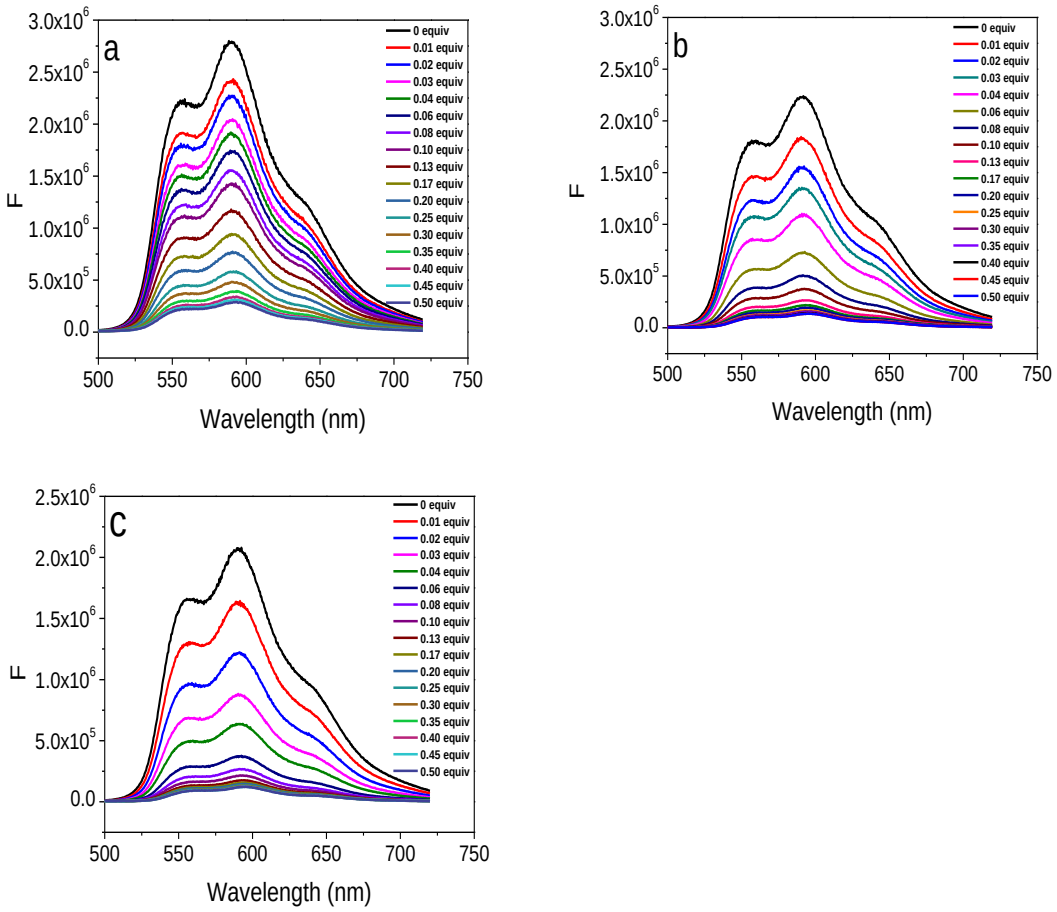

Figure 2.3. Fluorescence spectra of doxorubicin solution (10 μM) with increasing molar ratios of added dsDNAs (**a**) M1/MC3; (**b**) M2/MC3; (**c**) M3/MC3. (From top to bottom: 0, 0.01, 0.02, 0.03, 0.04, 0.06, 0.08, 0.1, 0.133, 0.166, 0.2, 0.25, 0.3, 0.35, 0.4, 0.45 and 0.5 equiv).

Figure 2.4 shows DOX fluorescence intensity at 590 nm (derived from Figure 2.3), plotted against the molar ratios of dsDNA to DOX. When the same amount

of dsDNA was added, the amount of DOX fluorescence quenched varied for different dsDNAs, and increased in the order of M1/MC3, M2/MC3 and M3/MC3 due to the different DNA lengths. The data in Figure 2.4 were also fitted by the Hill equation to get the Michaelis constant (*K*) and cooperative sites (*n*) (Table 2.2). In biochemistry, Hill equation ($y = V_{max}*x^n/(k^n + x^n)$) is used for enzyme kinetic study where a reaction can bind more than one ligand. In this equation, Vmax is the maximum reaction velocity, the Michaelis constant (*K*) is the ligand concentration at which an enzyme reaction rate is half of Vmax and cooperative sites (*n*) describe the cooperativity of ligand binding where, if $n = 1$ (non-cooperativity), the ligand binding affinity is independent on other bound ligands and if $n > 1$ (positive cooperativity) or $n < 1$ (negative cooperativity), the binding affinity increases or decreases after the first ligand binding. The Michaelis constant here represents the dsDNA equiv at which 50% of DOX is quenched (roughly equivalent to 50% DOX being intercalated) and the Michaelis constant ratio among M1/MC3, M2/MC3 and M3/MC3 is approximately 6:3:2, which corresponds to the ratio of the number of C-rich domains contained by M1, M2 and M3 (1:2:3), This suggests that DOX was mainly intercalated within the dsDNA structure formed at the *i*-motif domains, and not in the region containing 10 thymines, which was further confirmed in Chapter 3 (Figure 3.7) where when ssDNA MC2 was mixed with DOX, DOX fluorescence was only quenched slightly, presumably due to the electrostatic interaction. More importantly, by lengthening the DNA (increasing the number of *i*-motif units), a smaller amount of dsDNA is needed for the same amount of DOX to intercalate. In other words, the amount of DOX loading can be improved by lengthening DNA to form a longer dsDNA-DOX conjugate. In addition, it has been reported that DOX intercalates preferentially to GC pairs[135], so that the *i*-motif sequence containing C-rich domains is more favourable for DOX intercalating. The values of cooperative sites for the dsDNAs we used are all

above 1, which indicates that DOX intercalation is positively cooperative.

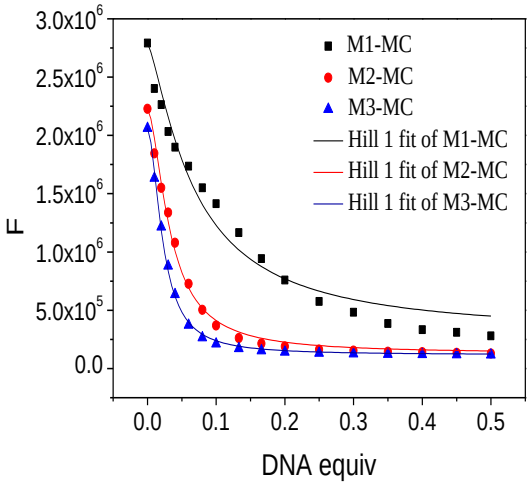

Figure 2.4. Plot of DOX fluorescence intensity versus dsDNA:DOX molar ratios for M1/MC3, M2/MC3 and M3/MC3, fitted by Hill equation.

Table 2.2. Michaelis constant (K) and cooperative sites (n) of different dsDNAs with with a different number of *i*-motif units.

	M1/MC3	M2/MC3	M3/MC3
k	0.068	0.033	0.022
n	1.32	1.68	1.82

2.2.1.2 Adding HCl into dsDNA-DOX conjugates (formation of C-quadruplex and free DOX)

Figure 2.5 gives the evolution of fluorescence spectra of the conjugates as the pH was lowered from 7.4 to weaker acidic conditions. Initially, almost no fluorescence increase was observed as the solution pH was decreased, indicating little DOX release. As the system pH further decreased to a certain critical acidic point of 5.2-5.4 (pH switching point), DOX flurescence intensity was found to increase dramatically, indicating the release of DOX from dsDNA-DOX physical conjugates. These phenomena likely resulted from the cytosine-rich domains in M1 (M2 or M3) forming C-quadruplex structures, leading to the detachment of complementary MC2 strands and release of

intercalated DOX from the systems (Figure 2.1), and hence a dramatic increase in DOX fluorescence intensity. When the system pH dropped further, the fluorescence intensity only increased slightly, suggesting that the majority of DOX had already been released from the system at the critical pH point (assuming that fluorescence intensity correlates with released free doxorubicin in solution). Thus we can conclude that DOX can indeed be released from M1/MC3-DOX, M2/MC3-DOX and M3/MC3-DOX conjugates in a pH responsive manner, and that their critical pH switching points are similar at around pH 5.2-5.4, despite the different numbers of *i*-motif domains.

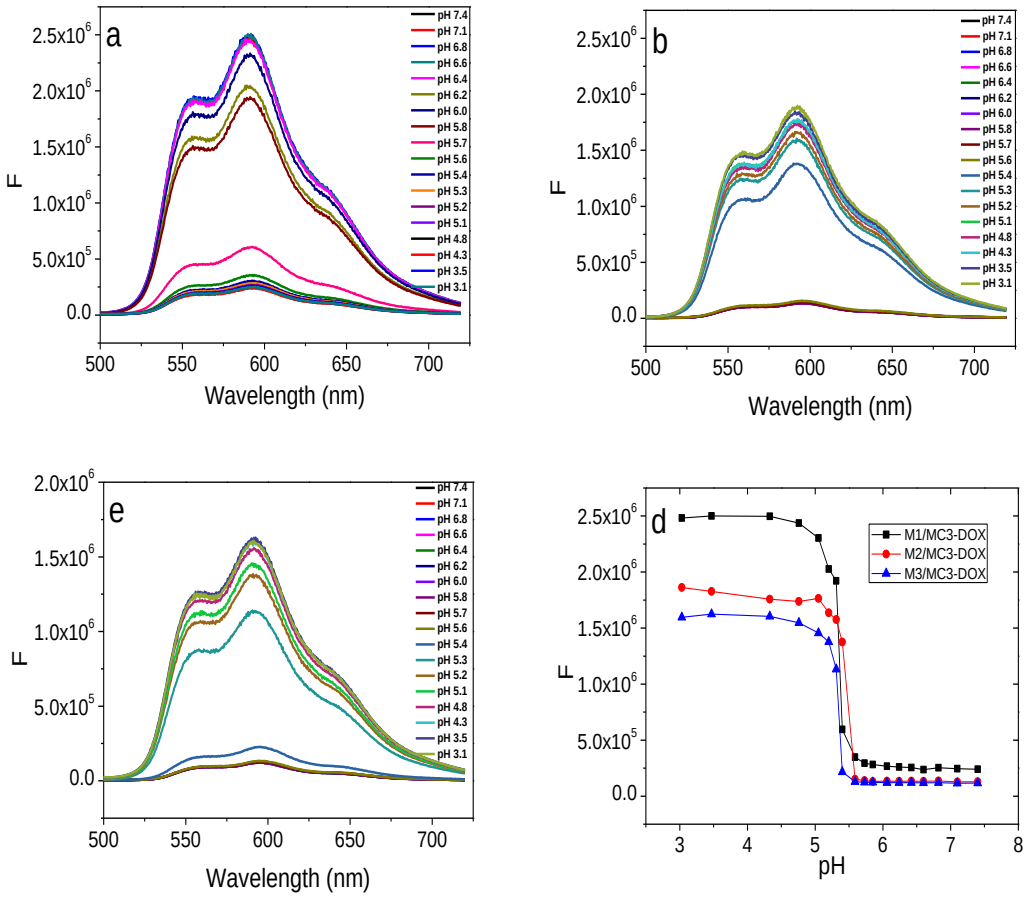

Figure 2.5. Fluorescence spectra of M1/MC3-DOX (**a**), M2/MC3-DOX (**b**) and M3/MC3-DOX (**c**) with pH adjustment (pH from bottom to top: 7.4, 7.1, 6.8, 6.6, 6.4, 6.2, 6.0, 5.8, 5.7, 5.6, 5.4, 5.3, 5.2, 5.1, 4.8, 4.3, 3.5 and 3.1); (**d**) plots of fluorescence intensity at 590 nm of M1/MC3-DOX, M2/MC3-DOX and M3/MC3-DOX as a function of pH.

To confirm the formation of *i*-motif, The structures of M1/MC2, M2/MC2 and M3/MC2 at pH 5 and 7 were also studied by CD spectroscopy (Figure 2.6). At pH 7, all DNAs exhibit the CD spectra characteristic of the dsDNA structure, where the positive band and the negative band appeared at around 275 nm and 249 nm with the crossover at 259 nm. When pH was changed 5, the positive and negative bands of all DNAs were shifted to ~285 nm and 254 nm respectively with a crossover at 266 nm, which are distinct characteristics of the *i*-motif structure. The results agreed well with the literature[157], revealing that it is the structure transformation from dsDNA to *i*-motif is the cause of DOX release at pH 5.

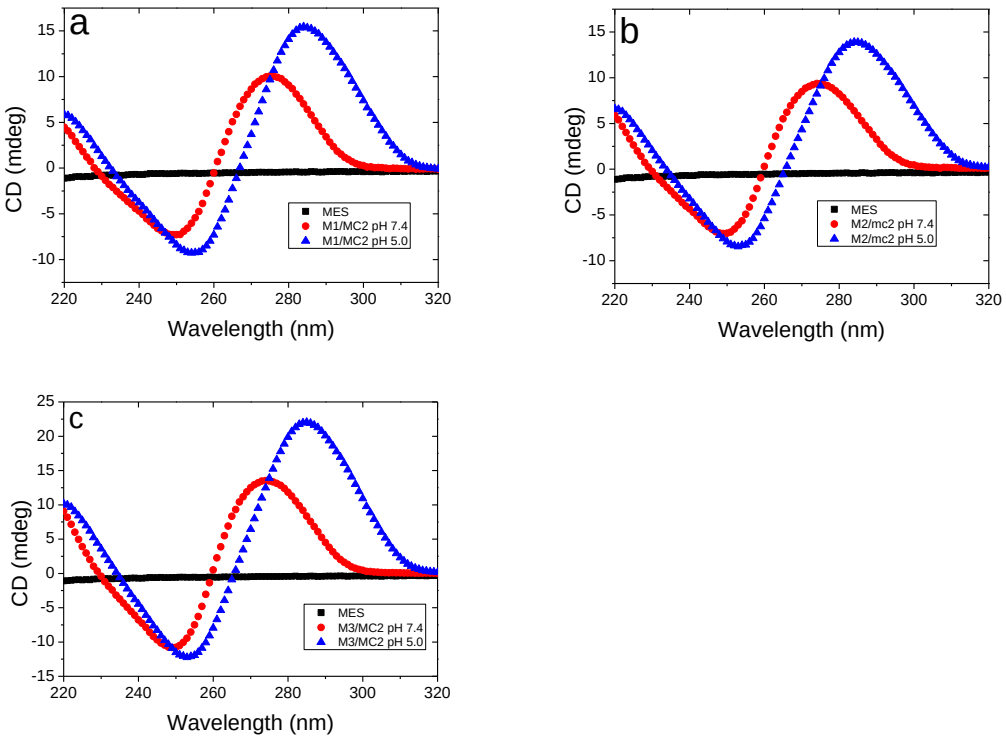

Figure 2.6. CD spectra of M1/MC2 (a), M2/MC2 (b) and M3/MC2 (c) at pH 5 and pH 7 respectively (20 °C). The spectra difference showed the structure transformation between dsDNA (pH 7) and i-motif structure (pH 5).

2.2.1.3 Reversibility of the pH-responsive DNA switch

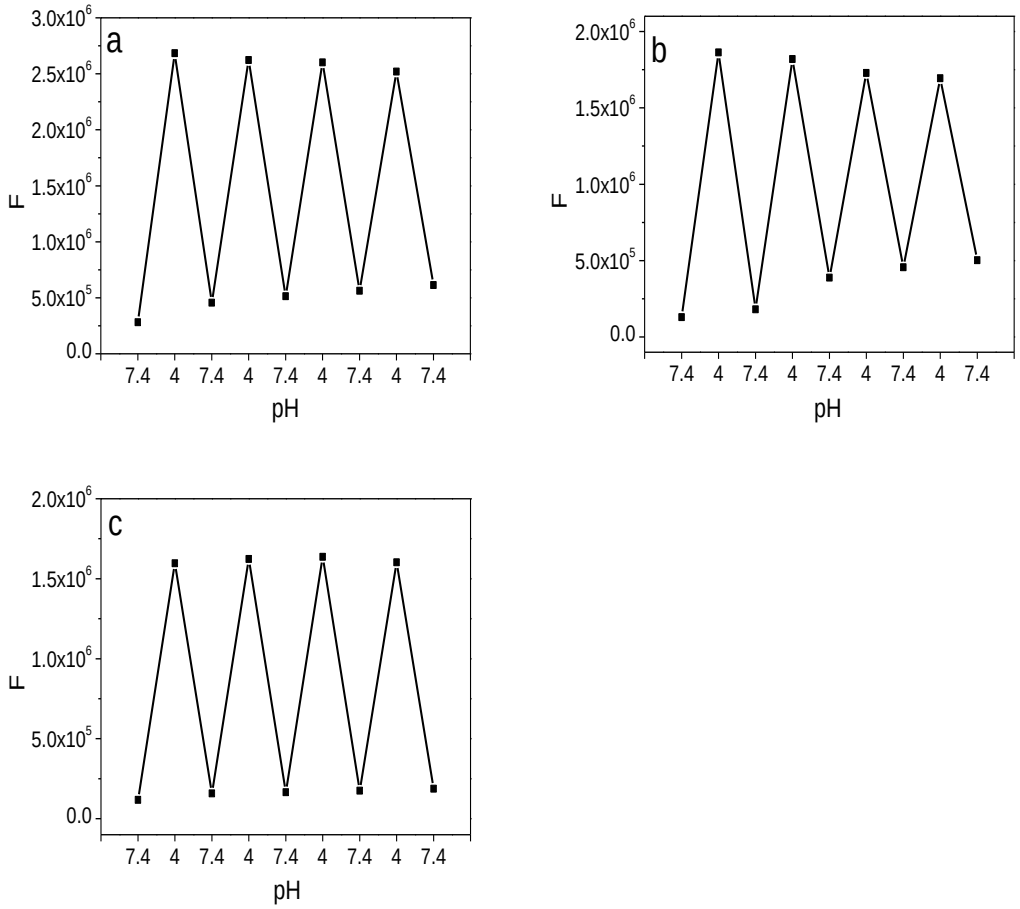

Figure 2.7. Fluorescence intensity at 590 nm of M1/MC3-DOX (**a**); M2/MC3-DOX (**b**) and M3/MC3-DOX (**c**) as the solution pH is cycled between 7.4 and 4.0 by alternate additions of 1M HCl or 1M NaOH.

When the pH of the solutions was adjusted back to 7.4, the cytosines were no longer protonated and so the driving force (the intramolecular C-CH^+ base-pairing) to form C-quadruplex structures broke down. The C-quadruplex unfolded into a random coil state, which could then hybridize with the complementary strand to form a dsDNA such that DOX can intercalate again, leading to DOX fluorescence being quenched. Figure 2.7 illustrates the fluorescence intensity changes as the pH of the system was cycled between 7.4 and 4.0 by alternate additions of 1 M HCl or 1 M NaOH. It is clear that the system is highly reversible, and that the fluorescence intensity follows the

expected trend (a strong fluorescence at pH 4 which decreases significantly at pH 7.4) as the solution pH was cycled, indicating that this system can be used for efficient and controlled DOX release using pH as a trigger. A control experiment with a DOX-only sample (without the dsDNA) showed no fluorescence change within the pH region of 4-7.4 (Figure 3.8a), confirming that the observed DOX fluorescence change is caused by the specific intercalation between DOX and dsDNA.

2.2.1.4 Measurement of DNA melting temperature

The melting temperature (Tm) of nucleic acids is the temperature at which 50% of base pairs have separated. The Tm value can be very useful in evaluating the stability of the DNA secondary structure, which depends on base pairing. It can be determined by measuring UV absorption at 260 nm while gradually increasing temperature of the dsDNA solution, as the double helical DNA has a hyperchromic shift when it denatures.

Figure 2.8 shows the temperature-dependent absorbances of different dsDNAs and dsDNA-DOX conjugates at 260, 360 and 480 nm, respectively. None of the components have significant absorptions at 360 nm, so the absorbance at this wavelength will help to identify whether there were artefacts such as bubbles and sample aggregates that might contribute to the absorbance changes. Figure 2.8 shows no observable artificial contribution to the melting curves.

The Tm values, shown in Table 2.3, were calculated from the first derivative by the spectrophotometer software. It is interesting to note that dsDNAs formed between different M-strands (M1, M2 or M3) and the same complementary strand (MC3) have similar Tm values, and so do the corresponding

dsDNA-DOX conjugates. This is not unexpected since the total number of *i*-motifs is similar. The concentration ratio of dsDNAs or dsDNA-DOX conjugates (from M1 to M3) is 8:4:3, while the ratio of cytosine rich domains is 1:2:3, which allows all dsDNAs to have roughly the same number of *i*-motif domains (absorbances). If the dsDNA concentration is the same, then we would expect the Tm value of M3/MC3 to be highest, followed by M2/MC3 and then M1/MC3; and the corresponding dsDNA-DOX conjugates would also show the same trend. In addition, due to the same complementary strand MC3 used to form dsDNAs, two and three MC3s are required to hybridize with each M2/M3 to form M2/MC3 and M3/MC3 duplexes, which should lead to lower Tms than their counterpart dsDNAs using one continuous complementary DNA with a double or triple length of MC3.

The Tm values of dsDNA-DOX conjugates are higher than their corresponding dsDNAs alone, which is mainly due to the contribution of extra stabilisation from the DNA base-DOX π–π stacking interactions as a result of DOX intercalation. In DNA, π–π stacking exists between adjacent nucleotides that are parallel to each other, allowing the bases to participate in π–π interactions. DOX has a polycyclic, aromatic and planar structure with a proper size, similar to a base pair, which allows DOX to intercalate and fit between base pairs to participate in π–π interactions. The aromatic interaction between adjacent bases and DOX makes dsDNA more stable.

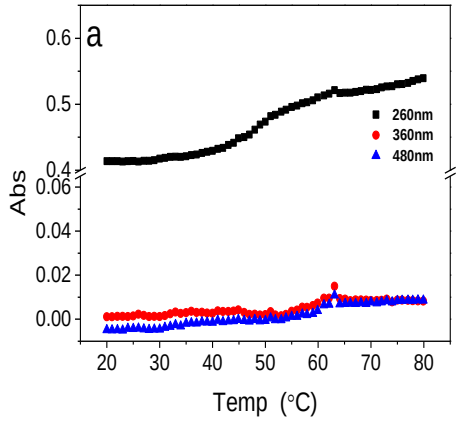
a
Abs
Temp (°C)
260nm
360nm
480nm

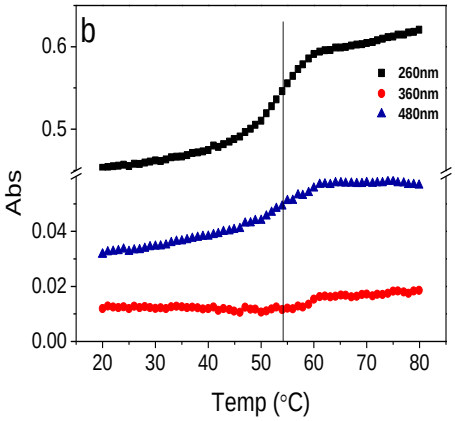
b
Abs
Temp (°C)
260nm
360nm
480nm

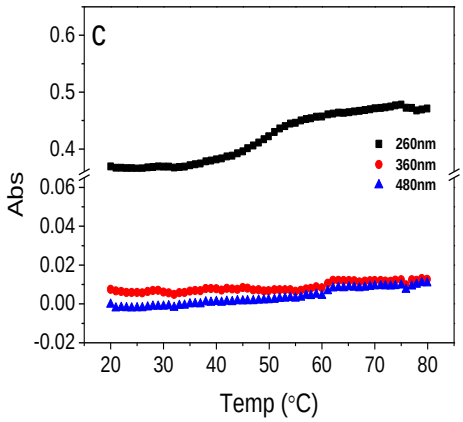
c
Abs
Temp (°C)
260nm
360nm
480nm

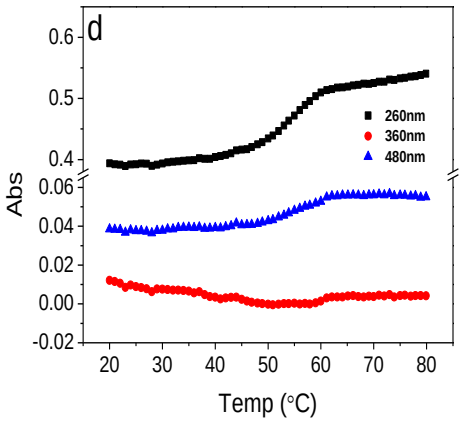
d
Abs
Temp (°C)
260nm
360nm
480nm

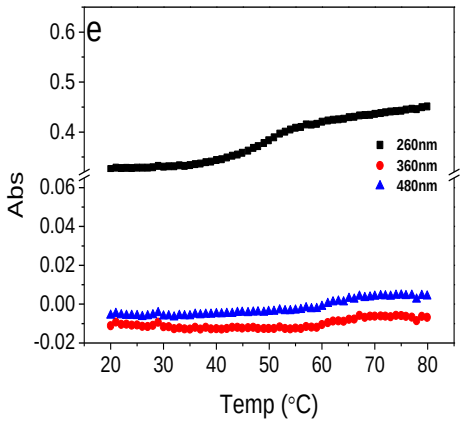
e
Abs
Temp (°C)
260nm
360nm
480nm

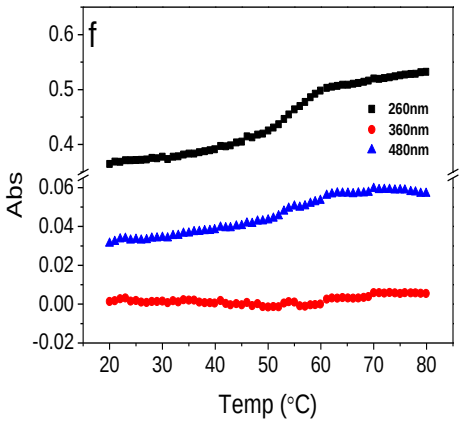
f
Abs
Temp (°C)
260nm
360nm
480nm

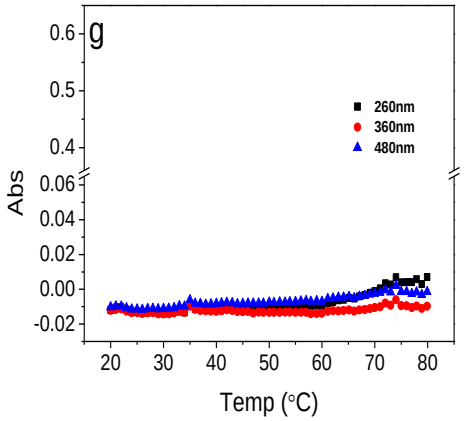

Figure 2.8. Temperature-dependent absorbance plots of M1/MC3 (**a**), M1/MC3-DOX (**b**), M2/MC3 (**c**), M2/MC3-DOX (**d**), M3/MC3 (**e**), M3/MC3-DOX (**f**) and MES buffer (**g**) at 260, 360 and 480 nm, respectively.

In these thermal denaturation experiments, we also monitored the absorbance at 480 nm which corresponds to the maximum absorption peak of DOX. From Figure 2.8, we can see that the DOX absorption profile at 480 nm matches the melting curve of dsDNA-DOX conjugate at 260 nm. When dsDNA dehybridised to ssDNAs in these experiments, the DOX which initially intercalated with the dsDNA was released from the conjugates, so that the increase in absorbance showed the same trend as the dsDNA.

Table 2.3. Tm values of different dsDNA and dsDNA-Dox conjugates measured by UV melting.

dsDNA	Tm (^{o}C)	DsDNA-Dox	
M1/MC3	49.0	53.9	M1/MC3-DOX
M2/MC3	49.9	53.7	M2/MC3-DOX
M3/MC3	50.0	53.6	M3/MC3-DOX

2.2.2 dsDNA-DOX conjugates with different numbers of mismatched bases (Comparison between MC2, MC3 and MC4)

In order to form a dsDNA-DOX conjugate that can respond to environmental pH changes, complementary DNAs, MC2, MC3 and MC4 (with two, three and four mismatched bases to M1 respectively) were designed to form M1/MC2-DOX, M1/MC3-DOX and M1/MC4-DOX conjugates to tune duplex stability. These mismatches may destabilise the resulting dsDNA structure, such that the formation of *i*-motifs could outcompete the dsDNA at less acidic pH with tunable conformation-switching points (pH switching points). In addition, these mismatches are able to prevent complementary DNAs from folding into G-quadruplexes (two or more stacked guanine tetrads)[203], which may interfere with the reversibility of dsDNA-DOX conjugates.

2.2.2.1 Stability comparison

Table 2.4. Melting temperatures (Tm) of the duplex DNAs with the different numbers of mismatches employed in this study with and without DOX in MES buffer.

dsDNAs	Tm (^{o}C, No DOX)	Tm (^{o}C, with DOX)
M1/MC4	42	48
M1/MC3	49	54
M1/MC2	54	58

The melting temperature measurements (Table 2.4) show that melting temperatures of dsDNAs decreased as the number of mismatched bases increased. The dsDNA M1/MC4 gives the lowest Tm (42 °C), which is 7 °C lower than M1/MC3 and 12 °C lower than M1/MC2, indicating that the stability of dsDNA decreases in this order: M1/MC2, M1/MC3 and M1/MC4; in fact, dsDNA stability can be tuned by varying the number of mismatches. The same trend can also be found among dsDNA-DOX conjugates. Observing their differences

in stability, we expected that their pH switching points could be tuned by choosing different complementary DNAs with different numbers of mismatches.

2.2.2.2 Formation, pH-responsiveness and reversibility of M1/MC$_n$-DOX

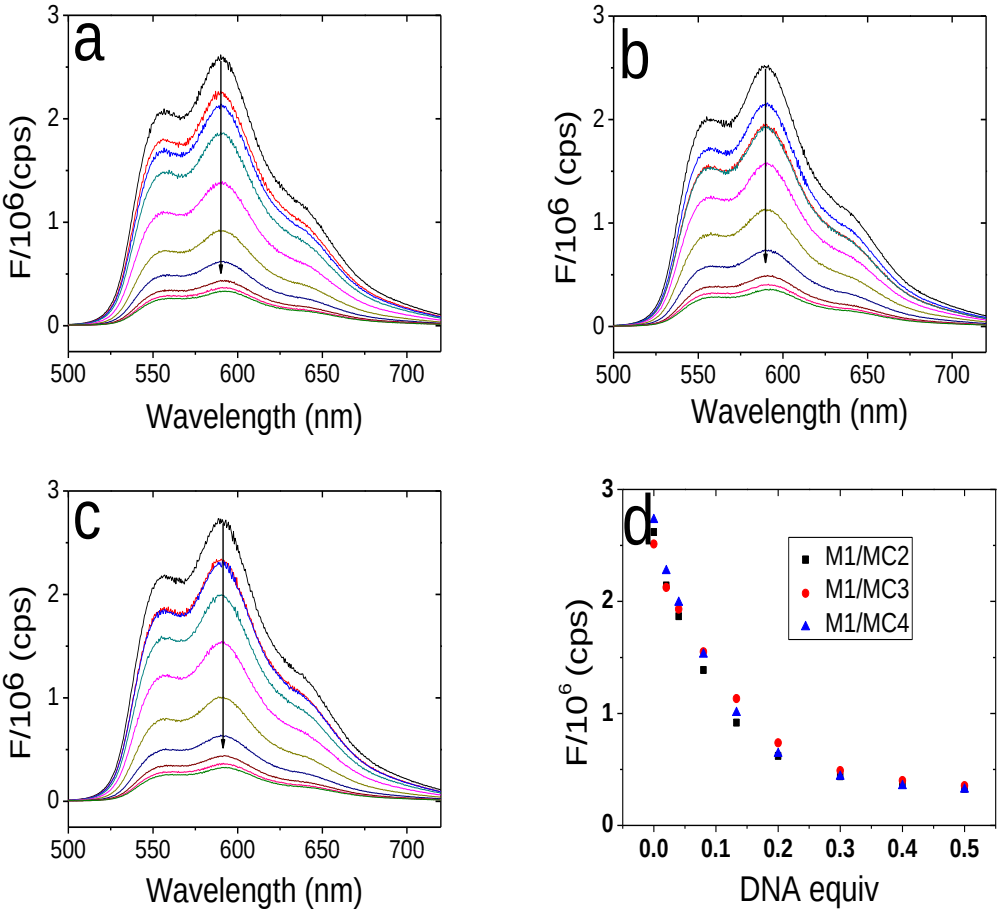

Figure 2.9. Fluorescence spectra of DOX solution (10 μM) with increasing molar ratios of added dsDNAs (**a**) M1/MC2; (**b**) M1/MC3; (**c**) M1/MC4; (from top to bottom: 0, 0.01, 0.02, 0.04, 0.08, 0.13, 0.2, 0.3, 0.4 and 0.5 equiv) and (**d**) plots of fluorescence intensity of 10 μM DOX at 590 nm versus the dsDNA:DOX molar ratios.

Table 2.5. Michaelis constant (K) and cooperative sites (n) of different dsDNAs.

dsDNA	*k*	*n*
M1/MC2	0.063	1.53
M1/MC3	0.070	1.59
M1/MC4	0.069	1.59

Figure 2.9 confirms that all dsDNAs, M1/MC2, M1/MC3 and M1/MC4, can form dsDNA-DOX conjugates with DOX. They also have a similar Michaelis constant (*K*) (Table 2.5), suggesting that varying the mismatch number from 2 to 4 has no significant influence on the amount of DOX that can be intercalated with the dsDNA. When the system pH was adjusted to acidic pH(pH switching point around 5.2-5.4), DOX was released from all the conjugates (Figure 2.10), and the systems were also reversible when pH was cycled between 7.4 and 4.7 (Figure 2.11), all of which indicates that all complementary DNAs (MC2, MC3 and MC4) with various numbers of mismatches are working properly in the pH-responsive dsDNA-DOX systems.

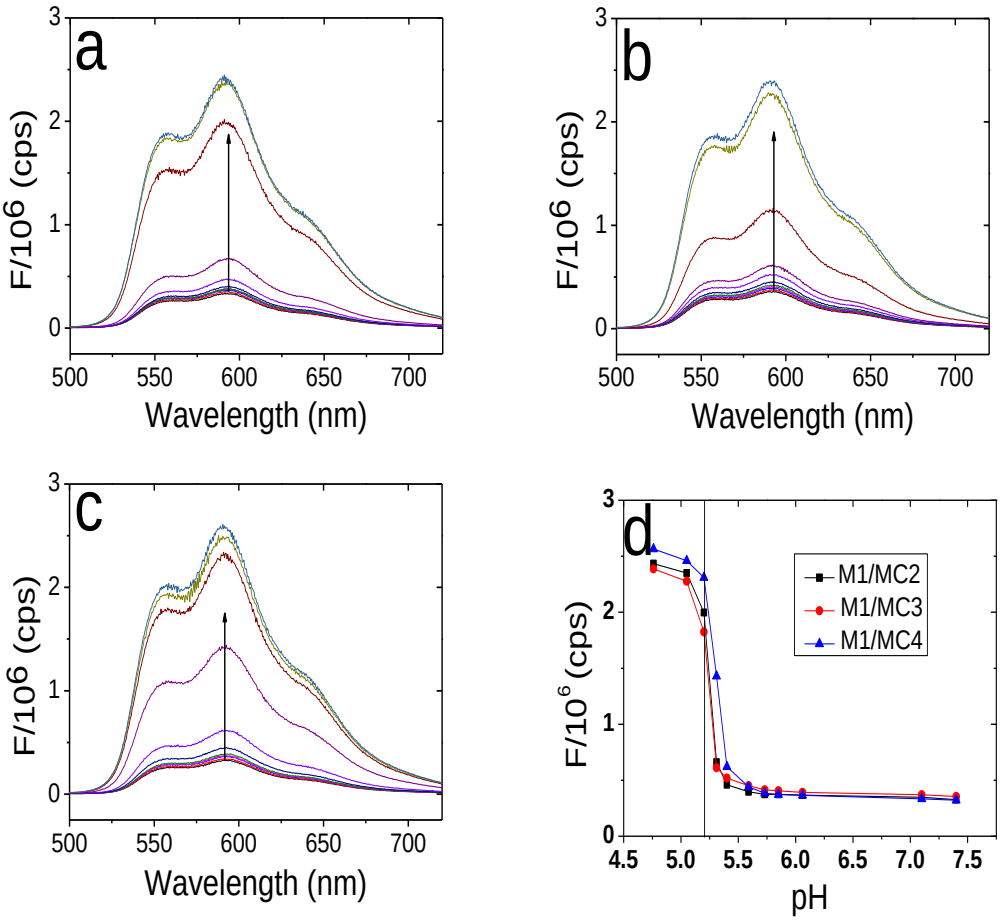

Figure 2.10. Fluorescence spectra of (**a**) M1/MC2-DOX, (**b**) M1/MC3-DOX, (**c**) M1/MC4-DOX, (pH from bottom to top: 7.4, 7.1, 6.1, 5.9, 5.7, 5.6, 5.4, 5.3, 5.2, 5.1, 4.7) and (**d**) Plots of fluorescence intensity at 590 nm of dsDNA-DOX as a function of pH.

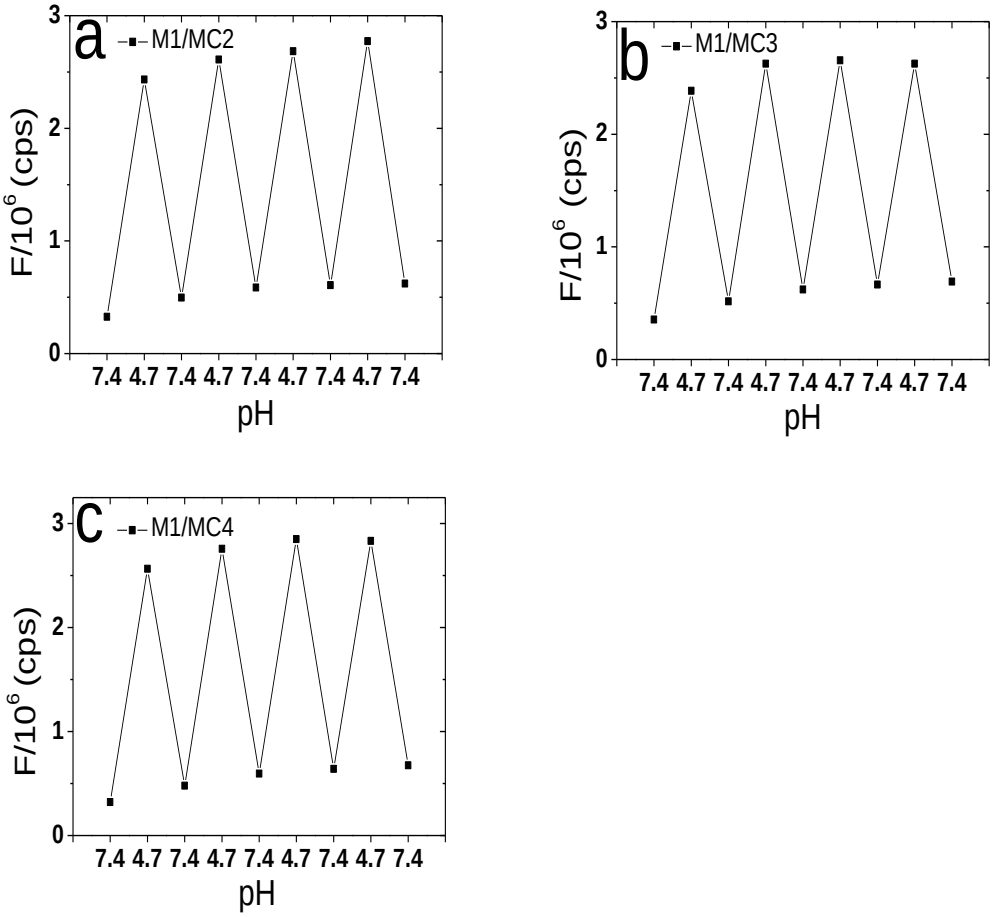

Figure 2.11. Fluorescence intensity at 590 nm of M1/MC2-DOX (**a**); M1/MC3-DOX (**b**); M1/MC4-DOX (**c**) as the solution pH is cycled between 7.4 and 4.7 by alternate additions of 1M HCl or 1M NaOH.

But no significant differences in pH switching points were observed among the different complementary DNAs, which was contrary to our expectation. M1/MC3-DOX has nearly the same pH switching point (around 5.2) as M1/MC2-DOX, although the pH switching point (about 5.4) of M1/MC4-DOX is slightly higher. Comparing their melting temperatures, we do see considerable differences in stability among the dsDNAs (M1/MC2, M1/MC3 and M1/MC4) and their responding DOX conjugates. For example, the Tms for M1/MC2-DOX, M1/MC3-DOX and M1/MC4-DOX are 58 °C, 54 °C and 48 °C, respectively (Table 2.4). We suspect that their differences in stability may not be large enough to cause significant pH switching point changes. Presumably the driving force of pH-dependent switching here is caused by the formation of an *i*-motif by

M1, which is able to outcompete and break up hydrogen bonds between the dsDNA base pairs, and the destabilizing effect caused by mismatches may be negligible.

2.2.3 M1/MC2 conjugates with and without PEG modification (Comparison among MC2, MC2(PEG250) and MC2(PEG750))

Because of the key role that PEG plays *in vivo* in reducing nonspecific interactions with proteins and prolonging the blood circulation time, two PEG-modified MC2s were also employed, MC2(PEG250) and MC2(PEG750), with PEG molecular weights of 250 and 750 respectively. They were used to form M1/MC2(PEG250)-DOX and M1/MC2(PEG750)-DOX conjugates to study how PEG modification affects the *i*-motif conformation switch in comparison to M1/MC2-DOX conjugate.

2.2.3.1 Thermal stability of M1/MC2 with and without PEG modification

Table 2.6. Melting temperatures (Tm) of the duplex DNAs employed in this study with and without DOX in MES buffer.

dsDNAs	Tm (^{o}C, No DOX)	Tm (^{o}C, with DOX)
M1/MC2	54	58
M1/MC2(PEG250)	52	56
M1/MC2(PEG750)	54	58

Table 2.6 shows the melting temperatures of M1/MC2s, and their counterpart conjugates with and without PEG modifications. PEG-modified dsDNAs and dsDNA-DOX conjugates have very similar Tms to their non-modified counterparts, suggesting that PEG modifications do not change the thermal

stability of the resulting dsNDA conjugates. This is because terminal PEG modification has no impact on base pairing or the total number of hydrogen bonds of dsDNA structure.

2.2.3.2 Formation of (PEG-modified) M1/MC2 conjugates

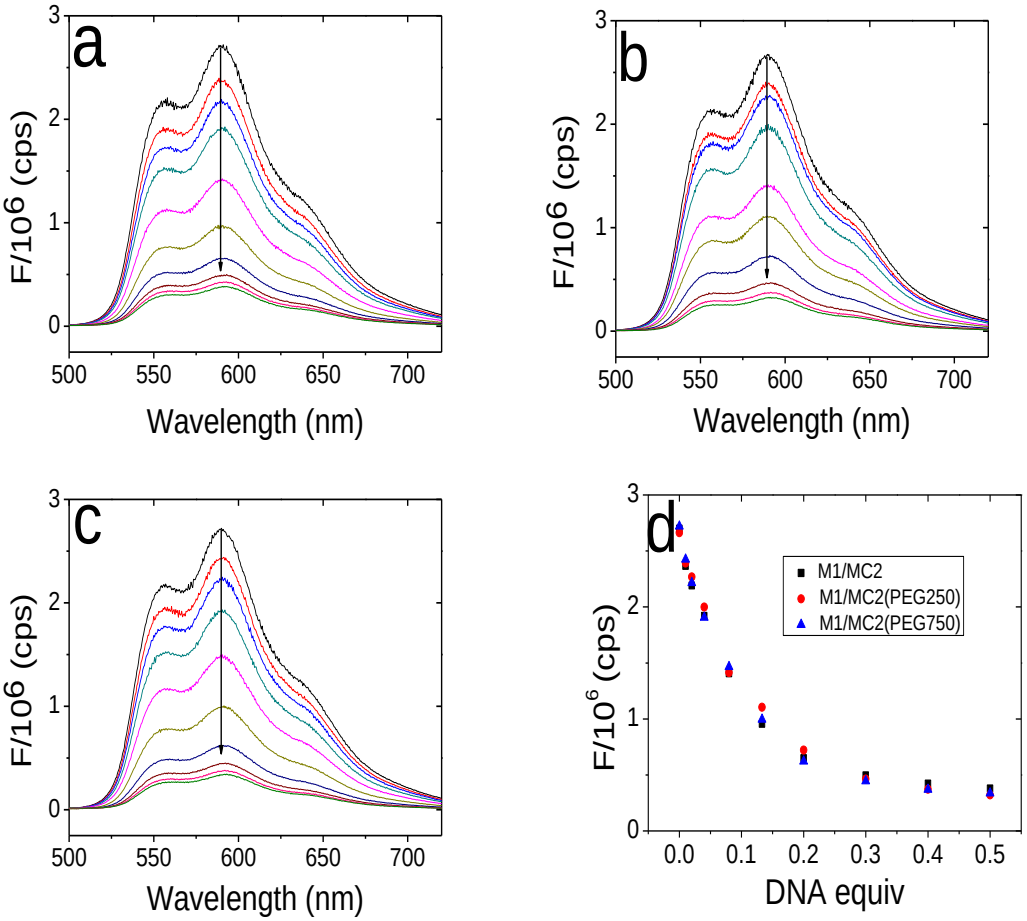

Figure 2.12. Fluorescence spectra of DOX solution (10 μM) with increasing molar ratios of added dsDNAs for (**a**) M1/MC2; (**b**) M1/MC2 (PEG250); (**c**) M1/MC2 (PEG750); (from top to bottom the dsDNA to DOX ratios are 0, 0.01, 0.02, 0.04, 0.08, 0.13, 0.2, 0.3, 0.4 and 0.5 equiv). (**d**) Plots of the DOX fluorescence intensity (10 μM) at 590 nm versus the dsDNA:DOX molar ratios.

Figure 2.12 shows DOX fluorescence spectra with increasing amount of different dsDNAs and plots of DOX fluorescence intensity at 590 nm as a function of the added amount of dsDNA. With the increasing molar ratio of

added dsDNA (with/without PEG), DOX fluorescence intensity was quenched dramatically, which confirms that as well as dsDNA M1/MC2, DOX can also intercalate into PEG-modified dsDNAs to form PEG-modified dsDNA-DOX conjugates (M1/MC2(PEG250)-DOX and M1/MC2(PEG750)-DOX). The data were also fitted by Hill 1 equation, and the resulting Michaelis constant (*K*), and the cooperative sites (*n*) of different dsDNAs (Table 2.7) were similar, suggesting that PEG modification at the end of complementary DNA MC2 does not affect DOX binding properties.

Table 2.7. Michaelis constant (K) and cooperative sites (n) of dsDNAs without and with PEG modifications.

dsDNA	***k***	***n***
M1/MC2	**0.063**	**1.53**
M1/MC2(PEG250)	**0.071**	**1.49**
M1/MC2(PEG750)	**0.061**	**1.44**

2.2.3.3 pH responsiveness and reversibility of (PEG-modified) M1/MC2 conjugates

When the pH of the conjugates was gradually adjusted to acidic, DOX fluorescence intensity at 590 nm from all dsDNA-DOX conjugates did not change noticeably until pH reached around 5.3 (pH switching point), at which point DOX intensity increased sharply (Figure 2.13). Again, PEG modifications on DNA MC2 did not cause any significant change regarding the pH switching point. As expected, PEG modifications did not have any impact on reversibility; this was confirmed by cycling pH of the conjugates between 7.4 and 4.7 (Figure 2.14).

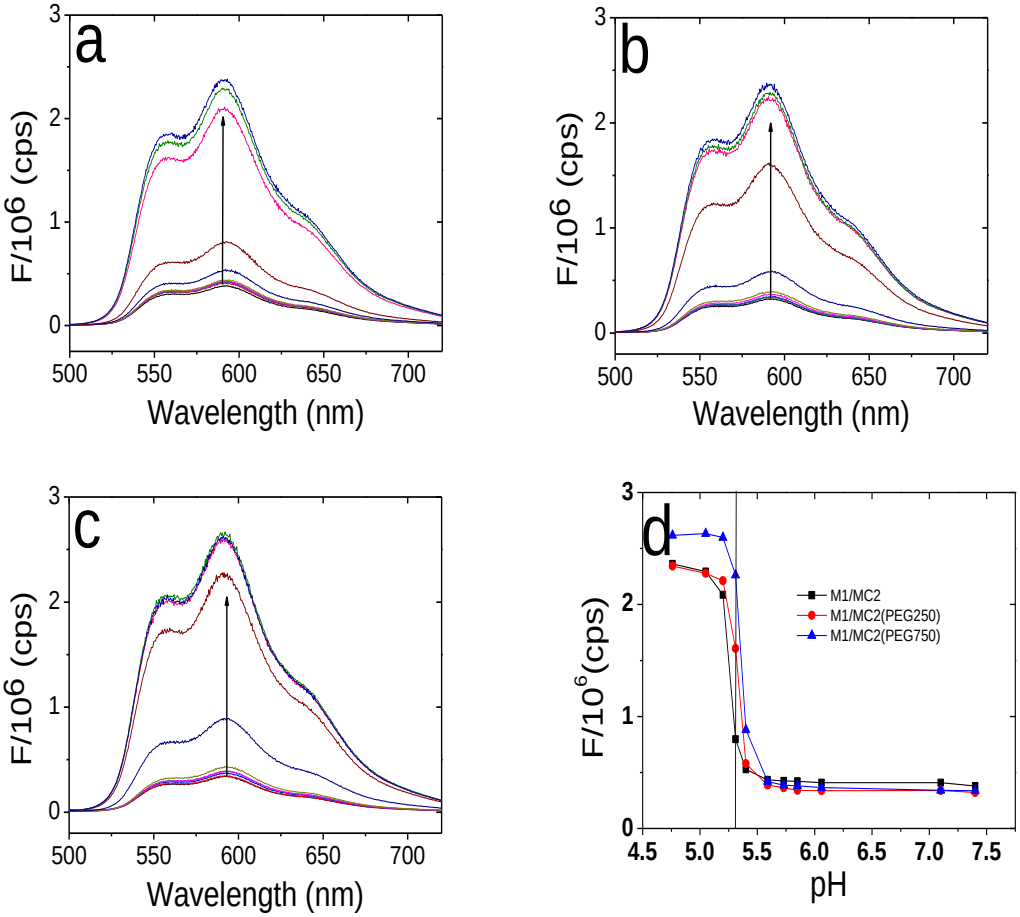

Figure 2.13. Fluorescence spectra of the (**a**) M1/MC2-DOX, (**b**) M1/MC2(PEG250)-DOX and (**c**) M1/MC2(PEG750)-DOX systems under different pH conditions. pH from bottom to top: 7.4, 7.1, 6.1, 5.9, 5.7, 5.6, 5.4, 5.3, 5.2, 5.1, 4.7. (**d**) Plots of fluorescence intensity at 590 nm as a function of pH for the dsDNA-DOX systems.

All three systems, M1/MC2-DOX, M1/MC2(PEG250)-DOX and M1/MC2(PEG750)-DOX, display very similar Michaelis constants (*K*) and pH switching points, revealing that PEG-modification of MC2 does not affect DOX binding properties, pH responsiveness and reversibility of the dsDNA-DOX conjugates. This is understandable given that the PEG modification happens at the 5' end of the MC2 strand, which does not participate/interfere in the DNA base-paring with the M1 strand.

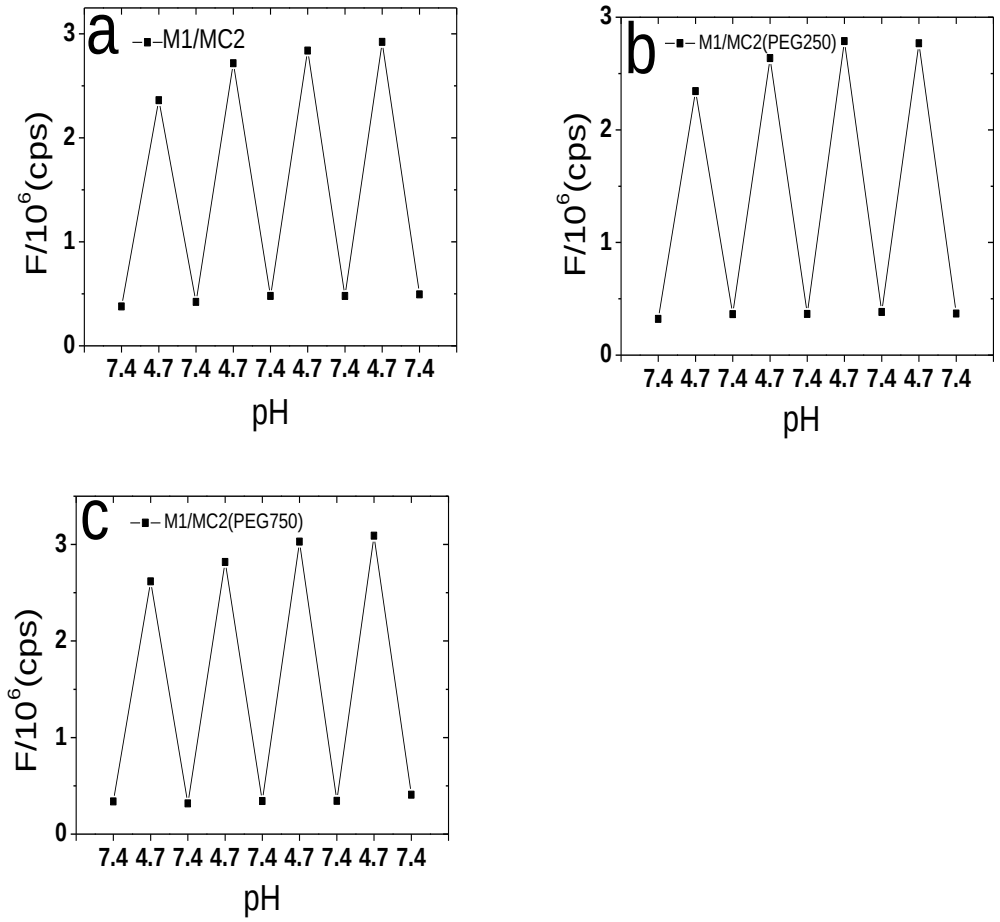

Figure 2.14. Fluorescence intensity at 590 nm of M1/MC2-DOX (**a**); M1/MC2(PEG250)-DOX (**b**); and M1/MC2(PEG750)-DOX (**c**) as the solution pH is cycled between 7.4 and 4.7 by alternative addition of 1M HCl or 1M NaOH.

2.3 Conclusion

M1, M2 and M3 (with two and three *i*-motif units, respectively) can successfully form pH responsive dsDNA-DOX conjugates, with very similar pH switching points of around 5.2-5.4 and pH reversibility, and DOX loading is positively correlated to the length of the DNA. These features can be exploited to improve DOX loading capacity in the next chapter through increasing the number of *i*-motif units.

The thermal stabilities of both dsDNAs and dsDNA-DOX conjugates can be

tuned by varying the number of mismatches (2-4) in the dsDNA (dsDNA-DOX conjugate) structure where the dsDNA containing less mismatches displays higher thermal stability. However, the changes in stability caused by differences of MC2, MC3 and MC4 do not seem sufficient to lead to an obvious change of pH switching point. Thus, in the following chapters MC2 will be chosen as the complementary DNA for developing a GNP-dsDNA drug delivery system because of its higher thermal stability.

PEG-modified complementary DNA MC2s can be employed to prepare PEG-modified dsDNA-DOX conjugates. Compared with non-PEG conjugates they display a very similar Michaelis constant and pH switching point (around 5.3). PEG modifications do not affect the DOX intercalation, pH-responsiveness and switching reversibility of the resulting dsDNA-DOX conjugates.

3 Chapter 3: GNP-dsDNA conjugate as a novel targeted NDDS

A new NDDS is designed, combining the pH-responsive dsDNA-DOX conjugate and a gold nanoparticle (GNP). The concept here is based on the following requirements for a drug nanocarrier for effective cancer therapy[10, 19, 204]: 1) to increase the DOX loading capacity; 2) to increase the carrier size to above the renal clearance threshold (~8 nm)[205], to prolong blood circulation for long lasting treatment as well as effective passive targeting *via* the enhanced permeation and retention (EPR) effect[10, 19, 204] (a characteristic property of many tumors); and 3) to increase carrier stability and resistance against nuclease degradation (polyvalent DNA-GNP conjugate has been reported to resist nuclease degradation)[206].

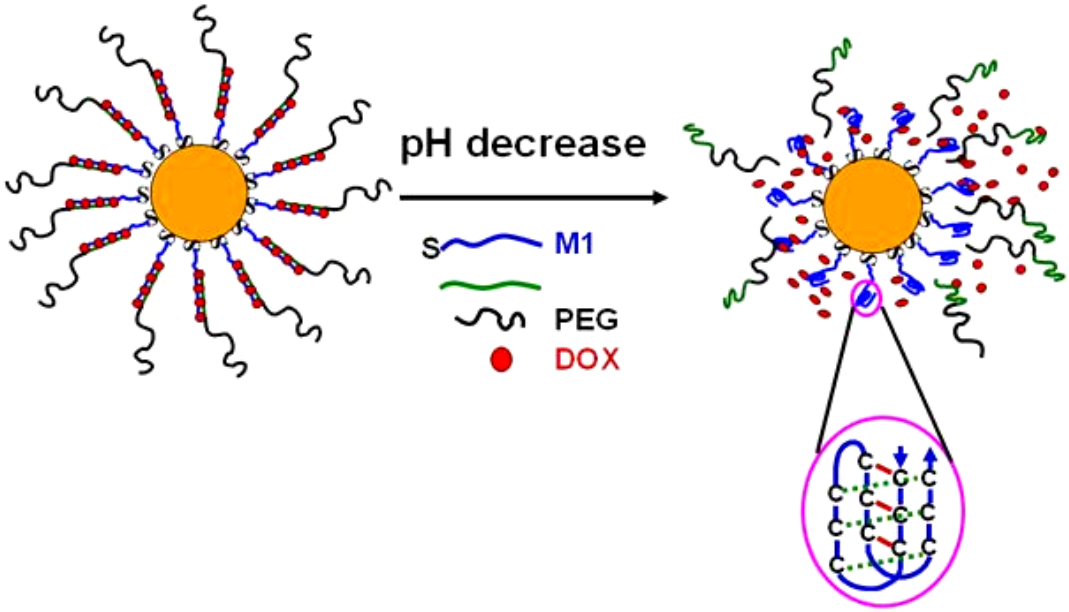

Figure 3.1. Schematic representation of a GNP-dsDNA conjugate acting as a novel pH-targeting NDDS for DOX.

In this NDDS, colloidal GNPs with uniform sizes of 14 nm and 27 nm are synthesized by citrate reduction methods. ssDNAs, M1 (M2 or M3) are attached to the GNP surface *via* its thiol linker, which is then followed by hybridisation with complementary ssDNAs (with or without PEG modification) to form a

GNP-dsDNA conjugate as a nanocarrier for DOX. We expect that when pH is lowered to acidic, DOX will be released from the systems in the same way as from dsDNA-DOX conjugates, due to the formation of C-quadruplex by M1 (M2 or M3) (Figure 3.1). These systems are then used for cellular study to evaluate the feasibility of the GNP-dsDNA-DOX as an anticancer drug delivery platform and to compare their cytotoxicity with free DOX.

3.1 Materials and Methods

3.1.1 Materials

Hydrogen tetrachloroaurate(III) hydrate, 99.9% (metals basis) were purchased from Alfa Aesar. Trisodium citrate dihydrate and HNO_3 (70%) were purchased from Fisher Scientific. DMEM (Dulbecco's Modified Eagle's Medium), Penicillin-Streptomycin (5,000 units/mL penicillin, 5 mg/mL streptomycin) and PEG 6000 (poly(ethylene glycol, average MW: 6000) were purchased from Sigma-Aldrich.

3.1.2 Synthesis of GNPs

Method 1. Direct citrate reduction without pH adjustment.

A critical requirement for this method to be successful is extremely clean glassware and utensils. The synthesis was carried out by following the literature procedures[99, 113].

1) Fresh aqua regia was prepared by mixing HCl and HNO_3 (3:1) in the fume hood (*caution: aqua regia is a strongly corrosive and oxidative, it should not get into contact with any organic solvents and protective goggles and gloves must be worn when handling it*). All glassware and utensils (*e.g.* 250 mL three-necked flask, magnetic stir bar, stoppers, condenser and other glassware) were soaked in aqua regia for 30 min and were then rinsed thoroughly with Millipore-filtered water. *This procedure should be done very carefully and goggles and gloves must be worn*.

2) 80 mg $HAuCl_4$ was weighed in a large beaker and 200 mL of ultrapure water was added to dissolve it. The solution was then transferred to a freshly-cleaned 250 mL three-necked flask connected to a condenser, with the other two necks capped by stoppers. The resulting solution was heated to reflux in a 180-200℃ oil bath under magnetic stirring.

3) When the solution began to reflux, an aqueous solution of trisodium citrate (228 mg in 20 mL water) was quickly added to the flask *via* one of the flask's side necks. The resulting solution was then continuously refluxed for a further period. The colour of the solution changed from yellow to deep red in ~1 min.

4) After refluxing for another 50 min, a stable deep red solution was obtained. The heat bath was then removed and the solution was allowed to cool to room temperature naturally (under stirring). The prepared gold nanoparticles solution was then transferred to a clean glass container and stored at room temperature.

Method 2. Synthesis of GNPs by citrate reduction with pH adjustment [207]**.**

The procedures are similar to those described above, except where 20 mg $HAuCl_4$ was dissolved in 200 mL of Millipore water, and the solution pH was adjusted to ~7 with 1M NaOH before being loaded in the three-necked flask. The resulting solution was heated to reflux under magnetic stirring, and then 147 mg tri-sodium citrate (dissolved in 3 mL water) was quickly added. The solution was refluxed for 1 h before being allowed to cool to room temperature.

The absorption spectra of synthesized GNP solutions by Method 1 (after a five-fold dilution) and Method 2 (after a four-fold dilution) were recorded on a Varian Cary 50 bio UV-Visible Spectrophotometer (ranging from 300-800 nm). The GNPs were then characterised by a Philips CM200 transmission electron microscope (TEM). The specimen for TEM study was prepared by depositing a

drop of the GNP solution onto a carbon-coated mesh grid.

3.1.3 Preparation and pH responsive study of GNP(27 nm)-M2/MC2-DOX and GNP(14 nm)-M2/MC2-DOX conjugates

Preparation of GNP(27 nm)-M2 and GNP(14 nm)-M2 conjugates

GNP(27 nm)-M2 and GNP(14 nm)-M2 conjugates were prepared by following the literature procedures[208]. 10 nmol DNA M2 was dissolved in 100 μL of Millipore water and added into 2.2 mL of GNP solution (27 nm in diameter, ~7.5 nM) or 2.2 mL of 14 nm GNP solution, 15 nM). The DNA M2/GNP solutions were allowed to incubate at room temperature overnight. Then NaCl solution (1 M) was added to the GNP solutions to increase the salt concentration to 0.1 M, followed by a 10-second sonication. The solutions were left for 30 min and then the same procedure was repeated until the NaCl concentration reached 0.3 M. The solutions were then left overnight for salt aging under these conditions. The unbound DNA M2 was then removed by centrifugation at 14000 rpm for 60 min on a Thermo Scientific Heraeus Fresco 21 microcentrifuge, and precipitates of the GNP(27 nm)-M2 and GNP(14 nm)-M2 conjugates were obtained; these were then dispersed in 3 mL of MES buffer (pH 7.4, 50 mM MES, 0.15 M NaCl). The clear supernatants were collected and used to determine the unbound DNA M2 concentrations by measuring the absorptions at 260 nm ($\varepsilon_{M2} = 4.87 \times 10^5$ $cm^{-1} \cdot M^{-1}$), which in turn allows calculation of the number of DNA strands attached to each GNP.

Preparation of GNP(27 nm)-M2/MC2 and GNP(14 nm)-M2/MC2 conjugates

The GNP-M2 conjugates were washed twice with MES buffer and concentrated in MES buffer, then mixed with ssDNA MC2 at M2:MC2 molar ratio of 1:2 and allowed to hybridise at room temperature for 3 h to make GNP(27 nm)-M2/MC2 and GNP(14 nm)-M2/MC2 conjugates.

Formation and pH responsive study of GNP(27 nm)-M2/MC2-DOX and GNP(14 nm)-M2/MC2-DOX conjugates

GNP(14 nm)-M2/MC2 and GNP(27 nm)-M2/MC2 conjugates were dispersed in 3 mL of MES buffer, and the fluorescence spectra of GNP(14 nm)-M2/MC2 and GNP(27 nm)-M2/MC2 conjugates with increasing amounts of DOX were recorded by titrating DOX to the solutions until DOX concentration reached 10.6 μM. Then 1M HCl was added to the system to adjust the solution pH to 4.7, and the resulting fluorescence spectra were recorded every 15 min for 2 h. Fluorescence spectra of the ssDNA MC2 (13 μM) and MES buffer with increasing amount of DOX were also measured and used as controls (final DOX concentration for controls: 2.1 μM).

3.1.4 Preparation of GNP-dsDNA-DOX NDDSs using 14-nm GNPs

40 nmol M1 (M2 or M3) was added to 8.8 mL GNP (14 nm) solution (132 nmol, molar ratio M1:GNP = 300:1) to prepare GNP-M1, GNP-M2 and GNP-M3 conjugates, respectively, using the same procedure as above. Then the amounts of unbound M1, M2 and M3 were estimated by measuring the absorbance at 260 nm and using $\varepsilon_{M1} = 2.65 \times 10^5\ cm^{-1} \cdot M^{-1}$, $\varepsilon_{M2} = 4.87 \times 10^5\ cm^{-1} \cdot M^{-1}$, and $\varepsilon_{M3} = 7.09 \times 10^5\ cm^{-1} \cdot M^{-1}$.

The red oily precipitates (GNP-M1, GNP-M2 and GNP-M3 conjugates) were washed twice and concentrated in MES buffer. MC2, MC2(PEG250) or MC2(PEG750) was added to the conjugate solutions to make the GNP-dsDNA nanocarriers (molar ratio M1:MC2 = 1:1, M2:MC2 = 1:2 and M3:MC2 = 1:3). After 3 h, DOX (500 μM, the exact volume varied from the sample sizes) was then added to make GNP-dsDNA-DOX NDDSs (molar ratio DOX:M1 = 3:1, DOX:M2 = 6:1 and DOX:M3 = 9:1).

3.1.5 Dynamic light scattering (DLS) measurement

The hydrodynamic sizes of the GNP-dsDNA nanocarriers were measured in MES buffer (pH 7.4) on a Brookhaven Instruments Corp BI-200SM Laser Light Scattering Goniometer with a BI-APD detector, using an He-Ne laser at 633 nm (scattering angle: 90°, temperature: 25 °C).

3.1.6 DOX release experiment

A certain amount of 1 M HCl was added to the GNP-dsDNADOX system in MES buffer (50 mM MES, 150 mM NaCl, pH = 7.4, with C_{DOX} = 5 μM) to change the system pH to 5.5, 5.1 or 4.7, and the resulting mixture was incubated at 37°C for a certain period (e.g. 2 h). Thereafter, the GNP-DNA conjugate was removed by centrifugation. The resulting clear supernatant was collected and its DOX fluorescence (originated from the released DOX) was measured against a pre-determined fluorescence intensity-concentration calibration curve of free DOX to determine the amount of DOX that had been released from the nanocarrier.

3.1.7 Cell culture

HeLa human cervix adenocarcinoma cells were grown in DMEM, supplemented with 10% foetal bovine serum (FBS), 100 U/mL penicillin and 100 μg/mL streptomycin, then cultured at 37 °C in a 5% CO_2 humidified atmosphere.

3.1.8 Confocal laser scanning microscopy

HeLa cells were cultured overnight on collagen-pretreated coverslips in a 24-well plate. They were then incubated with free DOX, GNP-M1/MC2 (PEG750)-DOX, GNP-M2/MC2 (PEG750)-DOX or GNP-M3/MC2 (PEG750)-DOX (all containing 5 μM DOX, molar ratio M1:DOX=1:3, M2:DOX=1:6 and M3:DOX=1:9) in media at 37 °C for 3, 24 and 48 h respectively. Thereafter the medium was removed and the cells were washed three times with PBS (pH 7.4).

The treated HeLa cells were then imaged using a Leica SP5 confocal laser scanning microscope using 488 nm excitation and detecting fluorescence over a range of 580-600 nm.

3.1.9 MTT cell viability assay[209]

10^4 HeLa cells per well were seeded in a 96-well plate and incubated overnight. The culture medium was then removed and 100 μL free DOX or GNP-dsDNA(PEG750) nanocarriers with or without different DOX concentrations (molar ratio M1:DOX = 1:3, M2:DOX = 1:6 and M3:DOX = 1:9) in media was added and incubated at 37 °C for 18 h. After that, the cells were washed with PBS and the MTT (100 μL, 0.5 mg/mL in DMEM) was added to each cell and incubated at 37 °C for 2 h. The MTT was then removed and 100 μL DMSO was added to each well. The plate was incubated at 37 °C for 30 min to dissolve the resulting formazan. Afterwards, absorbance was measured at 550 nm using an Opsys MR™ microplate reader, and the results were expressed in percentages of the untreated control cells.

3.1.10 Freeze drying

0.5 mL of GNP-M1/MC2(PEG750)-DOX (5 μM DOX in MES buffer, M1:DOX=1:3) in the presence of 0%, 1%, 5% or 10% PEG 6000 was freeze-dried on a Virtis Benchtop K freeze dryer, and the resulting powders were then redispersed in 0.5 mL of water.

3.2 Results and discussion

3.2.1 Characterisation of GNPs

The GNPs were prepared by two methods, and the main difference between the two was that in Method 2 the $HAuCl_4$ solution pH had been adjusted to pH 7 prior to citrate addition. As a result, the solution colour change in Method 2, from light yellow to red, happened much more slowly after tri-sodium citrate was

added and it took more than 10 min for the colour to become deep red, while in Method 1, the solution changed from pale yellow to deep red in 1 min. The appearance of red in the solution indicates the formation of unaggregated GNPs, caused by the strong plasmon absorption of isolated GNPs.

In Method 2, the slower reduction rate was ascribed to the higher solution pH which decreased the reactivity of starting Au(III) complexes, and led to production of bigger GNPs [207]. By using a simple pH adjustment to the starting solution, GNPs of a bigger size were synthesized. This was confirmed by the UV-vis absorption spectra (Figure 3.2) and TEM imaging (Figure 3.3 & 3.4).

Figure 3.2 illustrates absorption spectra of GNPs prepared by the above two methods, their plasmon absorption peaks appearing at 520 and 532 nm, respectively. The absorption peak of the GNPs prepared by Method 2 is red shifted compared to that obtained by Method 1, an indication of bigger particle sizes.

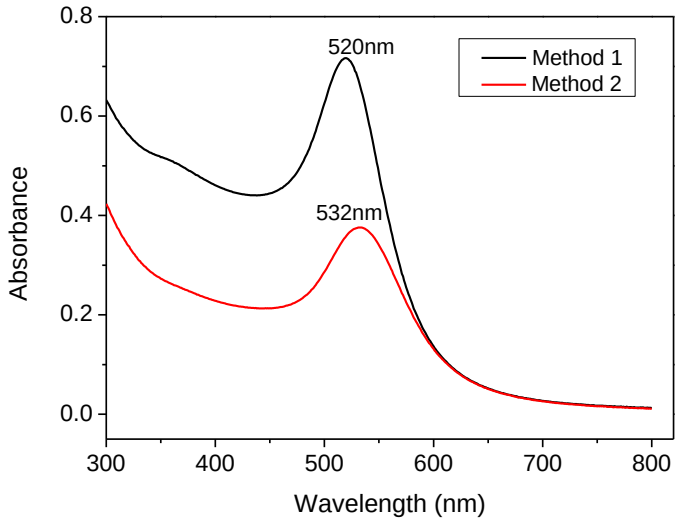

Figure 3.2. UV-Vis absorption spectra of GNP solutions prepared by Methods 1 & 2.

The absorbance values of the GNPs at their plasmon peak wavelengths were used to calculate their concentrations *via* the Beer-Lambert law ($A = \varepsilon bc$, where ε is the molar extinction coefficient, b is the optical path length and c is the concentration. The absorption extinction coefficients (ε) used are 2.4×10^{8} $M^{-1}\cdot cm^{-1}$ for 15 nm and 2.93×10^{9} $M^{-1}\cdot cm^{-1}$ for 25 nm GNPs [210, 211]. These gave calculated GNP concentrations of 15.3 (Method 1) and 0.75 nM (Method 2).

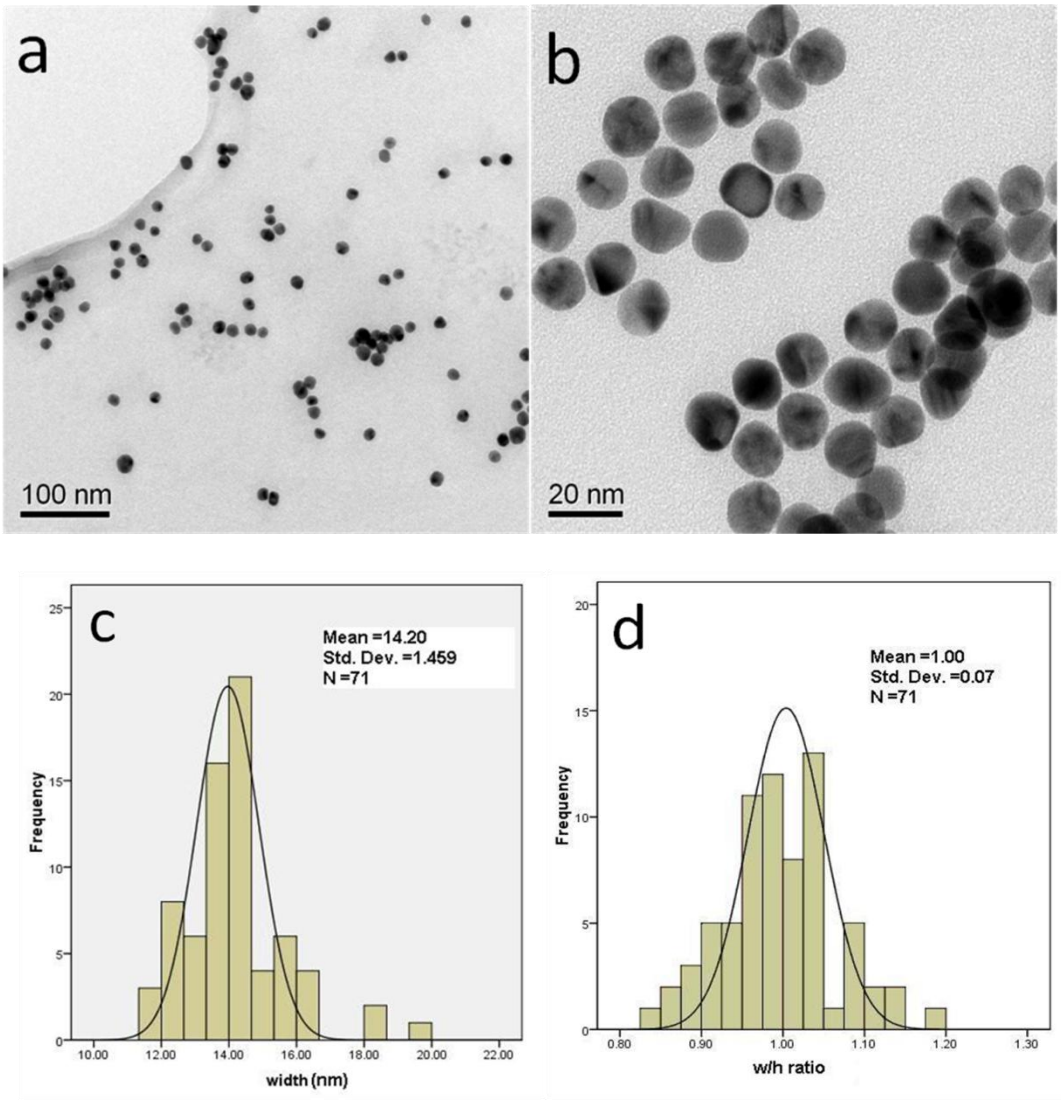

Figure 3.3. TEM images of GNPs prepared by Method 1(**a** and **b**); and the corresponding histograms of particle size (**c**) and width-to-height ratio distributions (**d**) for a total of 71 particles.

The TEM images of GNPs prepared by these two methods show that they are

both isolated and unaggregated. Their diameters were easily determined by the Digital Micrograph Software. By measuring the diameters of different particles appearing in the TEM images, histograms of the resulting particle sizes and their width-to-height ratios were obtained, and these are shown in Figures 3.3 and 3.4. The histograms provide a simple way of presenting GNP size distribution and particle shape. The sizes of GNPs prepared by Methods 1 and 2 are uniform, with relatively narrow size distributions of 14.2 ± 1.5 nm and 27.3 ± 3.7 nm, respectively, and the ratios of width to height are 1.00 ± 0.07 and 0.98 ± 0.10, indicating that all GNPs are roughly spherical in shape.

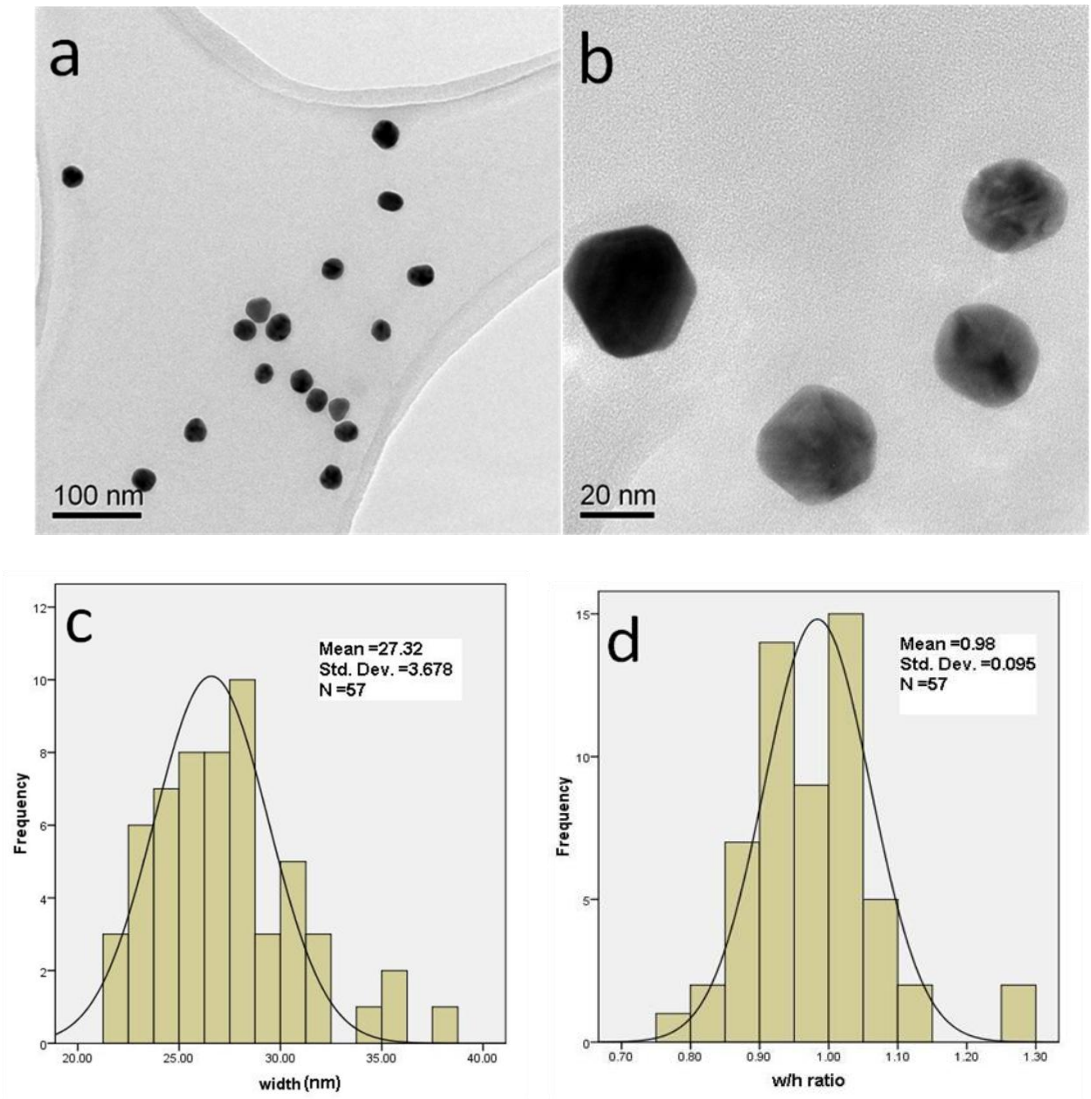

Figure 3.4. TEM images of GNPs prepared by Method 2 (**a** and **b**); and the corresponding histograms of particle size (**c**) and width-to-height ratio (w/h ratio) distributions (**d**) for a total of 57 particles.

From Figure 3.3 & 3.4, the relative polydispersity (Coefficient of variation) were derived as 10.3% and 13.5%, respectively, indicating that both GNPs are roughly monodisperse. In contrast, most synthetic polymer based drug carriers are a mixture of different lengths, which tend to have considerably higher polydispersities. Because of this, polymer molecular weights are usually average values, such as the number average molecular weight (MW) and the weight average molecular weight. Because the size (or MWs for polymers) of the drug carrier strongly affects its biodistribution and pharmakinetics, therefore, the use of monodisperse GNPs as drug carriers is advantageous, ensuring that the resulting NDDSs are of uniform sizes and components.

3.2.2 GNP(14nm)-M2/MC2-DOX and GNP(27nm)-M2/MC2-DOX conjugates

All the designed pH-responsive ssDNAs (M1, M2 and M3) contain not only *i*-motif domain(s) but also a T_{10} (10 thymines) spacer between the thiol group and the *i*-motif domain(s), which is used to extend the *i*-motif domain(s) away from the GNP surface, minimizing any non-specific interaction or steric effect that might interfere with *i*-motif formation and/or hybridisation[160, 172, 206, 212-214].

Here, M2 was chosen first to prepare GNP-DNA conjugates with 14-nm GNPs and 27-nm GNPs in order to explore the curvature effects of GNPs on DNA surface coverage, and to evaluate their feasibilities as drug nanocarriers in terms of DOX intercalation and pH-responsiveness.

3.2.2.1 Curvature effects on GNP-DNA conjugate

Standard citrate-stabilized GNPs will aggregate in the presence of NaCl due to the screening of electrostatic repulsion. When M2, a 5'-thiol-modified DNA, is added to a GNP solution it will displace the weakly-bonded citrate ligands and

attach to the GNP surface *via* a strong Au-thiolate (Au-S) bond to form a GNP-M2 conjugate that is stable. It does not aggregate even under 1M NaCl, due to the multiple negative charges from the DNA phosphate backbone which provide enhanced electrostatic stabilisation. The amount of DNA attached to each GNP surface can be increased significantly with the use of sonication[134, 208, 211]. DNA loading amount was calculated by measuring UV absorbance of the unbound DNA at 260 nm ($\varepsilon_{M2} = 4.87 \times 10^5$ $cm^{-1}.M^{-1}$) in the supernatant after centrifugation. This assumes that all the missing DNAs (initial amount – supernatant remains) have bound to the GNP. In the GNP(14nm)-M2 conjugate system, the concentrations of GNP and loaded M2 are 11 nM and 1.0 μM, while in the GNP(27nm)-M2 system, their concentrations are 5 nM and 0.66 μM, respectively. These values correspond to average numbers of DNA M2 loaded on a 14-nm GNP being 94, and 132 on a 27-nm GNP.

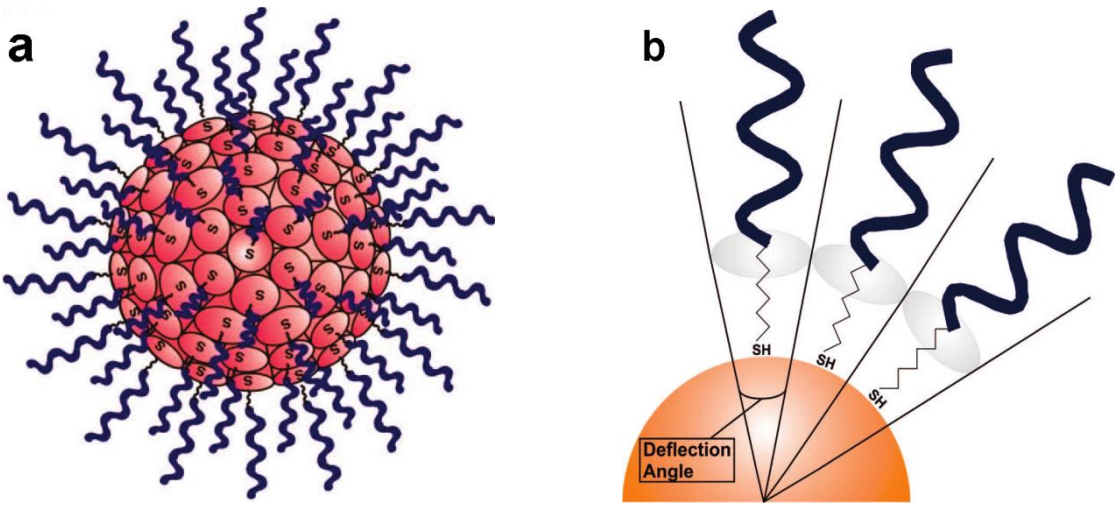

Figure 3.5. (**a**) Model used to calculate the oligonucleotide footprint; (**b**) Schematic of the deflection angle between oligonucleotides. Figures adapted from ref[208] .

Assuming that all GNPs are perfectly spherical in shape and are of identical sizes (mean size measured from TEM), and that the oligonucleotides are evenly distributed on the GNP surface, then the surface density of DNA (SDD), the

DNA footprint (*K*) (Figure 3.5(a)) and the deflection angle between neighbouring DNAs on the GNP surface (Figure 3.5(b)) can be calculated with the following equations:

$$SDD=\frac{N}{4\pi r^2} \quad (1)$$

Where N is the number of DNA strands attached on each GNP; *r*: GNP radius

$$K = \frac{4\pi r^2}{N} \quad (2)$$

$$\text{Deflection angle} = (\frac{2R}{r})\times\frac{180}{\pi} \quad (3)$$

$$R = \sqrt{\frac{K}{\pi}} \quad (4)$$

Where R is the radius of the footprint approximation on the GNP surface

These values can be used to evaluate the spatial arrangement of the DNA strands and the effects of the radius of curvature of GNPs on DNA surface coverage (Table 3.1). It is clear that DNA loading on the GNP surface can be influenced by the surface curvature. The M2 coverage on 14-nm GNPs are nearly three times higher (three times lower in terms of footprint) than that on 27-nm GNPs even though more M2 strands were attached to the latter. In other words, the GNP-M2 conjugate with smaller GNP diameter (14 nm) displays a higher surface density of DNA M2, which is in agreement with the trend reported in the literature[208].

Table 3.1. Surface coverage, effective footprint and deflection angle for the GNP-DNA conjugates prepared in this study.

GNP-ssDNA	Diameter (nm)	Oligos/particle	Coverage (oligos/cm^2)	Footprint (nm^2)	Deflection(deg)
GNP(14nm)-M2	14	94±11	(1.5 ± 0.2)×10^{13}	6.6±1.1	23.7±2.0
GNP(27nm)-M2	27	132±13	(5.8 ± 0.6)×10^{12}	17.5±2.4	20.0±1.4

3.2.2.2 The formation of GNP(14 nm)-M2/MC2-DOX and GNP(27 nm)-M2/MC2-DOX conjugate

We made the GNP-M2/MC2-DOX conjugates using GNP(14 nm)-M2 and GNP(27 nm)-M2 conjugates with final GNP and M2 concentrations of 11 nM/1.0 μM; and 5 nM/0.66 μM for the 14 and 27 nm GNP-M2/MC2-DOX systems, respectively. Figures 3.6 and 3.7 are the fluorescence spectra of GNP-M2/MC2 / DOX and fluorescence intensity plot (at 590 nm) after addition of a certain amount of DOX (10.6 μM). Both MES buffer and ssDNA MC2 (~13 μM in MES) with DOX addition (2.1 μM) were used as controls.

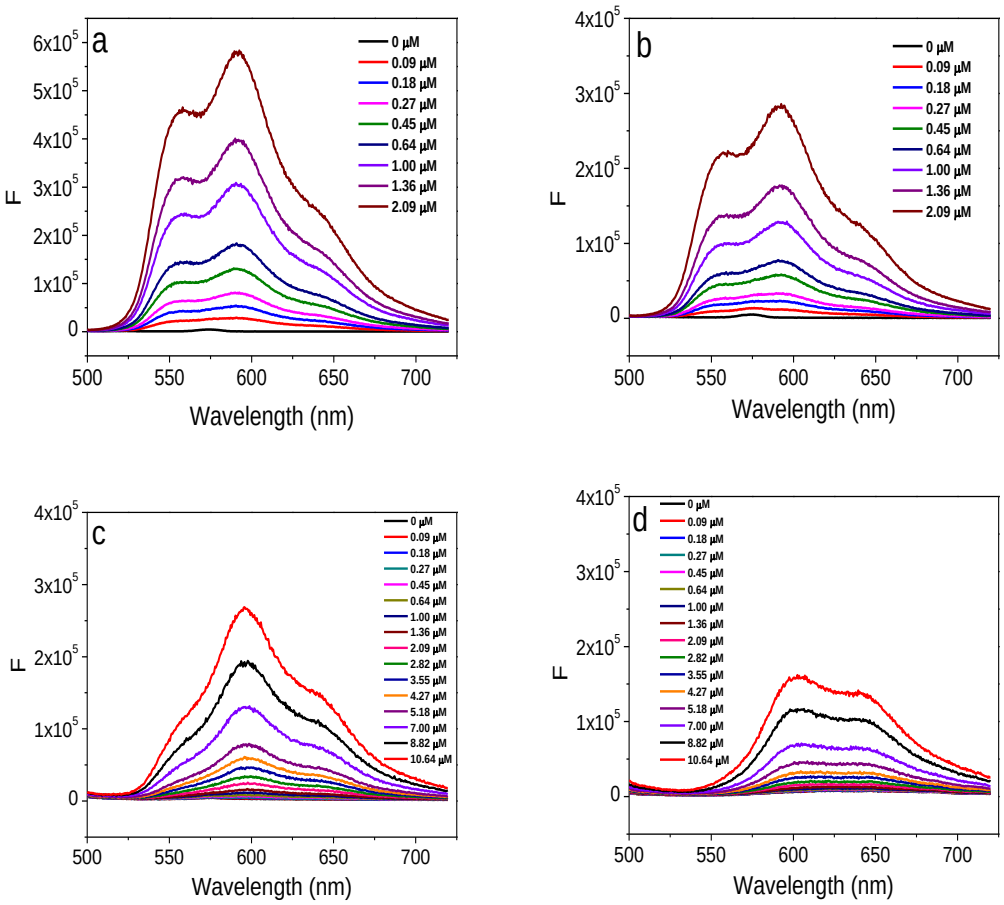

Figure 3.6. The fluorescence spectra of DOX in (**a**) MES buffer, (**b**) with ssDNA MC2, (**c**) with GNP(14nm)-M2/MC2 conjugate and (**d**) with GNP(27nm)-M2/MC2 conjugate with increasing DOX concentration (from bottom to top: 0, 0.09, 0.18, 0.27, 0.45, 0.64, 1, 1.36, 2.09, 2.82, 3.55, 4.27, 5.18, 7, 8.82 and 10.64 μM).

Fluorescence emission of DOX with both GNP-M2/MC2 conjugates present was

heavily quenched, and their emission spectra were red shifted compared to those of DOX alone and DOX with MC2, which suggests that DOX can intercalate into both GNP(14 nm)-M2/MC2 and GNP(27 nm)-M2/MC2 conjugates to form GNP-M2/MC2-DOX conjugates as expected, and that therefore both GNP-M2/MC2 conjugates can be exploited as drug (DOX) carriers. The difference between both conjugates using 14 nm and 27 nm gold NPs here is that the spectra of GNP(27 nm)-M2/MC2-DOX red shifted more than GNP(14 nm)-M2/MC2-DOX, probably due to the difference in size of the conjugates. The final molar ratios of M2 to DOX were 0.09 and 0.06 for the 14- and 27-nm GNP-M2/MC2-DOX systems, respectively. Both were higher than the Michaelis constant of M2/MC2 for DOX (0.033), so DOX intercalation in the dsDNA was not saturated. The fluorescence intensity of DOX with MC2 was lower than DOX alone at the same concentration. This is probably due to electrostatic interaction between DOX and ssDNA MC2 leading to slightly quenched DOX fluorescence.

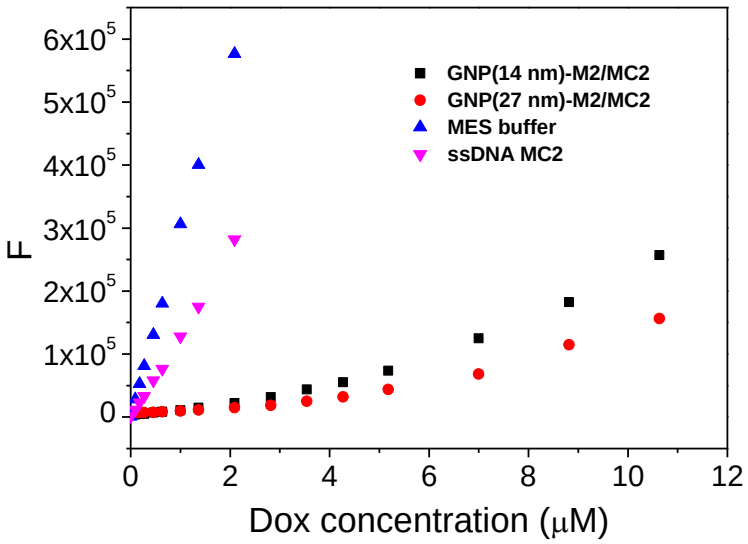

Figure 3.7. Plots of DOX fluorescence intensity at 590 nm in MES buffer, ssDNA MC2, GNP(14 nm)-M2/MC2 conjugate and GNP(27 nm)-M2/MC2 conjugate with increasing DOX concentration.

3.2.2.3 pH responsiveness of GNP-dsDNA-DOX conjugates

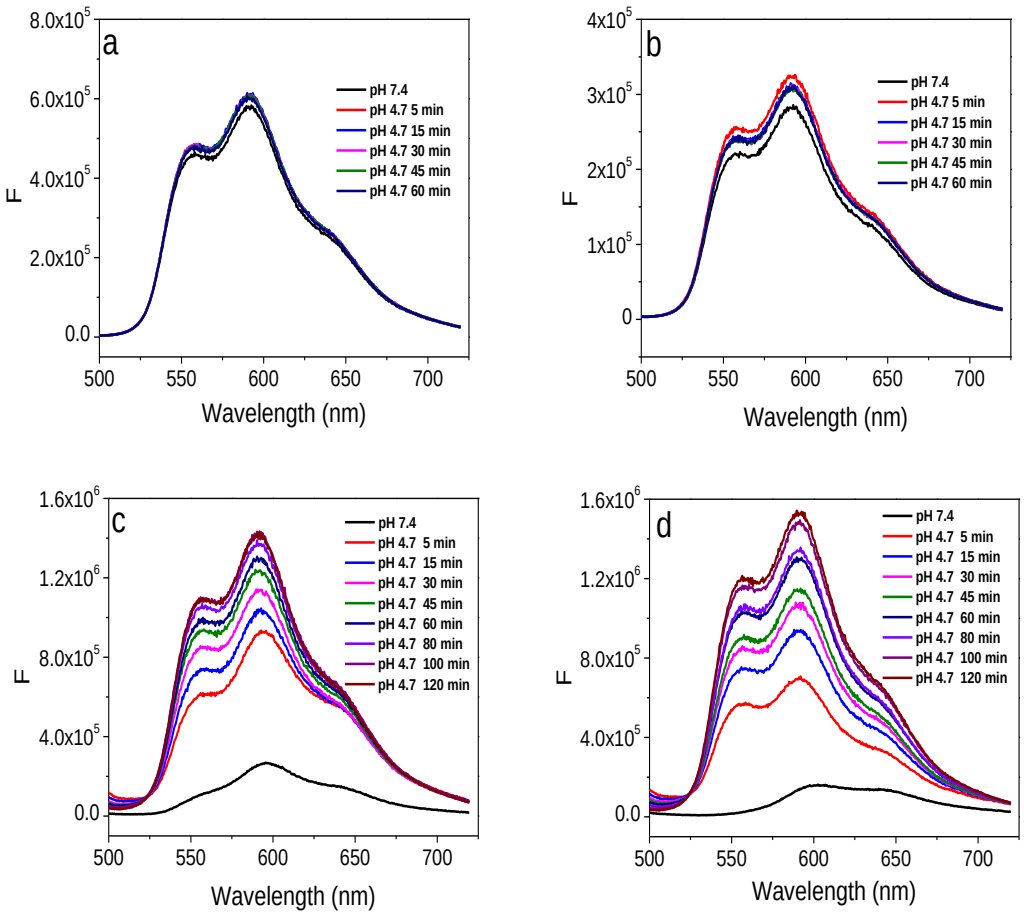

Figure 3.8. Time-dependent fluorescence spectra of (**a**) MES buffer+DOX(2.1 μM), (**b**) ssDNA MC2+DOX (2.1 μM), (**c**) GNP(14 nm)-M2/MC2-DOX (10.6 μM) conjugate and (**d**) GNP(27 nm)-M2/MC2-DOX(10.6 μM) conjugate after pH was adjusted to 4.7 (from bottom to top: pH 7.4, pH 4.7 5 min, pH 4.7 15 min, pH 4.7 30 min, pH 4.7 45 min, pH 4.7 60 min, pH 4.7 80 min, pH 4.7 100 min, pH 4.7 120 min).

Figures 3.8 and 3.9 show fluorescence spectra of GNP(14 nm)-M2/MC2-DOX and GNP(27 nm)-M2/MC2-DOX conjugates with pH changes. When pH was adjusted to ~4.7, their fluorescence peaks shifted back to the original position and fluorescence intensities gradually increased with time (over 2 h). This clearly indicates that the intercalated DOX was released slowly from both GNP-M2/MC2-DOX conjugates as the solution pH was decreased to weakly acidic, suggesting that both conjugates can be used in pH-targeted drug delivery applications. Furthermore, no obvious difference was found between

GNP(14 nm)-M2/MC2-DOX and GNP(27 nm)-M2/MC2-DOX conjugates regarding DOX release, suggesting that DOX release from GNP-dsDNA-DOX conjugate is mainly controlled by the dsDNA-DOX part, not the GNP particle size. In the controls, no significant change in fluorescence intensity was found from the DOX in the MES buffer or ssDNA MC2 solutions, confirming that release is specific for the conjugates because of *i*-motif formation.

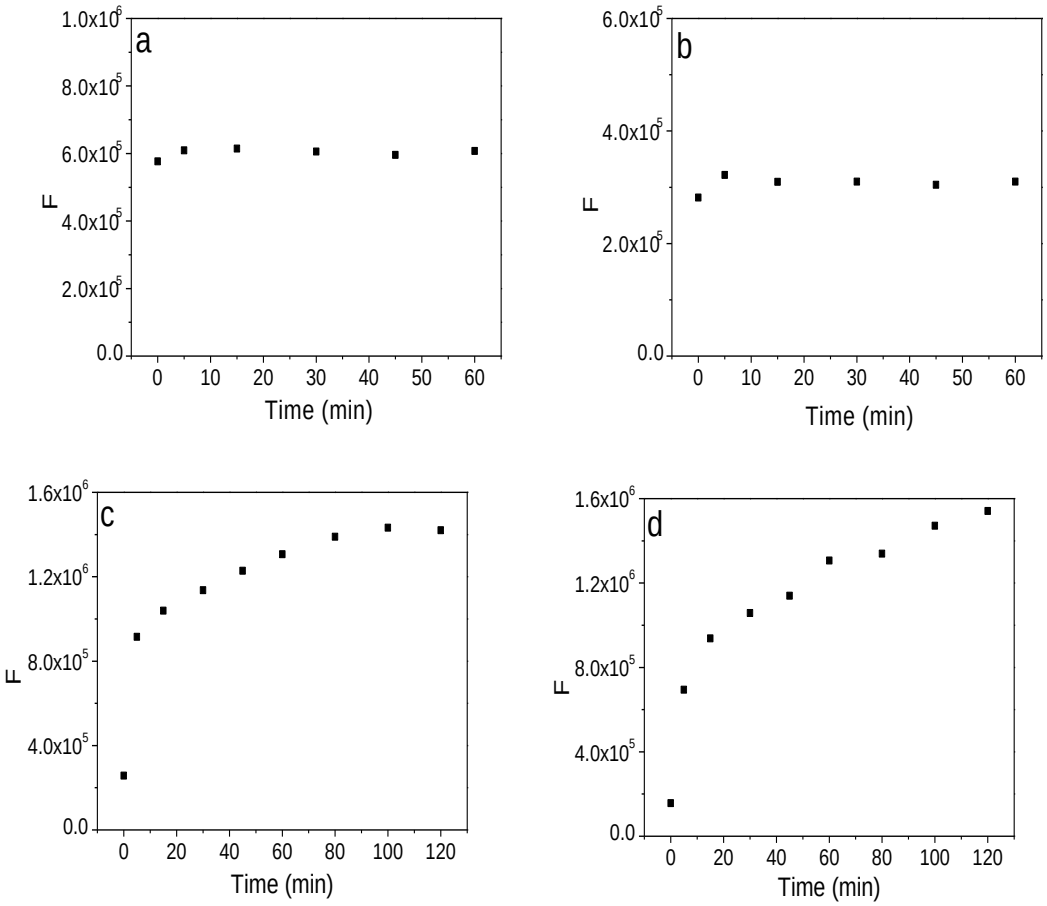

Figure 3.9. Plots of DOX fluorescence intensity at 590 nm versus time for (**a**) MES buffer + DOX(2.1 μM), (**b**) ssDNA MC2 + DOX (2.1 μM), (**c**) GNP(14 nm)-M2/MC2-DOX(10.6 μM) conjugate and (**d**) GNP(27 nm)-M2/MC2-DOX(10.6 μM) conjugate after pH was adjusted to 4.7.

3.2.3 GNP(14 nm)-dsDNA conjugate as a new system for drug delivery (GNP-dsDNA-DOX NDDS)

To exploit the EPR effect for effective cancer targeting *in vivo*, the carrier size should normally be between that of the renal clearance threshold (~ 8 nm)[205] and the average gap in leaky blood vessels in tumours (~100 nm)[10, 19]. The

hydrodynamic diameters (HD) of GNP(14 nm)-dsDNA conjugates measured by dynamic light scattering (Table 3.2) show that the size of GNP(14 nm)-M3/MC2 conjugate is around 70 nm, and it would be bigger if the conjugate was modified by PEG. To avoid the conjugate size exceeding the average gap in leaky blood vessels in tumours, 14-nm GNP will be used to prepare a pH-responsive GNP-dsDNA conjugate as a targeted NDDS, although GNP(27 nm)-dsDNA can also act properly *in vitro*.

Table 3.2. Hydrodynamic diameters (HDs) of GNP-M1/MC2, GNP-M2/MC2 and GNP-M3/MC2 in MES buffer.

GNP(14 nm)-dsDNA	HD in MES buffer (nm)
GNP(14 nm)-M1/MC2	49.5 ± 6.6
GNP(14 nm)-M2/MC2	63.5 ± 4.6
GNP(14 nm)-M3/MC2	69.4 ± 3.4

We also found that the average numbers of attached DNA strands on each GNP vary between GNP-M1, GNP-M2 and GNP-M3 conjugates (around 108 strands for M1, 94 for M2 and 80 for M3), indicating that the number of bound DNA strands decreased with increasing length of DNA, which agrees well with the reference[215]. Despite this, the DOX loading amount can still be improved by increasing DNA length, based on the calculation of the DOX loading ratio between GNP-M1, GNP-M2 and GNP-M3 (GNP-M1 : GNP-M2 : GNP-M3 = 108 : 2*94 : 3*80).

3.2.3.1 DOX releasing profiles

The following GNP-dsDNA-DOX NDDSs were prepared,: GNP-M1/MC2-DOX, GNP-M1/MC2(PEG250), GNP-M1/MC2(PEG750), GNP-M2/MC2(PEG750) and GNP-M3/MC2(PEG750), with the DOX:M1 molar ratio kept at 3:1 (6:1 for

DOX:M2 and 9:1 for DOX:M3), below the saturation binding capacity to ensure that DOX was efficiently bound to the nanocarriers.

The pH-dependent DOX releasing experiments were investigated by changing pH to acidic. It can be seen that for both GNP-M1/MC2-DOX and GNP-M1/MC2(PEG750)-DOX, little DOX (less than 4% or 9%) was released at pH 5.5 or 5.1, and only after pH was further lowered to 4.7 was efficient DOX release observed (approximately 90% release in 2 h) (Figure 3.10a). Interestingly, the pH switching points for GNP-dsDNA-DOX systems appeared to be lower than their dsDNA-DOX counterparts; in addition, the DOX-release rate was also significantly slower (it took 2 h for most DOX to be released from GNP-dsDNA-DOX systems, compared with 2 mins for dsDNA-DOX systems). The difference may result from the much higher DNA density on the GNP, where interaction between neighbouring strands may provide extra-stabilisation of the dsDNA, leading to a lower pH switching point and a slower release of DOX.

Figure 3.10b shows DOX-release profiles of non-PEG GNP-M1/MC2-DOX compared with PEG-modified GNP-M1/MC2-DOX NDDSs. Both GNP-M1/MC2(PEG250) and GNP-M1/MC2(PEG750) displayed very similar pH-dependent DOX-release behaviours to GNP-M1/MC2-DOX, which further confirms that PEG-modifications on the surface of GNP-dsDNA-DOX NDDSs do not influence DOX-release behaviour.

Also, despite different numbers of four stretches of C-rich domains among M1, M2 and M3, most DOX was also released from the GNP-M2/MC2(PEG750)-DOX and GNP-M3/MC2(PEG750)-DOX NDDSs within 2 h at pH 4.7 (Figure 3.10c), although the final amount of DOX released was slightly lower than that of GNP-M1/MC2(PEG750)-DOX, possibly due to

stronger electrostatic interaction of DOX with longer DNAs.

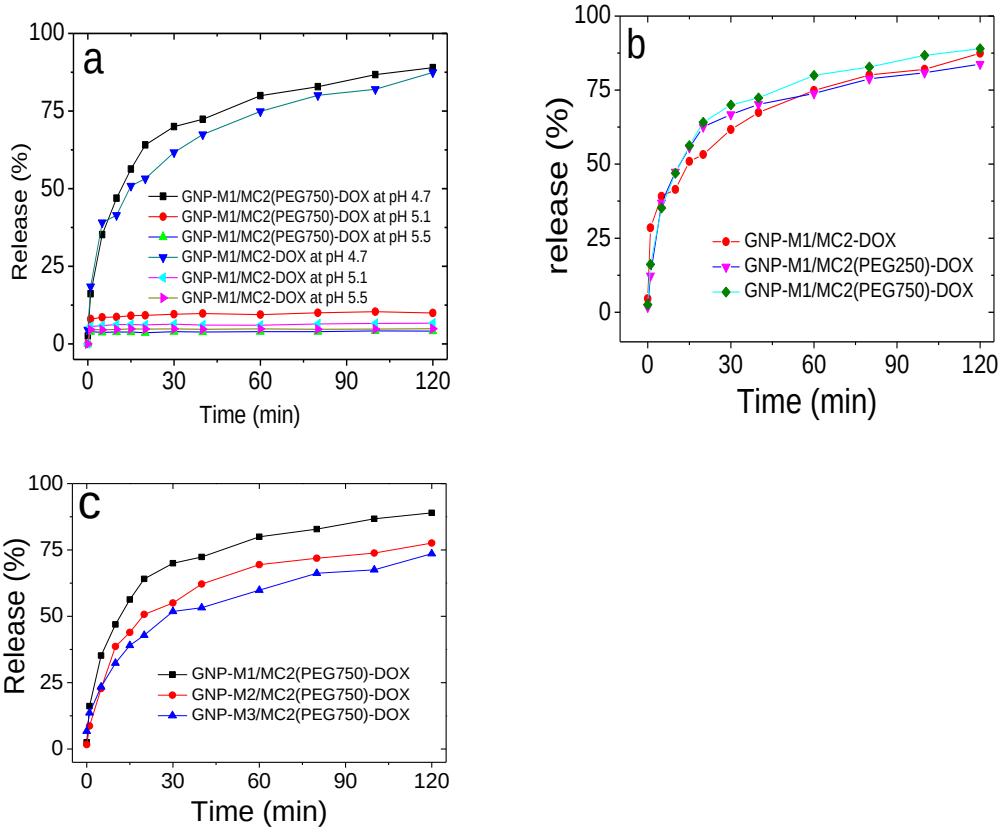

Figure 3.10. (**a**) DOX release from GNP-M1/MC2-DOX and GNP-M1/MC2 (PEG750)-DOX NDDSs at different acidic pHs (5.5, 5.1 and 4.7). (**b**) pH-triggered DOX-release profiles for different GNP-M1/M2-DOX systems with/without PEG-modifications at pH 4.7. (**c**) pH-triggered DOX-release profiles for GNP-M1/MC2(PEG750)-DOX, GNP-M2/MC2 (PEG750)-DOX and GNP-M3/MC2 (PEG750)-DOX at pH 4.7.

3.2.3.2 *In vitro* cell-based studies

In vitro DOX delivery by GNP-dsDNA(PEG750) nanocarriers to immortalized human cervix adenocarcinoma (HeLa) cells was evaluated using confocal fluorescence imaging (*via* DOX fluorescence). Figure 3.11 reveals that all the nanocarriers were highly efficient at delivering DOX into cancer cells, where strong DOX fluorescence was observed inside the cells after 3 h. Free DOX can enter and accumulate in cells by diffusing, while the polyvalent GNP-dsDNA is internalized mainly *via* scavenger receptor-mediated endocytosis[216]. After uptake, DOX is released from the GNP-dsDNA(PEG750) carrier in the acidic

environment of late endosomes or lysosomes whose pHs were reported to be as low as 4.3[169], lower than that required for efficient DOX release (~ pH 4.7). The released DOX can then diffuse across the endosomal/lysosomal membranes and reach the nucleus to exert its toxicity. This mechanism (see Chapter 4) is supported by TEM analysis on HeLa cells after 3 h incubation with the GNP-dsDNA(PEG750) NDDS, where the GNPs were found located exclusively in intracellular compartments. Furthermore, this *in vitro* DOX release experiment has confirmed that significant DOX release only happens in an acidic environment (pH < 5.1), but not in cell culture media or in the cytosol (pH 7-7.4).

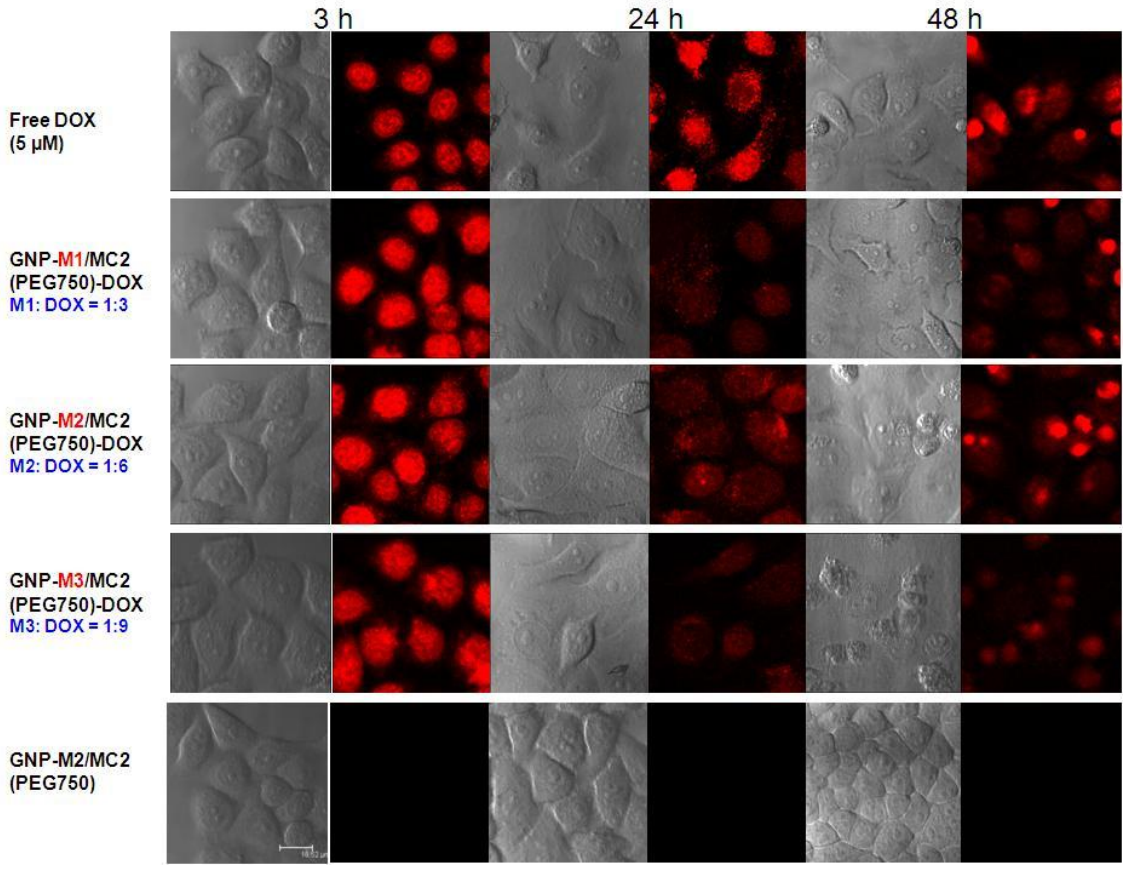

Figure 3.11. Confocal laser scanning microscopy images of HeLa cells treated with DOX and different GNP-dsDNA(PEG 750)-DOX NDDSs for 3 h, 24 h and 48 h (the left-side image of each set is a phase-contrast image and the right-side image of each set is a DOX fluorescence image).

After further incubation (24 h and 48 h) morphological changes, together with much weaker fluorescence, were observed in the cells treated with both free DOX and GNP-dsDNA(PEG750)-DOX, which indicates that treatment with free DOX or all GNP-dsDNA(PEG750)-DOX NDDSs induces cell apoptosis. In contrast, the cells incubated with GNP-M2/MC2(PEG750) (no DOX loading) appeared healthy even after 48 h incubation, and the number of live cells increased significantly, seeming to suggest that the GNP-dsDNA(PEG750) nanocarrier is non-toxic and compatible with HeLa cells *in vitro*.

The cytotoxicity towards HeLa cells of GNP-M1/MC2(PEG750) NDDSs with various DOX concentrations was studied by MTT-based cell proliferation assays (18 h in complete growth media). The nanocarriers without DOX were found to be non-cytotoxic. In fact, all systems (GNP-M1/MC2(PEG750)-DOX or free DOX) with DOX concentration ≤ 2.5 μM exhibited no measurable cytotoxicity towards HeLa cells under these conditions (Figure 3.12a). As DOX concentration was increased, cell viability progressively decreased, suggesting that cytotoxicity comes from the loaded DOX, and not the carrier. More importantly, the GNP-M1/MC2(PEG750)-DOX NDDSs exerted similar levels of cytotoxicity on HeLa cells to free DOX across the entire DOX concentration range studied (Figure 3.12a). Besides GNP-M1/MC2(PEG750)- DOX, the GNP-M2/MC2(PEG750)-DOX and GNP-M3/MC2(PEG750)-DOX NDDSs containing 5 μM DOX (molar ratio M2:DOX=1:6 and M3:DOX=1:9) exhibited comparable cell cytotoxicity (Figure 3.12b), which, together with the confocal imaging results, further confirms that using longer DNAs to improve DOX loading capacity, thereby reducing the amount of GNPs, is feasible and works efficiently.

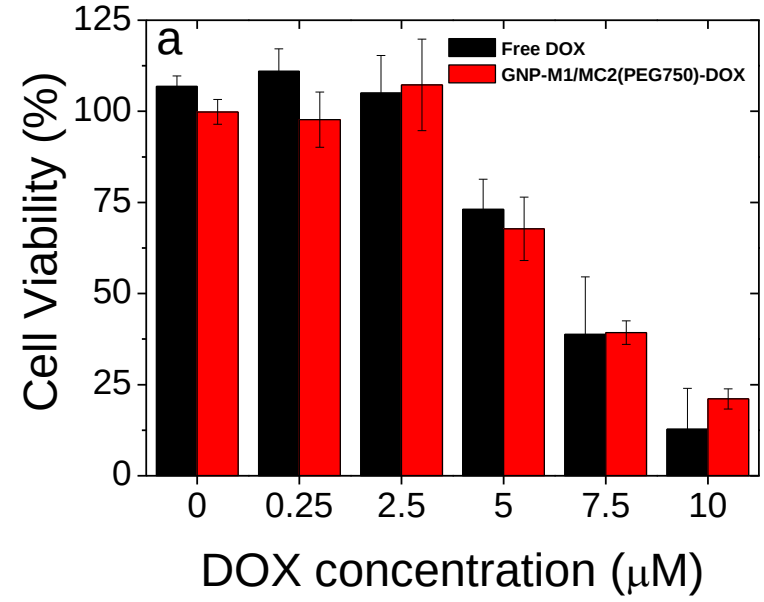

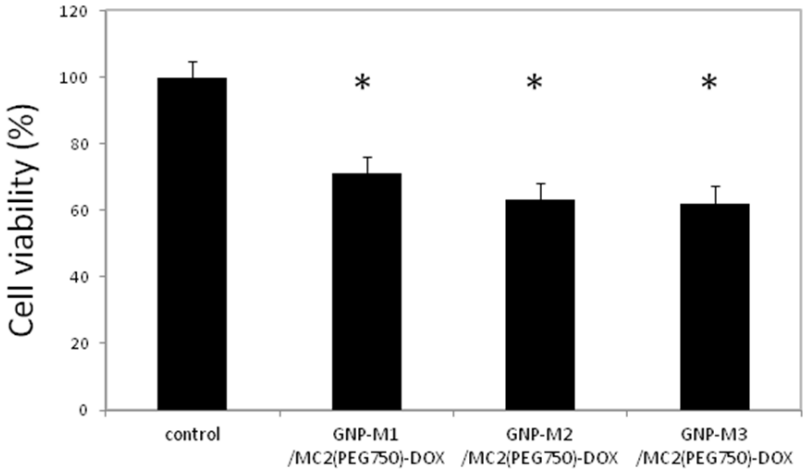

Figure 3.12. (**a**) MTT assay of HeLa cell viabilities after incubation with DOX and GNP-M1/MC2(PEG750)-DOX (DOX concentrations varied from 0 to 10 μM) for 18 h at 37 ℃. (**b**) MTT assay of HeLa cell viabilities after incubation with different GNP-dsDNA(PEG750)-DOX NDDSs (containing 5 μM DOX) for 18 h at 37 ℃. (*p < 0.05, compared with control)

3.2.3.3 Freeze-dried GNP-M1/MC2(PEG750)-DOX system

Stability is one of the essential requirements for regulatory approval of a drug or

formulation[217], as the product must retain the same properties throughout the storage period as at its packaging time. Because nanoparticles tend to aggregate due to their high surface-to-volume ratio[218-220] and because DOX aqueous solution is not stable during long-term storage, the feasibility of applying freeze-drying (lyophilisation) technique to the GNP-dsDNA-DOX NDDS was explored. Freeze-drying has been regarded as a very useful method for improving long-term stability of both colloidal nanoparticles[221] and DOX.

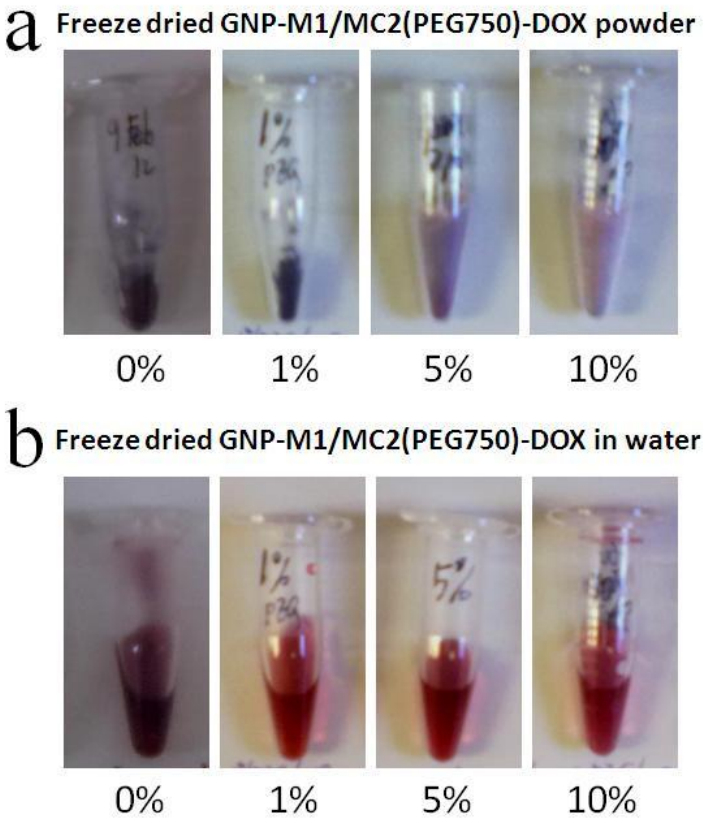

Figure 3.13. (**a**) Photographs of freeze-dried GNP-M1/MC2(PEG750)-DOX powders in the presence of 0%, 1%, 5% and 10% PEG 6000. (**b**) Photographs of the reconstituted solutions.

From Figure 3.13 we can see that, after freeze-drying, a GNP-M1/MC2(PEG750)- DOX powder was obtained (without any other additive), but the reconstituted solution turned purple, indicating aggregation of GNP-M1/MC2(PEG750)-DOX. But in the presence of 1%, 5% or 10% PEG

6000, the reconstituted solution remained red in colour. This suggests that with the addition of PEG the GNP-M1/MC2(PEG750)-DOX powder is well dispersed in water without observable aggregation, and that freeze-drying is applicable to the GNP-dsDNA-DOX NDDS for long-term storage, although further optimisation may still be required.

Our results suggest that GNP-dsDNA(PEG750)-DOX NDDSs may have good potential for effective cancer chemotherapy. A significant advantage of this nanocarrier is its simplicity, where the drug is loaded directly and conveniently in native form, eliminating any chemical modification or coupling steps that may alter the properties and/or therapeutic efficacy of the loaded drugs. More importantly, their distinct advantage over free DOX is nanoscale sizes (less than 100 nm), allowing for specific cancer targeting *via* the EPR effect (passive targeting), and significant reduction of the side-effects of free DOX based chemotherapy.

3.3 Conclusion

14-nm and 27-nm GNPs were prepared through citrate reduction. Both can be employed to develop an innovative pH-responsive GNP-dsDNA drug nanocarrier with the capability of rapid, efficient and pH-triggered drug release.

By using a PEG-modified complementary DNA to hybridise to the GNP-M1 conjugate, the surface of GNP-dsDNA-DOX NDDS can be fully and conveniently PEGylated, extremely important for future *in vivo* applications as PEGylation is well-known to provide “stealth effect” for the NDDS, reducing non-specific interaction with serum proteins and increasing blood circulation time. Moreover, GNP-dsDNA(PEG)-DOX NDDSs display the same pH responsiveness and DOX-release profiles as non-PEG GNP-dsDNA-DOX.

By increasing the number of *i*-motif units from 1 to 3, DOX-loading efficiency was further improved despite a slightly decrease in the number of DNA strands attached to each GNP. Cellular cytotoxicity studies show that GNP-dsDNA nanocarriers are non-toxic, and that all of the GNP-dsDNA(PEG)-DOX NDDSs (containing M1, M2 and M3, respectively) can efficiently deliver DOX into HeLa cells with similar cytotoxicity to free DOX.

In summary, the GNP-dsDNA(PEG) nanocarrier has numerous features essential for an 'ideal drug nanocarrier' for cancer treatment: uniform small nanoscale size (< 100 nm); the ability to resist non-specific interaction *in vivo* and to prolong its circulation time in blood (*via* PEG); high drug loading capacity (more than 300 molecules of DOX per GNP); the capacity for controlled release (*via* intracelluar endosomal/lysosomal acidic environments); it is non-toxic, biocompatible, water-soluble, and suitable for freeze-drying, which can greatly improve long-term stability. This system can be further developed into active targeting and/or multifunctional versions of the nanocarrier, by incorporating cancer cell-specific targeting ligands, or by replacing the GNP with other functioning nanoparticles that can provide additional therapeutic/imaging modalities (see Chapter 7 & 8).

4 Chapter 4: Mechanism of GNP-DNA cellular uptake

Substances such as small molecules, macromolecules and nanoparticles can enter or leave cells either by passive diffusion or by active transport such as endocytosis and exocytosis. Nanoscale objects, *e.g.* nanoparticles, are generally believed to be taken up by cells through endocytosis[222-225] . GNP-DNA conjugate, as one of the nanoparticle systems, has been reported to enter cells *via* scavenger receptor-mediated endocytosis[216] and can be taken up efficiently by more than 30 types of cells lines, primary cells and neurons [226]. Based on the above facts, the pH-responsive GNP-dsDNA-DOX system is assumed to enter cells through the same mechanism (Figure 4.1), where it can exploit the relatively low local pH of the endocytic compartments to achieve pH-triggered DOX release. To verify this assumption, which is also the foundation of a successful pH-triggered drug release system, a few cell -based studies were designed and carried out using confocal fluorescence imaging and TEM imaging.

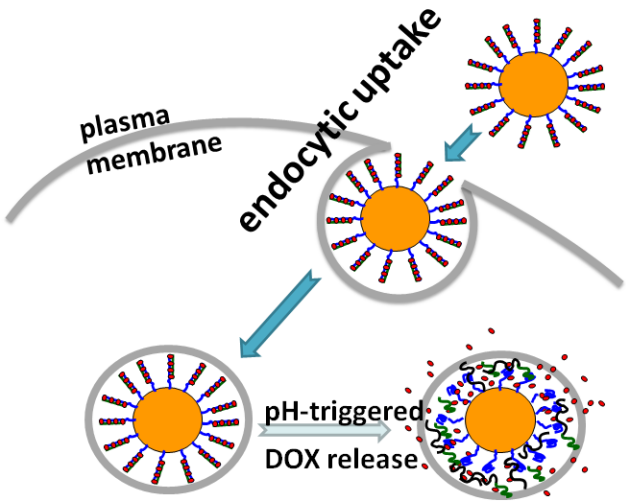

Figure 4.1. Schematics of endocytic uptake and subsequent pH-triggered drug release of the GNP-dsDNA-DOX system. The GNP-dsDNA system first enters cells *via* endocytosis. As a result of endosome maturation its local pH decreases, leading to the release of intercalated DOX molecules.

4.1 Materials and Methods

4.1.1 Materials

A dinuclear ruthenium(II) complex, $[(bpy)_2 Ru (tpphz) Ru (bpy)_2]^{4+}$ (denoted as BPY) was synthesized by Dr. Jim A. Thomas's Group at the University of Sheffield. Propidium iodide (PI) was purchased from Invitrogen.

4.1.2 Confocal Fluorescence Imaging

(a) Confocal fluorescence imaging of HeLa cells treated with free DOX and GNP-M2/MC2(PEG750)-DOX with different incubation times:

The HeLa cells were incubated with free DOX (5 μM) and GNP-M2/MC2(PEG 750)-DOX (containing 5 μM DOX; molar ratio of M2 to DOX = 1:6) in cell culture media for 5, 15, 30, 45 and 60 min, and then imaged by confocal laser scanning fluorescence microscopy (excitation/emission: 488 nm/580-600 nm).

(b) Confocal imaging of cells treated with GNP-M2/MC2(PEG750)-BPY:

BPY was dissolved in water and then mixed with GNP-M2/MC2-PEG750 to prepare GNP-M2/MC2(PEG750)-BPY in cell culture media (molar ratio of M2 to BPY = 1:18). The HeLa cells were treated with GNP-M2/MC2(PEG750)-BPY (containing 30 μM BPY) for 3 h, after which the cells were washed with PBS and subsequently imaged by confocal laser scanning microscopy using 488 nm excitation and fluorescence detection over a range of 630-670 nm.

(c) Confocal imaging of cells treated with GNP-M2/MC2(PEG750)-PI:

PI stock solution (1 mg/mL in water) was added to GNP-M2/MC2(PEG750) to form GNP-M2/MC2(PEG750)-PI in cell culture media (molar ratio of M2 to PI = 1:12). The HeLa cells were treated with GNP-M2/MC2(PEG750)-PI (containing 10 μM PI) for 3 h, after which the cells were washed with PBS and imaged by

confocal laser scanning microscopy using 488 nm excitation and fluorescence detection over a range of 600-630 nm.

4.1.3 Transmission electron microscopy

5×10^5 HeLa cells per well were seeded in 6-well plates and incubated overnight at 37 °C. The cells were treated with the GNP-M1/MC2(PEG750) -DOX in cell culture media for 3 h at 37 °C. After washing with PBS, the cells were detached and centrifuged. The cell pellets were fixed with 2.5% glutaraldehyde in 0.1 M phosphate buffer (pH 7.4) for 2.5 h, dehydrated using an ascending alcohol series (20, 40, 60, 80 and 100% twice) for 20 min each time, then embedded in Araldite resin at 65°C overnight. A 70 nm section was placed on a TEM grid and stained with saturated uranyl acetate and 0.2% Reynolds lead citrate before TEM imaging [189, 227].

4.2 Results and Discussion

4.2.1 HeLa cells treated by free DOX and GNP-M2/MC2(PEG750)-DOX for different incubation times

Although GNP-DNA conjugate has been reported to enter cells through the endocytic pathway, we cannot completely rule out the possibility that DOX could first dissociate from the GNP-DNA conjugate and then diffuse into the cells. This is because DOX was bound in dsDNA through intercalation rather than covalent chemical bonding, in spite of its high affinity. To confirm that DOX was mainly taken up by cells in the integrated form of GNP-dsDNA-DOX conjugate without dissociation, confocal laser scanning microscopy was employed to follow and compare the kinetics of DOX uptake by HeLa cells after treatments with free DOX and GNP-M2/MC2(PEG750)-DOX, respectively. Confocal fluorescence images for cells corresponding to the different incubation times (5, 15, 30, 45 &

60 min) are shown in Figure 4.2.

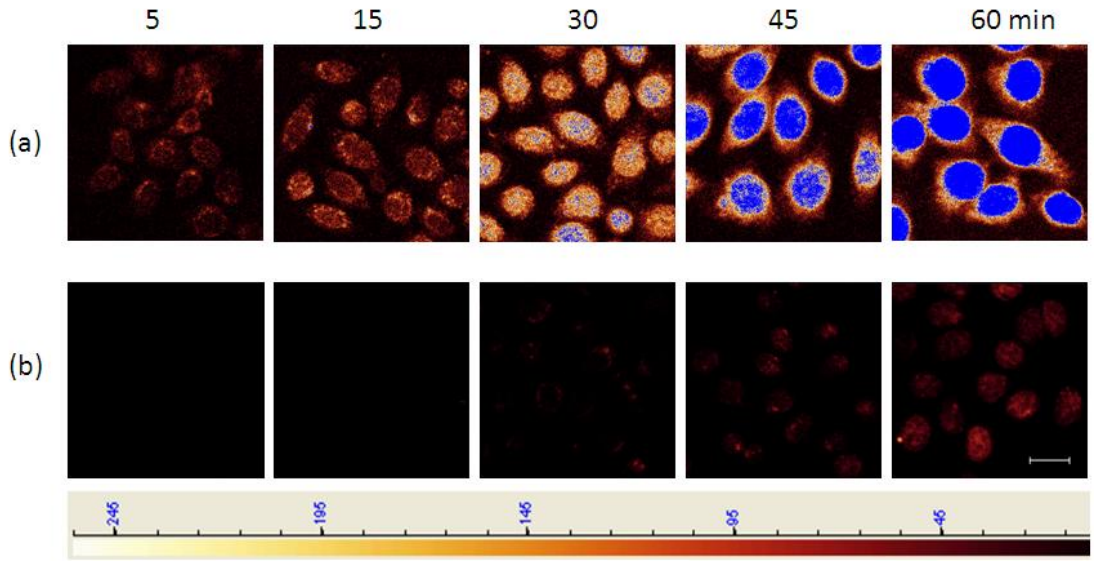

Figure 4.2. Confocal fluorescence images of HeLa cells after treatment with free DOX (5 μM) (a) and GNP-M2/MC2(PEG750)-DOX (containing 5 μM DOX) (b) for 5, 15, 30, 45 and 60 min, respectively. (Scale bar: 20 μm)

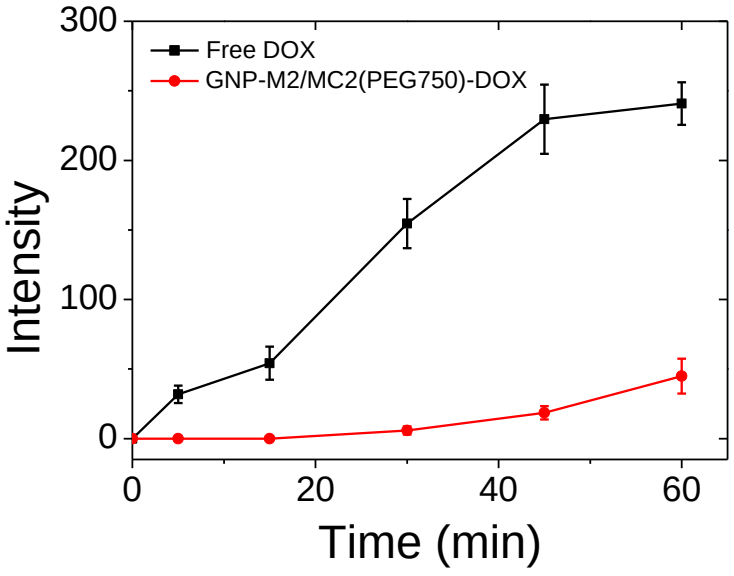

Figure 4.3. The average DOX fluorescence intensity inside HeLa cells as a function of incubation time.

Figure 4.2 clearly shows significant differences in DOX uptake kinetics (*via* DOX fluorescence intensity inside cells) between the free DOX and

GNP-dsDNA-DOX treated HeLa cells. In the cells treated by free DOX, DOX fluorescence was clearly visible after just 5 min, indicating that free DOX had entered the cells very rapidly. Also, fluorescence intensity increased rapidly with the increase in incubation time, and became saturated after just 45 mins. It is known that DOX, being a small molecule, can enter cells quickly through simple diffusion, driven by a concentration gradient. In contrast, no DOX fluorescence was detected inside cells treated with the GNP-DNA-DOX after a 15-min incubation under identical instrument setup conditions. Only a very weak fluorescence signal was observed after 30 min; this gradually became stronger as the incubation time was increased to 45 and 60 min, although it was still much weaker than that treated by free DOX.

To quantify the different uptake kinetics, the average fluorescence intensity inside cells was analysed at different incubation times. This was then plotted as a function of incubation time as shown in Figure 4.3, which reveals that the DOX fluorescence intensity of GNP-DNA-DOX-treated HeLa cells at 30 min is very weak, being only 1/25 of that of free DOX treated cells at the same incubation time. In addition, the DOX intensity of cells treated by GNP-DNA-DOX at 60 min was actually similar to that treated by free DOX for 5 min. These results suggest that compared to free DOX, there is approximately a one-hour delay for similar amounts of DOX being delivered into cells by the GNP-dsDNA carrier, despite both systems containing identical concentrations of DOX (5 μM). Although the diffusion coefficient of the GNP-DNA-DOX system, a much bigger nano objects, is expected to be significantly slower than that of free DOX, a small molecule drug, which may cause a delay for the GNP-DNA-DOX to reach extracellular membrane, the main factor affecting the different cell uptake kinetics observed here is believed to be mainly determined by the transmembrane process, not extracellular diffusion. This is because unlike small molecules which can directly

diffuse across the cell membrane (hence much faster kinetics), nanoscale objects however cannot across the cell membrane directly. Such distinctly different DOX uptake kinetics by HeLa cells between free DOX and GNP-DNA-DOX systems is strong evidence of different DOX uptake mechanisms. It is highly unlikely that DOX dissociated from the GNP-DNA conjugate first and then diffused into the cells. In other words, DOX was most probably carried by the GNP-DNA system and taken into the cells *via* endocytosis.

4.2.2 Delivery of membrane-impermeable DNA-binding dyes by the GNP-dsDNA system

Two other dsDNA intercalating agents were also studied: a dinuclear ruthenium (II) complex (BPY, Figure 4.4) and propidium iodide (PI). Like DOX, both compounds can bind with dsDNA through intercalation to form GNP-dsDNA-agent systems, but a major difference here is that both BPY and PI are cell membrane impermeable: they cannot enter the cells *via* simple diffusion. In addition, both compounds are fluorescent dyes, and their cellular uptake can be easily detected *via* their specific fluorescence. Moreover, as the compounds themselves are cell membrane impermeable, any fluorescence detected inside cells should only come from the carrier-induced delivery, allowing unambiguous confirmation of GNP-dsDNA carrier mediated intracellular delivery.

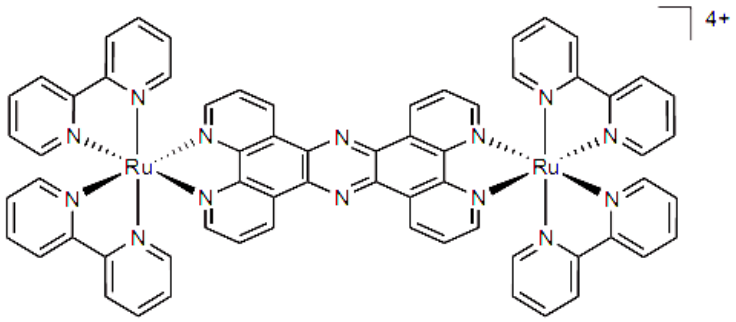

Figure 4.4. Chemical structure of the diruthenium(II) complex ($[(bpy)_2$ Ru (tpphz) Ru $(bpy)_2]^{4+}$ (BPY).

BPY is a DNA intercalating agent, which produces significantly enhanced fluorescence when forming dsDNA-BPY conjugate. Figure 4.5 shows the fluorescence spectra of BPY on its own, and its dsDNA-conjugate (excitation wavelength: 465 nm, which is also the wavelength of maximum absorption). It is clear that BPY on its own displayed an emission wavelength of around 590 nm with relatively low intensity, whereas for BPY-M2/MC2 conjugate the emission wavelength shifted to 650 nm, and the fluorescence increased according to the molar ratio of BPY to M2/MC2 (for example, the fluorescence of the conjugate at a ratio of 10:1 increased by about 5 times compared to that of BPY alone).

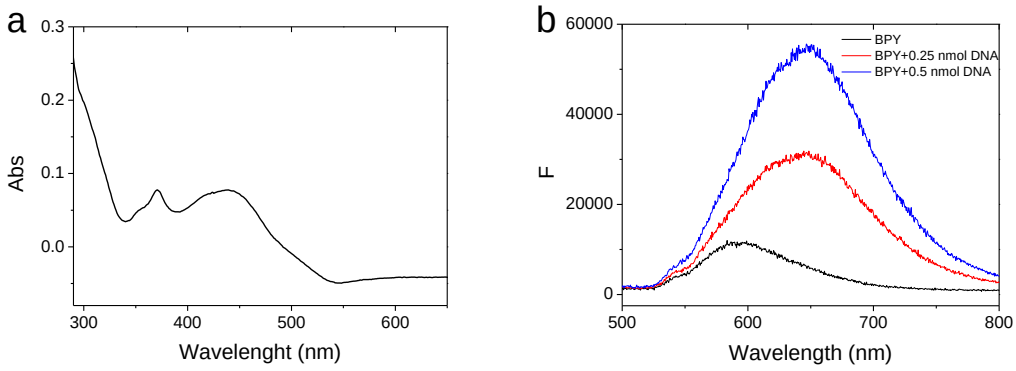

Figure 4.5. (**a**) UV-vis absorption spectrum of BPY (3 μM BPY). (**b**) Fluorescence spectra of BPY alone (500μL, 10 μM) and BPY- M2/MC2 conjugates (molar ratios of BPY to M2/MC2 are 20:1 (red) and 10:1 (blue).

BPY was found to be cell membrane impermeable, and so could not enter the cells on its own (Figure 4.6)[228]. It has been successfully delivered into cells by encapsulation in a biocompatible polymersome [229]. Here, BPY was added to GNP-M2/MC2(PEG750) using a molar ratio of 18:1 (BPY:M2) to form the GNP-dsDNA-BPY conjugate. After incubation with the GNP-dsDNA-BPY conjugate for 3 h, a confocal fluorescence microscope was used for imaging the HeLa cells. The resulting images (Figure 4.7) clearly show that BPY

fluorescence was detected inside HeLa cells, indicating that the GNP-dsDNA system had successfully delivered the BPY into cells with similar efficiency to the polymersome system reported in the literature.

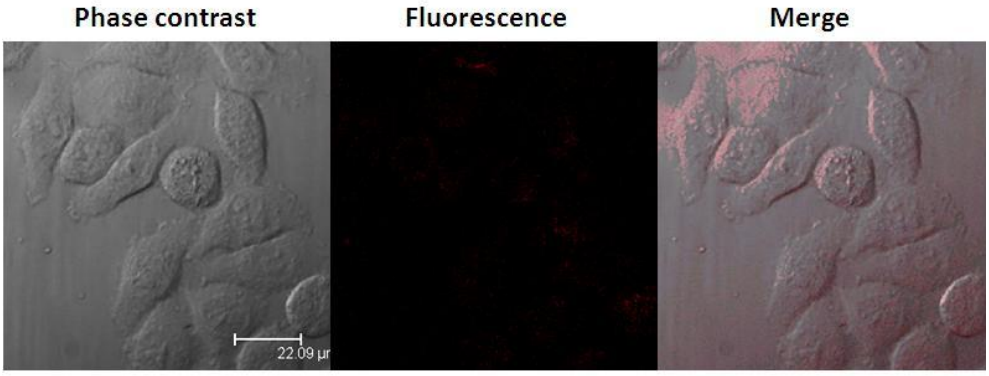

Figure 4.6. Confocal phase contrast (left), fluorescence (middle) and merged optical / fluorescence (right) images of HeLa cells after incubation with BPY alone for 3 h at 37 °.

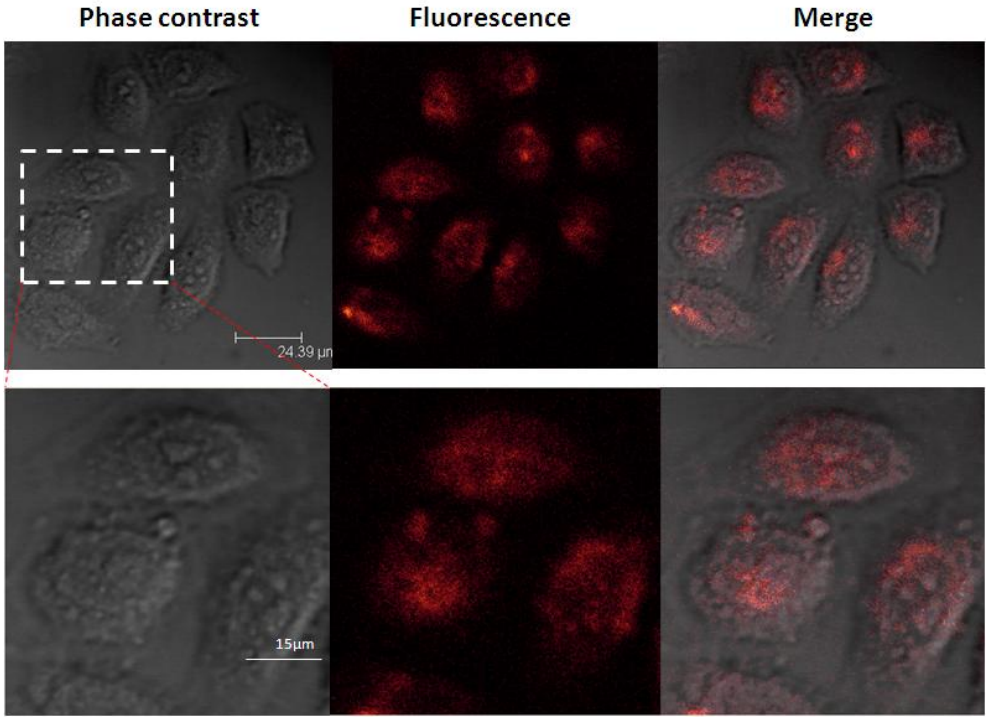

Figure 4.7. Confocal phase contrast (left), fluorescence (middle) and merged optical / fluorescence (right) images of HeLa cells after incubation with the GNP-M2/MC2(PEG750)-BPY for 3 h at 37 ℃.

We further tested the delivery of propidium iodide (PI), another DNA intercalating dye that is widely used for DNA staining of dead cells and known to

be live cell membrane-impermeable (see Figure 4.8 for its chemical structure), by our GNP-dsDNA carrier. After incubation of HeLa cells with a GNP-M2/MC2(PEG750)-PI conjugate (M2:PI molar ratio = 1:12) for 3 h, PI fluorescence was clearly detected in live HeLa cells (see Figure 4.9).

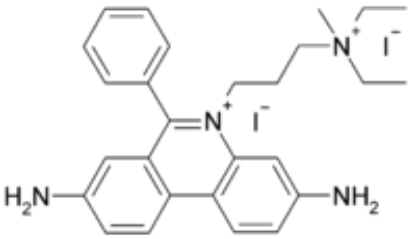

Figure 4.8. Chemical structure of PI.

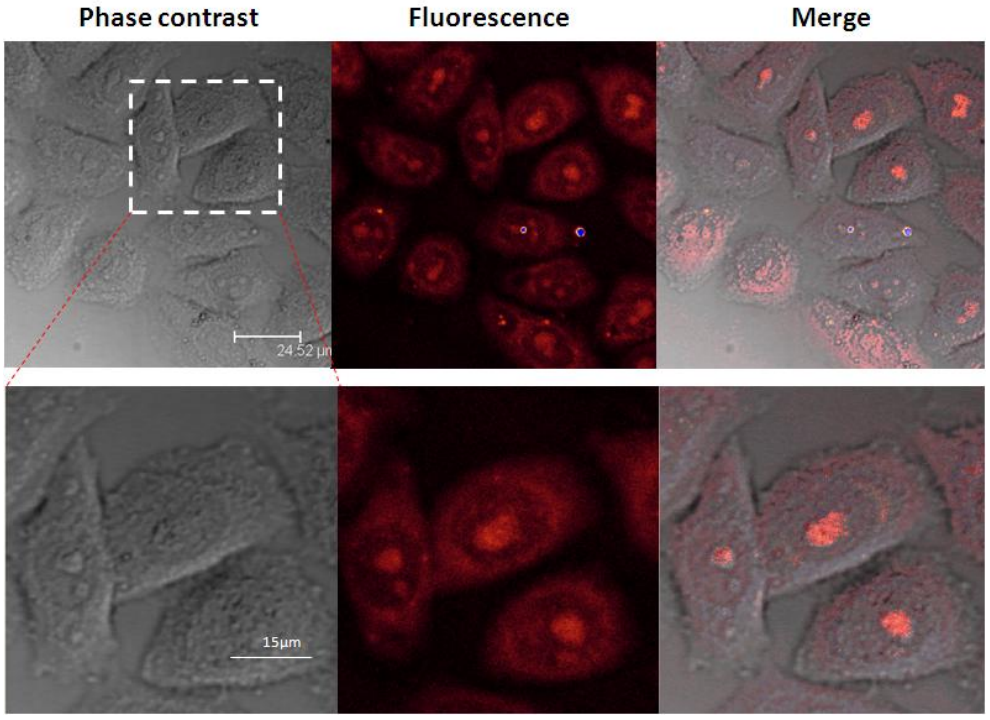

Figure 4.9. Confocal phase contrast (left), fluorescence (middle) and merged optical/fluorescence (right) images of HeLa cells after incubation with GNP-M2/MC2(PEG750)-PI for 3 h at 37 ℃.

The successful delivery of two different cell membrane impermeable agents by our GNP-dsDNA nanocarrier presented above, together with that of the delivery of DOX shown in the previous chapter, not only confirm their

non-simple-diffusion delivery mechanism but also suggest that our GNP-dsDNA carrier can potentially act as a general, efficient intracellular delivery system for DNA intercalating agents. Compared to other delivery systems, a significant advantage here is simplicity: the agents to be delivered can be directly and conveniently loaded to the carrier in native form, requiring no chemical modification or coupling step which may alter their pharmakinetics or therapeutic efficacies.

4.2.3 TEM imaging of HeLa cells treated with GNP-M2/MC2(PEG750)-DOX

Nanoscale objects are normally taken into cells *via* endocytosis, and GNP-DNA conjugate has also been reported to enter cells through endocytosis; therefore it is plausible to suppose that the GNP-dsDNA-DOX based drug delivery system is internalised by cells *via* the same mechanism. Thus, as the endosome matures into late endosome or lysosome, progressively decreasing pH triggers the release of DOX from the GNP-DNA-DOX system, and the release of free DOX can then diffuse across the endosomal/lysosomal membranes, finally reaching the nucleus to exert its cytotoxicity.

To further confirm this mechanism, TEM imaging was employed to trace the location of the GNP-DNA-DOX system after cell internalisation. After 3 h incubation with the GNP-DNA-DOX, the HeLa cells were fixed with glutaraldehyde, dehydrated, and sectioned for TEM imaging. Figure 4.10 shows TEM images representing two random HeLa cells, both of which clearly reveal that GNPs were exclusively located and accumulated within endosome- or lysosome-like intracellular compartments (the organic/biological components of the carrier cannot be observed clearly due to their low contrast to cellular components in TEM imaging). It has been reported that DNA remains chemically bonded to the GNP surface after being taken into cells[226, 230], therefore the TEM imaging results presented herein strongly support our

expectation that the GNP-dsDNA-DOX conjugates would be internalised through the endocytic pathway and located in endocytic compartments,. Therefore our proposal of exploiting the low local pH of endocytic compartments to trigger DOX release appears to be viable.

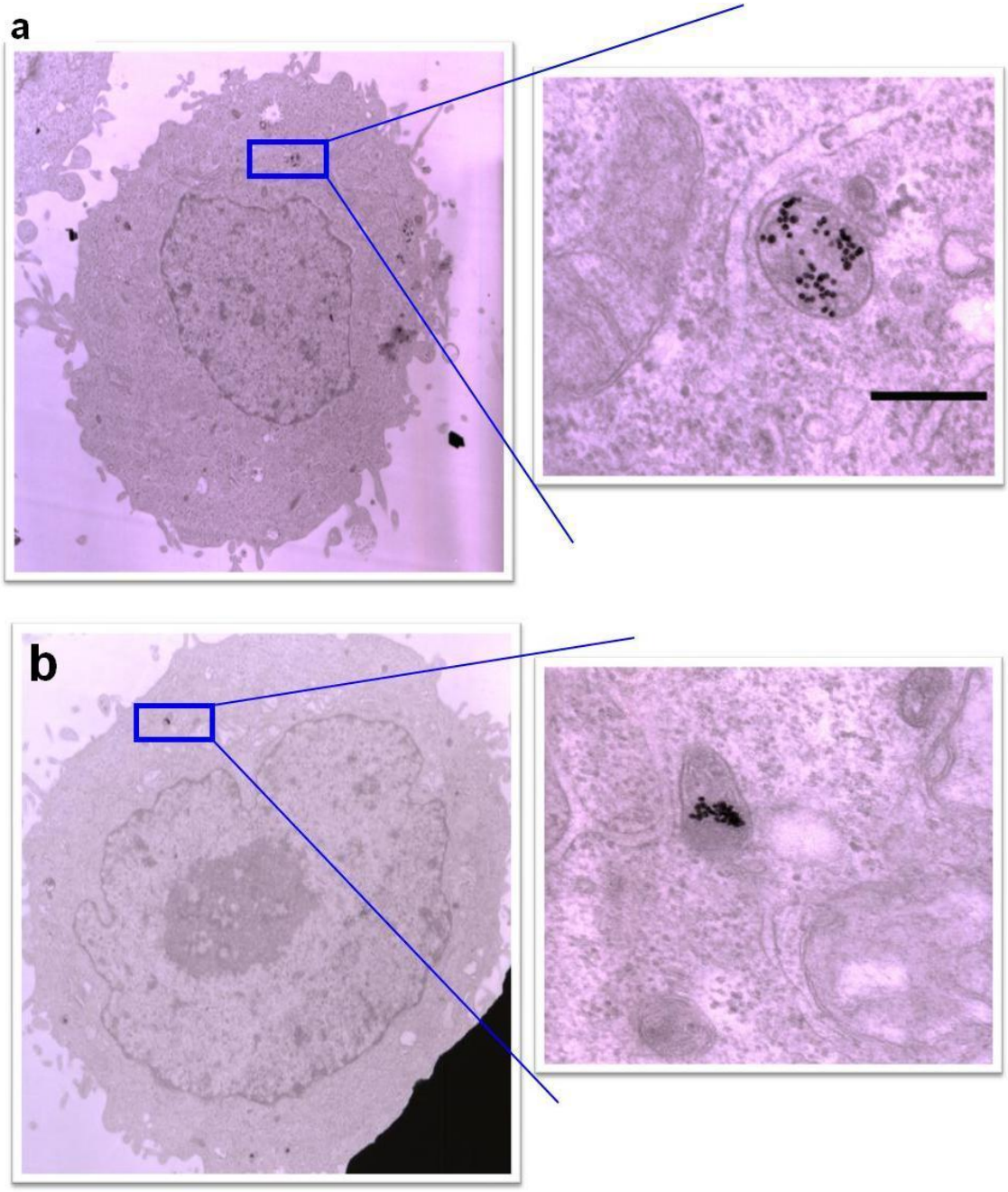

Figure 4.10. TEM images of two random HeLa cells (a & b) after incubation with GNP-M2/MC2(PEG750)-DOX for 3 h at 37 ℃, where the GNPs were found to exclusively locate in endosome- or lysosome-like compartments, giving another strong evidence that GNP-dsDNA-DOX conjugates were internalised *via* the endocytic pathway. (scale bar: 1 μm)

4.3 Conclusion

DOX can be efficiently delivered into HeLa cells in the form of GNP-DNA-DOX conjugate without dissociation *via* the endocytic route. This is supported by the successful delivery of two different types of cell membrane impermeable DNA intercalating agents, a dinuclear Ru(II) complex (BPY) and PI, by the GNP-dsDNA nanocarrier, demonstrating that the GNP-DNA system can act as an efficient general intracellular delivering platform for DNA intercalating agents. The TEM images of HeLa cells incubated with GNP-DNA-DOX further confirm that the GNP-DNA-DOX system was taken up by cells through the endocytic pathway as expected. This suggests that it is both feasible and practical to design efficient drug nanocarriers using GNP-pH-responsive DNA conjugates with their high cellular uptake and efficient, pH-triggered drug release characteristics.

5 Chapter 5: PEG effects on GNP-M1/MC2 system stability

The first use of Poly(ethylene glycol) (PEG) to modify biologically active macromolecules was in the 1970s, by Davis and Abuchowski[231-233]. It was found that PEG could prolong the circulation time of proteins and lower their immunogenicity. Since then PEGs of different MWs have been widely used in pharmaceutical and other biomedical fields[234-238]; indeed, PEG modification has become the gold standard, due to its 'stealth effect'. PEG modification (PEGylation) is able to mask bioactive molecules such as peptides[239-242], proteins[243-246], enzymes[247-249] and antibodies[250-253] from interacting with blood components, reducing non-specific recognition and clearance by the body, and hence leading to prolonged circulation time and improved stability[234, 254, 255]. Furthermore, PEGylation can also improve drug solubility, its long hydrophilic chain making it highly water-soluble [234, 256].

In 1990 the first PEGylated product, PEG-bovine adenosine deaminase (Adagen®)[257], was approved by the Food and Drug Administration (FDA) for clinical application in the USA. Since then the market has seen the emergence of many more approved PEGylated protein products, such as PEG-asparaginase (Oncaspar®)[258], PEG-interferons, PEG-intron® with a linear PEG (12 kDa)[259], and Pegasys® with a branched PEG (2×20 kDa)[260] *etc*; these have often exhibited improved pharmacokinetics. Pegylation can be applied not only to drugs themselves, but also to the delivery systems (drug carriers) such as pegylated-liposomal doxorubicin (Caelyx® / Doxil®)[261, 262], to offer improved system stability *in vitro*[263-266] and *in vivo*[234, 254, 255, 267] and improved pharmacokinetic effects.

Although DNA stability against nuclease degradation can be improved *via*

conjugation with gold nanoparticles[206], the 3-fold improved protection offered by conjugation to GNP alone may not be able to satisfy the *in vivo* requirements when administered intravenously, because of the long exposure to different enzymes and the need to protect the conjugate from detection and phagocytosis during blood circulation. In this project we designed pegylated GNP-M1/MC2 systems, using single-chain (linear) PEGs with different molecular weights, and a branched three-chain PEG. Their stabilities were then compared with unmodified GNP-M1/MC2 in a serum-containing cell culture medium as well as under a DNase I treatment.

5.1 Materials and Methods

5.1.1 Materials

DMSO (anhydrous, ≥99.7%) was obtained from Sigma-Aldrich. MC2-SH (5'-HS-TTT GTG TTA GGT TTA GGG TTA GGG-3') was purchased from IBA GmbH (Germany). $(Methyl\text{-}PEG12)_3$-PEG4-Maleimide (TMM) was purchased from Thermo Scientific. YO-PRO-1 was purchased from Life Technologies. DNase I was purchased from Fisher BioReagents.

5.1.2 Preparation of MC2(TMM)

100 nmol MC2-SH was dissolved in 1 mL of filtered (0.22 μm syringe filter) MES buffer (pH 7.4, 50 mM MES, 0.15 M NaCl) to make a 100 μM stock; TMM was dissolved in anhydrous DMSO to make a TMM stock solution of 40 mM. 0.5 mL of the MC2-SH stock solution (50 nmol) was mixed with 50 μL of TMM (the molar ratio of MC2-SH:TMM = 1:40) and the resulting mixture was allowed to react overnight at room temperature to form MC2(TMM). The prepared MC2(TMM) was stored at -20℃ before HPLC analysis and purification.

5.1.3 HPLC analysis and purification and MALDI-MS analysis

Both RP-HPLC analysis and purification were performed on a Gynkotek HPLC

Instrument at room temperature using an Phenomenex C18 column (4.6 X 250 mm, 5 µm) with mobile phase consisting of TEAA buffer (**A**) and acetonitrile (**B**). UV absorbance was monitored by a Gynkotek (UVD 340S) detector at 260 nm. Three different gradients were tried, (5-30% **B**) 30min, (5-95% **B**) 30min, and (10-70% **B**) 30min. The final gradient chosen for analysis and purification of the MC2(TMM) was 10-70% (**B**) for 30 min. The MC2(TMM) fraction was then lyophilized, stored at -20℃ and identified by Matrix-assisted laser desorption/ionisation time of flight mass spectrometry (MALDI-TOF MS).

5.1.4 Assembly of PEG-modified GNP-DNA systems

Three batches of 2.2 ml GNP solution (15 nM) were mixed with 33, 66 and 100 µL DNA M1 (100 µM) solution overnight, respectively (GNP:M1 molar ratios = 1:100; 1:200; 1:300), and the resulting solutions were then salt-aged (0.3M NaCl) overnight. The samples were then centrifuged (14800 rpm * 60 min) to yield GNP-M1 pellets, and the DNA M1 loadings were estimated at 60, 85, and 110 DNA M1 strands per GNP, respectively. Afterwards, the complementary MC2 strands (MC2, MC2(PEG250), MC2(PEG750) or MC2(TMM)) were added to the GNP-M1 pellets (DNA-M1:MC2 molar ratio = 1:1) and were allowed to hybridize in an MES buffer for 1 hr to make GNP-M1/MC2, GNP-M1/MC2(PEG250), GNP-M1/MC2(PEG750) and GNP-M1/MC2(TMM) systems (GNP-dsDNA nanocarriers).

5.1.5 Dynamic light scattering (DLS) measurement

The hydrodynamic sizes of the GNP-dsDNA systems were measured in both MES buffer (pH 7.4) and in complete DMEM media with 10% FBS. 30 µL of the GNP-dsDNA stock solution (0.46 µM GNP) was mixed with 1.2 mL of MES buffer or complete DMEM, and then filtered through a Whatman syringe filter (0.22 µm pore size). 3 h after mixing, the hydrodynamic sizes of the systems in complete DMEM were measured on a Brookhaven Instruments Corp BI-200SM

Laser Light Scattering Goniometer with a BI-APD detector, using an He-Ne laser at 633 nm (scattering angle: 90°).

5.1.6 GNP-M1/MC2 systems under deoxyribonuclease I (DNase I) degradation

The GNP-dsDNA samples were mixed with YO-PRO-1 and diluted with reaction buffer to 200 µL(10 mM Tris-HCl, 2.5 mM $MgCl_2$ and 0.5 mM $CaCl_2$, pH 7.5) to give a final DNA concentration of 80 nM, and YO-PRO-1 concentration of 400 nM. After 10-min equilibration at 37 °C, 10 µL of the DNase I mixed with reaction buffer (2 U/L) was added and the resulting fluorescence of the samples (λ_{EX} = 491 nm; λ_{EM} = 509 nm) was measured on a fluorescence plate reader every 90 seconds for 3 h.

5.1.7 GNP-M1/MC2(TMM) carrier for propidium iodide (PI) delivery

GNP-M1 conjugate was mixed with MC2(TMM) (M1:MC2(TMM) molar ratio = 1:1) in an MES buffer (pH 7.4), and allowed to hybridize for 3 h to make a GNP-M1/MC2(TMM) carrier; then PI stock solution (1 mg/mL in water) was added to form the GNP-M1/MC2(TMM)-PI system (M1: PI molar ratio = 1:6). The HeLa cells were then treated with GNP-M1/MC2 (TMM)-PI (containing 10 µM PI) for 3 h, after which the incubation buffer was removed, and the cells were washed with PBS three times before being imaged on a confocal laser scanning microscope, using 488 nm excitation and fluorescence detection over 600-630 nm.

5.2 Results and Discussion

5.2.1 Preparation, purification and identification of MC2(TMM)

5.2.1.1 Preparation of MC2(TMM)

In order to prepare three-chain PEG-modified MC2 (MC2(TMM)), a branched

sulfhydryl-reactive PEGylation reagent, (Methyl-PEG12)$_3$-PEG4-Maleimide (TMM, MW: 2360.75) (see Figure 5.1), was employed to react with thiol-modified MC2 (MC2-SH), and the reaction scheme is shown in Figure 5.2. Although TMM is water-soluble, and the maleimide group is relatively stable compared to other active functional groups (*e.g.* NHS ester), it still needs to be dissolved in an anhydrous organic solvent (*e.g.* DMSO) to avoid hydrolysis forming maleimic acid, after which it can no longer react with sulfhydryl.

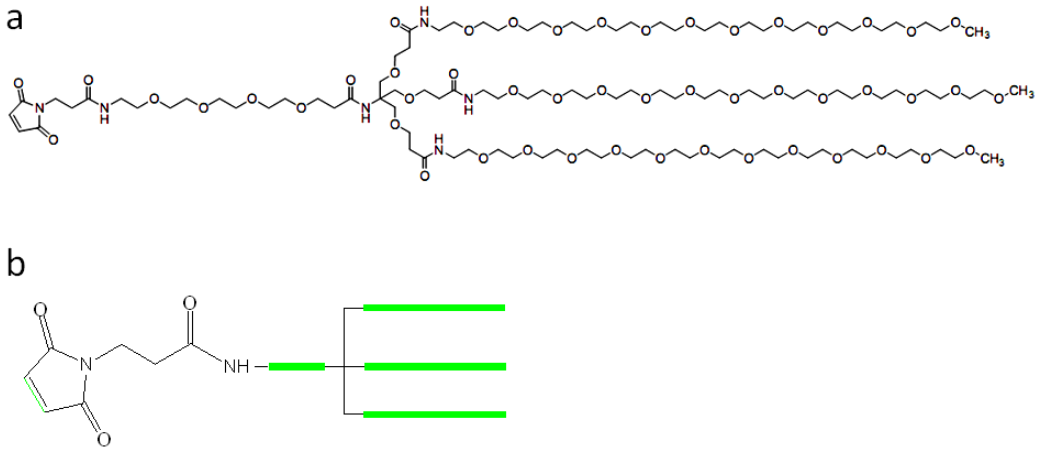

Figure 5.1. Chemical structure of TMM (**a**) and its schematic abbreviation (**b**).

This one-step modification to make branched PEGylated MC2 is quick and simple. The Michael addition between the maleimide and free sulfydryl groups, which forms a stable thioether bond, is very efficient and specific at pH 6.5-7.5 and was complete in just 2 h after TMM was mixed with MC2-SH at room temperature. The molar ratio of the reaction was 1:1, but excess TMM (*e.g.* 40 molar equivalent of MC2-SH) was used here to ensure complete PEGylation of the MC2-SH.

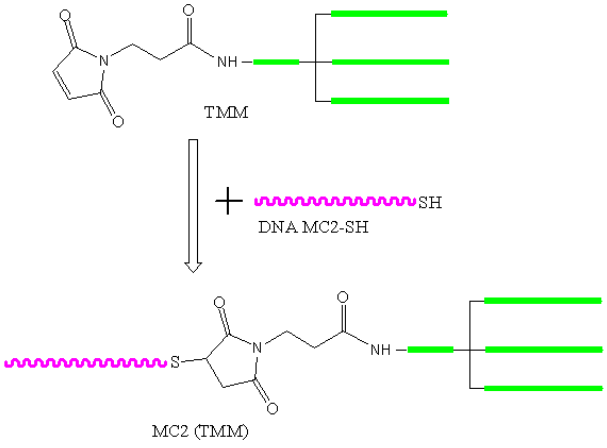

Figure 5.2. Schematic of the reaction between TMM and DNA MC2-SH.

5.2.1.2 HPLC analysis and purification

After the MC2-SH and TMM reaction described above, reverse-phase HPLC was employed to analyse and purify the resulting MC2(TMM). To identify the new peak (for the MC2(TMM)), MC2-SH was first run by HPLC under the same mobile phase. The HPLC profile and the main-peak UV absorption spectra are shown in Figure 5.3. The retention time of MC2-SH (the main peak) was found to be ~10.4 min, which was further confirmed by its UV absorption at ~ 260 nm, the characteristic peak of DNA absorption. In the MC2-SH HPLC profile, two tiny peaks with retention times of 13.4 and 18.9 mins were also found. In contrast, the HPLC profile of TMM showed no absorption peak at ~260 nm (results not shown here).

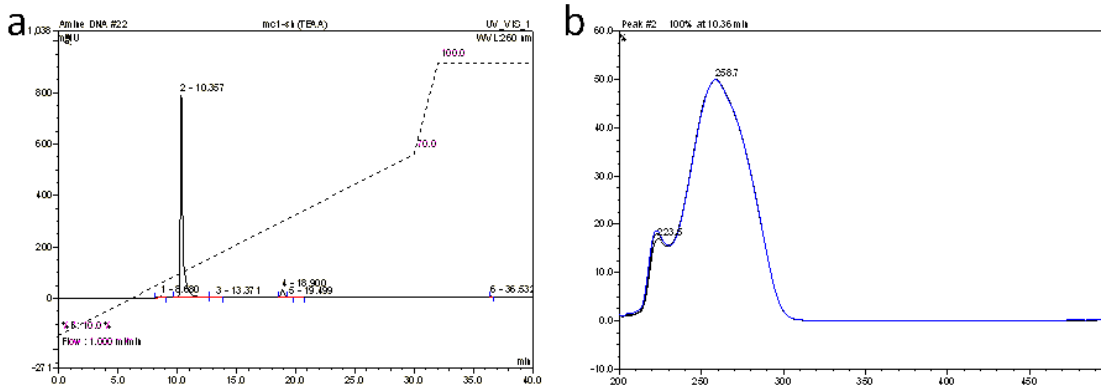

Figure 5.3. HPLC profile of MC2-SH (**a**) and UV spectrum of Peak at 10.4 min (**b**).

The reaction mixture was run by HPLC to confirm if the reaction took place, identify the new MC2(TMM) peak and calculate its synthetic yield. Figure 5.4 shows the HPLC profile and UV absorption spectra of the relevant peaks. Compared to the HPLC profiles of MC2-SH and TMM, it can be seen that peaks 3 (10.8 min), 6 (13.5 min) & 13 (19 min) are from the MC2-SH with peak 3 intensity (MC2-SH) being greatly reduced. Peaks 11 & 12, which do not have DNA characteristic absorptions, are from TMM. Two new peaks appeared (7 & 8), with retention times of 14.3 and 15.1 mins respectively. Both new peaks are

the main peaks in the HPLC profile, and their UV absorption spectra have DNA characteristic peaks. The observation of a greatly reduced MC2-SH peak, together with the appearance of two new main peaks with strong absorption at 260 nm, suggests that the MC2-SH was conjugated to TMM as expected.

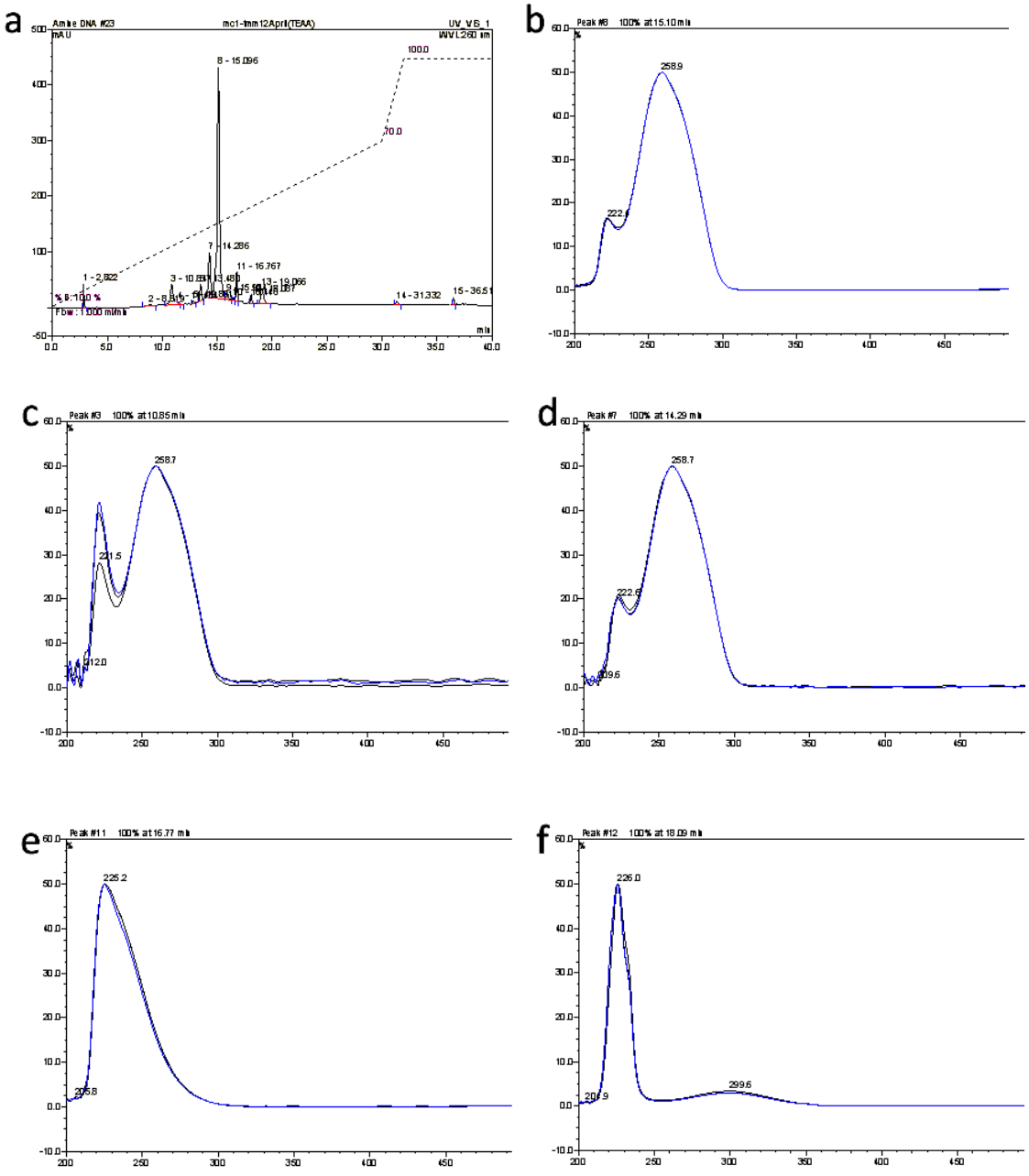

Figure 5.4. HPLC profile of reaction mixture (**a**) and the corresponding UV absorption spectra of peaks at 15.1 (**b**), 10.9 (**c**), 14.3 (**d**), 16.8 (**e**) and 18.1 (**f**) mins, respectively.

As the relative area of peak 8 is nearly 7 times greater than that of peak 7, it is highly likely that peak 8 is the MC2(TMM) peak and peak 7 may be a side

product. Most PEGylation reagents are heterogeneous mixtures containing PEGs of different chain lengths. Although the TMM used here is a so-called homogeneous reagent, it may not be 100% pure, which may lead to the formation of side products. With the above assumptions we can estimate that over 92% of the MC2-SH has been modified, and the synthetic yield for the MC2(TMM) is approximately 80%, calculated from the relative areas of peaks 3, 7 & 8. The high yield obtained here confirms an efficient reaction between the maleimide and free sulfhydryl groups.

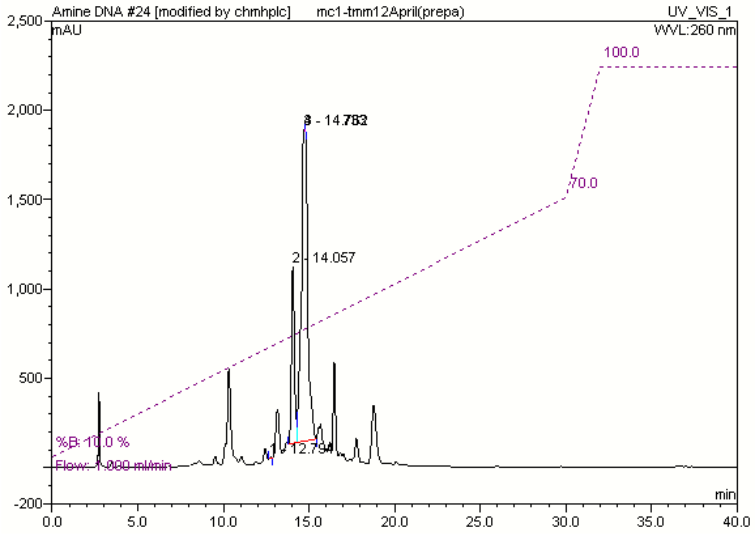

Figure 5.5. Profile of semi-preparative HPLC.

To further confirm that peak 8 is the correct MC2(TMM) peak, HPLC purification was performed using the same method as in the HPLC analysis above to get pure MC2(TMM) for mass spectrometry measurement. Due to the small amount of reaction mixture (≤ 50 nmol DNA in 500 µL), the same analysis column was also used for the DNA purification. The maximum injection amount for this HPLC column is 200 µL, so only three injections were required for the purification process. Figure 5.5 shows the HPLC purification profile, which exactly matches the HPLC analysis profile in Figure 5.4. The major peak with a retention time of around 15 min was collected. The peak intensity of a 200-µL injection is much

higher than the detection threshold, so the part of the peak with higher intensity could not be displayed properly in the profile, though this did not affect the purification process.

After collection, the fraction was freeze-dried and then dissolved in a small amount of pure water. 10 μL of this solution was injected into HPLC to evaluate its purity (see Figure 5.6) and only one main peak was found, with a relative area of > 95%, indicating that purification was successful. One may note that the retention time of the peak varies by ± 0.5 min, possibly caused by differences in the batches of liquid phase.

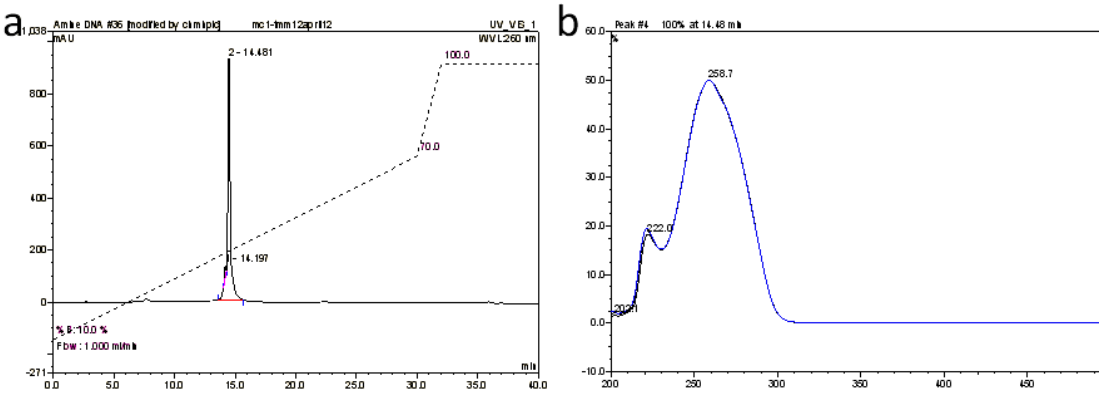

Figure 5.6. HPLC profile of purified MC2(TMM) (**a**) and corresponding UV absorption spectrum of the main peak (**b**).

5.2.1.3 Identification of MC2(TMM)

The purified fraction was then sent out for mass measurement, which was performed by Dr. Min Yang at University College London using MALDI-TOF MS; the result is shown in Figure 5.7. The main mass peak of the collected fraction is 10086 (10041+2Na-H), exactly matching what is expected for the MC2(TMM) (10041), as the molecular weights of MC2-SH and TMM are 7681 and 2360 respectively. No mass should be lost during the Michael reaction, which forms a thioether bond between the maleimide and thiol groups. The MALDI-MS

measurement further confirmed that the HPLC analysis results and the MC2(TMM) had been successfully prepared with a high yield, through the efficient one-step reaction between MC2-SH and TMM.

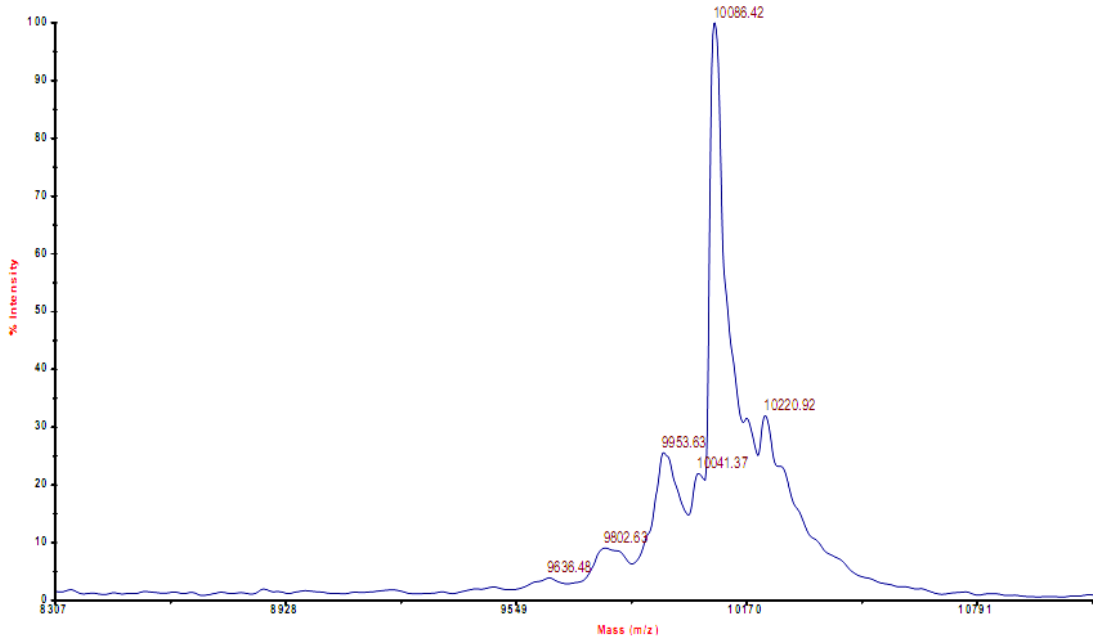

Figure 5.7. MALDI-TOF MS spectrum of MC2(TMM).

5.2.2 Assembly of PEG-modified GNP-DNA systems

The GNP-DNA systems were modified by single-chain PEGs of different molecular weights (MWs) and a three-chain PEG (MC2(TMM)) as prepared above (Figure 5.8). Here we used MC2(PEG250) (PEG MW: 250) bought from IBA, and MC2(PEG750) (PEG MW: 750) synthesized by our collaborators at Tsinghua University in China, to assemble the single-chain PEGylated GNP-DNA system; MC2(TMM) was used to make the three-chain PEGylated GNP-DNA system. The assembly procedures were exactly the same as for those without PEG-modification.

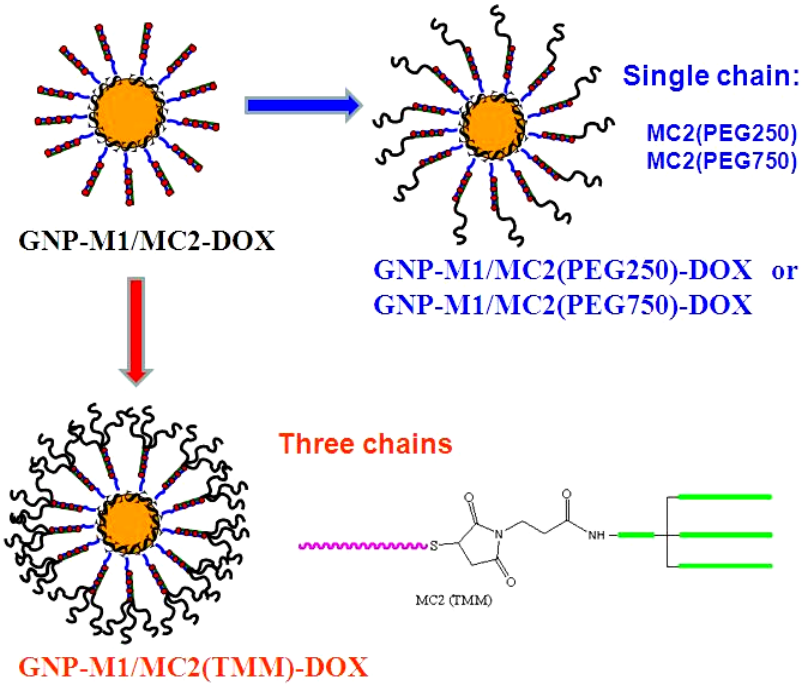

Figure 5.8. Evolution of GNP-dsDNA system by PEGylation.

Here, GNP-M1 conjugates with average M1 loadings of 60, 85 and 110 strands per GNP were obtained by incubating the GNP with different molar ratios of M1 at 1:100, 1:200 and 1:300, respectively. They were then hybridized with equal molars of MC2 or MC2(PEG)s (M1:MC2 molar ratio = 1:1) to assemble GNP-M1/MC2, GNP-M1/MC2(PEG250), GNP-M1/MC2(PEG750) and GNP-M1/MC2(TMM). These systems with their different DNA surface coverages and PEG modifications were then tested in turn for stability.

5.2.3 Effects of PEGylation on GNP-DNA system stability

5.2.3.1 GNP-M1/MC2 systems in a serum-containing cell culture

One way to study the PEGylation effect on GNP-DNA system stability is to monitor their hydrodynamic sizes, because the size of a nanocarrier is critical for its cancer targeting ability *via* the EPR effect. The ideal size of a targeted NDDS should be between the renal clearance threshold (~8 nm) [205, 268] and the average gap of leaky blood vessels in tumours (~100 nm)[269]. These sizes

will also minimise capture by fixed macrophages in the liver and spleen[270]. Also, to avoid being recognized and cleared by the body during systemic circulation before accumulating in the tumour region[271, 272], drug carriers should not interact with blood components (*i.e.* not change size),

Here dynamic light scattering was used to measure the hydrodynamic diameters (HDs) of the GNP-DNA systems and the number of M1 strands attached to each GNP of ~110. The HDs of the systems were monitored not only in MES buffer but also in cell culture media (DMEM) containing 10% Fetal Bovine Serum (FBS), to evaluate possible *in vivo* interactions between the serum proteins and the NDDSs which may threaten the NDDSs' survival in the circulation.

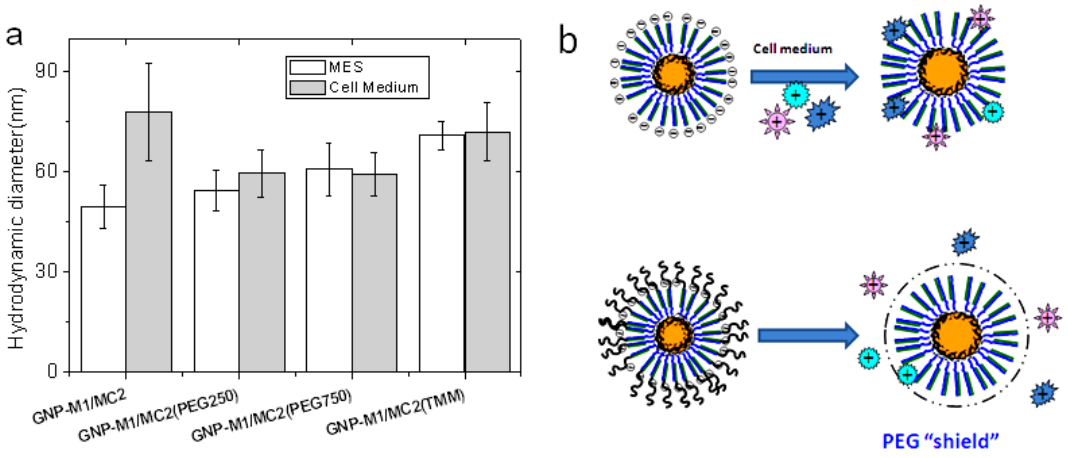

Figure 5.9. (**a**) Comparison of the hydrodynamic diameters of GNP-DNA systems in MES buffer and cell culture media. (**b**) Schematics of the interactions between the GNP-DNA systems and positively charged serum proteins: serum proteins can adsorb onto negatively charged GNP-DNA conjugate *via* electrostatic attractions, whereas the PEG chains on the PEGylated GNP-DNA conjugate can prevent serum protein adsorption.

The HD of the GNP-M1/MC2 system without PEG modification was found to be ~50 nm in an MES buffer, while those of the GNP-M1/MC2 systems with various PEG-modifications were all bigger, (HDs for GNP-M1/MC2(PEG250), GNP-M1/MC2(PEG750) and GNP-M1/MC2(TMM) were ~55, ~61 and ~70 nm,

respectively), due to the extra lengths of the hydrophilic PEG grafts (Figure 5.9). However, the HD of GNP-M1/MC2 in DMEM was found to have increased significantly, by ~30 nm to ~80 nm, indicating significant adsorption of serum proteins. This result is predictable due to the negative-charge nature of the GNP-M1/MC2 system, where positively charged serum proteins (or protein domains) can adsorb non-specifically through electrostatic interactions (Figure 5.9b), and similar results have been reported in literature by others[273, 274].

In contrast, HDs of the PEG-modified GNP-M1/MC2 systems in cell culture media were very similar to those found in MES buffer, showing little change. For example, the HD of GNP-M1/MC2(PEG250) increased by approximately 5 nm, while those for GNP-M1/MC2(PEG750) and GNP-M1/MC2(TMM) nanocarriers showed effectively no change, suggesting little or no non-specific adsorption of serum proteins to the PEG-modified carriers. PEGylation is a well-established strategy for resisting non-specific adsorption of biomolecules on surfaces, and has been widely used in drug delivery and biomedical applications to improve pharmacokinetics and to reduce non-specific uptake [275, 276]. Here we show for the first time that PEGylation can be successfully applied to strongly negative-charged polyvalent GNP-DNA conjugates. In this case, PEGs were covalently attached to 5'-ends of MC2 which were then hybridized with GNP-M1, to form GNP-M1/MC2 covered by highly flexible PEG chains. As the number of M1/MC2 strands on each 13 nm GNP was quite high (*ca.*110), where each MC2 carried one (or three) PEG chains, these dense, flexible, and hydrophilic PEGs on the nanocarrier surface were able to function as an effective shield, masking the negative charges of DNAs (Figure 5.9b) and effectively reducing their electrostatic interaction with positively-charged components in the serum.[265, 277, 278] As a result, in cell culture media the sizes of these carriers did not show significant changes. GNP-M1/MC2(PEG750) showed much better

resistance to non-specific adsorption than GNP-M1/MC2(PEG250). This is due to its longer chain (with ~18 EG repeating units), which has better charge-masking effects than the PEG250 chain (with 6 EG units) [279, 280]. The charge-masking effect can be further improved by introducing a branched three-chain PEG (in GNP-M1/MC2(TMM)), to increase PEG density on the carrier surface and thus improve protein adsorption resistance [281, 282]. This was proved to be true in our experiments where the GNP-M1/MC2(TMM) showed effectively no size change in serum containing media.

5.2.3.2 GNP-M1/MC2 systems' resistance to DNase I digestion

Besides the ability to resist non-specific adsorption of proteins, an effective drug nanocarrier should also have sufficient stability *in vivo* against nuclease degradation once it enters the body. This has been a significant challenge for DNA based drug carriers because of the presence of numerous nucleases *in vivo* that can degrade the carrier. The Mirkin group has reported that dense DNA packing on the GNP-DNA conjugate can improve the resistance of DNA to nuclease degradation by ~ 3 times. Despite such an improvement in stability, it may still not be able to satisfy the requirements of an effective drug nanocarrier *in vivo*.

To investigate whether the stability of GNP-DNA systems can be further improved by PEGylation and hence have potential for *in vivo* applications, I have evaluated the PEG-modification effects on GNP-DNA stability against nuclease degradation. Here the experiment was designed after referring to the literature[206], and the GNP-DNA system was treated with an enzyme, deoxyribonuclease I (DNase I). A different approach was used to monitor the DNA digestion process, using a fluorescent DNA-binding dye, YO-PRO-1

(λ_{EX}/(λ_{EM}: 491/509 nm), for a readout signal, instead of a covalently attached fluorescein on the complementary DNA. The DNase I digestion process was followed by monitoring YO-PRO-1 fluorescence with fluorescence spectroscopy.

The advantages of using YO-PRO-1 as a readout signal are as follows: (1) YO-PRO-1 binds strongly with dsDNA by intercalation, just like DOX. Because the GNP-DNA system under development here is to be an anticancer NDDS, based on the intercalation of certain anticancer drugs (such as anthracycline) into DNAs for drug loading, the stability of GNP-dsDNA-YO-PRO-1 against nuclease degradation should be similar to those of GNP-DNA systems carrying anticancer drugs. (2) Unlike the covalently fluorescein-labelled DNA used in the literature, where each DNA strand contained just one fluorescence label, multiple YO-PRO-1 molecules can bind to each dsDNA, allowing a stronger fluorescence readout signal. Furthermore, unlike DOX which selectively binds to GC pairs of the DNA[135], YO-PRO-1 intercalation takes place throughout the dsDNA structure and does not depend on GC content[283]. So the change in YO-PRO-1 fluorescence intensity should present a much better reflection of the dsDNA degradation process by DNase I than those relying on covalent fluorescein labelling and/or DOX intercalation. Moreover, YO-PRO-1 by itself is effectively non-fluorescent, and becomes strongly fluorescent only upon dsDNA binding, allowing unambiguous differentiation between DNA-bound and free YO-PRO-1 (after DNase digestion).

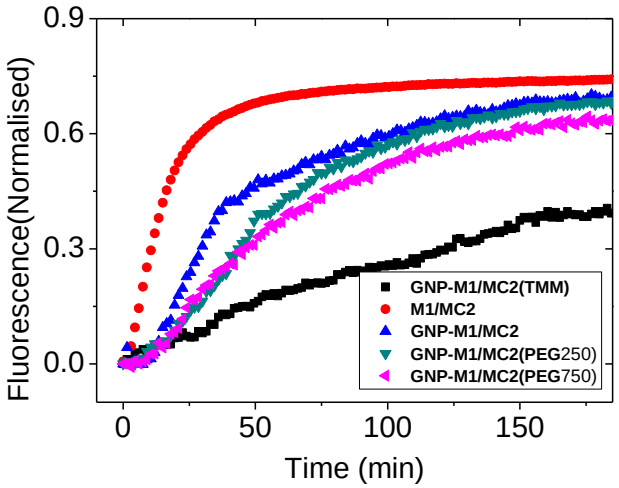

Figure 5.10. Comparison of the degradation rates of the dsDNA and GNP-dsDNA systems by DNase I *via* time-dependent fluorescence changes.

The following samples were mixed with YO-PRO-1 with a molar ratio of M1/MC2 to YO-PRO-1 of 1:5 : dsDNA only (M1/MC2), GNP-M1/MC2, and various PEGylated GNP-M1/MC2 systems all of which have the same final M1/MC2 concentration (80 nM) and the same DNA loading for all GNP-DNA conjugates (85 strands of M1 per GNP),. The fluorescence changes of YO-PRO-1 with DNase I were monitored for 3 h and the normalised results are shown in Figure 5.10. Here the initial rate of the DNase I degradation reaction for each system was obtained from the slope of the normalised curve of the linear range (within the first 30 mins), and the results are given in Table 5.1.

Table 5.1. Comparison of initial degradation reaction velocity (min^{-1}) over the first 30 min derived from Figure. 5.10.

Carriers	Initial degradation reaction velocity (min^{-1})
M1/MC2	3.03% ± 0.03%
GNP-M1/MC2	1.13% ± 0.12%
GNP-M1/MC2(PEG250)	0.75% ± 0.08%
GNP-M1/MC2(PEG750)	0.73% ± 0.04%
GNP-M1/MC2(PEG12)3	0.32% ± 0.06%

From Figure 5.10 and Table 5.1 it can be seen that the dsDNA on its own (M1/MC2) was digested very rapidly with an initial degradation rate of 3.03% min^{-1}, and the whole degradation process was complete within 50 mins. Unsurprisingly, once the M1/MC2 was conjugated to GNP the degradation process was significantly slower; it did not complete even after 3 h with an initial velocity of 1.13% min^{-1}, ~ three times slower than the dsDNA alone. This result is consistent with that of the literature[206], which reported similar enhanced stability against enzyme degradation for GNP-DNA conjugates. This is probably due to the strongly negative-charged surface of the GNP-DNA conjugate, resulting in a high local Na^+ concentration which can inhibit the activity of DNase I and other relevant nucleases [38]. In fact, this is the proposed mechanism for the improved DNA stability against nuclease degradation by attaching DNA to GNP[206].

All PEG-modified systems were found to exhibit slower degradation processes than the parent GNP-M1/MC2 without PEGylation. The single PEG chain modified systems, GNP-M1/MC2(PEG250) and GNP-M1/MC2(PEG750) showed very similar initial degradation rates, approximately 0.7% min^{-1}. The slowest degradation velocity, at around 0.32% min^{-1}, was obtained for GNP-M1/MC2(TMM), the three-chain PEG-modified system. This is > two times slower than the single-chain PEG-modified systems, > three times slower than GNP-M1/MC2 without PEGylation, and nearly ten times slower than dsDNA on its own. Furthermore, the degradation process of GNP-M1/MC2(TMM) had not been completed after 3 h of DNase I incubation, as shown in Figure 5.10, indicating that the branched, multiple PEG chain-modified GNP-M1/MC2(TMM) system can provide much higher resistance to enzyme degradation.

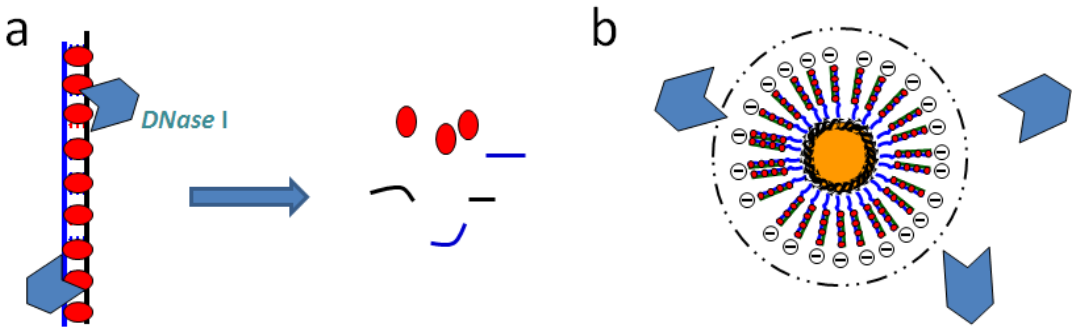

Figure 5.11. Schematics of dsDNA (a) and PEG-modified GNP-DNA systems (b) under degradation by DNase I.

The mechanism of a PEGylated GNP-DNA system for enhanced resistance to enzymatic degradation is likely to combine both steric hindrance and high local Na^+ concentration, thereby inhibiting enzymatic activity [38]. The former is due to the existence of a dense PEG 'shield' (Figure 5.11), known as a 'conformational cloud'.[255, 276] The high flexibility of PEG chains leads to a huge number of possible conformations which constantly switch from one to another. This swiftly-changing conformational cloud can significantly reduce interactions of PEGylated objects with blood components, including enzymes. At the same time, the strong negative charge of densely-packed DNAs beneath the PEG conformational cloud can still induce high local Na^+ concentrations to inhibit the activity of enzymes that have penetrated the PEG shield. Therefore, all PEG-modified GNP-DNA systems can be expected to show slower enzymatic degradation than non-PEGylated systems. Among these is the GNP-M1/MC2(TMM), which is modified by three-PEG chains and hence has a much higher PEG density on the surface. In addition, each branched PEG consists of 40 EG units, far more than those of the single-chain PEG-modified systems (*e.g.* 6 and 18 EG units per PEG for GNP-M1/MC2(PEG250) and GNP-M1/MC2(PEG750), respectively) Therefore a branched PEG-modified system with the same DNA coverage can generate a tighter and more efficient

'conformational cloud' to shield it from interacting with DNase I, and hence a greatly reduced rate of enzymatic degradation, as observed above[247, 249, 281, 284].

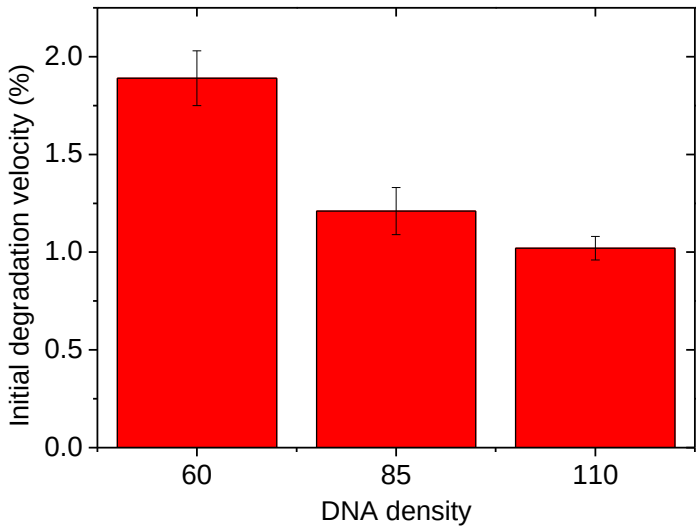

Figure 5.12. Comparison of initial degradation reaction rates (min^{-1}) for non-PEGylated GNP-M1/MC2 at different DNA strand densities per GNP (60, 85 and 110).

As system stability against DNase I degradation can be improved both by attaching DNA to GNP and by PEG modifications, it is expected that the combination of higher DNA density on GNP surface and a longer-branched PEG 'conformational cloud' may result in higher stability for the GNP-M1/MC2(PEG) system. To test whether this is true, two further experiments were designed.

First, a series of non-PEGylated GNP-M1/MC2 systems, with M1 loadings of 60, 85 and 110 strands per GNP, were used to investigate how DNA density affects its stability as reported by the Mirkin Group[38]. Indeed, the higher the DNA loading per GNP, the slower the degradation rate that was obtained (see Figure 5.12). This accords well with the literature[206], as higher DNA density causes a more unfavourable high local Na^+ concentration, more effectively inhibiting DNase activity. Compared to systems with DNA loadings of 60 and 85 strands

per GNP, the initial degradation rate for the system with 110 strands per GNP was 36% and 16% slower, respectively. A general trend of decreasing rates of degradation was found as DNA density rose from 60 to 110, and with higher density, the decreasing amplitude became smaller (Figure 5.12).

Then the same experimental procedures was performed using the three-chain PEG-modified GNP-M1/MC2(TMM), with DNA densities of 85 and 110, against DNase I degradation. The normalised fluorescence response curves are shown in Figure 5.13, where initial degradation rates are 0.32%±0.06% and 0.25%± 0.05% min^{-1} respectively, confirming that the DNA degradation process was further slowed by increased DNA loading. The degradation rate drop here is 22%, which is greater than that observed without PEGylation (16%), confirming that the improved stability of PEGylated GNP-DNA systems is due to the synergistic effects of DNA density and PEGylation.

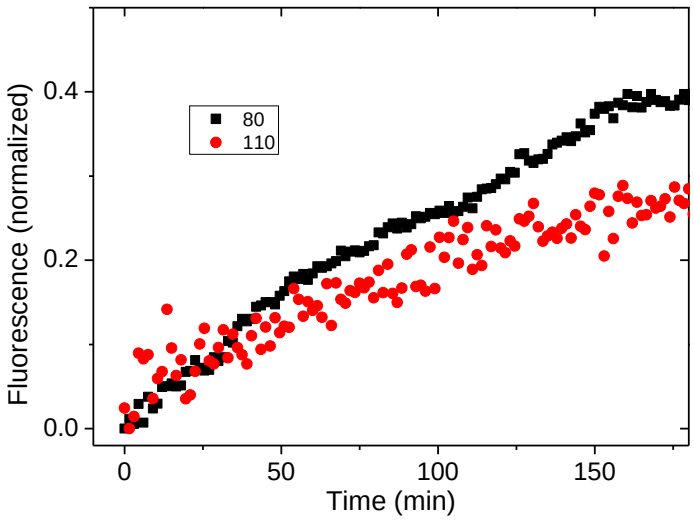

Figure 5.13. Comparison of the degradation rates of GNP-M1/MC2(TMM) with DNA strand densities of 85 and 110 per GNP.

5.2.4 GNP-M1/MC2(TMM) system for PI delivery

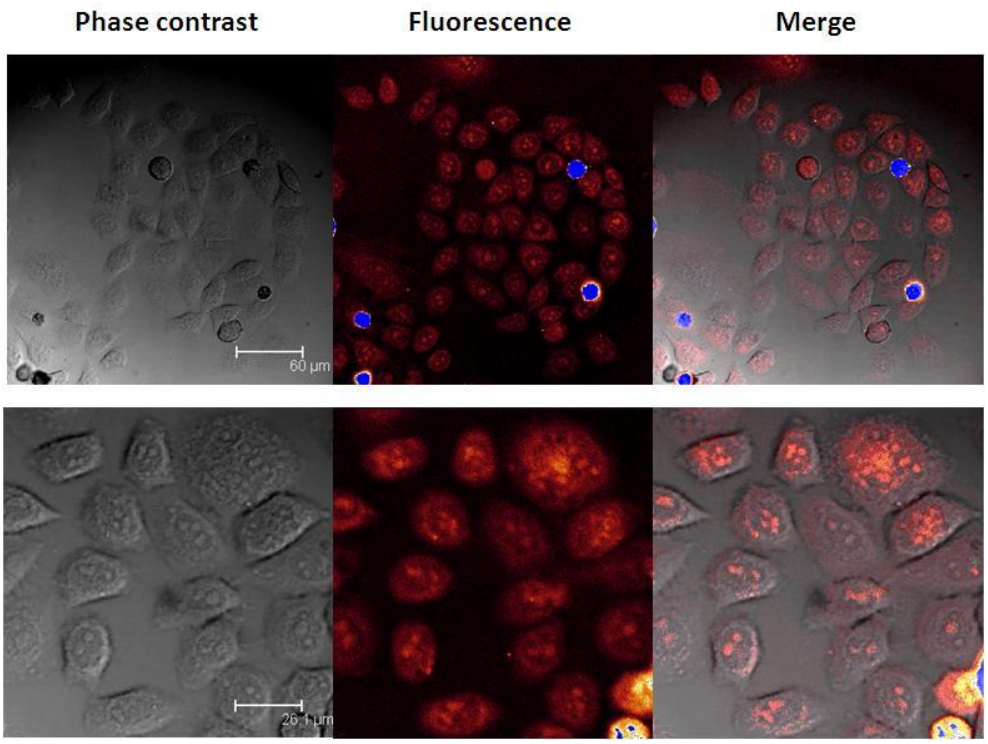

Figure 5.14. Confocal phase contrast (left), fluorescence (middle) and merged optical/fluorescence (right) images of HeLa cells after incubation with GNP-M1/MC2(TMM)-PI for 3 h at 37 °C.

The three-chain PEG-modified system has shown better resistance to serum protein adsorption and DNase I degradation, indicating that the GNP-M1/MC2(TMM) system may have strong potential as a promising platform for drug delivery. Therefore, a further test was performed employing GNP-M1/MC2(TMM) to deliver a membrane-impermeable agent, Propidium Iodide (PI), into HeLa cells. After 3 h incubation with the cells, PI fluorescence was found clearly inside the cells through confocal fluorescence imaging (see Figure 5.14). This confirms that the GNP-M1/MC2(TMM) system can deliver intercalating agents into the cells just as well as the single-chain PEGylated system, as described in Chapter 4. In addition, GNP-M1/MC2(TMM)-PI system

showed greater stability during storage *in vitro*, even with excess PI (more free PI exists in the system), where no aggregation was observed. This is most probably because the long, hydrophilic branched PEG-chains produced by TMM modification offer greatly enhanced water-solubility and steric hindrance against aggregation. Therefore its stability is provided by not only electrostatic repulsion (true for non-PEGylated GNP-DNA systems) but also by steric hindrance due to PEGylation. .

5.3 Conclusion

A three-chain PEG-modified DNA, MC2(TMM), was successfully prepared through a one-step reaction, then purified by HPLC and identified by MALDI-TOF Mass Spectrometry. Hybridization of PEGylated MC2s with the GNP-M1 conjugate produced a series of GNP-M1/MC2(PEG) systems covered with a PEG 'shield' on their surface, which can efficiently mask the negative charges of DNA, preventing non-specific adsorption of positively charged serum proteins and greatly reducing nuclease degradation. Compared to unmodified systems, GNP-M1/MC2(PEG) systems showed little or no obvious change in size when mixed with cell culture media containing 10% FBS, and much slower degradation rates by DNase I (up to 10 fold). The stability *of* a GNP-M1/MC2(PEG) system can be further improved by prolonging the PEG length and using branched PEGs. Among all PEG-modified systems studied in the project, the branched three-chain PEG-modified system (GNP-M1/MC2 (TMM)) appears to be the most promising drug delivery platform and has great potential for *in vivo* applications.

6 Chapter 6: Preparation, characterisation and cellular study of DOX dimer

DOX, an anthracycline antibiotic, is one of the most widely-used active chemotherapeutic agents with a wide spectrum of activity against different types of cancer[175, 176]. However it has serious side effects, particularly irreversible cardiac damage and inducement of multi-drug resistance (MDR), that can limit its clinical applications[180, 181, 285]. In order to improve its chemotherapeutical index two strategies have been exploited, including development of new analogues and targeted NDDSs [286]. Analogues of DOX based on the same main chemical structure, such as chemical modifications of 3'-N-amino group[287, 288] and 4'-hydroxy group[180, 289] and the synthesis of DOX dimers[290-292], were widely studied, with some showing greater anti-tumour efficacy[287, 293, 294] and/or less cardiotoxicity[295, 296].

A targeted NDDS, GNP-dsDNA-DOX, can exploit the EPR effect to target tumour tissue and reduce side effects without DOX modification. However, as DOX was carried by the GNP-dsDNA nanocarrier *via* intercalation, and DNA intercalation is considered one of main mechanisms for anticancer activity of anthracyclines *in vivo*[180], a covalently linked DOX dimer was also synthesized with the expectation that it may improve its DNA binding affinity to favour DOX (DOX dimer) loading, which in turn may lead to even higher anti-tumour acitivity *in vivo*.

6.1 Materials and Methods

6.1.1 Materials

Bis-*N*-succinimidyl-(pentaethylene glycol) ester ($BS(PEG)_5$) was purchased

from Thermo Scientific. Triethylamine and isopropanol were purchased from Fisher Scientific. Formic acid was purchased from Sigma-Aldrich.

6.1.2 Preparation of DOX dimer

5 mg DOX (8.6 μmol) dissolved in 5 ml methanol was mixed with 16.5 μL of $BS(PEG)_5$ DMSO solution (208.6 mM) and 1.3 μL of TEA for reaction overnight in a 4 ℃ fridge (molar ratio of DOX to $BS(PEG)_5$ = 2.5:1 and DOX to TEA = 1:1.1).

6.1.3 Analysis of DOX dimer

After reaction the reaction mixture, together with the two reactants (DOX and $BS(PEG)_5$), were analysed by an HPLC-MS system. Their electrospray (ES+) ionisation mass spectra were obtained on a Bruker HCT Ultra mass spectrometer after separation by HPLC using a C18 column with mobile phase consisting of water (+0.1% formic acid) and acetonitrile (+0.1% formic acid). The process was performed within 3 min using a gradient of 5-95% B and a flow rate of 1.5 mL/min.

6.1.4 Purification of DOX dimer

6.1.4.1 Column chromatography

0.5 mL of the reaction mixture containing DOX dimer was loaded onto a silica gel column, followed by addition of methanol (eluting solvent). When the coloured components started to elute, equal-sized (3 mL) fractions were collected and labelled sequentially for HPLC-MS analysis, and the fractions containing the peak corresponding to maximum mass-to-charge ratio (max. m/z) of 1411 were combined.

6.1.4.2 Semi-prep HPLC-MS

The reaction mixture was injected into an Agilent 1260 Mass Directed

Preparative HPLC using the same mobile phase and gradient as DOX dimer analysis above (flow rate: 5 mL/min), and the fraction containing the peak with 1411 (m/z) was collected automatically, freeze dried on a Virtis Benchtop K freeze dryer, and then injected into the Bruker HCT Ultra mass spectrometer to determine the purity of the DOX dimer.

6.1.4.3 'Solvent-rinse' method

1 mL of DOX dimer methanol solution was evaporated under reduced pressure, washed by 1 mL of isopropanol once and 250 µL of water three times, then dissolved in 5 mL of water. As its solubility in water (calculated *via* the Lambert-Beer law) is low, all the DOX dimer was finally dissolved in DMSO. The solution was monitored at each step by a Bruker HCT Ultra mass spectrometer.

6.1.5 Stability of DOX dimer

A saturated aqueous solution of DOX dimer was stored in a fridge at 4℃ for two weeks, and then HPLC-MS was employed to monitor any change in DOX dimer profiles by comparing the number of peaks and their relative areas.

6.1.6 UV-vis and fluorescence spectroscopy

UV-vis absorption spectra of DOX (38 µM) and DOX dimer (16 µM) were recorded on the Varian Cary 50 bio UV-visible spectrophotometer in the range 350-650 nm. Fluorescence excitation spectra (emission wavelength: 590 nm) and emission spectra (excitation wavelength: 480 nm) of DOX (38 µM) and DOX dimer (16 µM) were recorded on the Spex Fluoro Max-3 Spectrofluorometer.

6.1.7 Titration of DOX dimer with dsDNA M1/MC2

90 µL of dsDNA M1/MC2 (16.67µM) in MES buffer were titrated into DOX dimer (16 µM, 500 µL) in an MES buffer, and the resulting DOX dimer fluorescence

spectra were recorded.

6.1.8 Confocal laser scanning microscopy

HeLa cells were cultured overnight on collagen-pretreated coverslips in a 24-well plate. They were incubated with DOX dimer (5 μM) for 3 h at 37°C and then the supernatant medium was removed and the cells were washed three times with PBS. The treated HeLa cells were then imaged using a Leica SP5 confocal laser scanning microscope with excitation wavelength of 488 nm.

6.1.9 MTT assay (DOX dimer and DOX)

HeLa cells were treated using free DOX and DOX dimer in different concentrations (0.75, 1.5, 3, 4.5 and 6 μM) in full DMEM. The samples were removed after 18 h of incubation at 37 °C. Treated cells were washed with PBS and 100 μL of MTT (0.5 mg/mL in Hank's buffer) was added to the cells at 37 °C for 4 h. The MTT was then removed and 200 μL DMSO was added to each well. The plate was incubated at 37 °C for 2 h to dissolve the formazan, after which absorbance was measured at 550 nm using a microplate reader. The results were expressed in percentages related to a control of cells not treated with either sample.

6.2 Results and Discussion

6.2.1 Synthesis of DOX dimer

DOX dimer was synthesized in a one-step reaction by employing a homo-bifunctional crosslinker, $BS(PEG)_5$, which contains two *N*-hydroxysuccinimide (NHS) esters, to bridge two DOX monomers by forming covalent amide bonds between NHS-ester active carbonyl groups and the primary amine group of DOX (see Figure 6.1). With PEG as a flexible spacer arm, the use of $BS(PEG)_5$ is expected to provide specific advantages such as maintained (or increased)

solubility and non-immunogenic response to the spacer itself. It is further anticipated that, owing to the high flexibility of the PEG chain (5 repeated units), the PEG spacer arm should have minimum effect on DOX intercalation, as the length of PEG spacer arm (2.17 nm, more than 6 DNA bases long) allows the two conjugated DOX molecules enough 'space' for both intercalations. Also, after intercalation the PEG spacer arm can improve the stability of GNP-dsDNA-DOX dimer by reducing its tendency to aggregate during storage *in vitro,* and by exerting the 'stealth effect' *in vivo* to prolong circulation time.

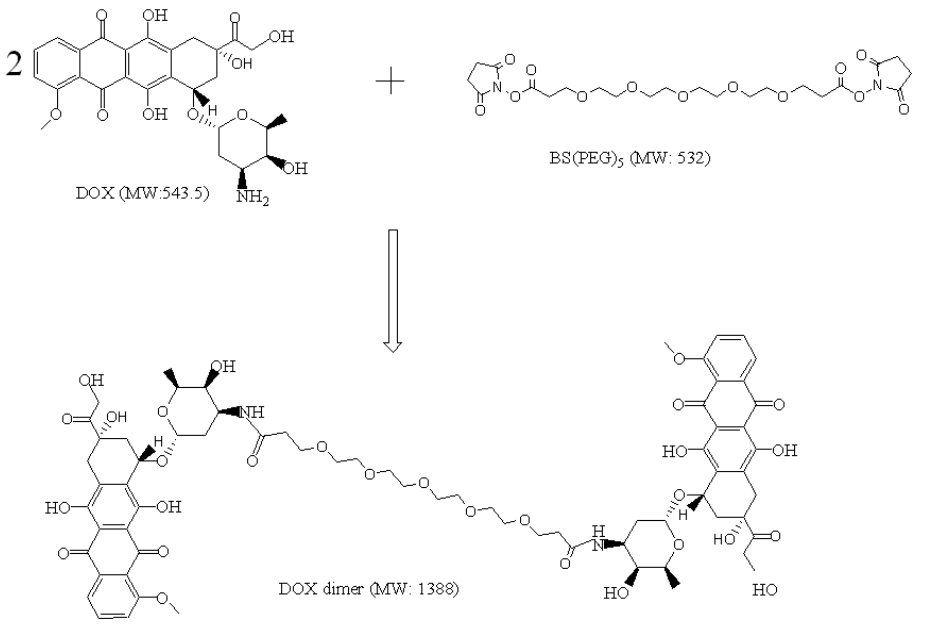

Figure 6.1. Schematic procedure of DOX dimer preparation.

As DOX exists in the form of the hydrochloride salt, the one-step conjugation was performed in the presence of TEA for pH adjustment to favour the formation of amide bonds. Also excess DOX was used for conjugation (the mixing molar ratio of DOX to $BS(PEG)_5$ = 2.5:1) to ensure that both NHS-ester groups within one $BS(PEG)_5$ molecule were involved in conjugation with two DOX molecules to form a DOX dimer (DOX-PEG-DOX) rather than the other possible by-product *i.e.* DOX-PEG.

6.2.2 HPLC-MS analysis

6.2.2.1 HPLC-MS analysis of the reactants

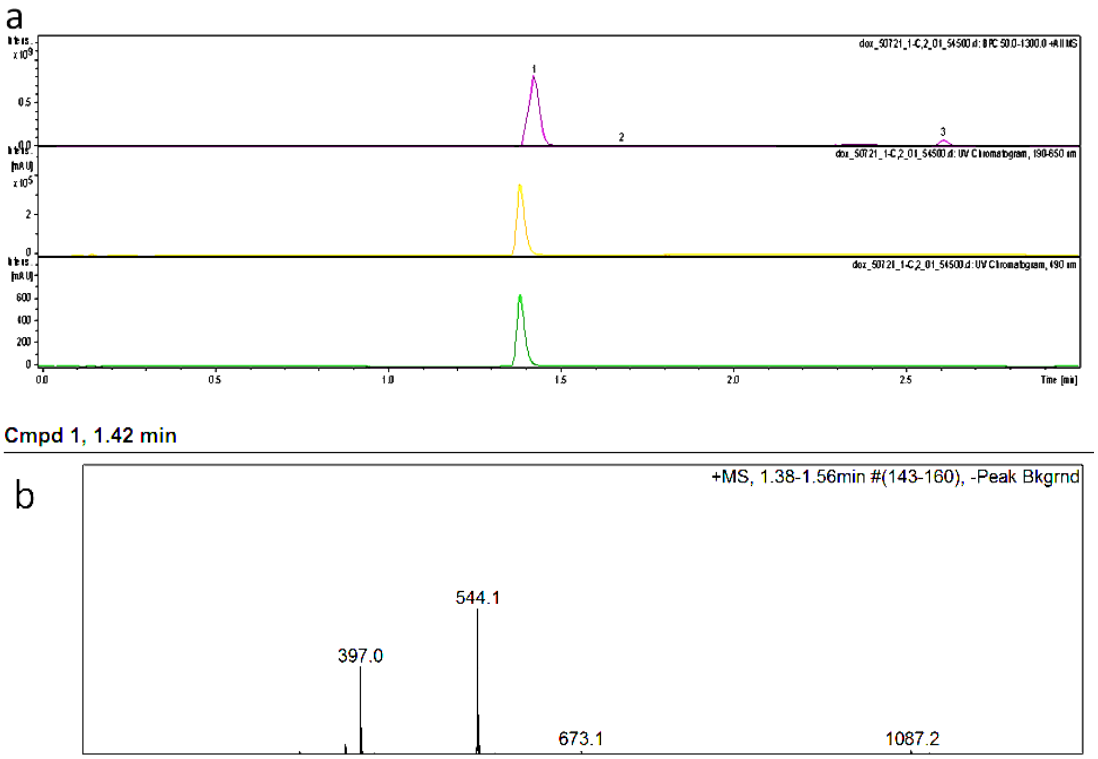

Figure 6.2. Representation of HPLC-MS profiles of DOX. (**a**) HPLC profiles detected by the mass spectrometer and a UV detector at ranges of 190-650 nm and at 490 nm, (from top to bottom); (**b**) mass spectrum of peak 1 of the HPLC profile under mass spectral detection (m/z: 544).

The conjugation reaction was monitored by HPLC-MS, and Figures 6.2 & 6.3 show HPLC-MS profiles of the reactants (DOX and $BS(PEG)_5$). It can be seen that only one peak at 1.4 min was detected from DOX by both MS detector and UV-vis detector and its max. m/z was 544. This corresponded to the mass of DOX (543) with adduction of H, which together with the UV-vis absorption peak under the detection wavelength of 490 nm confirms that the peak was from DOX with a high purity of 92%.

However, more than 10 peaks were detected from $BS(PEG)_5$ by the MS

detector (Figure 6.3a), with peaks 5 & 6 at around 1.5 min corresponding to the mass of $BS(PEG)_5$ (532) with adduction of 23 (Na) (Figure 6.3b). The max. m/z of the other peaks in Figure 6.3a (Table 6.1) did not match any mass of $BS(PEG)_n$ (n = 1-17) (Table 6.2). These results suggest that $BS(PEG)_5$ was not a heterogeneous mixture of different PEG chain lengths and might contain other chemical species.

A UV-vis absorption peak at 1.5 min, corresponding to peaks 5 & 6 in the HPLC-MS profile, was also detected in the range of 190-650 nm but not under the detection wavelength of 490 nm, and was possibly from the NHS group[297, 298]. This would not affect the detection of DOX dimer by UV-vis detector under the detection wavelength of 490 nm.

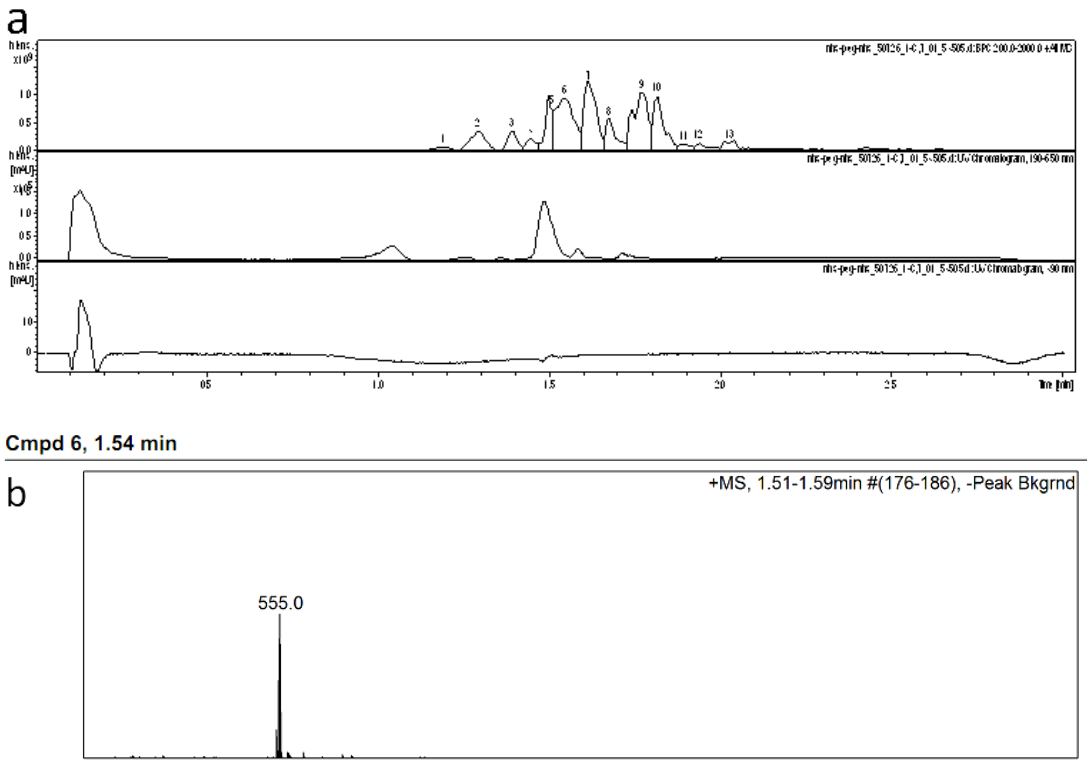

Figure 6.3. Representation of HPLC-MS profiles of $BS(PEG)_5$. (**a**) HPLC profiles detected by mass spectrometer and UV detector under the range of 190-650 nm and at 490 nm, respectively from top to bottom; (**b**) mass spectrum of peak 6 of the HPLC profile under mass spectral detection (max. m/z: 555).

Table 6.1. Maximum m/zs of each peak of the HPLC profile of $BS(PEG)_5$ in Figure 6.3.

#	Cmpd. Label	RT [min]	Range [min]	Max. m/z
1	Cmpd 1, 1.19 min	1.19	1.13 - 1.23	271.1
2	Cmpd 2, 1.29 min	1.29	1.23 - 1.35	386.1
3	Cmpd 3, 1.39 min	1.39	1.36 - 1.42	458.1
4	Cmpd 4, 1.44 min	1.44	1.42 - 1.47	626.1
5	Cmpd 5, 1.51 min	1.51	1.47 - 1.51	555.0
6	Cmpd 6, 1.54 min	1.54	1.51 - 1.59	555.0
7	Cmpd 7, 1.62 min	1.62	1.59 - 1.66	803.2
8	Cmpd 8, 1.67 min	1.67	1.66 - 1.72	1051.3
9	Cmpd 9, 1.77 min	1.77	1.72 - 1.80	514.1
10	Cmpd 10, 1.81 min	1.81	1.80 - 1.87	762.2

Table 6.2. Mass of BS $(PEG)_n$ (or with adduction of Na or H) (n=1-17).

n of BS $(PEG)_n$	Mass of BS $(PEG)_n$	Mass + 23 (Na)	Mass + 1 (H)
1	356	379	357
2	400	423	401
3	444	467	445
4	488	511	489
5	532	555	533
6	576	599	577
7	620	643	621
8	664	687	665
9	708	731	709
10	752	775	753
11	796	819	797
12	840	863	841
13	884	907	885
14	928	951	929
15	972	995	973
16	1016	1039	1017
17	1060	1083	1061

6.2.2.2 HPLC-MS analysis of DOX dimer

The HPLC-MS profile of the reaction mixture (Figure 6.4) also shows that more than 10 peaks were detected, probably due to the impurity of $BS(PEG)_5$, and a UV-vis absorption peak at around 1.6 min, corresponding to peak 5 in HPLC-MS profile, was detected under the detection wavelength of 490 nm. This suggests

that peak 5 at 1.6 min was from the DOX-related product, since DOX can be excluded according to the result in Figure 6.2, in which DOX was eluted at around 1.4 min under the same HPLC condition. From the MS spectrum of peak 5, which displayed a max. m/z of 1411 (Figure 6.4b), it can be concluded that peak 5 at 1.6 min corresponds exactly to the expected mass of DOX dimer (MW: 1388) with adduction of 23 (Na), and that the preparation of DOX dimer using $BS(PEG)_5$ as the crosslinker was successfully performed.

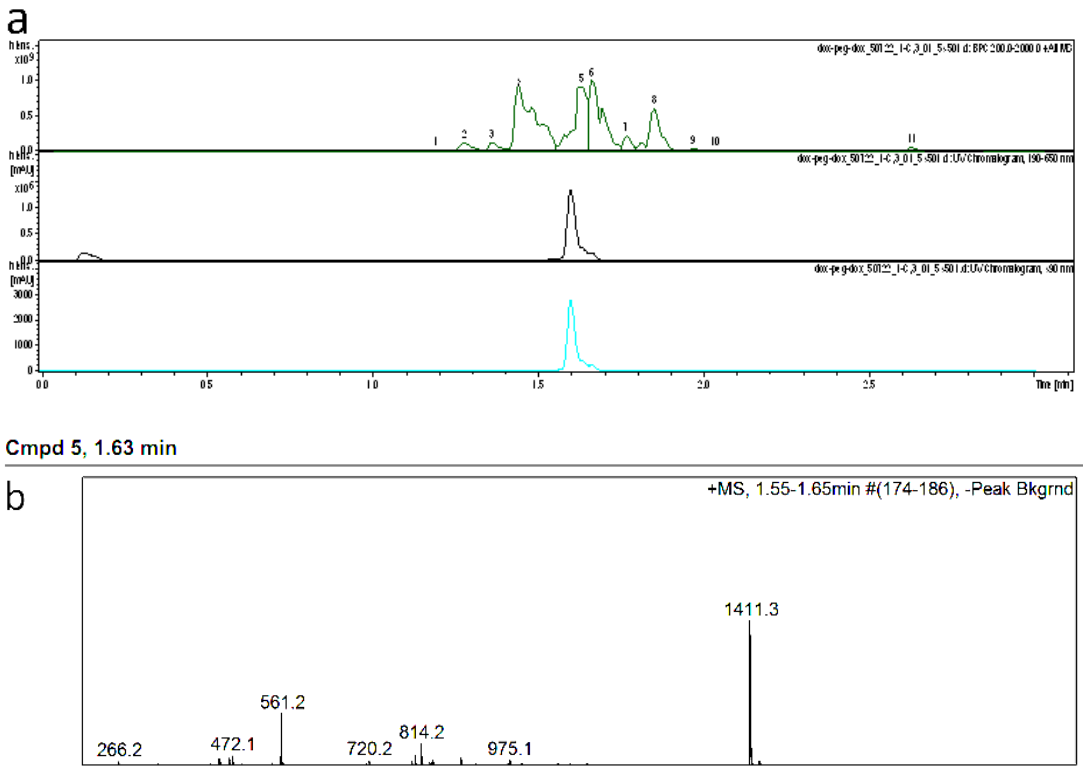

Figure 6.4. Representation of HPLC-MS profiles of the reaction mixture. (**a**) HPLC profiles detected by mass spectrometer and UV detector in the range of 190-650 nm and at 490 nm, respectively from top to bottom; (**b**) mass spectrum of peak 5 of the HPLC profile under mass spectral detection (m/z: 1411).

6.2.3 DOX dimer purification

Three different methods were tried for DOX dimer purification : silica gel column chromatography (CC), semi-preparative HPLC-MS purification and 'solvent-rinse'.

6.2.3.1 CC and Semi-preparative HPLC-MS purification

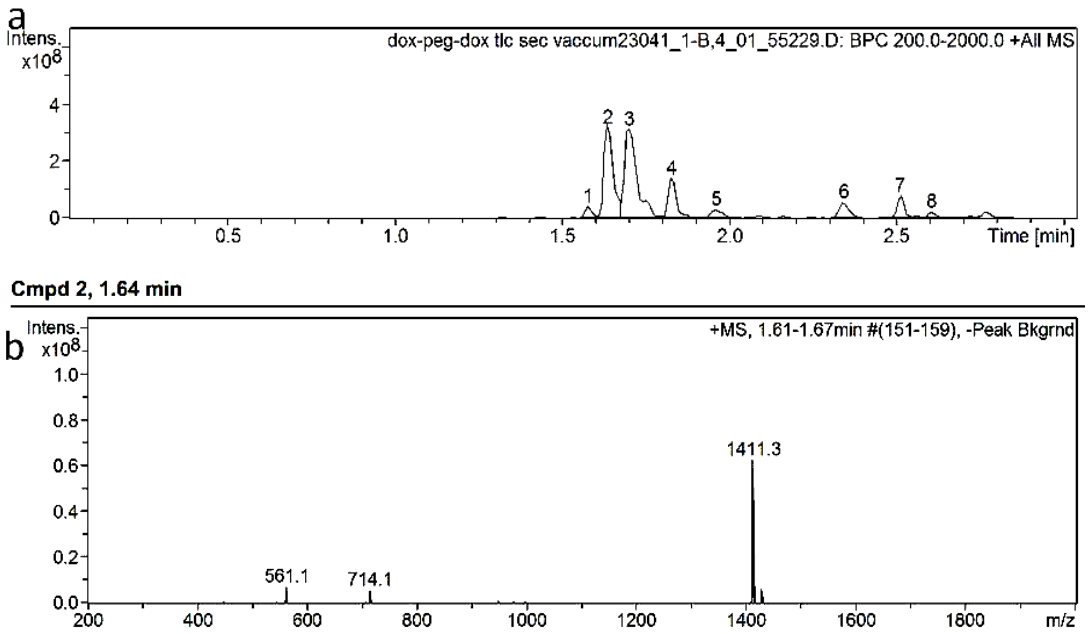

Figure 6.5. Representation of HPLC-MS profiles of the reaction mixture after purification by CC. (**a**) HPLC profile detected by mass spectrometer; (**b**) mass spectrum of peak 2 of the HPLC profile (m/z: 1411).

Figure 6.5 shows HPLC-MS results of the fraction with the peak of DOX dimer (peak 2 at 1.6 min with max. m/z of 1411) purified by CC. Besides the dimer peak, two other main peaks (3 & 4) were also detected and remained in the section. By calculating the relative area of each peak, the purity of DOX dimer after CC purification was estimated to be around 30%, revealing that the CC method was not adequate for DOX dimer purification.

Compared to CC, semi-preparative HPLC-MS shows higher detection sensitivity and resolution, and the fraction containing DOX dimer (max. m/z: 1411) can also be collected automatically. From Figure 6.6 it was observed that after the HPLC-MS purification the fraction with a single main peak of DOX dimer was still hardly achieved. Because of the existence of other peaks, the purity of DOX dimer was calculated as being only approximately 33%, which was as inefficient

as the CC method.

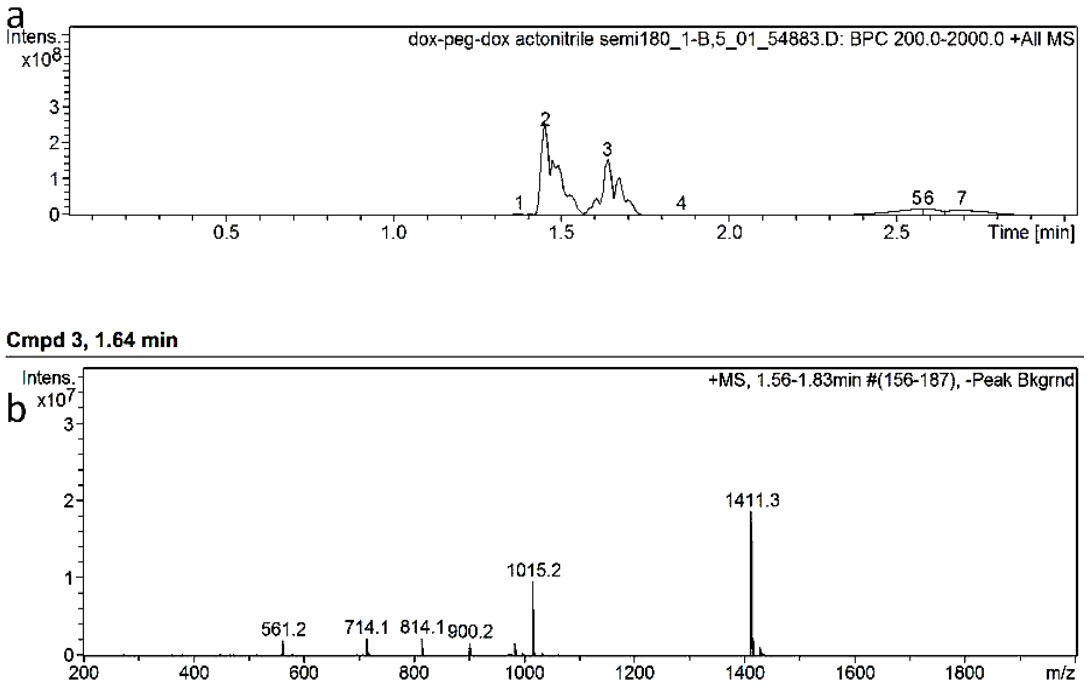

Figure 6.6. Representation of HPLC-MS profiles of the reaction mixture after purification by semi-preparative HPLC-MS. (**a**) HPLC profile detected by mass spectrometer; (**b**) mass spectrum of peak 3 of the HPLC profile (m/z: 1411).

Although CC and HPLC are two standard purification methods, they appeared not to be suitable for DOX dimer. This is probably because so many peaks were detected by the highly-sensitive MS detector in both $BS(PEG)_5$ and the reaction mixture, and besides, it is difficult to find an optimum mobile phase for achieving ideal resolution (the degree of separation between two chromatographic peaks) for DOX dimer purification. This resulted in coexistence of other peaks (chemical species) after CC or semi-preparative HPLC-MS, leading to low purity of DOX dimer.

6.2.3.2 Purification *via* solvent-rinse method

After the conjugation reaction, a crystal was obtained from the reaction mixture

by evaporation, and different solvents such as propanol, water and DMSO were used to dissolve the crystal. By monitoring their HPLC-MS profiles, we found that the solubilities of DOX dimer and other species in propanol, water and DMSO varied highly. By exploiting the different solubilities of the mixture in a variety of solvents, a method using sequential rinses with propanol and water was established (solvent-rinse method).

Compared to the HPLC-MS profile of the reaction mixture in methanol (Figure 6.7a), peaks 3 & 4 at 1.49 and 1.54 min in the propanol rinsing solution (Figure 6.7b) displayed much higher intensity than DOX dimer (peak 5 at 1.64 min) and other components, suggesting that the main species, which were dissolved in 1 mL of propanol and discarded, corresponded to the two peaks at 1.49 and 1.54 min. (According to the results in Figure 6.7c they were only partially removed.)

During the water rinsing steps (Figure 6.7c-e), each water rinsing solution contained not only peaks at 1.67 min (with the highest intensity) and 1.86 min, but also the dimer peak (1.64 min), indicating the loss of DOX dimer as well as the removal of the species eluted at 1.67 and 1.86 min. But considering that the water volume of each rinsing step was only 250 μL, and that the main purpose of purification here was to get a DOX dimer with reasonably high purity for characterisation and cytotoxicity evaluation, a small proportion of DOX dimer loss was acceptable. In addition, with water rinsing, the intensities of the peaks with retention times earlier than 1.6 min (DOX dimer), particularly the two main peaks at 1.49 and 1.54 min, declined significantly and were hardly detectable in the third water rinsing solution, revealing that most species eluted before DOX dimer were dissolved and removed by both propanol and water rinsing steps.

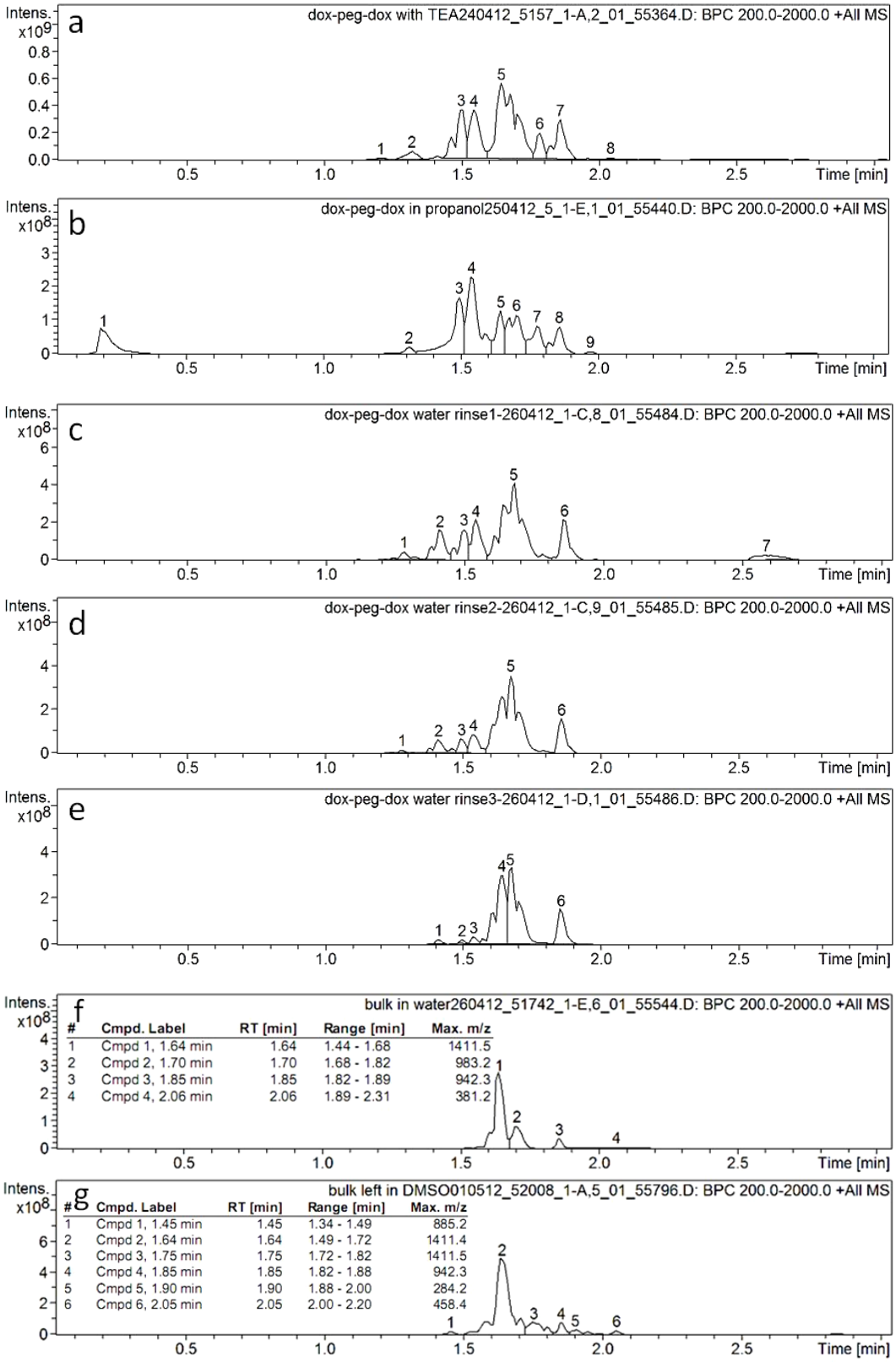

Figure 6.7. Representations of HPLC-MS profiles of each step of 'solvent-rinse' method, from top to bottom: (**a**) methanol solution of reaction mixture; (**b**) propanol rinsing solution; (**c**) first water rinsing solution; (**d**) second water rinsing solution; (**e**) third water rinsing solution; (**f**) DOX dimer water solution; (**g**) DOX dimer DMSO solution.

After the rinsing steps, 5 mL of water was added to the remaining crystal and the HPLC-MS profiles of the water solution (Figure 6.7f) displayed only one main peak at 1.64 min (max. m/z: 1411), which corresponded to DOX dimer, together with two small peaks at 1.7 and 1.85 min, indicating that most of the species eluted after DOX dimer were also successfully removed by the rinsing steps and that the purity of DOX dimer in water was around 65%.

We also found that after rinsing the crystal was only partially dissolved in 5 mL of water, suggesting a low solubility of DOX dimer in water. The remaining crystal was finally dissolved in 1 mL of DMSO, and its HPLC-MS profile (Figure 6.7g) further confirmed that DOX dimer was purified successfully through the simple solvent-rinse method. By reference to the relative areas of DOX dimer peaks, the purity of DOX dimer dissolved in DMSO was calculated at approximately 86%, much higher than that dissolved in water (65%). This is because of the DOX dimer's low solubility in water, leading to a calculated purity (65% in water) much lower than the real value. It was also noted that the remaining crystal was further purified, with the small proportion of other species, which still remained in the crystal after rinsing(1.7 and 1.85 min), being removed by their dissolution in 5 mL of water.

6.2.4 Characterisation of DOX dimer and comparison with DOX

6.2.4.1 UV-vis absorption

Figure 6.8 shows digital images of DOX and DOX dimer dissolved in DMSO, and both display the same solution colour (orange-red) as they had very similar UV-vis absorption spectra with absorption peaks at 480 nm (Figure 6.9). This is understandable because the main structure of monomers in a DOX dimer remains identical with DOX, and the modification of primary amine groups,

together with the PEG linker, does not contribute to the UV-vis spectrum in the detection range of 350-650 nm[299, 300].

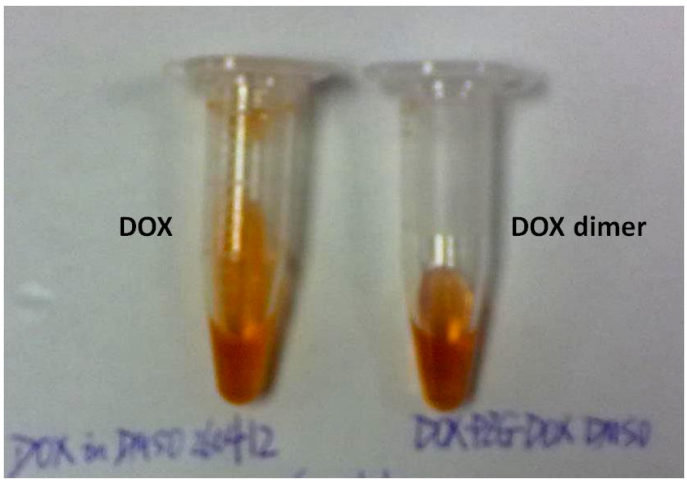

Figure 6.8. Photographs of DOX and DOX dimer in DMSO.

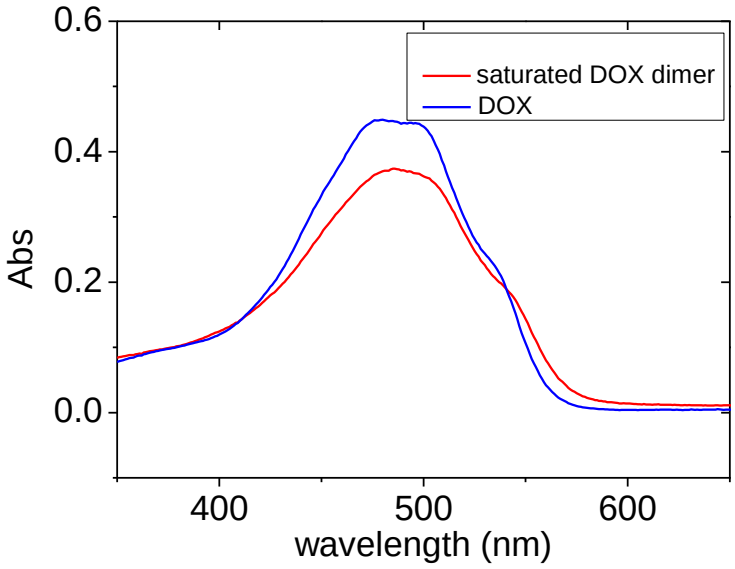

Figure 6.9. UV-vis spectra of DOX (blue) and DOX dimer (red) in water.

6.2.4.2 DOX dimer solubility in water

Since the molar extinction coefficient of DOX is 11500 $M^{-1}\cdot cm^{-1}$ at 480 nm[301, 302], the extinction coefficient of DOX dimer was expected to be around 23000 $M^{-1}\cdot cm^{-1}$. The solubility of DOX dimer in water at room temperature was calculated according to absorbance (0.372) at 480 nm, which was derived from

the UV-visible spectra of the saturated aqueous solution of DOX dimer, approximately 16 μM.

6.2.4.3 Stability of DOX dimer aqueous solution

HPLC-MS profiles of DOX dimer aqueous solution before and after 2 weeks' storage (Figure 6.10) show that no new peak was observed after storage, and that the relative area of DOX dimer after two weeks (77.8%), was decreased by 1.9%, compared with that before storage (79.3%). This suggests that DOX dimer is relatively stable in aqueous solution at 4 ℃, and that a newly prepared DOX dimer solution would be acceptable for further characterisation or cellular study within two weeks.

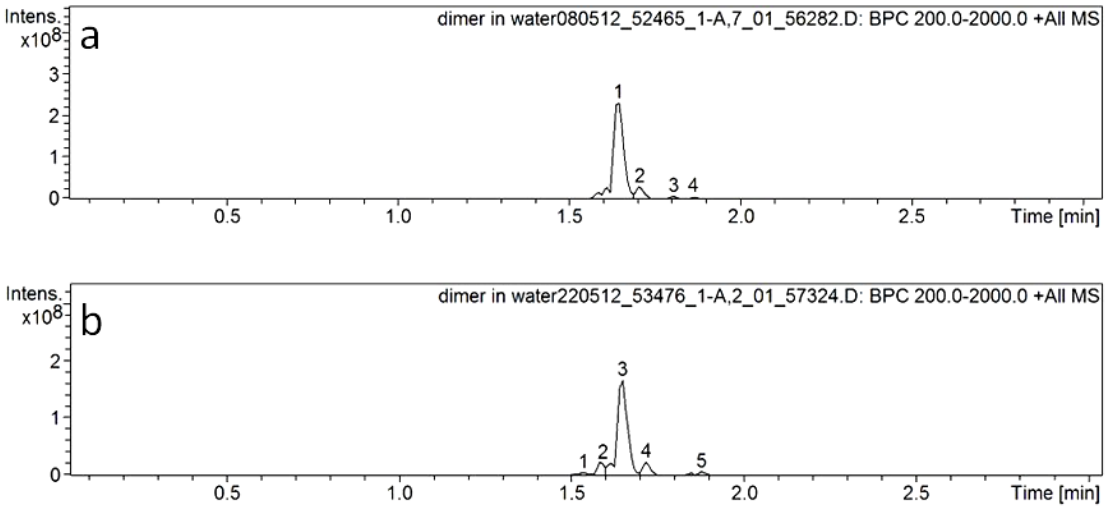

Figure 6.10. Representive HPLC-MS profiles of DOX dimer aqueous solution on day 1 (**a**) and day 14 (**b**) of storage at 4 °C.

6.2.4.4 DOX dimer fluorescence and DNA-binding

DOX dimer displayed a very similar fluorescence emission spectrum (excitation wavelength: 480 nm) to DOX, with the same emission peak observed at 590 nm (Figure 6.11) because the chemical structure remains largely unchanged. This would facilitate the subsequent observation of HeLa cells treated with DOX

dimer by confocal laser scanning microscopy.

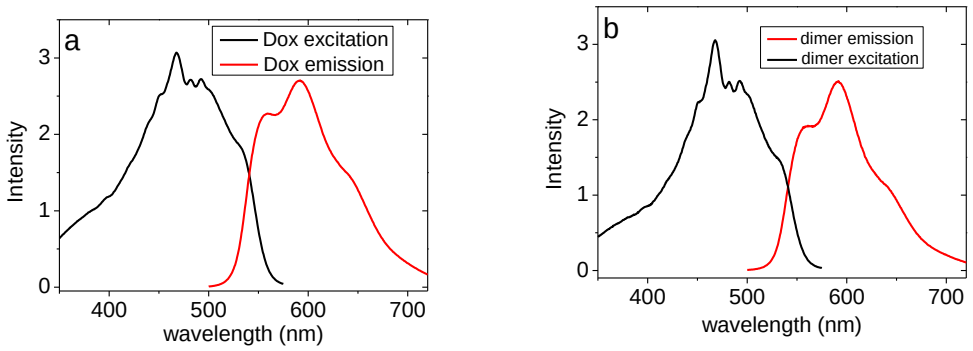

Figure 6.11. Fluorescence excitation and emission spectra of DOX (38 μM) (**a**) and DOX dimer (16 μM) (**b**) aqueous solution.

Since one of the main antitumour mechanisms of DOX is DNA intercalation, which leads to inhibition of biosynthesis[180, 303], *in vitro* DNA-binding efficiency of DOX dimer was obtained by monitoring the fluorescence quenching of DOX dimer with the addition of DNA (Figure 6.12) before cellular study to evaluate its cytotoxicity.

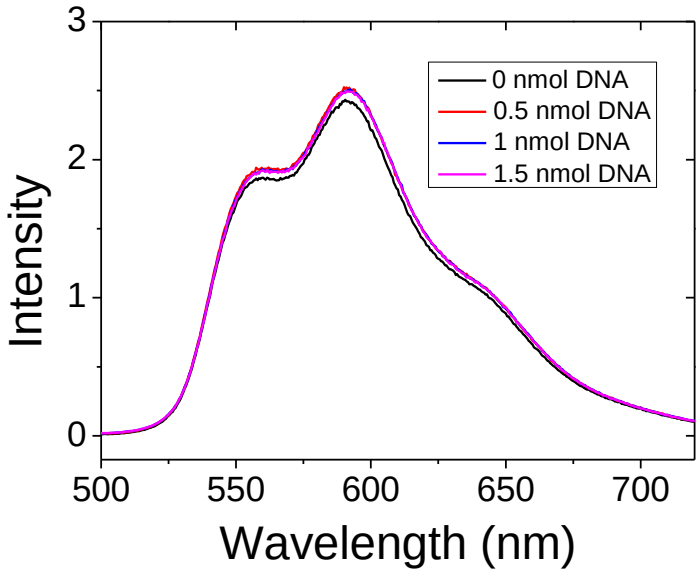

Figure 6.12. Fluorescence emission spectra of DOX dimer (16 μM, 50 μL) with the addition of dsDNA M1/MC2 (16.67 μM) at pH 7.4.

Unfortunately, no significant fluorescence quenching was observed with dsDNA

M1/MC2 added to DOX dimer, and the intensity of DOX dimer with dsDNA was consistent with that before the addition of DNA, which seems to suggest that the DOX dimer did not bind into dsDNA in the same way as DOX.

6.2.4.5 Celluar study

Besides the unexpected DNA titration result, confocal images of HeLa cells treated with the DOX dimer (2.5 μM, 3 h incubation) further confirmed that DOX dimer did not intercalate with dsDNA (Figure 6.13). Unlike DOX, which is mostly localised inside the cell nuclei (see Figure 3.11 in Chapter 3), DOX dimer seemed only to associate with membranes of the nuclei. Also, MTT assay (Figure 6.14) showed that DOX dimer is non-cytotoxic to HeLa cells after 18 h incubation even at a high concentration (*i.e.* 6 μM), whereas DOX showed significant cytotoxicity at this concentration.

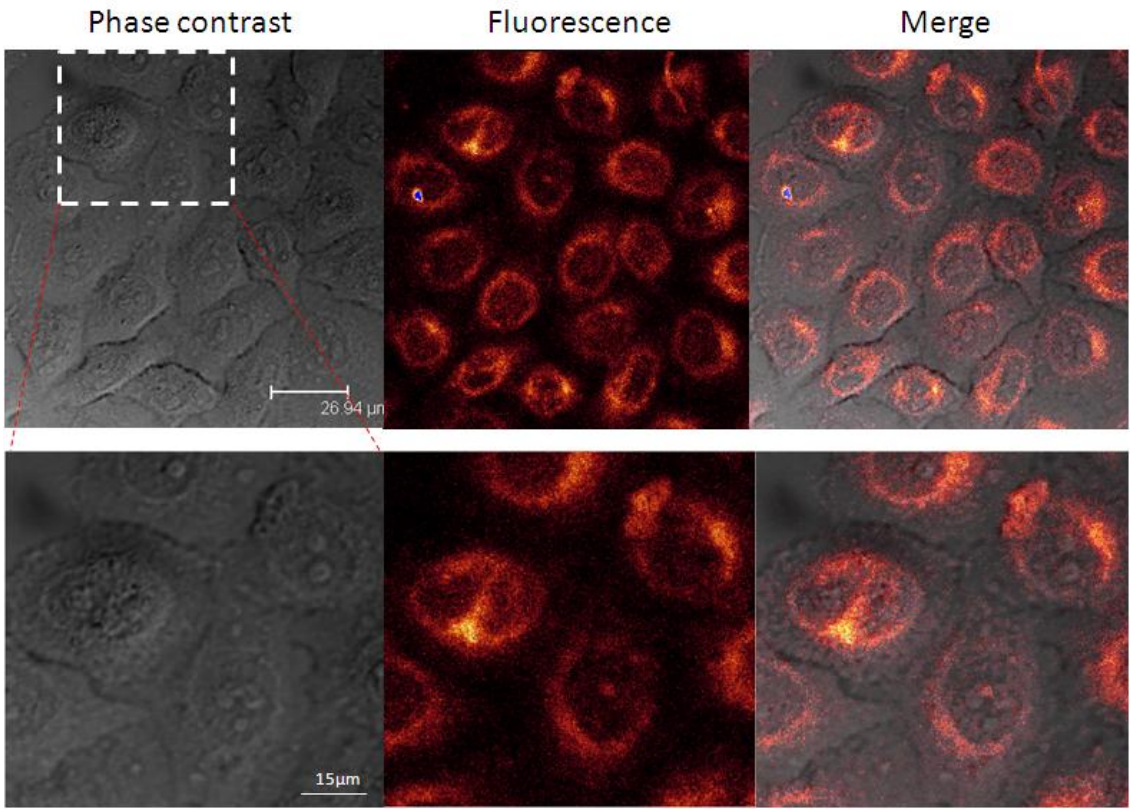

Figure 6.13. Confocal phase contrast, fluorescence and merged optical/fluorescence images of HeLa cells after incubation with DOX dimer (2.5 μM) for 3 h at 37 ℃.

The main difference between the structures of DOX and DOX dimer is found in modification at the primary amino group. Since the role of the amino group in binding macromolecules has been reported[291, 301, 304, 305], we can assume that the amino group plays a key role in intercalation and that a change of amino group will tend to result in DOX dimer failing to intercalate in dsDNA, thus not causing cytotoxicity.

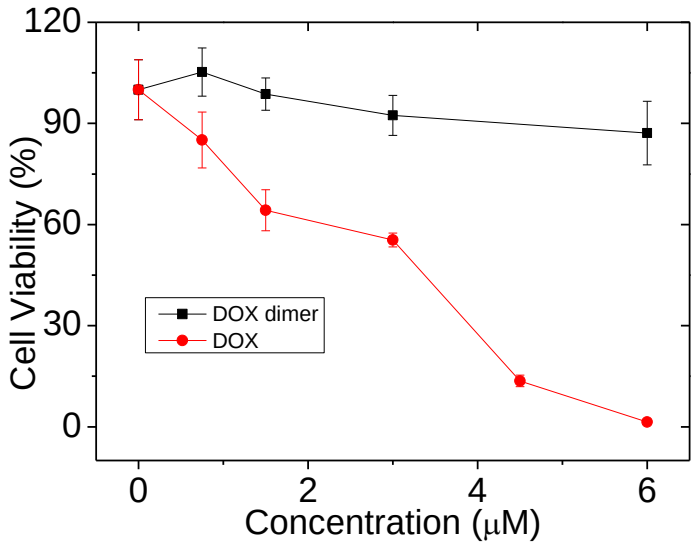

Figure 6.14. MTT assay of HeLa cell viabilities after incubation with DOX and DOX dimer with different concentrations for 18 h at 37 ℃. Error bars are standard deviations of 8 samples (n=8).

6.3 Conclusion

A DOX dimer was successfully synthesized in one step by using a PEG crosslinker, BS(PEG)5, to bridge two DOX monomers *via* the primary amino groups. It was purified by a simple 'solvent-rinse' method with purity of approximately 86%, which remains relatively stable in water at 4 ^{o}C during a 2-week period of stability evaluation. The DOX dimer displays nearly identical

colour, UV spectra and fluorescence spectra to the DOX monomer, as its main chemical structure does not change. However, both DNA titration and confocal fluorescence imaging results showed that DOX dimer cannot intercalate into DNA, probably because of the modification of the amino group, and as a result, the prepared DOX dimer displayed virtually no cytotoxicity.

7 Chapter 7: Towards multifunctional NDDSs for cancer treatment

The use of nanometer-sized gold particles as part of the DOX delivery vehicle allows such NDDSs to explore the specific features of tumour architecture (EPR effect) and achieve passive targeting. Besides GNP-based nanocarriers, other inorganic nanoparticles such as magnetic nanoparticles (MNPs)[306-312] and gold nanorods (GNRs)[313-316] have also been employed in anticancer drug delivery. The advantages of using MNPs and GNRs are that not only can they target cancer *via* their nanoscale sizes[317], but their unique magnetic and optical properties can also diagnose and treat cancer. Thus MNPs and GNRs can be exploited to assemble multifunctional NDDSs for simultaneous cancer imaging, and more effective combined multimodal therapies[126, 318-324].

The strong magnetic properties of MNPs (*e.g.*superparamagnetic iron oxide nanoparticles (SPIO)) can generate a greater contrast between the targeting tissue and the background region for magnetic resonance imaging (MRI) through the strong effects on T1 and T2 proton relaxation times[325-327], which can potentially be applied for cancer imaging[195, 328-331]. Furthermore, MNPs can produce 'inductive heating' in an alternating magnetic field to destroy malignant cells and deliver hyperthermia cancer treatment[89, 332]. Due to their strong surface plasmon resonance, GNRs have extremely high levels of absorption and light scattering in the near-infrared (NIR) region of electromagnetic frequencies (650-900 nm); this allows efficient heat generation and hence kills cancer *via* photothermal therapy. Moreover, such wavelengths overlap the NIR transparent window of the human body, where laser irradiation can penetrate tissues up to 10 cm with very little absorption by cells, so GNRs can also be applied for cell imaging and hyperthermia cancer treatment[90, 323, 333, 334].

In this project, MNPs and GNRs were synthesized to assemble MNP- or GNR-based multifunctional NDDSs. In order to facilitate the attachment of DNAs to MNPs, gold shells were grown on the surface of MNPs to form gold coated magnetic nanoparticles (Fe@Au NPs). The prepared Fe@Au-M1/MC2(PEG750)-DOX or GNR-M1/MC2(PEG750)-DOX can simultaneously achieve passive-targeting, DOX delivery, tumour diagnosis and hyperthermia therapy.

7.1 Materials and Methods

7.1.1 Materials

$FeCl_3 \cdot 6H_2O$, $FeCl_2 \cdot 4H_2O$, mercaptosuccinic acid (MSA), $FeSO_4 \cdot 7H_2O$, hexadecyltrimethyl ammonium bromide (CTAB), octane, sodium borohydride and poly(ethylene glycol) methyl ether thiol (PEG-SH) were purchased from Sigma-Aldrich. Ammonium hydroxide, hydroxylamine, $AgNO_3$, chloroform, methanol and ascorbic acid were purchased from Fisher Scientific. Tetrakis (hydroxymethyl) phosphonium chloride (THPC) and 1-butanol were purchased from Acros Organics.

7.1.2 Preparation of Fe@Au NPs

7.1.2.1 Method 1 (citrate reduction method)

MNPs (Fe_3O_4 NPs) were first prepared by the co-precipitation method[335-338]. Briefly, 4.3 mL of NH_4OH (28%, w/w) in 50 mL water was added to a mixture of iron salts (2.7g $FeCl_3 \cdot 6H_2O$ and 1.0 g $FeCl_2 \cdot 4H_2O$ in 100 mL water) to adjust pH to 10, during which the reaction solution was darkened by the production of black precipitates. The reaction mixture was heated at 80°C for 30 min and then at 90°C for 2 h with N_2 bubbled throughout the reaction. Then 2.94 g tri-sodium citrate dissolved in 50 mL water was added to the mixture. When the solution

was cooled down to room temperature, the black precipitates (MNPs) were separated from the supernatant using a permanent magnet, washed twice with water, and re-dispersed in 50 ml of water (approximately 20 mg/mL).

Fe@Au NPs were then prepared by citrate reduction of $HAuCl_4$ to grow gold on the surface of MNPs. 30 mg of $HAuCl_4$ was dissolved in 100 mL of water and heated to boiling. A certain quantity (45 mg or 15 mg) of MNPs, prepared as above, were added into the reaction solution, followed by the addition of 5 mL tri-sodium citrate solution (0.08 M), and the solution colour changed from brown to burgundy within 1 min. The solution was further boiled for 15 min.

7.1.2.2 Method 2 (Fe_3O_4-s-Au)

MNPs (Fe_3O_4) were first prepared using the same co-precipitation method as Method 1, but instead of using tri-sodium citrate, 50 mL of 0.2 M MSA was added to the reaction solution as a stabiliser. When the solution was cooled down to room temperature, the MNPs were washed twice with water and re-dispersed in 50 mL of water (20 mg/mL).

Preparation of 1.5-nm gold seeds[339, 340]: 12 µL of THPC (80% in water, w/w) was mixed with 1 mL of 1M KOH solution and 45 mL of de-ionised water as the reducing solution; 2 mL of freshly prepared 25 mM $HAuCl_4$ was rapidly injected into the reducing solution under vigorous stirring to produce brown colloidal gold.

Preparation of Fe_3O_4-S-Au: 60 µL of MNPs (20 mg/mL) were mixed with 6 mL of gold seeds overnight to form Fe_3O_4-S-Au, which was then washed with pure water under magnetic attraction and dispersed in water (3 ml).

Formation of gold shells: Gold shells were expected to form on the surface of Fe_3O_4-S-Au *via* an iterative reduction[341, 342] of $HAuCl_4$ by hydroxylamine (four iterations), and this reduction reaction was first tried in the presence of 1.5-nm GNPs before using Fe_3O_4-S-Au. Basically, 0.5 mL of Fe_3O_4-S-Au was first rinsed with 1 mL of 0.1 M tri-sodium citrate and re-dispersed in 0.5 mL of water. During each iterative reduction, 40 µL of 40 mM hydroxylamine and 40 µL of $HAuCl_4$ (2.5 mM) were alternately added into 0.5 mL of GNPs or 0.5 mL of Fe_3O_4-S-Au.

7.1.2.3 Method 3: reverse micelle method

First the following solutions (Table 7.1) were prepared, and then solution A was mixed with solution B under stirring and nitrogen protection; after 1h, solution C was added to the mixture followed by the addition of solution D, which was then stirred overnight.

Table 7.1. The components of the solutions.

Solution	Components
A	1.2 mL water, 0.067 g $FeSO_4 \cdot 7H_2O$, 3.0 g CTAB, 2.5 g 1-butanol, 7.5 g Octane
B	1.2 mL water, 0.045 g $NaBH_4$, 3.0 g CTAB, 2.5 g 1-butanol, 7.5 g Octane
C	0.9 mL water, 0.064 g $HAuCl_4$, 1.5 g CTAB, 1.25 g 1-butanol, 5 g Octane
D	0.9 mL water, 0.054 g $NaBH_4$, 1.5 g CTAB, 1.25 g 1-butanol, 5 g Octane

Phase transfer: the gold-coated magnetic nanoparticles were washed twice with a mixture of chloroform and methanol (v/v 1:1) and a mixture of methanol and water (1:1) respectively, and collected using a permanent magnet. The nanoparticles were then re-dispersed in 50 mM citrate sodium solution, sonicated for 30 min, separated by centrifugation (21.1 kg, 10 min) and finally

re-dispersed in water (25 ml).

Magnetisation measurement (VSM): The prepared Fe@Au NPs were dried in a vacuum oven at 80 ℃ overnight, and measured on a MagLab vibration sample magnetometer (Oxford Instruments) operating at 55 Hz with an amplitude of 1.5 mm. The sensitivity of the instrument is about 2 μemu, with a field range of up to 9 T. The samples were measured at room temperature (298 K) at a magnetic field scan rate of 9.17 mT s^{-1}.

7.1.3 Preparation of GNRs *via* seed-mediated growth method

Seed solution preparation: 1.0 mL of 0.5 mM $HAuCl_4$ was mixed with 1mL of 0.2 M CTAB and stirred at 25 °C. Then 0.12 mL of ice-cold 0.01 M $NaBH_4$ was added, which resulted in the formation of a seed solution with a brownish yellow colour. The seed solution was kept under vigorous stirring at 25 °C.

Growth solution: 50 mL of 0.2 M CTAB, 2.5 mL of 0.004 M $AgNO_3$ and 50 mL of 0.001 M $HAuCl_4$ were mixed together and then 670 μL of 0.079 M ascorbic acid, a mild reducing agent, was added to the above solution, and the solution colour changed from yellow to colourless.

CTAB-stabilised GNRs: 120 μL of seed solution was added to the growth solution under gentle stirring at 25-30 °C. The colour of the solution gradually changed from yellow to brownish-red over the course of 20 min. The growth of the GNR solution was monitored by UV-visible spectra. After 2 h the GNR solution was centrifuged (21.1 kg, 10 min) to remove the excessive CTAB, washed twice with water and then re-dispersed in water (12 mL).

GNR-PEG conjugate: the CTAB-stabilised GNR pellet obtained above *via* centrifugation (21.1 kg, 10 min) was added into 2.5 mM PEG-SH aqueous solution (24 mL) and mixed overnight. It was then centrifuged to remove the

excessive PEG-SH, washed twice with water and re-dispersed in water (12 mL).

7.1.4 TEM imaging of Fe@Au NPs and GNRs

Images of Fe@Au NPs and GNRs were taken using a Philips CM200 transmission electron microscope at 200 kV. The specimen for TEM study was prepared by depositing a drop of the Fe@Au NPs (or GNRs) aqueous solution onto a carbon-coated mesh grid, and then air-dried.

7.1.5 Preparation of Fe@Au-M1/MC2(PEG750)-DOX and GNR-M1/MC2(PEG750)-DOX NDDSs

0.75 mL Fe@Au NPs (or 1.5 mL GNR-PEG) aqueous solution were centrifuged (21.1 kg, 15 min) to get pellets, which were then mixed with 30 nmol DNA M1 overnight to form Fe@Au-M1 (or GNR-M1) conjugate. The excess unattached M1 was removed by centrifugation (21.1 kg,15 min), and the amount of attached M1 was calculated by determining the unattached amount through the UV absorbance at 260 nm. In the presence of MES buffer, the same amount of complementary DNA MC2 (PEG750) as attached M1 was then hybridised to the Fe@Au-M1 (or GNR-M1) conjugate for 3 h to prepare the Fe@Au-M1/MC2(PEG750) nanocarrier (or GNR-M1/MC2(PEG750)), which was followed by DOX addition (the molar ratio of DOX to M1 was 3:1) to form Fe@Au-M1/MC2(PEG750)-DOX (or GNR-M1/MC2(PEG750)-DOX).

7.1.6 Confocal laser scanning microscopy

HeLa cells were incubated with the Fe@Au-M1/MC2(PEG750)-DOX, CTAB-stabilised GNRs, PEG-GNRs, and GNR-M1/MC2(PEG750)-DOX for 3 h (DOX concentration was fixed at 5 μM; the amounts of GNRs were identical). They were then imaged by Confocal laser scanning microscopy (excitation/emission: 488 nm/580-600 nm).

7.1.7 Transmission electron microscopy

5×10^5 HeLa cells per well were seeded in 6-well plates and incubated overnight at 37 °C. The cells were treated for 3 h at 37 °C with the Fe@Au-M1/MC2(PEG750)-DOX (containing 5 μM DOX) in media. After washing with PBS, the cells were detached and centrifuged and then the same procedures described in the Chapter 4 were followed, to fix the cells for TEM imaging.

7.1.8 MTT cell viability assay

10^4 HeLa cells per well were seeded in a 96-well plate and incubated overnight. The culture medium was then removed and 100 μL Fe@Au-M1/MC2(PEG750) or GNR-M1/MC2(PEG 750) nanocarrier with or without 5 μM DOX in media was added, followed by incubation at 37 °C for 18 h, and then the same MTT assay procedures as in Chapter 3.

7.2 Results and discussion

7.2.1 Characterisation of Fe@Au NPs

7.2.1.1 Method 1

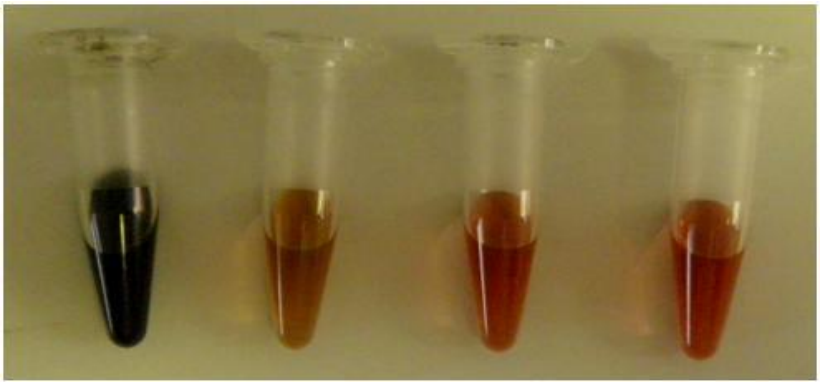

Figure 7.1. Photographs of prepared nanoparticles. From left to right: Fe3O4 NPs, Fe@Au NPs (45 mg MNP seeds), Fe@Au NPs (15 mg MNP seeds), 14-nm GNPs.

Citrate reduction is a simple method, reported in the literature[343-345], for preparing core-shell gold-coated magnetic nanoparticles (Fe@Au NPs), where

MNPs (Fe_3O_4 NPs) synthesized by co-precipitation are used as seeds, and gold reduced by citrate is supposed to grow on the surface of Fe_3O_4 NPs. Though it is argued that gold cannot grow on the surface of Fe_3O_4 NPs by the citrate reduction method due to the different surface energy[339], this was the first method tried in the project because of its simplicity.

The digital images of the prepared Fe_3O_4 NPs and Fe@Au NPs, together with GNPs solution (Figure 7.1) shows that, unlike black Fe_3O_4 NPs and red GNPs, the colour of Fe@Au NPs varied depending on the amount of Fe_3O_4 seeds added. The Fe@Au NPs prepared with more Fe_3O_4 seeds (45 mg) were brown in colour, while those with less Fe_3O_4 seeds (15 mg) were red, closer to the colour of GNPs. The proportion of Fe_3O_4 seeds in the reaction solution appeared to correlate with the colour of Fe@Au NPs.

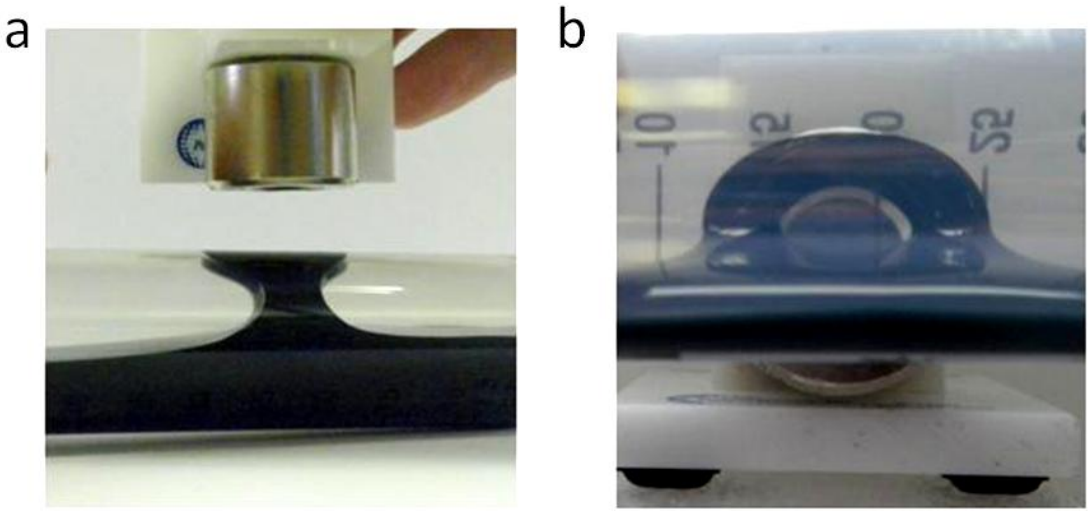

Figure 7.2. Photographs of Fe_3O_4 NPs under the attraction of a permanent magnet ('工' shape (**a**); 'O' shape (**b**)).

Fe_3O_4 NPs have a strong tendency to aggregate to minimize the high surface energy caused by the large surface-to-volume ratio of nanoparticles; this is unfavourable for further reaction and potential applications. By adding biocompatible tri-sodium citrate, which acts as an electrostatic stabilizer[346,

347] with one or two carboxylic groups coordinating with Fe_3O_4 NPs, a stable colloidal dispersion ('aqueous ferrofluid') can be formed. The surface bond citrates can offer sufficient electrostatic repulsion to prevent MNP aggregation even under an applied external magnetic field, where the Fe_3O_4 NPs still remain in the form of a dispersion and they can not be isolated from the medium by the magnet (Figure 7.2).

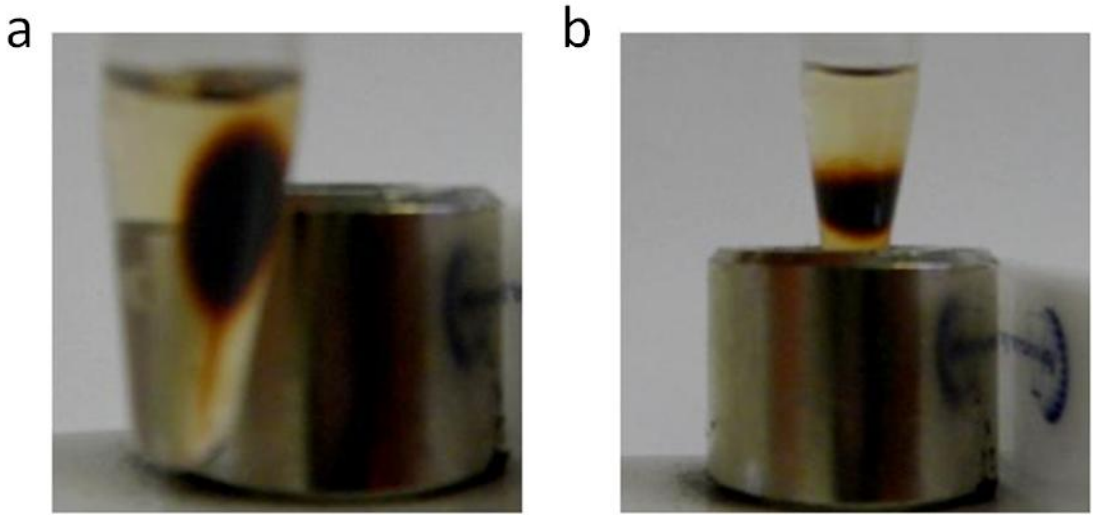

Figure 7.3. Photographs of Fe@Au NPs under the magnetic attraction (**a**) and repulsion (**b**).

One way to test whether Fe@Au NPs have been successfully synthesized through the simple citrate reduction method is to apply an external magnetic field to the Fe@Au NPs solution, as it is assumed that a permanent magnet can attract Fe@Au NPs, or separate Fe_3O_4 NPs from GNPs where gold growth on MNPs is unsuccessful. Because of the difficulty of attracting and separating Fe@Au NPs from the system, which was stabilised by tri-sodium citrate, the Fe@Au dispersion was first centrifuged to get the Fe@Au pellets to the bottom of the eppendorf tube before applying the permanent magnet.

Figure 7.3 shows that all Fe@Au pellets were attracted or repelled by the external magnet without any separation between Fe_3O_4 and gold, which seemed

to suggest that Fe_3O_4 NPs were successfully coated with gold. But afterwards we were surprised to notice that if the Fe_3O_4 NPs were simply mixed with 14-nm GNPs, after centrifugation all mixed pellets including both Fe_3O_4 NPs and GNPs were attracted or repelled by the magnet without separating. Because the same phenomenon was observed with both prepared Fe@Au pellets and the mixture of Fe_3O_4 NPs and GNPs, we could not conclude that the preparation had been successful.

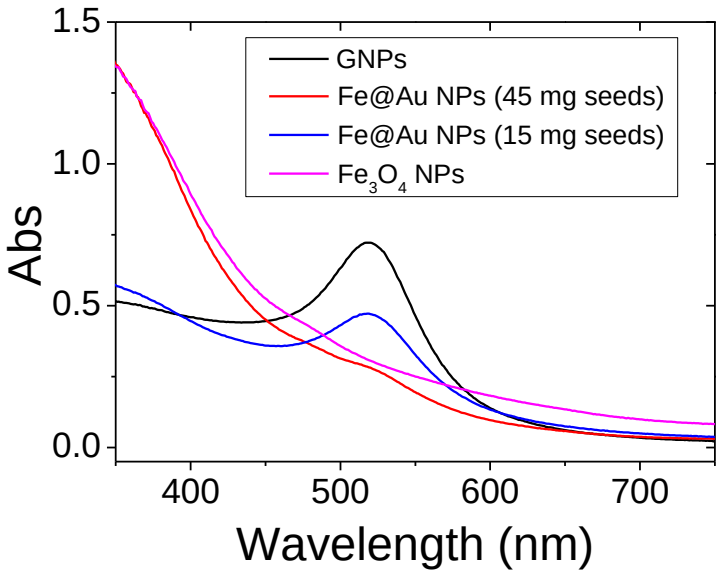

Figure 7.4. UV-visible absorption spectra of Fe_3O_4 NPs, Fe@Au NPs and GNPs, which were all dispersed in water.

To further evaluate the prepared Fe@Au NPs, the UV-visible spectra of Fe@Au NPs, Fe_3O_4 NPs and 14-nm GNPs were recorded (Figure 7.4). Regardless of the difference in quantity of Fe_3O_4 seeds, both Fe@Au NPs displayed the same Au absorption peak at around 520 nm as GNPs only. In addition, the mixture of Fe_3O_4 NPs and GNPs showed similar UV-visible spectra with Fe@Au NPs (Figure 7.5). Because no red-shift (one of the features of successfully-prepared Fe@Au NPs[342, 348, 349]) was observed in the spectrum of Fe@Au NPs, we suspect that the Fe_3O_4 NPs were not coated with gold. Also, after incubation of the Fe@Au NP solution with DNA M1 overnight, followed by subsequent

introduction of 0.1 M NaCl to the solution, we observed black aggregation at the tube bottom (aggregated MNPs) with red supernatant (M1-coated GNPs) above, suggesting that GNPs were formed by citrate reduction but existed independently without growing on the surface of Fe_3O_4 NPs.

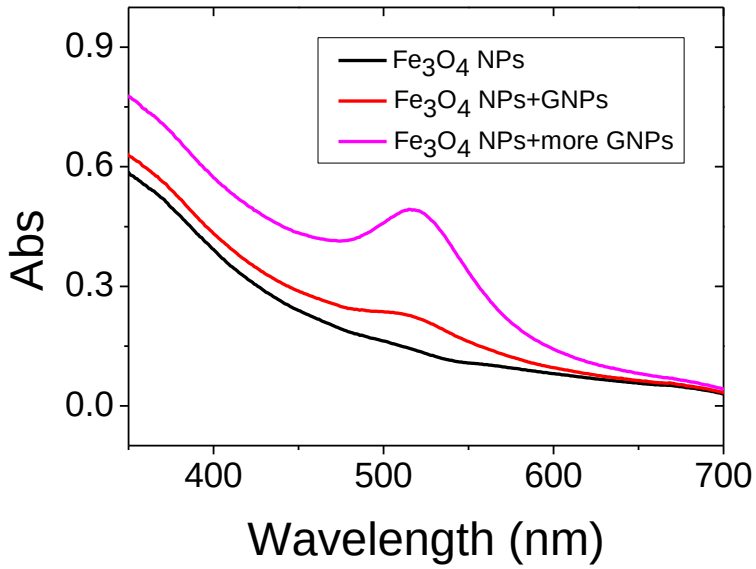

Figure 7.5. UV-visible absorption spectra of Fe_3O_4 NPs and mixtures of Fe_3O_4 NPs and GNPs. The mixture of Fe_3O_4 NPs and GNPs displayed the GNP absorption peak at 520 nm, the intensity of which became stronger with the addition of more GNPs.

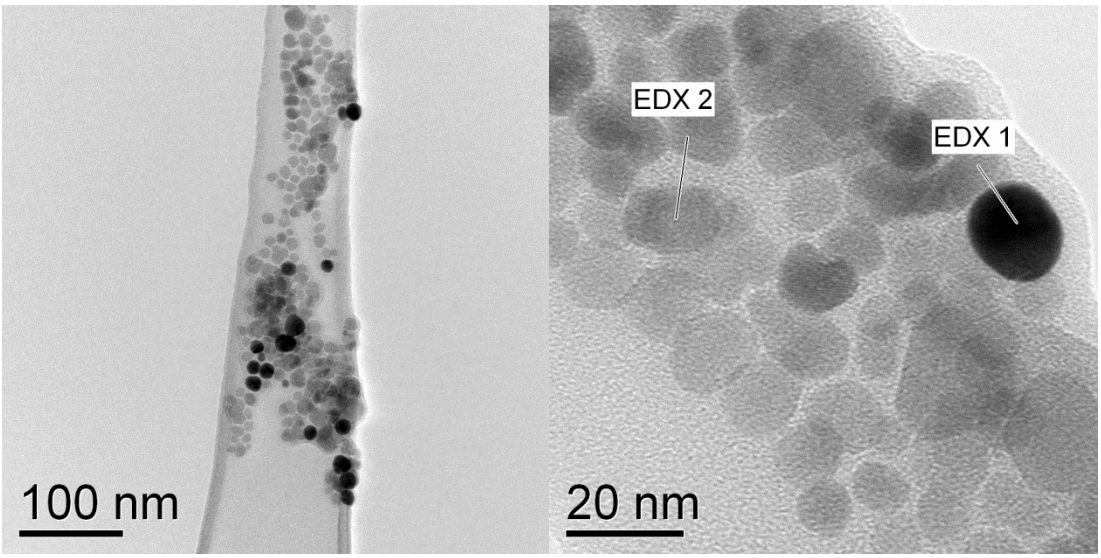

Figure 7.6. TEM images of Fe@Au NPs prepared by citrate reduction method showing two kinds of nanoparticles (black and grey) in the Fe@Au NPs solution. (left: scale bar 100 nm and right: scale bar 20 nm)

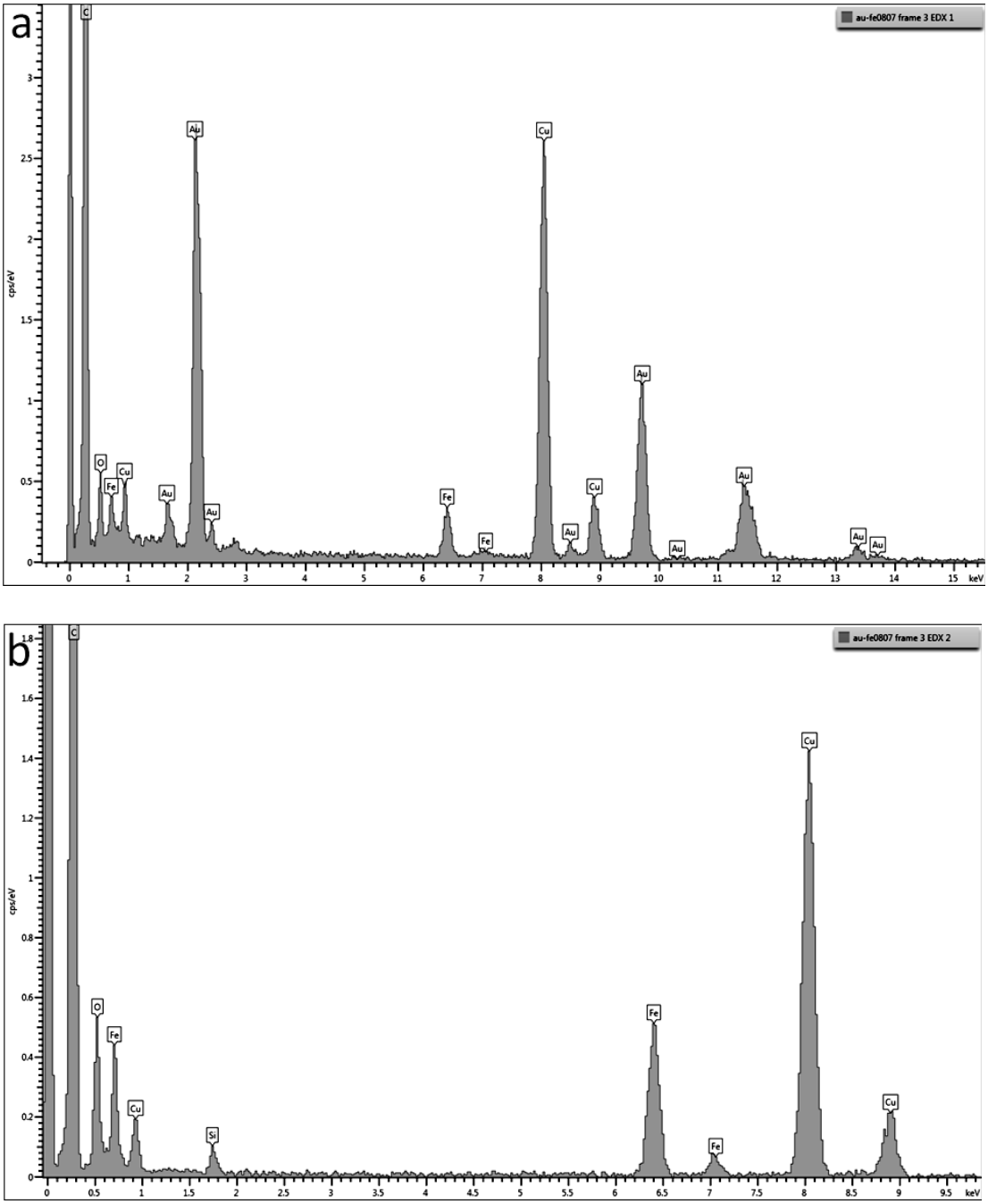

Figure 7.7. EDX spectra of black nanoparticles (EDX 1) (**a**) and grey nanoparticles (EDX 2) (**b**).

This view was confirmed by TEM images (Figure 7.6) and energy dispersion X-ray (EDX) spectra (Figure 7.7) of the prepared Fe@Au NPs. The TEM images show that two different nanoparticles, black and grey in colour, respectively,

appear to co-exist in the system with very similar sizes of around 15 nm. Their EDX spectra confirmed that the grey nanoparticles were Fe_3O_4 NPs with a peak at 6.4 keV corresponding to Fe, while the black ones were GNPs with peaks at 2.5 and 9.5 keV corresponding to Au. A small Fe signal was also observed, probably because the black GNPs were surrounded by the grey Fe_3O_4 NPs. Based on the TEM images and EDX results, we concluded that indeed gold was not grown on the surface of Fe_3O_4 NPs, and that the preparation of Fe@Au NPs by this citrate reduction method was unsuccessful. Both Fe_3O_4 NPs and GNPs existed independently in the solution, and the colour of the solution (Figure 7.1) was affected by the proportion of Fe_3O_4 NPs and GNPs.

7.2.1.2 Method 2

Because gold cannot grow stably on the surface of Fe_3O_4 NPs, due to the surface energy difference, a molecular linker, mercaptosuccinic acid (MSA) was employed in this project to bridge the 15-nm Fe_3O_4 NPs with much smaller gold clusters (*i.e.* 1.5 nm). MSA contains two carboxylic groups and a thiol group, which can attach or bind to Fe_3O_4 NPs and gold clusters to form Fe_3O_4-S-Au NPs[339]. Due to the great difference in nanoparticle sizes, a number of smaller gold clusters are expected to attach to one of the bigger Fe_3O_4 NPs. Following further reduction more gold atoms will grow on the gold clusters which act as the growth seeds, eventually forming a tight gold shell around the surface of the Fe_3O_4 NP. This is called “seed and grow method” in the literature[49]

15-nm Fe_3O_4 NPs synthesized by the co-precipitation method were stabilised by MSA with the thiol group stretching out to bind colloidal gold clusters (seeds) through the formation of an Au-S bond. According to the refs[339, 350], the size of gold seeds produced by the reduction of $HAuCl_4$ with THPC is 1.5-2 nm, and

the size ratio of Fe_3O_4 NPs to gold clusters is expected to be 7-10.

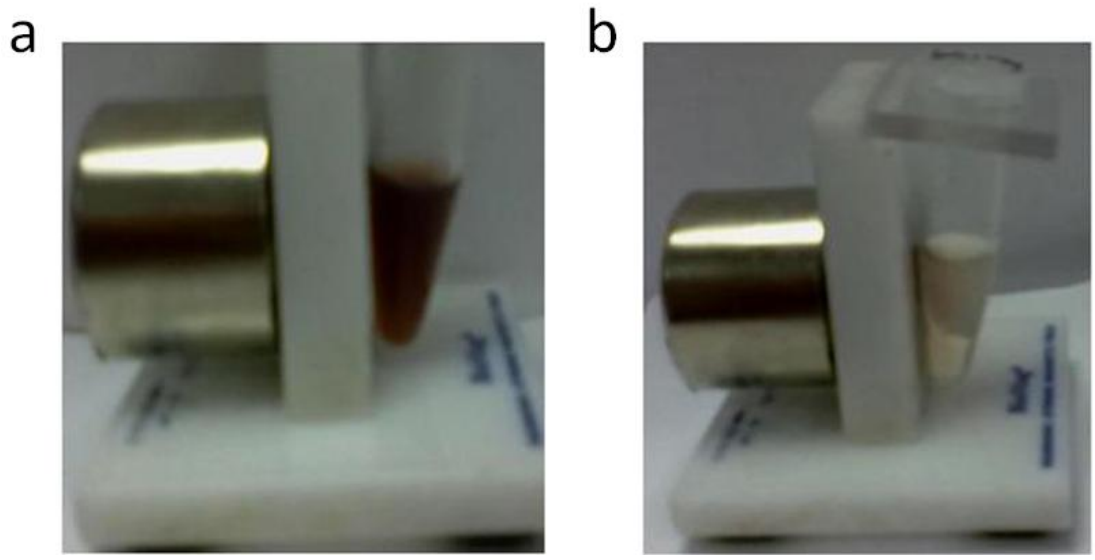

Figure 7.8. Photographs of prepared Fe_3O_4-s-Au NPs under magnetic attraction for 0 min (**a**) and 5 min (**b**).

Figure 7.8 shows the prepared Fe_3O_4-S-Au NPs by the 'seed and grow' method were attracted to the side wall within 5 min by a permanent magnet. Unlike the nanoparticles prepared by the unsuccessful citrate reduction method above, which were hardly attracted or repelled by the permanent magnet before centrifugation, the Fe_3O_4-S-Au NPs were easily collected under an external magnetic field without centrifugation.

After washing with water, the Fe_3O_4-S-Au NPs were re-dispersed in water and their UV-visible spectra, together with those of the gold seeds and MSA-stabilised Fe_3O_4 NPs (washed and re-dispersed in water), were recorded, and are depicted in Figure 7.9. Compared to the gold seeds, no clear red-shift of the gold NP plasmon absorption peak (an indication of forming larger NPs) was seen for the Fe_3O_4-S-Au NPs before the further reduction.

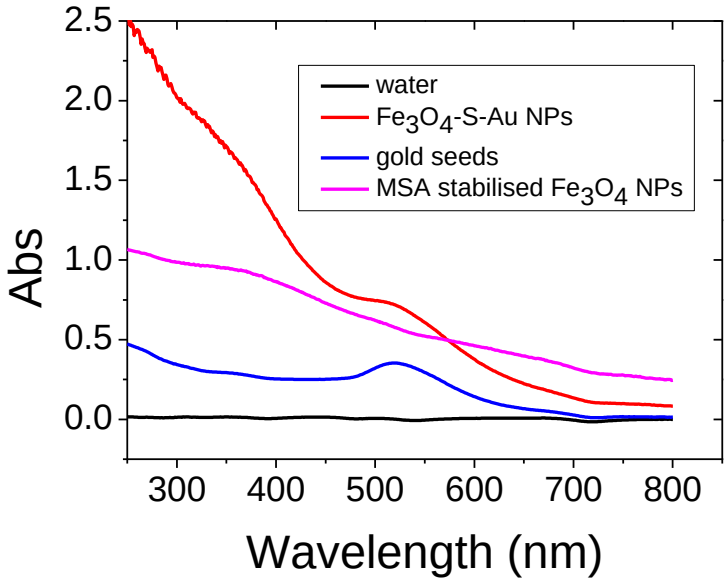

Figure 7.9. UV-visible spectra of MSA-stabilised Fe_3O_4 NPs, gold seeds and Fe_3O_4-S-Au.

Before growing additional gold on the surface, the Fe_3O_4-S-Au NPs were first dispersed in 0.1 M tri-sodium citrate for stabilisation and then re-dispersed in water. Figure 7.10 shows that the gold absorption peak was red shifted when the Fe_3O_4-S-Au NPs were dispersed in the tri-sodium citrate solution; this could interfere with the evaluation of gold growth by UV-visible spectrometry. However, this red shift disappeared after the Fe_3O_4-S-Au NPs were re-dispersed in water.

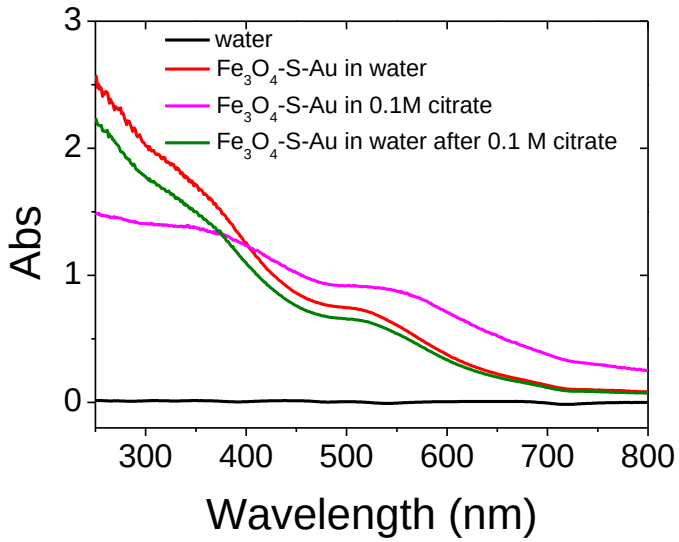

Figure 7.10. UV-visible spectra of Fe3O4-S-Au NPs re-dispersed in water and 0.1 M tri-citrate sodium.

Hydroxylamine was chosen as a reducing agent to promote further gold growth. Before being used on Fe_3O_4-S-Au NPs, gold growth was first tested on the 1.5-nm gold seeds. After the addition of hydroxylamine and $HAuCl_4$ to the gold seeds solution, the gold plasmon absorption peak displayed an obvious red shift compared to gold seeds only (Figure 7.11), indicating that the gold seeds did become bigger. Therefore the use of hydroxylamine based reduction is a feasible method for promoting gold nanoparticle growth.

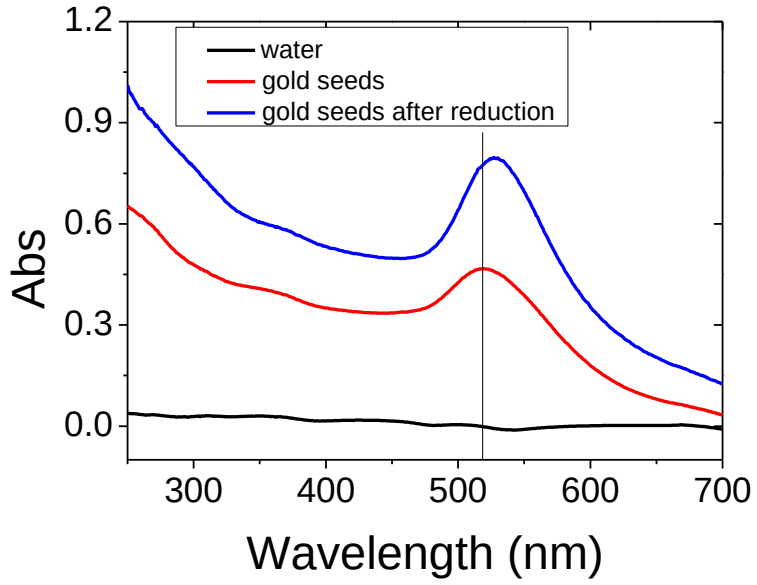

Figure 7.11. UV-visible spectra of gold seeds before and after the reduction of $HAuCl_4$ with hydroxylamine.

Gold growth on the surface of Fe_3O_4-S-Au NPs, expected to form a tight gold shell, was then performed through an iterative reduction. The UV-visible spectrum of each iteration was recorded in Figure 7.12, which shows that the gold NP plasmon absorption peak exhibits a red shift after each reduction step, and that the absorbance value became higher and higher during the first three iterations, indicating that additional gold was grown on the Fe_3O_4-S-Au NPs. Whereas after the fourth iteration, the solution became darker and a further red shift of the gold NP plasmon absorption peak was observed, but with decreased

absorbance, suggesting that gold NPs had aggregated during the fourth reduction. To avoid aggregation during reduction, three iterations would be appropriate for gold growth on Fe_3O_4-S-Au NPs.

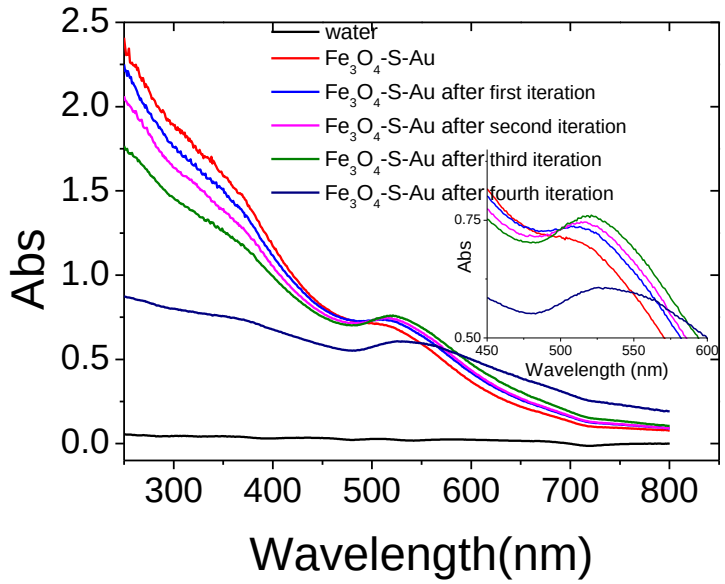

Figure 7.12. UV-visible spectra of the Fe_3O_4-S-Au NPs after each iterative reduction and gold NP growth.

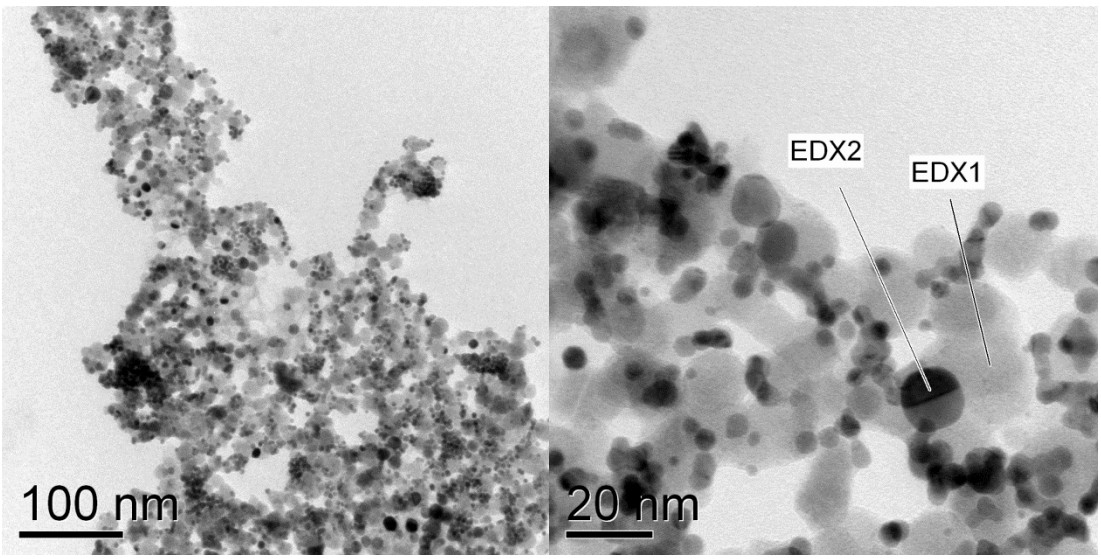

Figure 7.13. TEM images of Fe_3O_4-S-Au before reduction showing two different kinds nanoparticles (black and grey) observed. (left: scale bar 100 nm and right: scale bar 20 nm)

To further characterise the Fe_3O_4-S-Au NPs before and after reduction by TEM

imaging, a 0.22-μm syringe filter was used to remove big particles. Surprisingly, none of the Fe_3O_4-S-Au NPs could pass through the filter even before iterative reduction. To find out the cause of this phenomenon, TEM images of Fe_3O_4-S-Au NPs before reduction (Figure 7.13) and after the first reduction (Figure 7.16) were taken without filtration. Two different kinds of nanoparticles were observed: grey ones with an average size of 13-15 nm and black ones with an average size of 4-5 nm. By EDX measurement it was confirmed that the grey nanoparticles were Fe_3O_4 NPs and the black ones were GNPs (Figure 7.14). Although the same literature procedure [339, 350] was adopted to synthesize the gold seeds, the average size (4-5 nm) here was 2-3 times larger than that reported(1.5-2 nm). According to the TEM images, the size of single particles should not affect the ability of nanoparticles to pass through the filter. The problem could come from the cross-linking of Fe_3O_4-S-Au clusters by MSA linker molecules (see Figure 7.15), where each gold seed bound with multiple linkers can bind to multiple Fe_3O_4 NPs, leading to the assembly of a three-dimensional Fe_3O_4-S-Au 'network' with a 'whole' size greater than 0.22 μm pore size, and hence unable to pass through the filter.

From Figure 7.13, it can also be seen that each Fe_3O_4 NP was not completely covered by gold seeds, which had been the premise of the following reduction step for forming a gold shell. It is believed that the mixing molar ratio of Fe_3O_4 NPs to gold seeds may affect coverage. Here too many Fe_3O_4 NPs were mixed with too few gold seeds to form Fe_3O_4-S-Au NPs, leading to low coverage (on average only 3-4 gold seeds were attached to each Fe_3O_4 NP). The molar ratio of Fe_3O_4 NPs to gold seeds needs to be further optimised in order to improve coverage. In addition, the size ratio of Fe_3O_4 NPs to gold seeds may also affect the formation of the gold shell. The typical size ratios reported in the refs were at least 10:1, while some were even up to 100:1[318, 339, 350, 351]. The gold

seeds prepared here were much bigger than those in the literatures and the actual size ratio was only around 3/4:1, not big enough to integrate a complete layer of gold seeds onto the Fe_3O_4 NP surface.

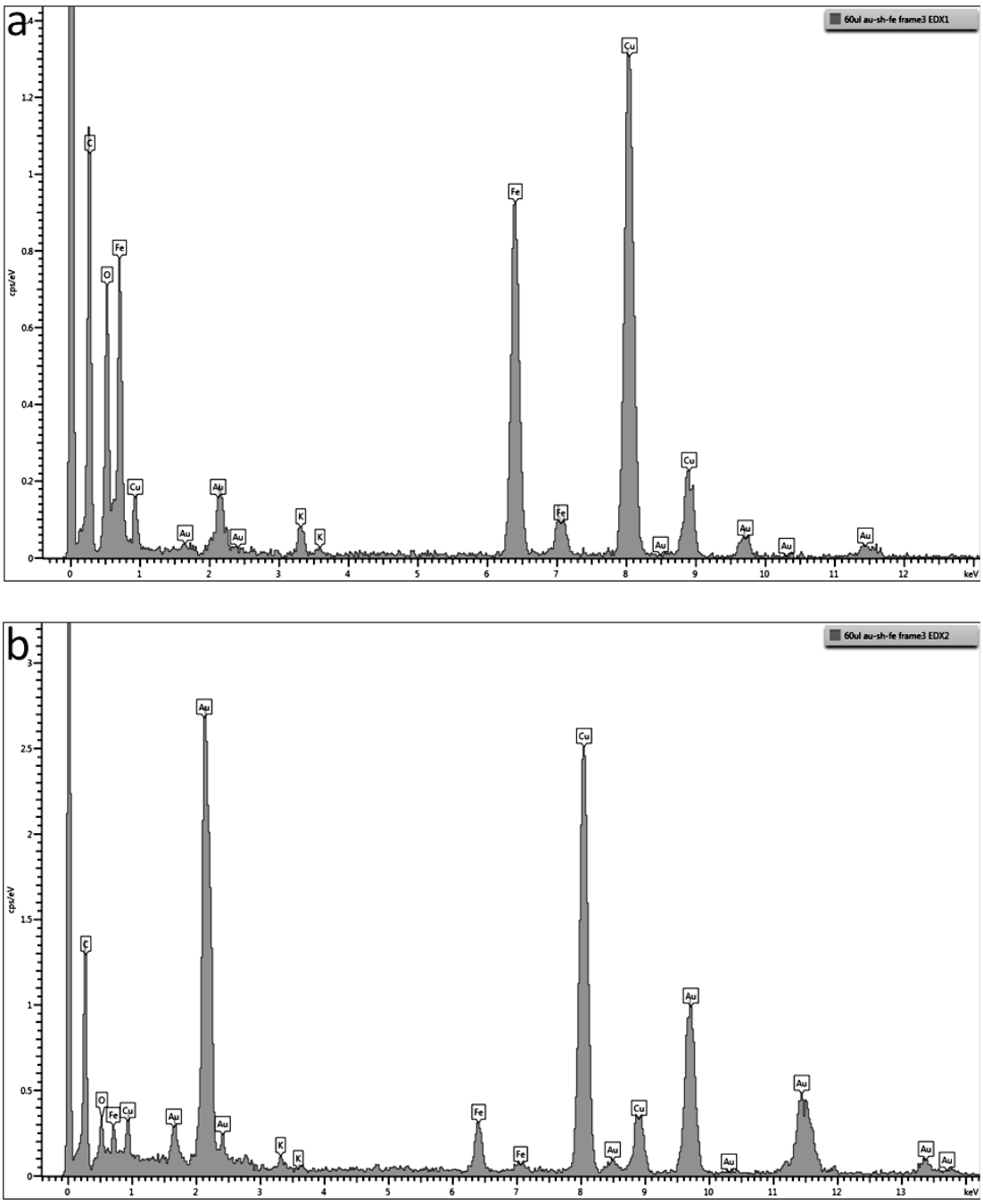

Figure 7.14. EDX spectra of grey nanoparticles (EDX 1) (**a**) and black nanoparticles (EDX 2) (**b**).

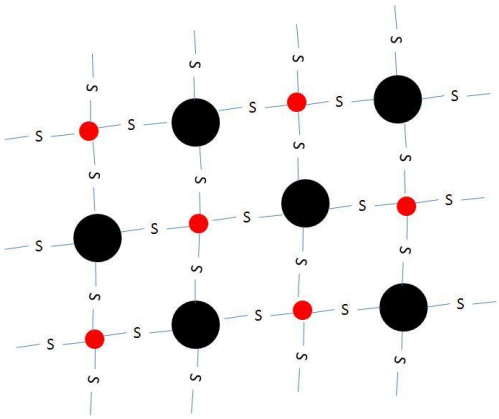

Figure 7.15. Schematic of the Fe_3O_4-S-Au 'network' caused by cross-linking.

The TEM image of Fe_3O_4-S-Au NPs after the first reduction (Figure 7.16) shows that the size of gold seeds became bigger than the original Fe_3O_4-S-Au NPs (Figure 7.13), indicating that the gold reduction reaction had taken place, and that more gold had grown on the gold seeds. Unfortunately, the gold shells were not formed successfully, probably due to an inappropriate mixing molar ratio and the size ratio of Fe_3O_4 NPs to gold seeds mentioned above. These were not further optimised because a cross-linking issue may still exist between Fe_3O_4 NPs and gold seeds, and single isolated Fe_3O_4-S-Au NPs might not be obtained by this method even if gold shells were successfully formed on the surface of Fe_3O_4 NPs.

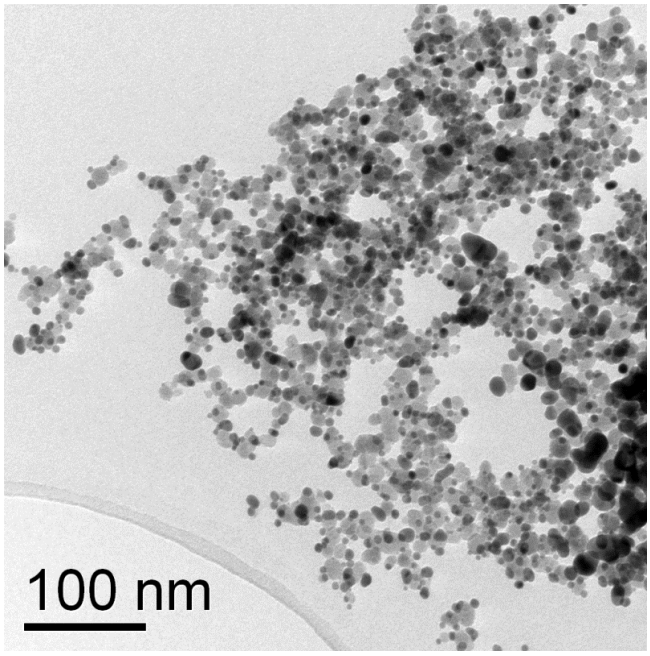

Figure 7.16. TEM images of Fe_3O_4-S-Au after the first iteration.

7.2.1.3 Method 3: Micelle Method

A reverse micelle method adapted from the literatures[352-355] was also performed using CTAB as the surfactant, 1-butanol as the co-surfactant and octane as the oil phase. Iron nanoparticles were prepared as 'cores' through the reduction of ferrous sulphate by sodium borohydride within the micelles, and within minutes the solution became dark, indicating the formation of the iron cores. The size of the cores was determined by the size of the micelles, which can be varied by adjusting the molar ratio of water to surfactant. Here, the ratio of 8:1 (water : surfactant) was chosen for micelle formation. By the sequential addition of $HAuCl_4$ and sodium borohydride, gold shells were formed on the iron cores, the thickness of which was determined by the amount of $HAuCl_4$.

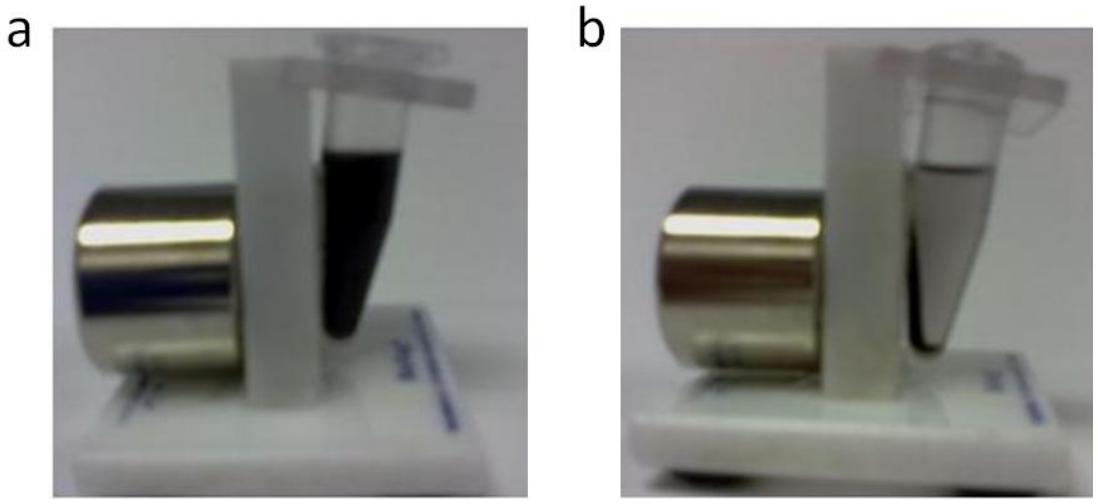

Figure 7.17. Photographs of prepared Fe@Au NPs under magnetic attraction for 0 min (**a**) and 5 min (**b**).

Fe@Au NPs prepared by the reverse micelle method are shown in Figure 7.17. These were black in colour and attracted by a permanent magnet within 5 mins. Vibrating sample magnetometry (VSM) measurement of the Fe@Au NPs at 290 K (Figure 7.18) showed that no coercivity (Hc) or remanence (M_r) was observed in the magnetisation curve, and it appeared that magnetisation did not reach

saturation even in a high magnetising field (9 T), which agrees with the result in the literature[352].

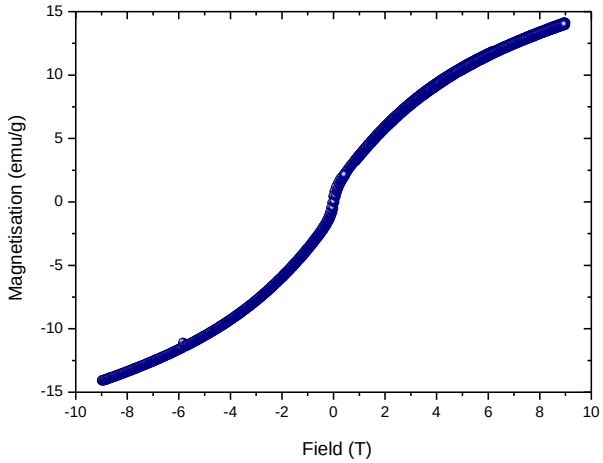

Figure 7.18. Vibrating sample magnetometry (VSM) measurement of the Fe@Au NPs at 298 K.

To attach thiolated DNAs (*i.e.* M1) to Fe@Au NPs, phase transfer was first performed to disperse the Fe@Au NPs in water. Here, a new phase transfer method was established. Surfactants were removed by washing with a mixed solvent of chloroform and methanol (v/v = 1:1), followed by rinses with a methanol/water mixture (v/v = 1:1), after which a rinse of 50 mM tri-sodium citrate solution seemed to be the critical step to successful phase transfer. Most literatures only used mixtures of either chloroform/methanol[356] or methanol/water for phase transfer[357], where the Fe@Au NPs eventually aggregated. Whereas by adapting sequential washings with both mixtures, and then treating with tri-sodium citrate under sonication, the Fe@Au NPs were successfully and stably re-dispersed in the aqueous phase.

The TEM image of the Fe@Au NPs (Figure 7.19) reveals that the nanoparticles are small and uniform with average sizes of ～6 nm, and the EDX result (Figure 7.20) displays peaks at 2.2 and 6.4 keV, corresponding to Au and Fe, respectively. This result agrees with the ref[358], suggesting that the Fe@Au

NPs were successfully prepared by the reverse micelle method. As mentioned earlier, the size of Fe@Au NPs and the shell thickness can be further optimised in the future if needed, by varying the molar ratio of water to surfactant and the amount of $HAuCl_4$.

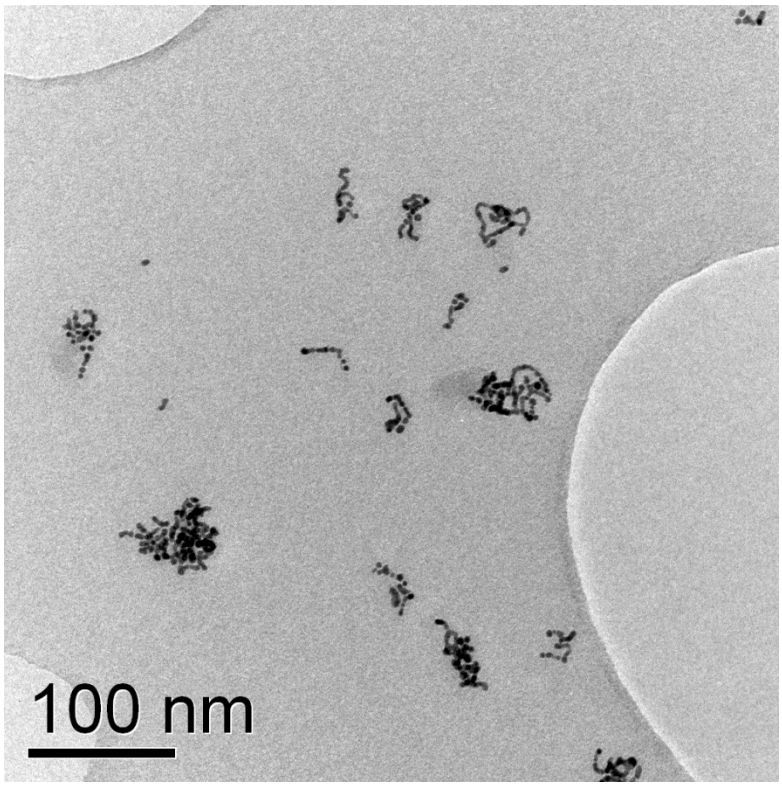

Figure 7.19. TEM image of Fe@Au NPs prepared by the reverse micelle method.

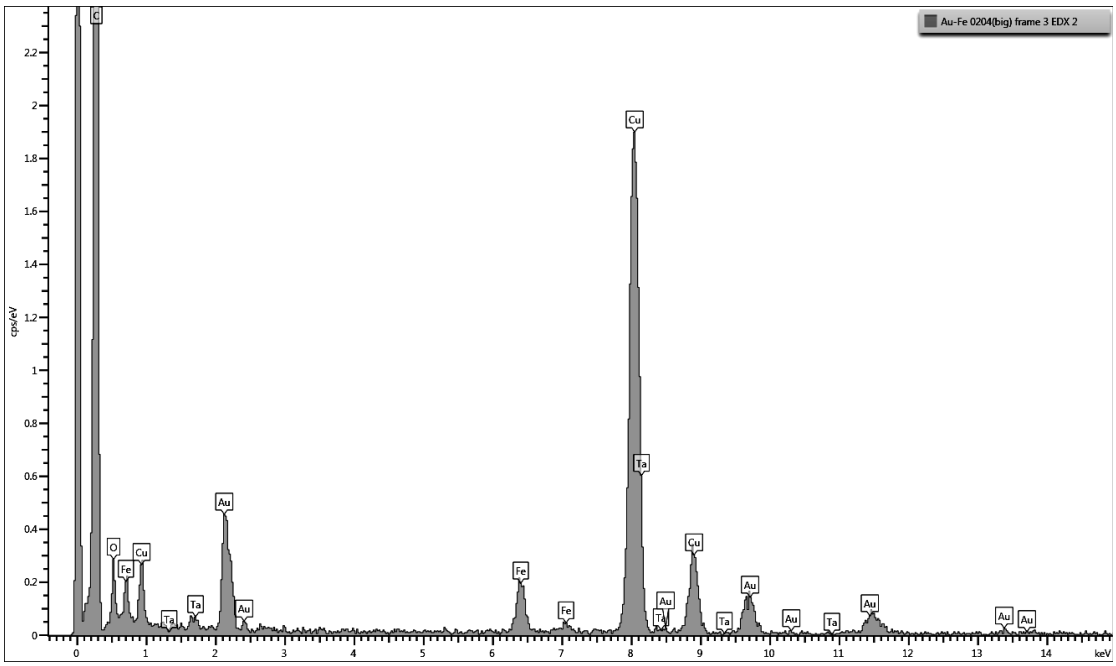

Figure 7.20. The EDX spectrum of a Fe@Au NP.

7.2.2 Cellular studies using Fe@Au-M1/MC2(PEG750)-DOX

The multifunctional NDDS, Fe@Au-M1/MC2(PEG750)-DOX, was prepared by attaching thiolated M1 to the gold shell of Fe@Au through Au-S bond, followed by the sequential additions of MC2(PEG750) for hybridisation and DOX for intercalation (M1/MC2(PEG750)/DOX = 1/1/3). The confocal image (Figure 7.21) reveals that after 3 h incubation with HeLa cells, strong DOX fluorescence was observed inside the cells, indicating that the Fe@Au-M1/MC2(PEG750) nanocarrier had successfully delivered DOX into them. It can be further confirmed by the TEM image of HeLa cells treated with Fe@Au-M1/MC2(PEG750)-DOX (Figure 7.22), in which Fe@Au-based nanocarriers were found inside endosome/lysosome-like compartments of the cells, confirming that Fe@Au-M1/MC2 (PEG750) nanocarriers can efficiently deliver DOX into cells *via* the endocytic pathway like the GNP-M1/MC2 (PEG750) nanocarriers, where the low pH inside endosomes/lysosomes can trigger DOX release from the system, leading to strong DOX fluorescence inside the cells.

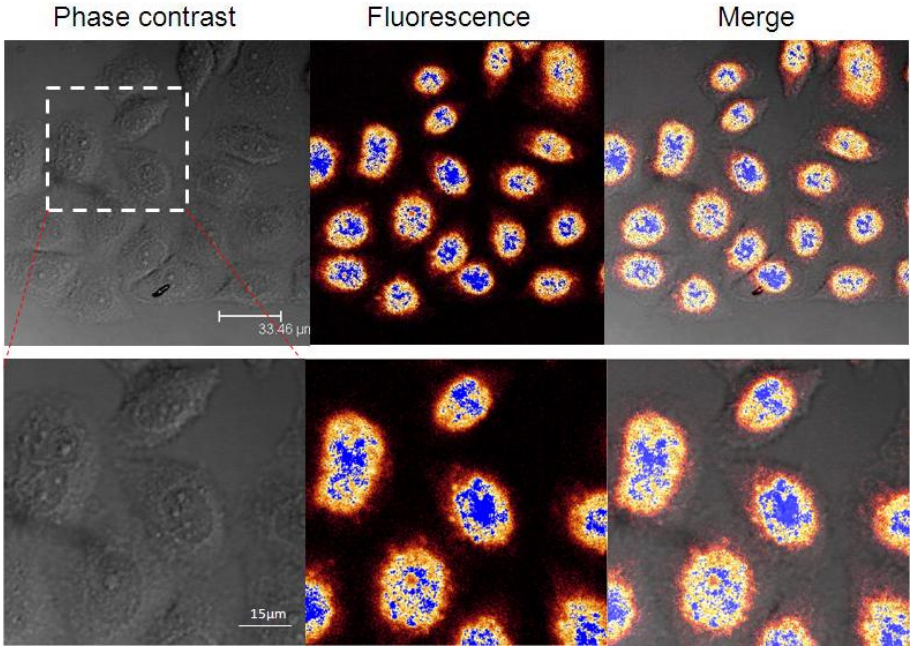

Figure 7.21. Confocal phase contrast, fluorescence and merged optical/fluorescence images of HeLa cells after incubation with Fe@Au-M1/MC2 (PEG750)-DOX for 3 h at 37 °C.

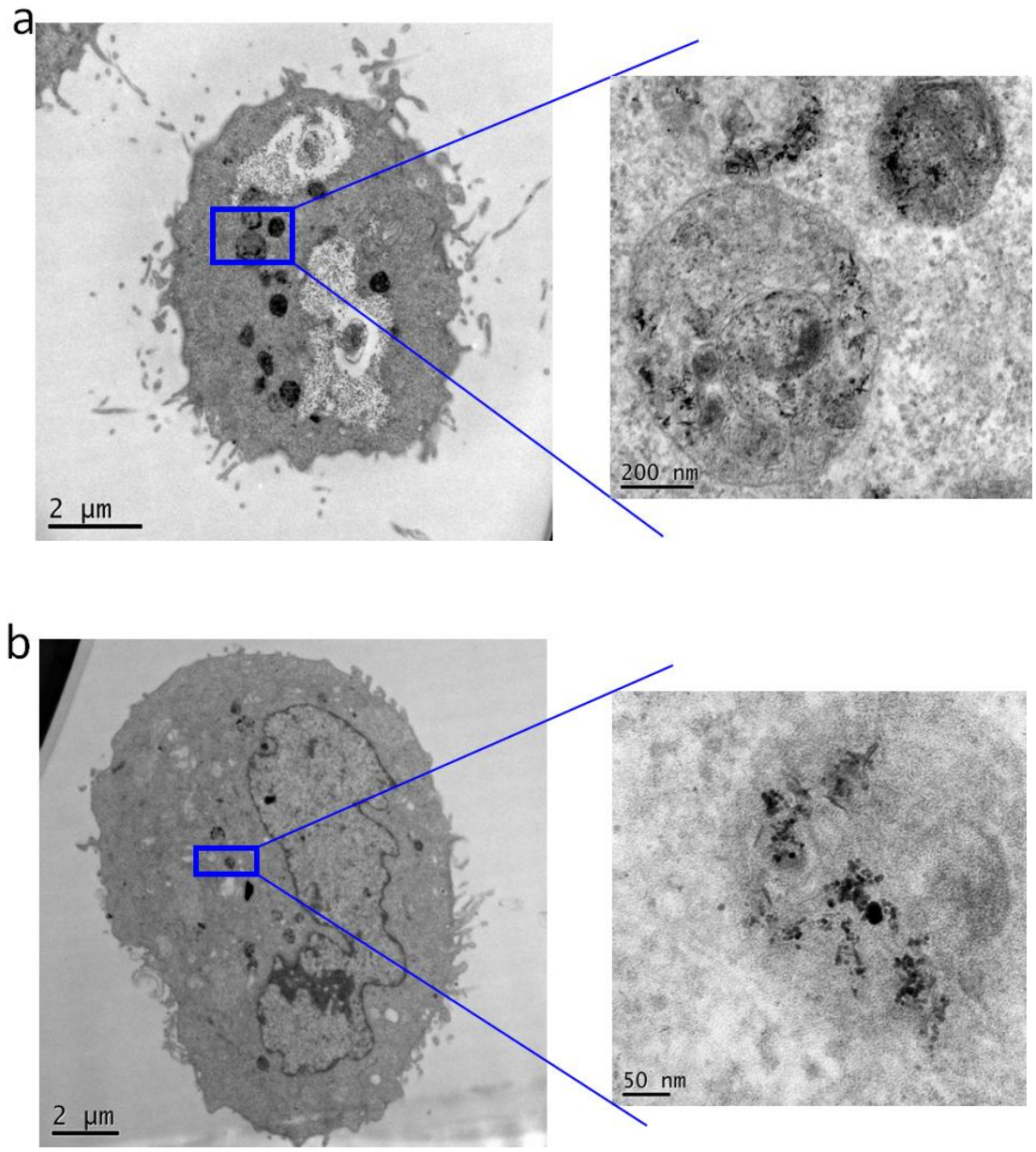

Figure 7.22. TEM images showing uptake of GNP-M1/MC2(PEG750)-DOX by HeLa cells (3 h incubation at 37 °C) ((**a**) Cell One and (**b**) Cell Two).

An MTT assay was performed to evaluate the cytoxicity of Fe@Au-M1/MC2 (PEG750) nanocarriers and the Fe@Au-M1/MC2(PEG750)-DOX NDDS (Figure 7.23). Compared with the control (HeLa cells only), the Fe@Au-based nanocarrers were non-toxic, as expected, whereas the NDDS loaded with DOX showed cytoxicity comparable to that of the free DOX shown in Chapter 3 (Figure 3.12). These results show great potential for the multifunctional

Fe@Au-M1/MC2(PEG750)-DOX NDDS in DOX delivery.

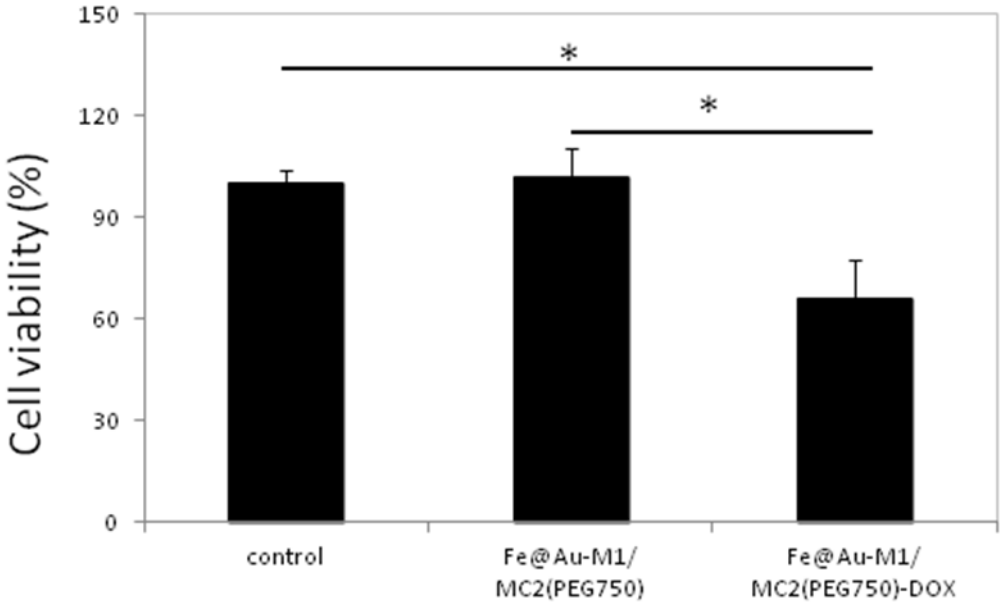

Figure 7.23. MTT assay of HeLa cell viabilities after incubation with Fe@Au-M1/MC2(PEG750) and Fe@Au-M1/MC2(PEG750)-DOX (containing 5 μM DOX) for 18 h at 37 °C (*$p < 0.05$).

7.2.3 Characterisation of GNRs

Gold nanorods (GNRs) (Figure 7.24) were synthesized by a seed-mediated growth method[359, 360] in the presence of CTAB and silver nitrate, where CTAB acts as a capping agent (stabiliser) and the concentration of silver nitrate determines the aspect ratio of GNPs[90, 109, 360]. Figure 7.25 shows the visible-NIR spectra of the gold growth solution just after adding gold seeds. Beside the absorption peak at ～510 nm (cross-sectional plasmon absorption), another peak in the region of 700-900 nm was also observed, corresponding to the longitudinal plasmon absorption, and indicating GNRs formation. The intensity of both peaks increased for up to 40 min, but showed no further increase afterwards, suggesting that the GNR formation was complete in 40 min. We also found a blue-shift of the longitudinal plasmon peak during the GNR developing period, similar to that described in the literature[361]. This was

thought to correlate with the change of aspect ratio during the GNR growth process.

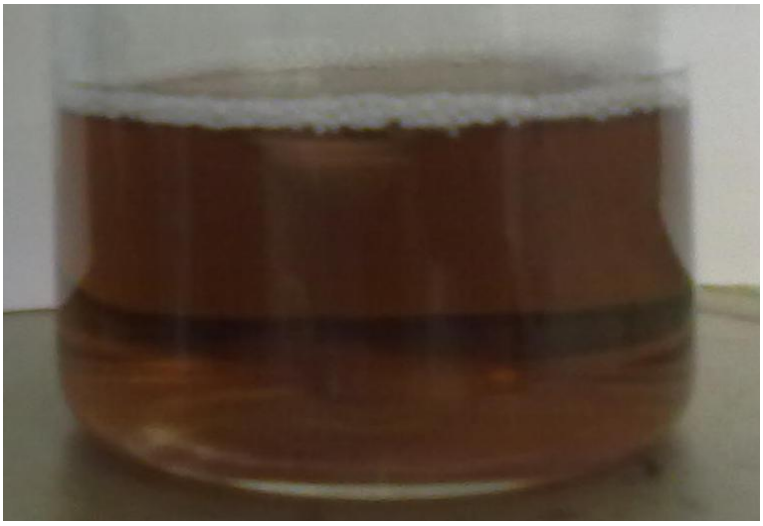

Figure 7.24. Photo image representing GNRs prepared by the seed-mediated growth method and stabilised by CTAB.

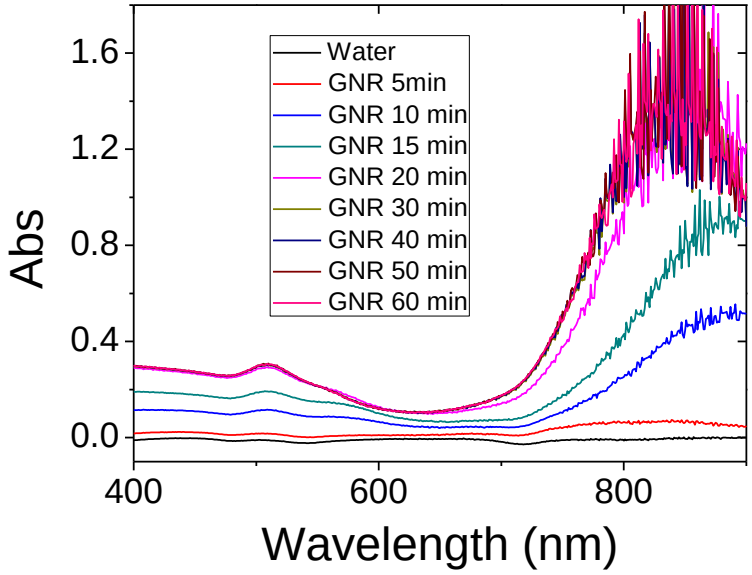

Figure 7.25. Visible-NIR spectra of GNRs solution growing from gold seeds as a function of time just after seed addition.

After preparation, excess CTAB was removed through centrifugation and the GNR pellets were then re-dispersed in water (Figure 7.26). Its visible-NIR spectrum (Figure 7.27) is almost the same as that of GNRs in CTAB solution in

terms of absorption peak positions and absorption intensity, while the clear supernatant (CTAB solution) showed no absorption in the range of 400-900 nm, confirming that CTAB did not contribute to the absorption spectra of GNRs, and both absorption peaks were related to GNRs only.

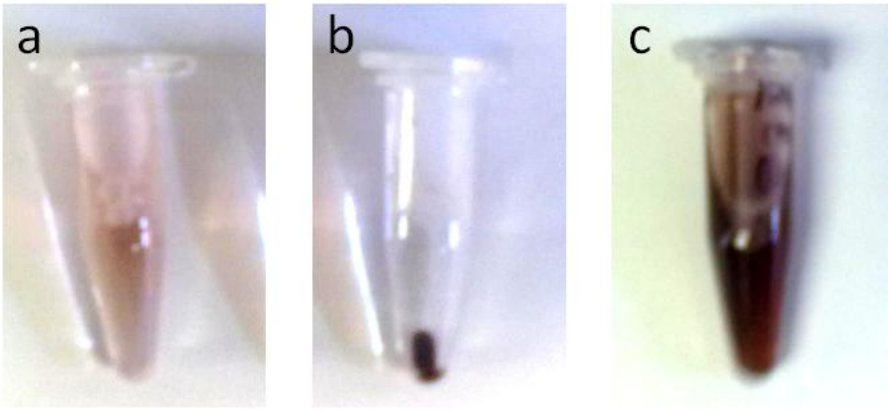

Figure 7.26. Photographs of GNRs solution before (**a**) and after centrifuging (**b**) and GNRs concentrated and redispersed in water (**c**).

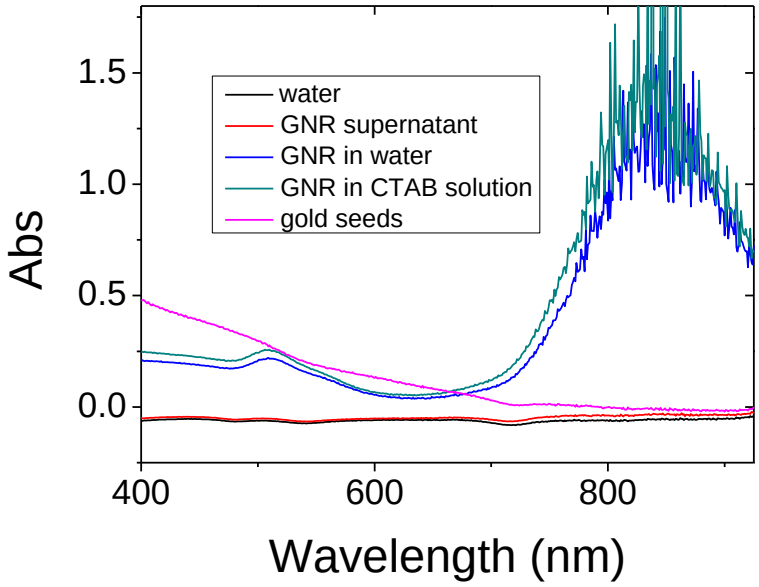

Figure 7.27. Visible-NIR spectra of the seed solution and GNRs in CTAB solution and water.

The TEM image of GNRs is shown in Figure 7.28. Based on particle analysis *via* Digital micrograph software, the length of GNRs were 39±7 nm and the aspect ratio of GNRs were calculated at 3.67±0.54 (n=45), which is similar to that in the

literature[90].

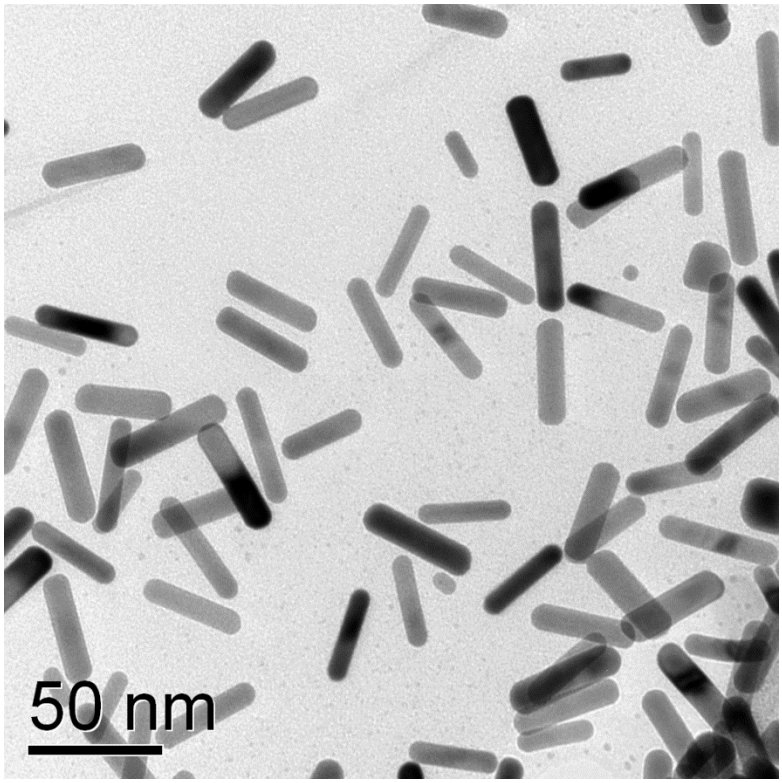

Figure 7.28. TEM image representing prepared GNRs.

7.2.4 Cellular studies using the GNRs based NDDS

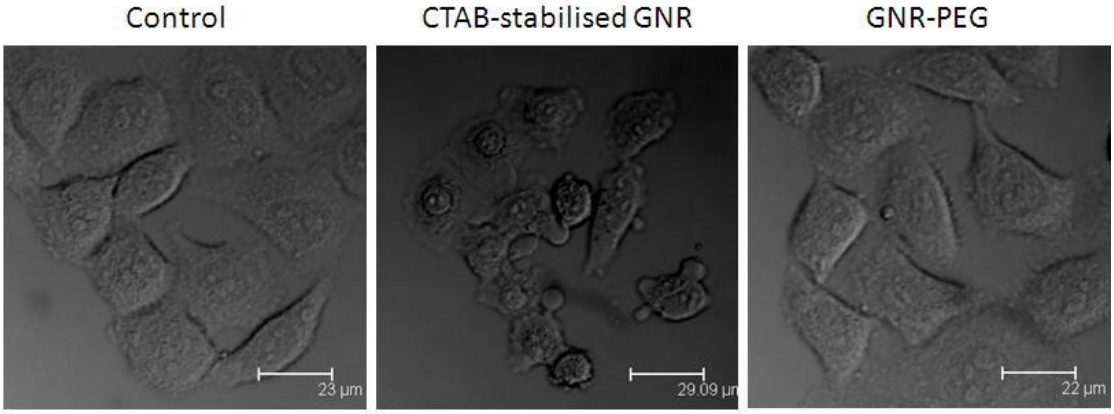

Figure 7.29. Phase contrast images of HeLa cells after incubation with CTAB-stabilised GNR and GNR-PEG for 3 h at 37 °C.

The CTAB (a cationic surfactant) surface cap was found to be highly cytotoxic (Figure 7.29), therefore PEG-SH was employed to coat the GNRs *via* the formation of strong Au-S bonds that successfully displace the CTAB. The displaced CTAB was readily removed by centrifugation. Figure 7.29 reveals that the GNR-PEG conjugate was non-toxic to HeLa cells, suggesting that all CTAB was successfully removed and that PEG-SH stabilised GNRs were not cytotoxic.

Then DNA M1 was attached to GNR-PEG through ligand exchange to form the GNR-M1 conjugate. Following the same preparation procedure as Fe@Au-M1/MC2 (PEG750)-DOX, including MC2 (PEG750) hybridisation and DOX loading, the GNR-M1/MC2 (PEG750)-DOX NDDS was prepared. After incubation with HeLa cells it proved that, like GNP-based and Fe@Au-based NDDSs, the GNR-M1/MC2 (PEG750)-DOX had succeeded in delivering DOX into cells (Figure 7.30). In addition, MTT assay results (Figure 7.31) revealed that the GNR-M1/MC2 (PEG750) nanocarriers were not toxic to cells, indicating that GNR-based nanocarriers are suitable for cell-based drug delivery. With DOX loaded, the NDDS exhibited similar cytotoxicity to GNP-based and Fe@Au-based systems. This is to be expected because during the 18-h incubation with HeLa cells, it is the released DOX from the nanosytems that exerts the cytotoxicity, and the process is mainly dependent on the structure change (*i*-motif formation) of the DNA nanomachine, triggered by the low pH of endosomes/lysosomes. Therefore the differences in size and shape of nanoparticles have little influence on this process.

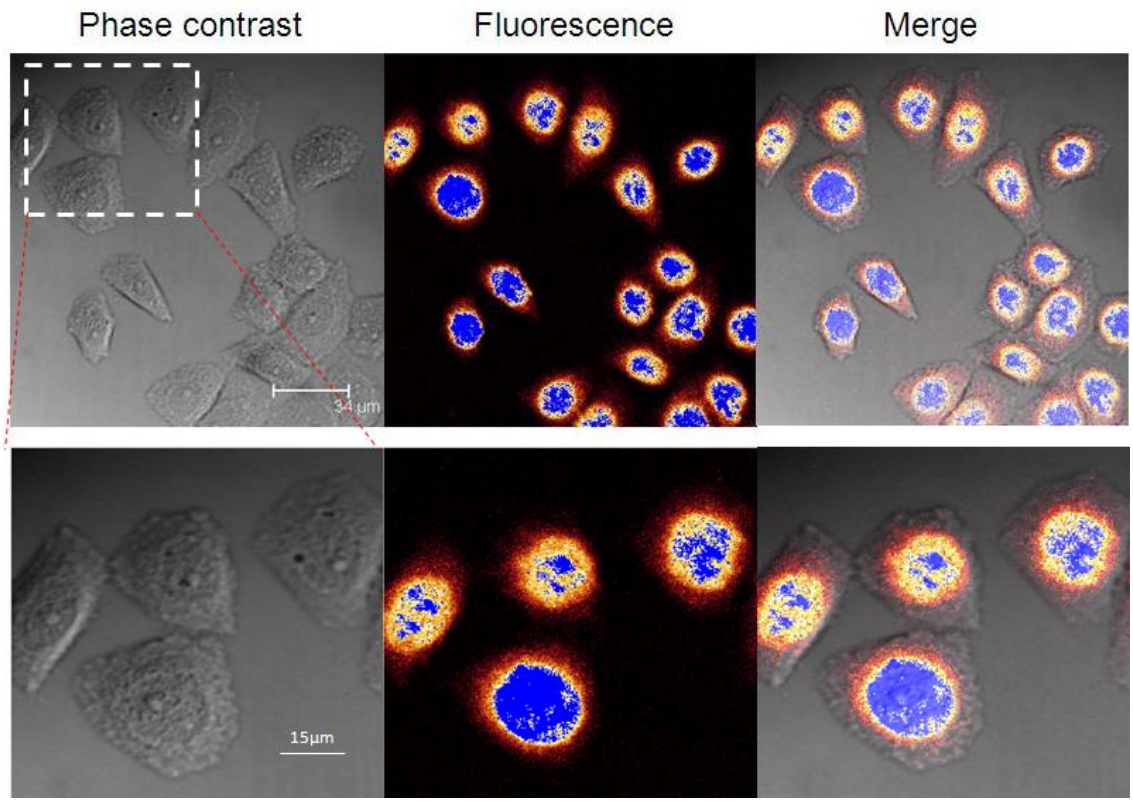

Figure 7.30. Confocal phase contrast, fluorescence and merged optical/fluorescence images of HeLa cells after incubation with GNR-M1/MC2 (PEG750)-DOX for 3 h.

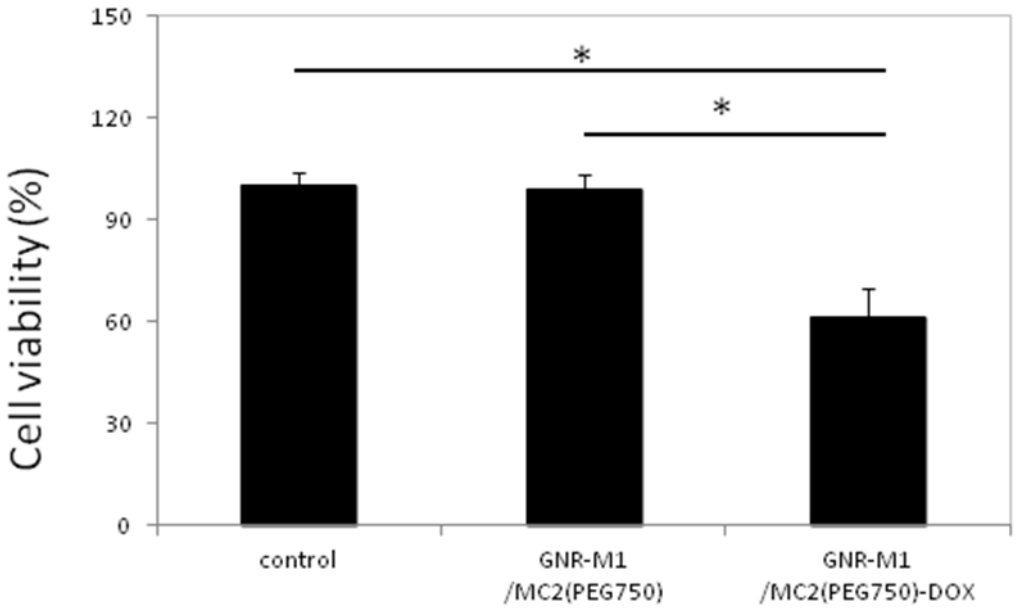

Figure 7.31. MTT assay of HeLa cell viabilities after incubation with GNR-M1/MC2(PEG750) and GNR-M1/MC2(PEG750)-DOX (containing 5 μM DOX) for 18 h at 37 °C (*$p < 0.05$).

7.3 Conclusion

Three different methods have been tried to synthesize the Fe@Au NPs. Results show that gold cannot grow stably on the surface of Fe_3O_4 NPs due to different surface energy (Method 1), and the use of bi-functional linkers (*e.g*. MSA) can cause cross-linking among gold clusters and Fe_3O_4 NPs (Method 2). The reverse micelle method (Method 3) appears to be suitable for the preparation of small, uniform Fe@Au NPs (*e.g.* ~6 nm). After phase transfer, the Fe@Au NPs can be dispersed stably in water after treatment with tri-sodium citrate, which has been successfully used to prepare Fe@Au-based drug nanocarriers.

CTAB-stabilised GNRs have been successfully synthesized *via* a seed-mediated growth method with the aspect ratio of ~3.7. In addition, PEG-SH has been successfully used to displace the cytotoxic CTAB surfactant *via* the formation of strong Au-S bonds, leading to non-toxic GNR-PEG; this has further been successfully used to develop a GNR-pH responsive DNA drug nanocarrier.

Cell based studies revealed that both the Fe@Au-M1/MC2(PEG750) and GNR-M1/MC2(PEG750) nanocarriers were non-cytotoxic and can efficiently deliver DOX into HeLa cells, with comparable cytotoxicity to free DOX. These NDDSs have the potential to achieve simultaneous passive-targeting, DOX delivery, tumour diagnosis and hyperthermia therapy in the future.

8 Chapter 8: Preparation of active targeted NDDSs

By exploiting the EPR effect, the unique characteristic of tumour vasculature, passive targeted NDDSs have exhibited higher efficiency and fewer side effects. This is due to the selective accumulation of such NDDSs in tumour tissues[10, 19, 204]. In fact, this is the strategy employed for most nanomedicines in trials and clinical use. While active targeted NDDSs can be obtained by attaching targeting ligands (Figure 8.1), such as antibodies[362, 363], aptamers[364-366] and other small molecules including vitamins[367-370] and carbohydrates[371, 372]. These can target the surface receptors which are overexpressed on cancer cells or cancer endothelia and then aid internalisation by cells *via* receptor-mediated endocytosis[270, 373, 374] (Figure 8.2). Compared with passive targeting, it is believed that active targeted systems do not alter the whole-body distribution, nor increase the accumulation amount in tumours, but do affect the distribution within tumour tissues[375-377], as the attached targeting ligands can increase their selectivity for the cancer cell or endothelium target over other unrelated cells[270, 378, 379]. Thus active targeted NDDSs can show further improved anticancer effects[374, 380].

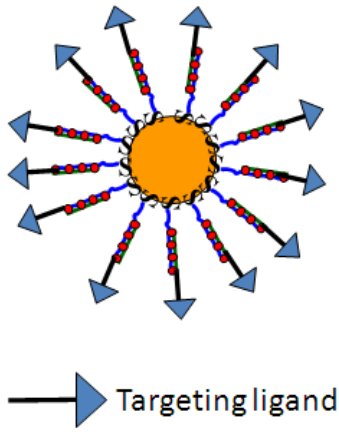

Figure 8.1. Schematic of active targeted NDDS.

In this project, active targeted GNP-dsDNA-DOX NDDSs can conveniently be prepared by attaching targeting ligands to the complementary DNA strand MC2. Here, Folic acid (FA) and a RGD peptide are chosen to demonstrate the feasibility of preparing MC2(FA) and MC2(RGD), which can then be used to assemble GNP-dsDNA(FA)-DOX and GNP-dsDNA(RGD)-DOX systems to specifically target cancer cells and cancer vasculature, respectively.

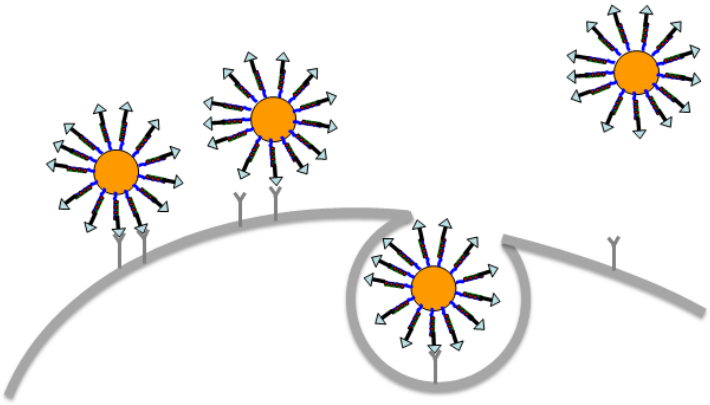

Figure 8.2. A schematic illustration of the receptor-mediated endocytosis. Targeting ligands (*e.g.* FA or RGD) on the surface of the GNP-dsDNA-DOX system bind specifically to the surface receptors overexpressed on cancer cells or cancer endothelia, which triggers cell internalisation through endosomes. The acidic pH inside the endosome/lysosome leads to DOX release from the NDDS.

8.1 Materials and Methods

8.1.1 Materials

MC2-amine (NH_2C_6-TTT TTT GTG TTA GGT TTA GGG TTA GGG) for preparation of MC2(FA) and new MC2-amine (NH_2C_6-TTT GTG TTA GGT TTA GGG TTA GGG) for MC2(RGD) preparation (lack of TTT compared to the MC2-amine) were obtained from IBA. Succinimidyl-[(N-maleimidopropionamido) -octa(ethylene glycol)] ester (NHS-PEG_8-Maleimide) was purchased from Thermo Scientific. Cyclo (Arg-Gly-Asp-D-Phe-Cys) (cyclo (RGDfC)) was purchased from Peptides International, Inc. Folic acid and

dicyclohexylcarbodiimide (DCC) were purchased from Sigma-Aldrich. N-hydroxysuccinimide (NHS) was purchased from Alfa Aesar. Anhydrous dimethylsulfoxide (DMSO), ethanol, sodium acetate, NaCl, KCl, Na_2HPO_4 and KH_2PO_4 were purchased from Sigma-Aldrich. Triethylamine (TEA) was purchased from Acros Organics.

8.1.2 Preparation of FA-NHS ester

A literature procedure[381, 382] was used. FA (110 mg, 0.25 mmol) and 0.06 mL triethylamine (TEA) were added into 3 mL anhydrous DMSO. The resulting mixture was stirred under nitrogen in the dark at room temperature until the Folic acid was dissolved. Then, a solution of 62 mg DCC (0.3 mmol) and 35 mg NHS (0.3 mmol) dissolved in 2 mL DMSO were added to the above solution. The resulting solution was stirred in the dark at room temperature under nitrogen protection for over 24 h to make activated folate-N-hydroxysuccinimidyl ester (FA-NHS). The reaction solution containing FA-NHS was then filtered to remove the by-product dicyclohexylurea (DCU), wrapped in foil and stored in the fridge. According to the literature[381], the yield of FA-NHS is around 77%, based on which the estimated FA-NHS concentration is approximately 0.03 M.

8.1.3 Preparation of MC2(FA)

100 nmol DNA MC2-amine was dissolved in 100 µL of mixture of DMSO and water (v/v 1:1) to make the stock solution, which was then used to make the MC2(FA) by the following two methods:

Method 1: 30 µL MC2-amine (30 nmol) was mixed with 30 µL filtered FA-NHS (900 nmol) (the molar ratio of MC2-amine to FA-NHS 1:30) and kept to react overnight; meanwhile 30 µL filtered FA-NHS was mixed with 30 µL mixture of DMSO and water (1:1) as control.

Method 2: 20 µL MC1-amine (20 nmol) was mixed with 20 µL filtered FA-NHS (600 nmol) and 20 µL water and kept overnight.

Samples made by methods 1 and 2 were mixed with 200 µL water, respectively, and centrifuged (21.1 kg, 15 mins) to remove precipitated unreacted FA-NHS. The supernatants were further filtered with a 0.2 µm Whatman syringe filter and dialysed (MWCO: 1 kDa) against 1 litre of pure water for 48 h. The absorption spectra before and after the dialysis were measured on a UV-vis spectrometer (5 µL of each sample was diluted with 1 mL water).

8.1.4 HPLC analysis and purification of MC2 (FA)

TEAA buffer (HPLC mobile phase A) preparation: 5.6 mL of acetic acid and 13.86 mL of TEA were added to 950 mL of water. The pH of the solution was adjusted to 7.0 with acetic acid, and then the final volume was adjusted to 1 L by adding water.

Both RP-HPLC analysis and purification were performed on the Gynkotek HPLC instrument at room temperature using a Phenomenex C18 column (4.6 X 250 mm, 5 µm) with a mobile phase consisting of TEAA buffer (A) and acetonitrile(B)[383]. UV absorbance was monitored by a Gynkotek (UVD 340S) detector at 260 nm. The process was run for 30 min using a gradient of 5-30% B for analysis and purification.

8.1.5 Purification of MC2(FA) *via* GNP-M2 mediated capture and dehybridization

5 µL of FA-NHS stock was mixed with 5 µL of MC2-Amine (5 nmol) to make MC2(FA). After 12 h, GNP-M2 (M2: 3 nmol) in 100 µL MES buffer was mixed with the MC2(FA) solution for 3 h to capture the MC2(FA) by forming GNP-M2/MC2(FA). The GNP-M2/MC2(FA) pellets were then collected and washed four times with 1.5 mL MES buffer by 90-min centrifugation (21.1 kg) to remove unreacted FA-NHS and DMSO. Though a small proportion of DMSO existed in the reaction mixture, it has been proved that less than 5% DMSO in the system will not affect the centrifuging process. The supernatants of each washing step were collected and monitored by UV-vis spectroscopy.

Thermal dehybridisation of GNP-M2/MC2(FA): 0.8 mL of water was added very slowly to the collected GNP-M2/MC2(FA) pellets and the pellets were kept at the bottom of an Eppendorf tube, which was then heated to 80°C for 8 min on a dry bath for dehybridization. The spectrum of the supernatant, containing MC2(FA), was recorded after centrifugation (21.1 kg, 90 min).

8.1.6 Two-step reaction to prepare MC2-$(PEG)_8$-RGD (also denoted as MC2(RGD))

The preparation of MC2-$(PEG)_8$-Maleimide (Step One)

100 nmol new MC2-amine was dissolved in 250 μL of pH 7.4 PBS (137 mM NaCl, 2.7 mM KCl, 10 mM Na_2HPO_4 and 2 mM KH_2PO_4) to make the stock. NHS-PEG_8-Maleimide was dissolved in DMSO to make 250 mM of stock solution. 125 μL of new MC2-amine stock (50 nmol) was mixed with 20 μL of NHS-PEG_8-Maleimide stock (5000 nmol) (new MC2-amine:NHS-PEG_8-Maleimide molar ratio = 1:100) and the mixture was incubated at room temperature for 2 h to make MC2-$(PEG)_8$-Maleimide.

MC2-$(PEG)_8$-Maleimide precipitation

The prepared MC2-$(PEG)_8$-Maleimide was purified by ethanol precipitation. Briefly, the mixture containing MC2-$(PEG)_8$-Maleimide was divided between two tubes (around 72 μL each tube), 1.28 mL of ethanol and 0.15 mL of 3 M sodium acetate (pH 5.2) were added to each tube (final volume: 1.5 mL and final sodium acetate concentration: 0.3 M). Both samples were placed in a -20 ℃ freezer overnight and then centrifuged at 14800 rpm (21.1 kg) for 30 mins at 4 ℃ to get DNA precipitate, which was washed twice with cold 70% ethanol and dried by N_2.

Preparation of MC2-$(PEG)_8$-RGD (Step Two)

1 mg cyclo (RGDfC) (1730 nmol) was dissolved in 1 mL of de-gassed pure water to make RGD stock with a final concentration of 1.73 mM. The DNA precipitates obtained above were combined and dissolved in 200 µL of PBS (pH 7.4) and then mixed with 30 µL of cyclo (RGDfC). The mixture was allowed to react at room temperature for 2 h and then stored in the -20 ℃ freezer before HPLC analysis and purification.

8.1.7 HPLC analysis and purification of MC2-$(PEG)_8$-RGD

The HPLC instrument and mobile phase for MC1-$(PEG)_8$-RGD analysis and purification are the same as MC2(FA) analysis. Three different methods were tried; (5-95% B) 30min, (10-70% B) 30min and (5-40% B) 40min. In the end (5-40% B) 40min was chosen for analysis and purification.

8.2 Results and discussion

8.2.1 MC2(FA) preparation and GNP-M2/MC2(FA) assembly

Folic acid (FA), also called vitamin B9 (see Figure 8.3 for its structure), is a vitamin involved in nucleotide biosynthesis and other bodily functions. It has been exploited as an attractive targeting ligand for cancer diagnosis and treatment[384, 385]. This is because folate receptors are overexpressed in many human tumours, including ovarian, lung, breast, kidney, brain, endometrial and colon cancers, but not in most normal tissues. A wide variety of folate conjugates have been prepared, including folate-imaging agents[386, 387], folate-chemotherapeutics [388-390] and folate-drug carriers[391-394], and these have shown promising results in sensitive and specific cancer imaging

and therapy. Several products have been tested in clinical trials[395, 396].

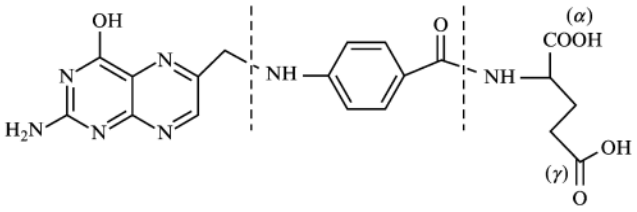

Figure 8.3. Chemical structure of folic acid.

There are quite a few advantages in exploiting FA as a targeting ligand[392, 397]. Compared with monoclonal antibodies, folic acid, a small molecule with a molecular weight of 441 Da, is relatively stable, inexpensive, non-immunogenic and easily conjugated to chemotherapeutics and carriers. Folic acid has a high affinity to the folate receptor with Kd around 0.1 nM, and retains this affinity in nM range after conjugation[398, 399]. Folate conjugates can be taken in by cells *via* folate receptor-mediated endocytosis with high efficiency.

8.2.1.1 Preparation and characterisation of MC2(FA)

To prepare folic acid modified complementary DNA (MC2(FA)), folic acid was first activated in form of FA-NHS, then reacted with amine modified MC2 (MC2-NH_2) to make MC2(FA) conjugate (Figure 8.4) through the stable amide bond formation. The conjugation reaction can be accomplished in two steps under mild conditions.

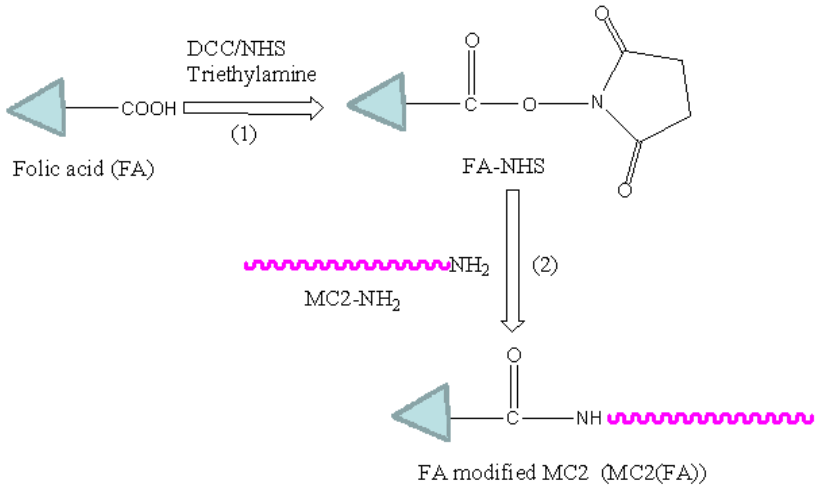

Figure 8.4. Schematic procedure of MC2(FA) preparation.

In the second step FA-NHS was mixed with MC2-NH_2 to prepare MC2(FA). A mixed solvent of DMSO and water was used as the reaction medium because the solubilities of FA-NHS and MC2-NH2 in DMSO and water are different; FA-NHS is soluble in DMSO but its solubility in water is low, whereas MC2-NH2 is not soluble in anhydrous DMSO. Here, the mixing ratios (DMSO:water) of 3:1 (Method 1) and 1:1 (Method 2) were used for the reaction. A mixing ratio of 3:1 was found to be the minimum proportion required to dissolve MC2-NH_2. Also, excess FA-NHS (a molar ratio of FA-NHS to MC2-NH2 30:1) was used to increase the reaction yield of DNA, even though the reaction ratio was 1:1.

After reaction, 200 µL water was added to 60 µL of the reaction mixture to precipitate excess FA-NHS resulting from its low solubility in water; this was then removed by centrifugation and filtration. Figure 8.5 shows the UV spectra of the filtered reaction mixtures made by methods 1 and 2 and the control (FA-NHS only). No obvious difference in the two main peak positions was observed between the mixtures in methods 1 and 2 . But when compared to the control, their peaks in the 260-280 nm range were slightly blue shifted by 4 nm due to DNA absorption at 260 nm.

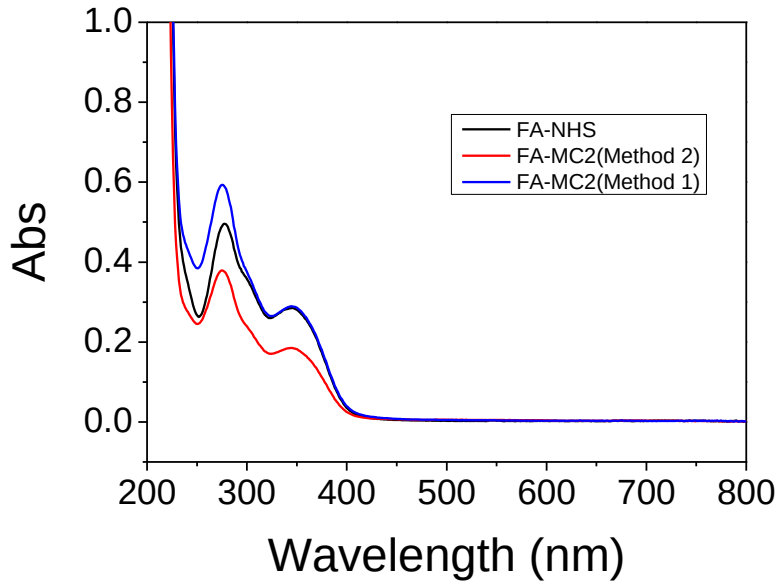

Figure 8.5. UV-vis spectra of the reaction mixtures made by methods 1 and 2 before dialysis.

The reaction mixtures and the control were then dialysed (MWCO:1 kDa) against pure water for 48 h to remove DMSO and excess FA-NHS, and the UV-vis spectra after dialysis are shown in Figure 8.6. Again, after dialysis the peaks in the 260-280 nm range of both reaction mixtures were blue-shifted by 5-6 nm in comparison with FA-NHS. Compared to those measured before dialysis, the UV absorption of both mixtures and the control dropped by approximately 50%, together with much weaker 'end absorption' in the 200-220 nm range, indicating that a large proportion of FA-NHS and DMSO had been removed. Figure 8.6 also shows the UV spectrum of the mixture of FA-NHS and MC2 (without amine modification) which had the same UV absorption peaks as both reaction mixtures, suggesting that the UV-vis spectra alone cannot give a definitive conclusion as to whether the MC2(FA) has been successfully prepared.

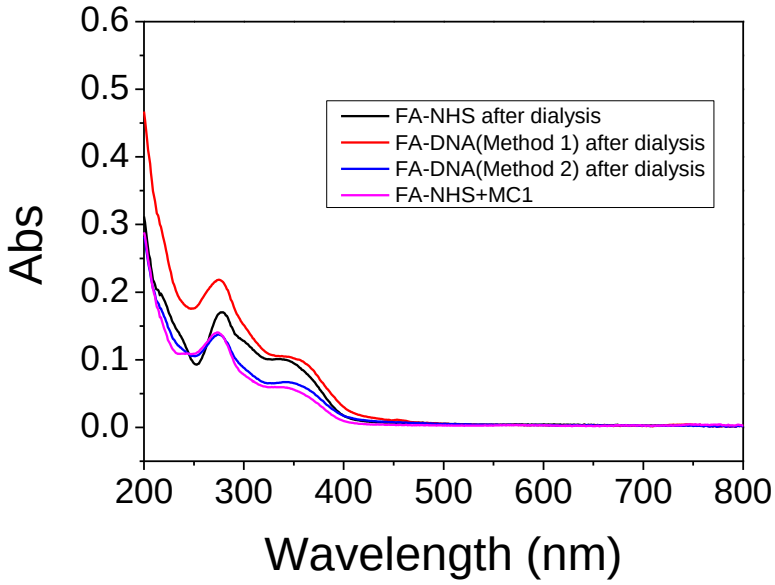

Figure 8.6. UV-vis spectra of the reaction mixtures made by methods 1 & 2 after dialysis.

8.2.1.2 HPLC analysis of reactants and MC2(FA)

To confirm whether the MC2(FA) conjugate was successfully synthesised, a reversed phase HPLC analysis was employed. The reactants, MC2-NH_2 and FA-NHS, were first injected to confirm the retention times of their own peaks. Figure 8.7a shows the HPLC profile of MC2-NH_2 which had a retention time of 18.5 min, and was identified through the characteristic absorption peak of DNA at 260 nm (Figure 8.7b). The HPLC profile of FA-NHS (Figure 8.8a) shows three main peaks with retention times of 11.8, 15.7 and 16.7 min, respectively. Based on their UV-vis spectra, the peak at 11.8 min was believed to be FA-NHS and no strong evidence was found to confirm the other two peaks at 15.7 and 16.7 min, both of which displayed similar UV-vis spectra, although it was assumed that they were FA-related by-products because no further purification was performed at the step of FA-NHS synthesis. The uncertainty of the other two peaks should not affect the identification of the MC2(FA) peak, because it would be easy to exclude peaks having the above UV-vis spectra and retention times.

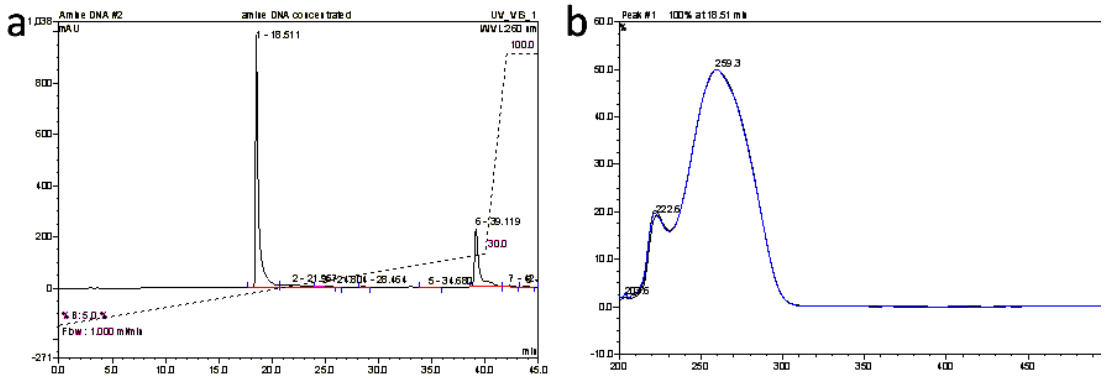

Figure 8.7. amine-MC2 HPLC spectra (**a**) and UV-vis spectra (**b**) corresponding to the peak at 18.5 min.

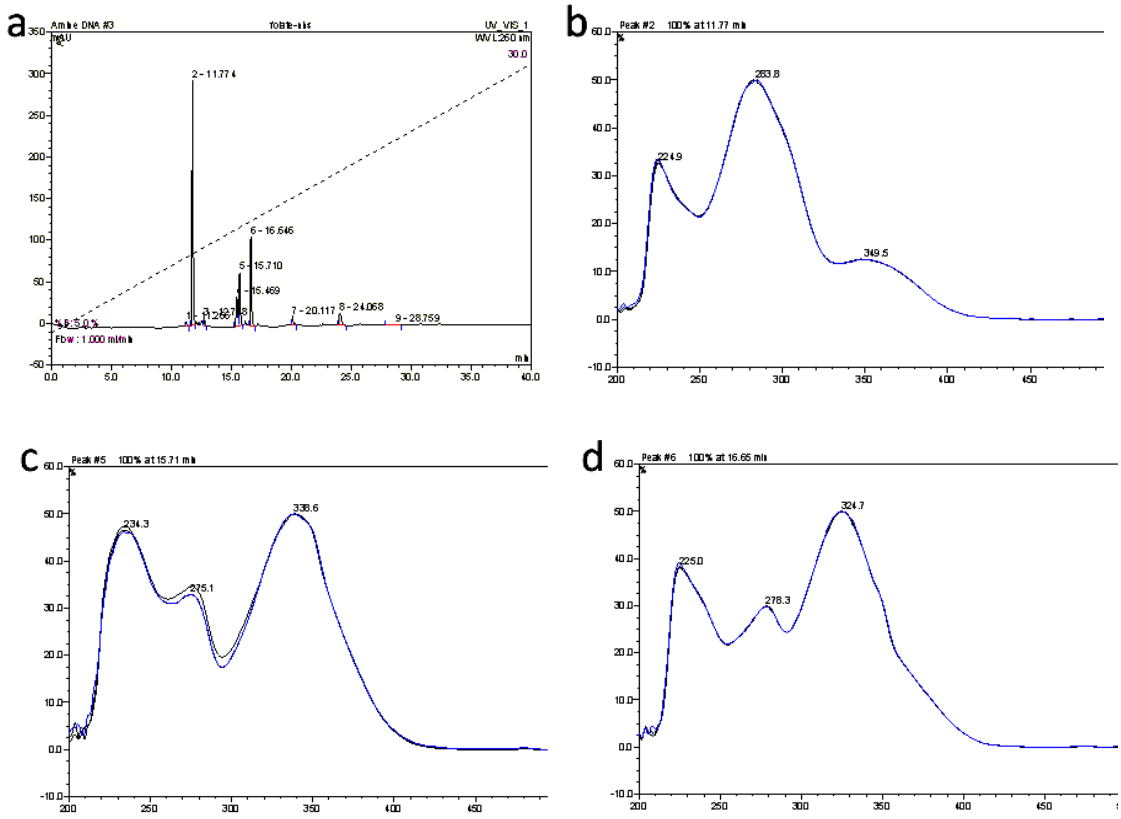

Figure 8.8. FA-NHS HPLC spectra (**a**) and UV-vis spectra corresponding to the peak at 11.8 min (**b**), 15.7 min (**c**) and 16.7 min (**d**).

After the confirmation of reactant peaks, the reaction mixtures prepared by methods 1 and 2 were then injected in turn, and their combined HPLC profiles are shown in Figure 8.9. Compared to the reactants, the first three peaks had the same retention times as those of the FA-NHS, indicating that they were from

FA-NHS. Peak B had the same retention time as the main peak of MC2-NH_2, which together with its UV-vis spectrum (Figure 8.9b), suggests that peak B is from unreacted MC2-NH_2. Peak A, with a retention time of 20.5 min, was the only new peak not found in the reactants, suggesting it is possibly from the reacted product. This was further confirmed by the UV-vis spectrum of peak A, where we can see characteristic absorption peaks of the DNA at 260 nm (likely due to the overlap of the DNA and FA peaks in this range) and an absorption at 355 nm from the FA part. All this evidence strongly suggests that peak A is the MC2(FA) peak and that the conjugation reaction was successful.

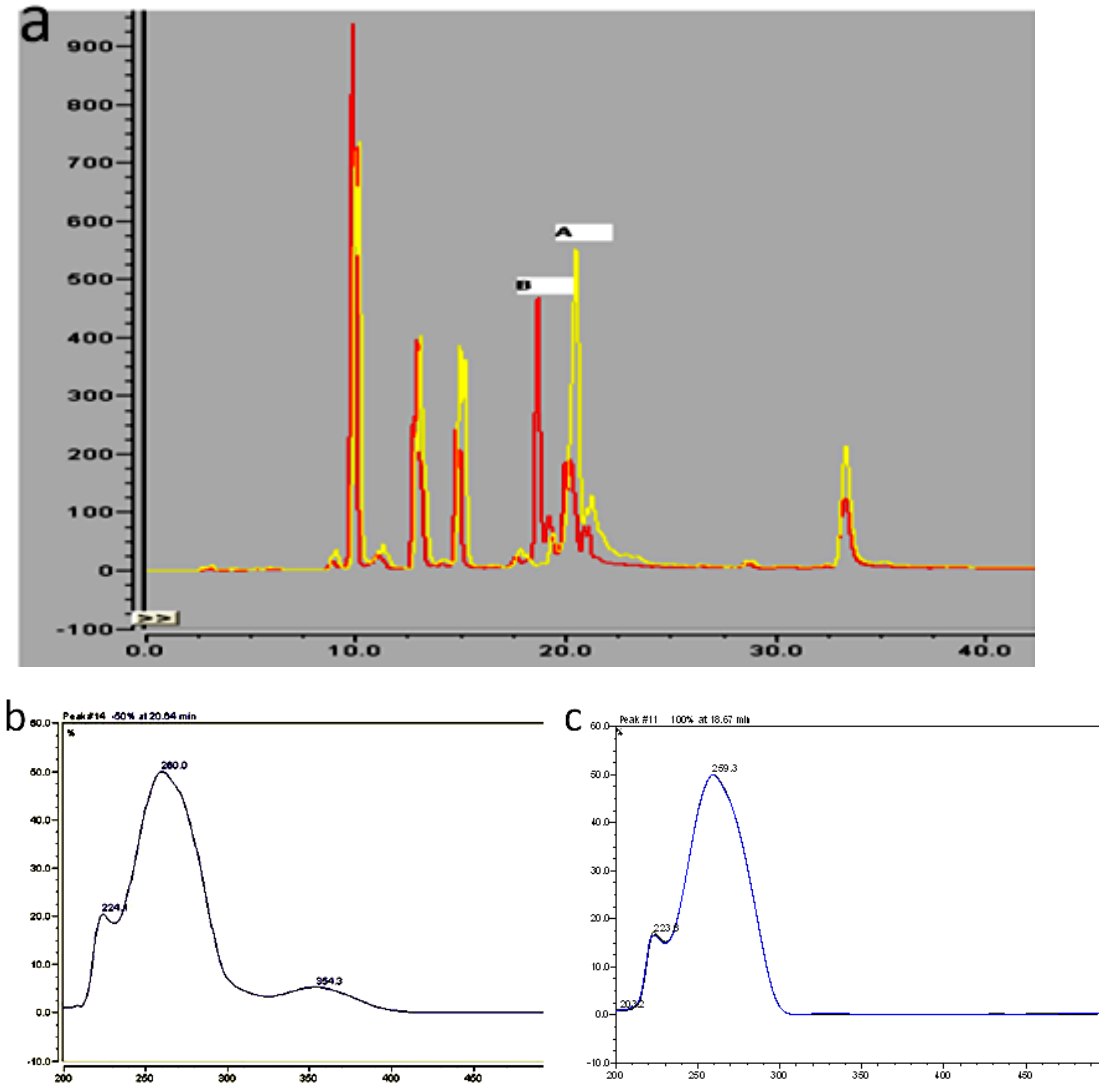

Figure 8.9. (**a**) HPLC spectra of reaction mixtures made by Method 1 (yellow colour) and Method 2 (red colour); (**b**) UV-vis spectrum corresponding to peak A at 20.5 min; (**c**) UV-vis spectrum corresponding to peak B at 18.67 min.

From this combined HPLC profile, it can also be seen that the yields of MC2(FA) prepared by Methods 1 and 2 are quite different. Peak A was found in both methods, showing that conjugation happened in both, but the HPLC profile of method 2 gave a large peak B with a small peak A, indicating that MC2-NH_2 had not fully reacted, even though > 30 molar equivalent of FA-NHS was used. This is possibly due to the low solubility of FA-NHS in the DMSO/water mixture with a ratio of 1:1. According to the relative areas of peak A and B, the synthetic yield of MC2(FA) prepared by method 2 was estimated at 38%. In contrast, peak B was not observed in the HPLC profile of the product prepared by method 1, but only a large peak A, suggesting that almost all the MC2-NH_2 had reacted, and that the synthetic yield for MC2(FA) was close to unity. This demonstrates that the DMSO:water (v:v) 3:1 ratio in Method 1 is more suitable for the conjugation.

8.2.1.3 Purification of MC2(FA) *via* GNP-M2 mediated capture and dehybridization

Although HPLC is the most common method for conjugated DNA purification, it is expensive and laborious. Therefore a simpler approach was proposed, using GNP-M2 mediated target capture and subsequently release. First, MC2(FA) was efficiently captured by the GNP-M2 *via* hybridisation, allowing easy separation and removal of non-target species by centrifugation, and then the captured MC2(FA) was released from the GNP-M2 conjugate by reducing salt concentration and heating-induced dehybridisation. To investigate whether this was feasible, UV-vis spectroscopy was employed to monitor the hybridisation, centrifugation and dehybridisation steps *via* absorbances of the supernatants.

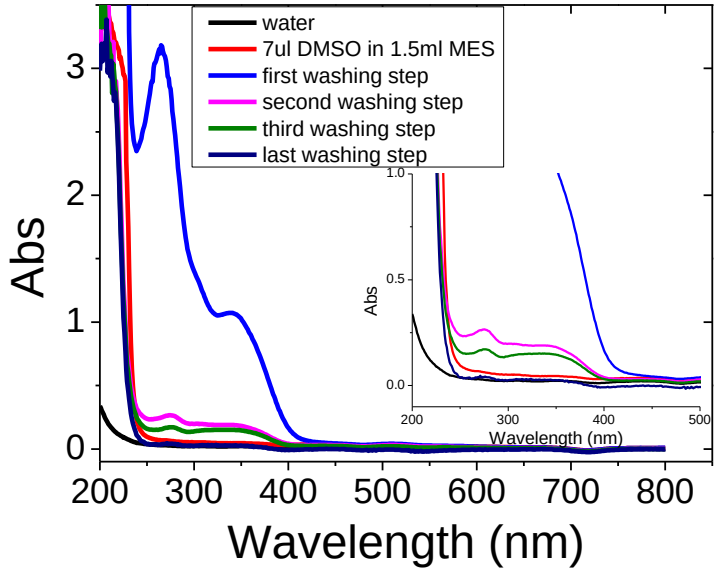

Figure 8.10. The UV-vis absorption spectra of the supernatant at each washing step.

Figure 8.10 shows strong absorbance with peaks corresponding to the typical absorption of FA-NHS found in the supernatant of the first washing step, indicating that a large amount of excess unreacted FA-NHS was removed from the pellets. During the second and third washing steps, absorption levels of the supernatants were much lower, and no detectable absorption was found in the supernatant of the fourth and last washing step, suggesting that all the unreacted FA-NHS were removed from the GNP-M2/MC2(FA) pellets during the first three washing steps; and that ~ 85% of the FA-NHS and related side products were removed in the first washing step. Therefore purification of MC2(FA) appeared to be highly possible *via* capture by the GNP-M2 conjugate, followed by washing steps.

Next, thermal dehybridisation was performed to release MC2(FA) from the GNP-M2/MC2(FA) pellets. Here, 0.8 mL of pure water, instead of MES buffer, was gently added to GNP-M2/MC2(FA) pellets to keep the pellets at the bottom of the tube. It is well-known that the stability of DNA duplex is strongly salt dependent, and pure water without added salt favours dehybridisation[400]. The

tube, without shaking, was heated to 80 ℃ to dehybridise the MC2(FA) from the GNP-M2 conjugate. After that the 'water' supernatant was removed, centrifuged (to remove any residue GNP-M2) and then checked by the UV-vis spectroscopy. The dehybridisation processes were carried out three times and the corresponding UV-vis spectra of the supernatants are shown in Figure 8.11.

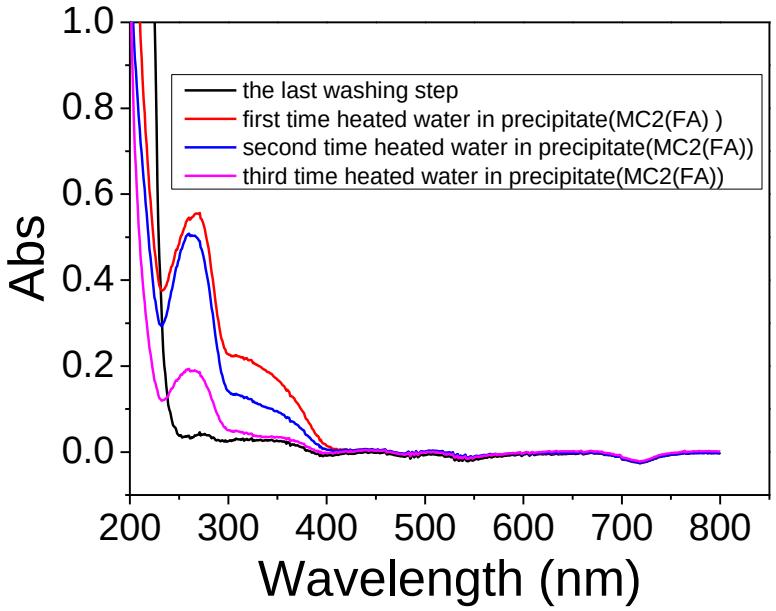

Figure 8.11. Spectra of supernatants containing MC2(FA).

Figure 8.11 shows the UV-vis spectra of these supernatants exhibiting absorption peaks at 265 nm and in the 330-360 nm range, typical for MC2(FA) as observed in the previous HPLC spectra (Figure 8.9b). Because all the free FA-NHS had been removed in previous washing steps, the absorptions here must have come from the MC2(FA) dehybridised from the pellets during heating in pure water.

To show the difference between FA-NHS from the washing steps and MC2(FA) from the heating steps, UV-vis spectra from the second washing and the second heating steps are plotted in Figure 8.12. This clearly shows that the absorption peak of MC2(FA) in the 260-280 nm range was blue shifted by 10 nm compared

to that of FA-NHS, the result of DNA absorption at 260 nm, revealing that MC2(FA) was released from the pellet during thermal dehybridisation. These results confirm that GNP-M2 based MC2(FA) capture and subsequent heat-induced release was successful. This is a simple, effective way to separate and purify FA-modified DNA

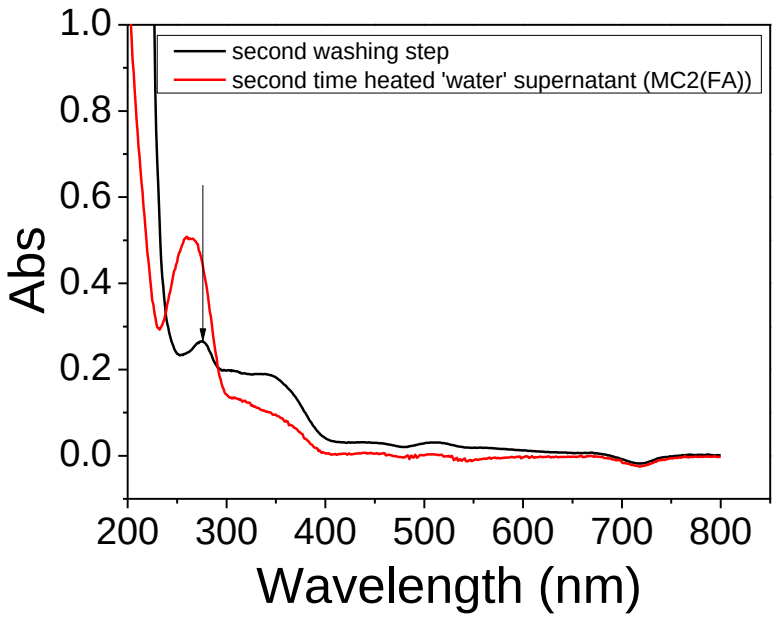

Figure 8.12. Comparison of the UV-vis absorption spectra of the supernatants obtained during the washing step (black line) and heat-induced release step (red line).

8.2.2 Preparation, analysis and purification of MC2(RGD)

Arginine-Glycine-Aspartic acid (RGD) is an essential cell adhesion sequence recognised by cell surface receptors (integrins). It was first discovered by Pierschbacher and Ruoslahti in 1984[401]. Its selectivity can be further improved by designing cyclic RGD peptides[402] which show higher binding affinity[403] and stability[404, 405]. It has been reported that synthetic cyclic RGD peptides can selectively bind to the $\alpha_V\beta_3$ integrin, which is highly expressed in tumour vasculature (but not on blood vessels in normal tissues) and is associated with angiogenesis, malignant tumour growth and

metastasis[403, 406]. Targeting tumour vasculature by RGD peptides has drawn significant attention for cancer therapy and diagnosis, for example through the attachments of chemotherapeutic molecules[407, 408], imaging agents[409-415] and drug carriers[416-419]. Here we demonstrate that RGD can also be attached to the complementary DNA MC2, which can be used to develop an RGD linked GNP-DNA-DOX system for active targeting in the future.

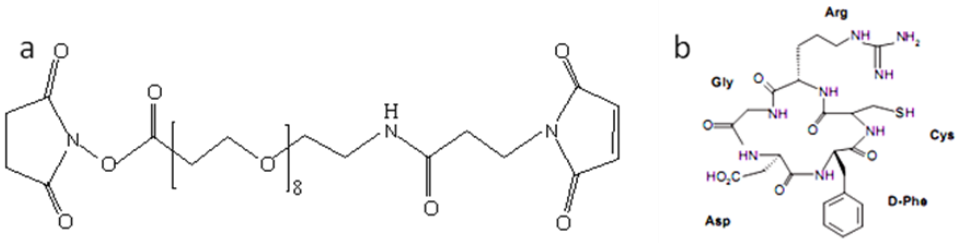

Figure 8.13. (**a**) Chemical structures of NHS-$(PEG)_8$-Maleimide and (**b**) cyclo (RGDfC) (Molecular Formula: $C_{24}H_{34}N_8O_7S$).

8.2.2.1 Preparation of MC2(RGD)

RGD-attached MC2 (MC2-$(PEG)_8$-RGD) was prepared *via a* two-step reaction (Figure 8.14), using NHS-$(PEG)_8$-Maleimide (Figure 8.13a) as a heterofunctional linker. This first reacted with MC2-NH_2 to form MC2-$(PEG)_8$-Maleimide through the amide bond formation between NHS and primary amine, and then reacted with a thiolated RGD, cyclo (RGDfC) (Figure 8.13b) to form MC2-$(PEG)_8$-RGD through the thioether bond formation between maleimide and thiol groups. This reaction sequence is based on the different stabilities of the NHS ester (unstable, readily hydrolysed) and the maleimide (relatively stable) functional groups in the reaction media (pH 7.4 PBS). .

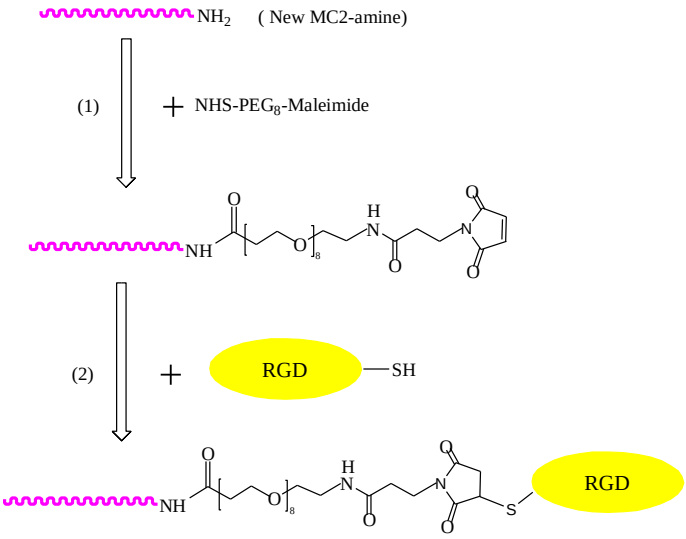

Figure 8.14. Reaction schematic of MC2(RGD) preparation.

The use of a PEG linker not only facilitates RGD attachment to the 5' end of MC2 in two steps, but also gives the active targeted NDDS improved stability and prolonged circulation. Furthermore, as PEG length is also an important factor in 'stealth' effect, the PEG length of the linker can be adjusted by the PEG repeating units where required. For example, NHS-$(PEG)_{12}$-Maleimide and NHS-$(PEG)_{24}$-Maleimide are both commercially available. Here, a PEG linker containing 8 PEG repeating units (NHS-$(PEG)_8$-Maleimide) was chosen to demonstrate the feasibility of the RGD-MC2 conjugation, which can be further optimised in future work.

In the first step, a 100-fold molar excess of NHS-$(PEG)_8$-Maleimide was reacted with amine-modified MC2 in PBS (pH7.4) to ensure complete reaction of the MC2-NH_2. After 2 h the reaction mixture was purified by ethanol precipitation to remove the excess unreacted NHS-$(PEG)_8$-Maleimide which could interfere with the second step reaction.

After precipitation by ethanol and dried by N_2, the obtained DNA precipitates

were dissolved again in pH 7.4 PBS and then reacted with excess HS-RGD (DNA: HS-RGD molar ratio = 1:2) to form MC2-$(PEG)_8$-RGD. The reaction process was monitored by HPLC. The final product was purified by HPLC instead of ethanol precipitation, because the latter can separate DNA from a non-DNA containing compound, but not MC2-$(PEG)_8$-RGD from MC2-NH_2 and MC2-$(PEG)_8$-Maleimide.

8.2.2.2 HPLC analysis and purification of MC2-$(PEG)_8$-RGD

Three solvent gradients, (5-95% B) 30 min, (5-70% B) 30 min and (5-40% B) 40 min were tried for HPLC analysis to obtain the maximum retention time differences for MC2-NH_2, MC2-$(PEG)_8$-Maleimide and MC2-$(PEG)_8$-RGD, in order to facilitate MC1-$(PEG)_8$-RGD purification. The gradient of RP (5-40%) 40 min was found to be the optimum condition and was chosen for HPLC analysis and purification.

Only a single peak at ~15 min was observed in the HPLC profile of MC2-NH_2, seen here in Figure 8.15a, which also shows the characteristic DNA absorption peak at 260 nm in the corresponding UV-vis spectrum; this suggests that MC2-NH_2 was eluted out at ~15 min. One may note that the retention time of MC2-NH_2 was different from that in the MC2(FA) part(18.5 min). There are two reasons for this earlier retention time: MC2-NH_2 in this part (new MC2-NH_2) is shorter than that used in MC2(FA) as it lacks three cytosines; also, the HPLC gradient used here is (5-40% B) 40min instead of (5-30% B) 40min in the MC2(FA) part

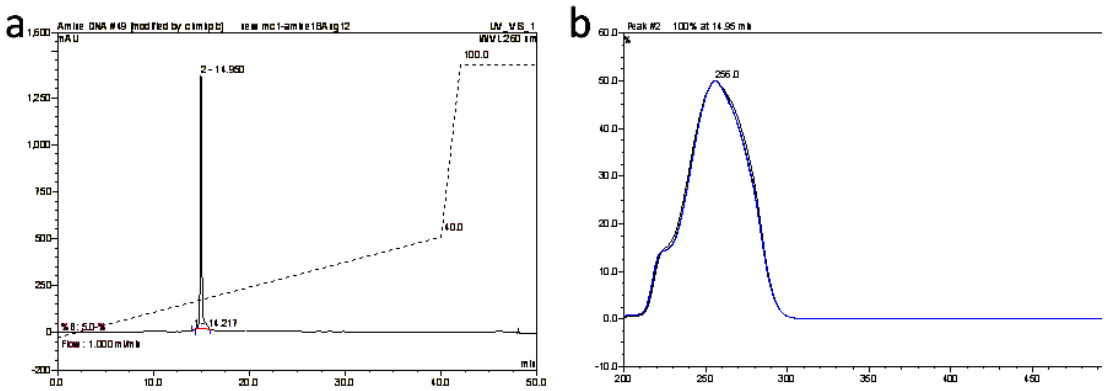

Figure 8.15. (**a**) HPLC profile of new MC2-NH_2 and (**b**) UV-vis spectrum of the main peak at 15 min.

The HPLC profile of the reaction mixture at the first step, before ethanol precipitation, with the UV-vis spectrum of the peak at 19.5 min, is shown in Figure 8.16. As the reaction mixture contained DMSO, a sharp peak at around 2.9 min was assigned to DMSO. Apart from the DMSO peak, the retention time of the main peak (Peak 1) appeared at 19.5 min, 4.5 min later than that of MC2-NH_2, confirming it as a new peak. Moreover, it has the characteristic absorp.tion peak of DNA at 260 nm (Figure 8.16b), suggesting that this peak was most likely the desired MC2-$(PEG)_8$-Maleimide. Its yield was estimated at 83%, based on the relative area calculation.

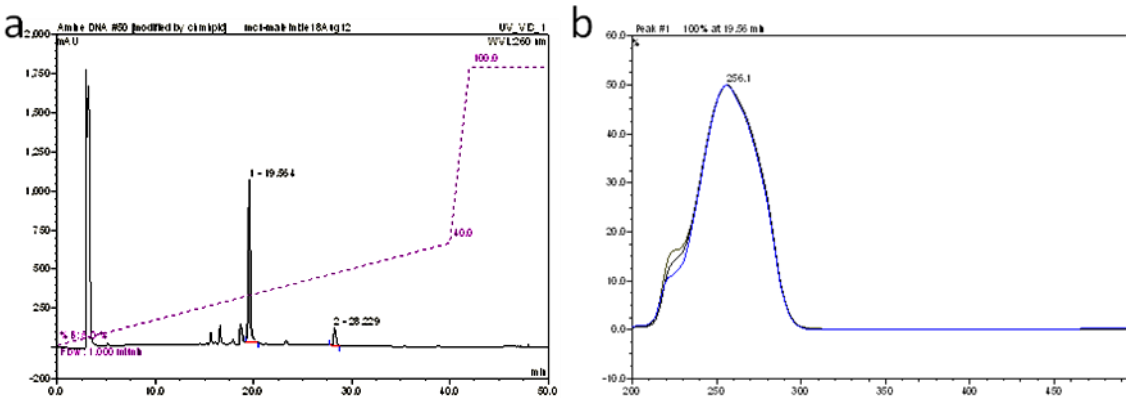

Figure 8.16. (**a**) HPLC profile of MC2-$(PEG)_8$-Maleimide and (**b**) UV-vis spectrum of the peak at 19.5 min.

After confirmation of the peaks from MC2-NH_2 and MC2-$(PEG)_8$-Maleimide, the reaction mixture of the second step was injected, and its HPLC profile is shown in Figure 8.17. Compared to Figure 8.15 and Figure 8.16, the main peak appears at 21.5 min, 6.5 min later than MC2-NH_2 and 2 min later than MC2-$(PEG)_8$-Maleimide. It also displays the DNA characteristic absorption peak at 260 nm (Figure 8.17b), confirming that the main peak at 21.5 min is due to MC2-$(PEG)_8$-RGD. The HPLC results suggested that RGD has been successfully attached to MC2 to form MC2-$(PEG)_8$-RGD *via* a two-step reaction using NHS-$(PEG)_8$-Maleimide-mediated cross-linking. Based on the relative peak areas, the overall yield of MC2-$(PEG)_8$-RGD was estimated as being 71%.

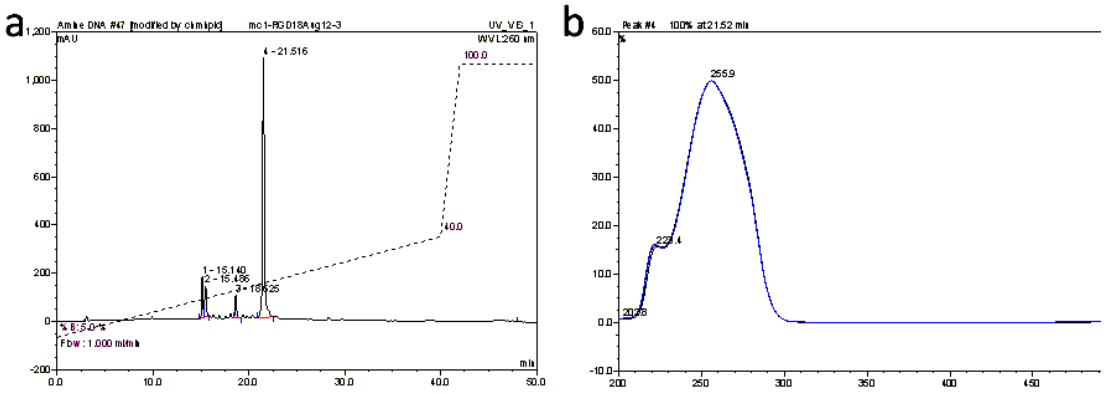

Figure 8.17. (**a**) HPLC profile of MC1-$(PEG)_8$-RGD and (**b**) UV-vis spectrum of the main peak at 21.5 min.

In view of the small amount of DNA (≤ 50 nmol), MC2-$(PEG)_8$-RGD was purified using the same C18 analysis column, but with the injection of 200 µL. Again, due to the intensity of MC2-$(PEG)_8$-RGD beyond the HPLC detection range, its peak and retention time in Figure 8.18 were not shown properly, but this did not affect the purification process. The purification was complete after two injections and the collected fraction could be lyophilised for assembly of GNP-M1/ MC2-$(PEG)_8$-RGD and future cell-based studies.

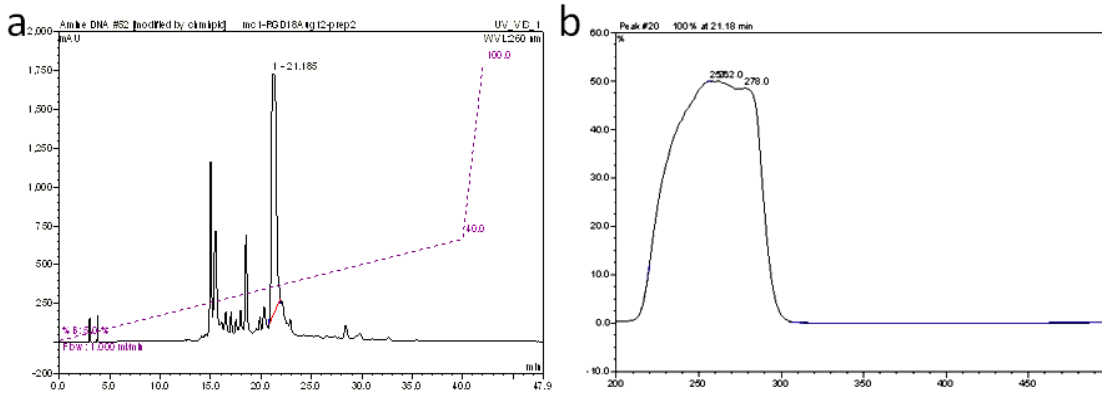

Figure 8.18. (a) HPLC profile of MC2-$(PEG)_8$-RGD purification and (b) UV-vis spectrum of the collected fraction with retention time of 21.2 min.

8.3 Conclusion

A highly promising active targeting ligand, folic acid (FA), has been successfully conjugated to a complementary DNA to form MC2(FA). Moreover, the purification and assembly of MC2(FA) to form an active targeted GNP-M2/MC2(FA) delivery system can be achieved simultaneously by hybridisation to a GNP-M2 conjugate, followed by simple washing steps. In addition, another active targeting ligand, cyclo (RGDfC), modified MC2 has also been prepared successfully *via* a two-step reaction using a PEGylated heterofunctional cross linker (HNS-PEG_8-maleimide). These conjugation reactions are simple and can be performed in two steps under mild conditions. Due to the ease of DNA hybridisation, surface modifications of the GNP-DNA-DOX system can be readily achieved by simply modifying the 5' end of the complementary DNA MC2. Therefore it is relatively straightforward to graft functional ligands onto the GNP-dsDNA system, making it highly attractive for the development of effective, targeted drug delivery for cancer therapy. However, owing to the time constraint of the project it is not possible to carry out the cellular evaluations of such active targeting systems (*e.g.* cell specific uptake, delivery efficiency and cell specific cytotoxicity etc). These will

most likely be carried out by future group members.

9 General conclusions and future research

9.1 Summary

All of the three *i*-motif DNA nanomachines we designed containing one to three *i*-motif domains (M1, M2 and M3) have been successfully used to form pH-responsive dsDNA-DOX conjugates, exhibiting similar critical DOX releasing pH points and pH-dependent DOX binding/releasing profiles. These conjugates form the functional part of pH-responsive nanocarriers, where DOX is readily loaded in native format at physiological pH to form dsDNA-DOX conjugates, and released at acidic pH (around 5.2-5.4 for conjugates alone) in response to the formation of *i*-motifs that trigger disassembly of the conjugates.

dsDNA-DOX conjugates have been successfully conjugated to GNPs to develop a new pH-responsive targeted GNP-dsDNA drug nanocarrier which is capable of rapid, efficient and pH-triggered drug release. The surface of this nanocarrier can be 'covered' by PEGs *via* PEGylation of the 5' end of the complementary DNA. It has been proven that PEG modification does not alter DOX release profiles, but can provide an effective 'shield' to improve stability against nuclease degradation and resistance to non-specific serum protein adsorption of the nanocarrier. Nanocarrier stability can be further improved by increasing PEG length and using branched PEGs.

It has been confirmed that the GNP-dsDNA(PEG) nanocarrier can efficiently deliver DOX into HeLa cells in the form of intact conjugates without dissociation *via* the endocytic pathway, and release the loaded DOX inside cancer cells to

achieve similar cytotoxicity to free DOX. This nanocarrier has also been successfully used to deliver DNA-binding but cell membrane-impermeable agents (*e.g.* a dinuclear Ru-complex and PI). Therefore, this nanocarrier can act as a general, efficient intracellular delivery platform not only for DOX but also for other DNA intercalating agents, such as other drugs of the anthracycline family and DNA-binding agents.

This pH-responsive GNP-dsDNA(PEG) nanocarrier displays numerous features necessary for an 'ideal' drug nanocarrier for cancer treatment: uniform nanoscale size (< 100 nm); the potential for resisting non-specific interaction *in vivo* and prolonging blood circulation time (*via* PEGylation); a high capacity for simple drug loading in native format without involving any chemical modification and/or coupling; pH-trigger release (*via* intracellular endosomal/lysosomal acidic environments); it is non-toxic, biocompatible, water-soluble, and suitable for freeze-drying for long-term storage.

In addition, I have demonstrated that specific targeting ligands (*i.e.* cyclo(RGDfC) and folic acid) can be successfully grafted onto the surface of the nanocarrier by straightforward coupling chemistry to the 5' end of complementary DNA, making the development of active targeted drug delivery systems highly feasible. Furthermore the GNP can be readily replaced by GNRs or Fe@Au NPs, allowing the development of more effective, multifunctional drug nanocarriers that combine multiple therapeutic modalities and imaging ability.

In summary, the inorganic nanoparticle-pH-responsive DNA based drug nanocarrier developed in this thesis appears to be a very promising platform for drug delivery with the potential to achieve effective, multiple modal therapeutic treatments for cancer patients with significantly reduced side-effects.

9.2 Future research

1) PEG is known to play a key role in determining the *in vitro* and *in vivo* stability of drug delivery systems, as demonstrated in Chapter 5. In the future, therefore, PEG can also be introduced to the GNP-M2/MC2(FA) system as required, by preparing MC2(PEG)FA instead of MC2(FA) conjugate. Figure 9.1 shows the schematic of proposed MC2(PEG)FA preparation. Firstly FA-NHS is prepared using the same procedure as in Chapter 8, and this can then react with cysteamine to form FA-SH [381]. By employing a heterofunctional PEG linker[420] (Maleimide-PEG-NHS), MC2-PEG-Maleimide can be obtained by the amide bond formation between MC2-NH_2 and the PEG linker, which will further react with FA-SH to eventually form PEG modified MC2-FA conjugate (MC2(PEG)FA), with potential for improved stability and stealth effect.

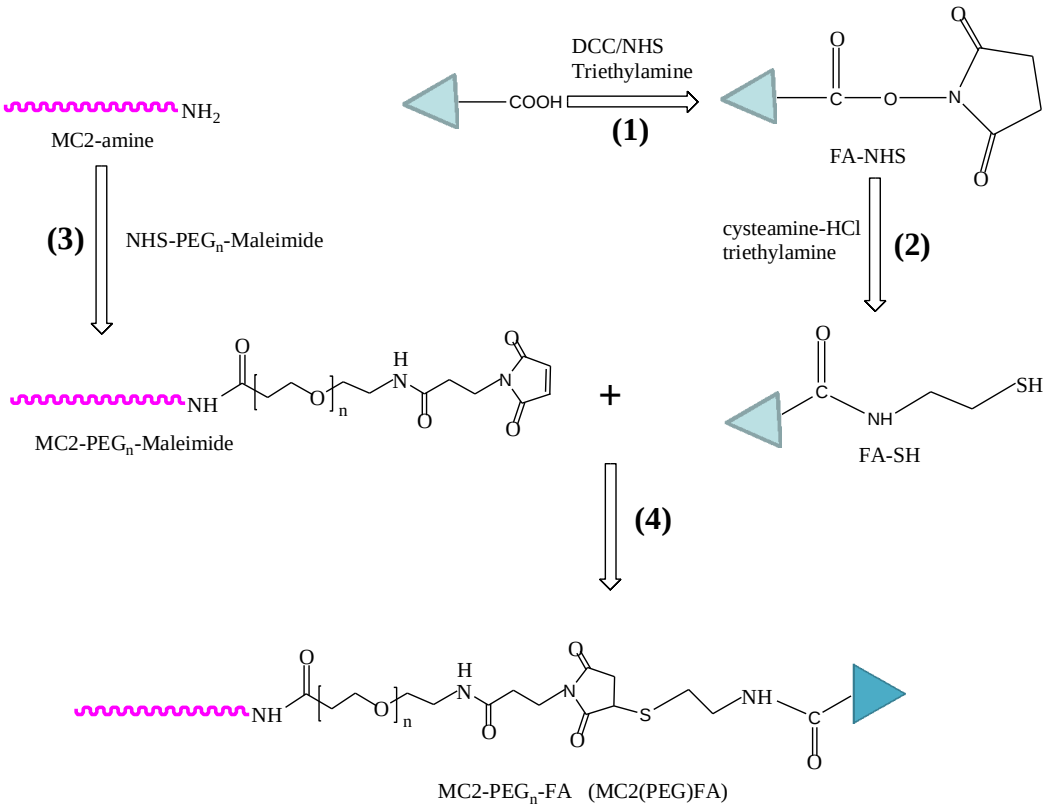

Figure 9.1. Schematic of MC2-PEG_n-FA preparation.

2) Further cell studies will be performed on the active targeted drug delivery systems (*i.e.* GNP-dsDNA(FA)-DOX and GNP-dsDNA(RGD)-DOX systems) to investigate their cell uptake specificity and cell-specific cytotoxicity.

3) Cell based evaluation of multi-functional drug nanocarriers: GNR-dsDNA(PEG) and Fe@Au-dsDNA(PEG) systems can be evaluated with or without the exposure of an infrared laser light (for the GNR system) or an alternating magnetic field (for the Fe@Au system) to evaluate effects and synergy of combined chemo/photothermal or chemo/hyperthermia treatments against single modal treatments.

4) The most promising of these new drug delivery systems at cellular levels can be further studied in *in vivo* animal models to investigate their real pre-clinical potential.

10 References

1. Ochekpe, N.A., P.O. Olorunfemi, and N.C. Ngwuluka, *Nanotechnology and Drug Delivery Part 1: Background and Applications.* Tropical Journal of Pharmaceutical Research, 2009. **8**(3): p. 265-274.
2. Farokhzad, O.C. and R. Langer, *Impact of Nanotechnology on Drug Delivery.* Acs Nano, 2009. **3**(1): p. 16-20.
3. Arruebo, M., et al., *Magnetic nanoparticles for drug delivery.* Nano Today, 2007. **2**(3): p. 22-32.
4. Williams, D., *The relationship between biomaterials and nanotechnology.* Biomaterials, 2008. **29**(12): p. 1737-1738.
5. Bogunia-Kubik, K. and M. Sugisaka, *From molecular biology to nanotechnology and nanomedicine.* Biosystems, 2002. **65**(2-3): p. 123-138.
6. Kawasaki, E.S. and A. Player, *Nanotechnology, nanomedicine, and the development of new, effective therapies for cancer.* Nanomedicine, 2005. **1**(2): p. 101-109.
7. Caruso, F., T. Hyeon, and V.M. Rotello, *Nanomedicine.* Chem Soc Rev, 2012. **41**(7): p. 2537-2538.
8. Kiparissides, C. and O. Kammona, *Nanotechnology advances in controlled drug delivery systems.* Physica Status Solidi C - Current Topics in Solid State Physics, Vol 5, No 12 2008, 2008. **5**(12): p. 3828-3833.
9. Shi, J., et al., *Nanotechnology in drug delivery and tissue engineering: from discovery to applications.* Nano Lett, 2010. **10**(9): p. 3223-3230.
10. Davis, M.E., Z. Chen, and D.M. Shin, *Nanoparticle therapeutics: an emerging treatment modality for cancer.* Nature Reviews Drug Discovery, 2008. **7**(9): p. 771-782.
11. *Nanomedicine market will be worth US$160 billion by 2015.* Nanomedicine, 2009. **4**(6): p. 610-610.
12. LaVan, D.A., T. McGuire, and R. Langer, *Small-scale systems for in vivo drug delivery.* Nature Biotechnology, 2003. **21**(10): p. 1184-1191.
13. Ferrari, M., *Cancer nanotechnology: Opportunities and challenges.* Nature Reviews Cancer, 2005. **5**(3): p. 161-171.
14. Farokhzad, O.C., J.M. Karp, and R. Langer, *Nanoparticle-aptamer bioconjugates for cancer targeting.* Expert Opin Drug Deliv, 2006. **3**(3): p. 311-324.
15. Zhang, L., et al., *Nanoparticles in medicine: Therapeutic applications and developments.* Clinical Pharmacology & Therapeutics, 2008. **83**(5): p. 761-769.
16. Langer, R., *Drug delivery and targeting.* Nature, 1998. **392**(6679): p. 5-10.
17. Langer, R., *NEW METHODS OF DRUG DELIVERY.* Science, 1990. **249**(4976): p.

1527-1533.
18. Farokhzad, O.C., *Nanotechnology for drug delivery: the perfect partnership.* Expert Opinion on Drug Delivery, 2008. **5**(9): p. 927-929.
19. Peer, D., et al., *Nanocarriers as an emerging platform for cancer therapy.* Nature Nanotechnology, 2007. **2**(12): p. 751-760.
20. Shi, J.J., et al., *Self-Assembled Targeted Nanoparticles: Evolution of Technologies and Bench to Bedside Translation.* Accounts of Chemical Research, 2011. **44**(10): p. 1123-1134.
21. Wang, B., et al., *Polymer-drug conjugates for intracellar molecule-targeted photoinduced inactivation of protein and growth inhibition of cancer cells.* Scientific Reports, 2012. **2**.
22. Kopecek, J., *Polymer-drug conjugates: Origins, progress to date and future directions.* Advanced Drug Delivery Reviews, 2013. **65**(1): p. 49-59.
23. Greco, F. and M.J. Vicent, *Combination therapy: Opportunities and challenges for polymer-drug conjugates as anticancer nanomedicines.* Advanced Drug Delivery Reviews, 2009. **61**(13): p. 1203-1213.
24. Duncan, R., *Polymer conjugates as anticancer nanomedicines.* Nature Reviews Cancer, 2006. **6**(9): p. 688-701.
25. Hrkach, J.S., et al., *Nanotechnology for biomaterials engineering: Structural characterization of amphiphilic polymeric nanoparticles by H-1 NMR spectroscopy.* Biomaterials, 1997. **18**(1): p. 27-30.
26. Danhier, F., et al., *PLGA-based nanoparticles: An overview of biomedical applications.* Journal of Controlled Release, 2012. **161**(2): p. 505-522.
27. Calvo, P., et al., *Chitosan and chitosan ethylene oxide propylene oxide block copolymer nanoparticles as novel carriers for proteins and vaccines.* Pharmaceutical Research, 1997. **14**(10): p. 1431-1436.
28. Garcia-Fuentes, M. and M.J. Alonso, *Chitosan-based drug nanocarriers: Where do we stand?* Journal of Controlled Release, 2012. **161**(2): p. 496-504.
29. Elsamaligy, M.S. and P. Rohdewald, *RECONSTITUTED COLLAGEN NANOPARTICLES, A NOVEL DRUG CARRIER DELIVERY SYSTEM.* Journal of Pharmacy and Pharmacology, 1983. **35**(8): p. 537-539.
30. Nitta, S.K. and K. Numata, *Biopolymer-Based Nanoparticles for Drug/Gene Delivery and Tissue Engineering.* International Journal of Molecular Sciences, 2013. **14**(1): p. 1629-1654.
31. Nicolas, J., et al., *Design, functionalization strategies and biomedical applications of targeted biodegradable/biocompatible polymer-based nanocarriers for drug delivery.* Chemical Society Reviews, 2013. **42**(3): p. 1147-1235.
32. Aryal, S., C.M. Hu, and L. Zhang, *Polymeric nanoparticles with precise ratiometric control over drug loading for combination therapy.* Mol Pharm, 2011. **8**(4): p. 1401-1407.
33. Matsumura, Y., et al., *Phase I clinical trial and pharmacokinetic evaluation of*

NK911, a micelle-encapsulated doxorubicin. British Journal of Cancer, 2004. **91**(10): p. 1775-1781.

34. Papahadjopoulos, D., et al., *Sterically stabilized liposomes - improvements in pharmacokinetics and antitumor therapeutic efficacy.* Proceedings of the National Academy of Sciences of the United States of America, 1991. **88**(24): p. 11460-11464.
35. Pisano, C., et al., *Clinical trials with pegylated liposomal Doxorubicin in the treatment of ovarian cancer.* J Drug Deliv, 2013. **2013**: p. 898146.
36. Yokoyama, M., *Polymeric micelles as a new drug carrier system and their required considerations for clinical trials.* Expert Opinion on Drug Delivery, 2010. **7**(2): p. 145-158.
37. Slingerland, M., H.J. Guchelaar, and H. Gelderblom, *Liposomal drug formulations in cancer therapy: 15 years along the road.* Drug Discov Today, 2012. **17**(3-4): p. 160-166.
38. Chang, H.I. and M.K. Yeh, *Clinical development of liposome-based drugs: formulation, characterization, and therapeutic efficacy.* Int J Nanomedicine, 2012. **7**: p. 49-60.
39. Sharma, A. and U.S. Sharma, *Liposomes in drug delivery: progress and limitations.* International Journal of Pharmaceutics, 1997. **154**(2): p. 123-140.
40. Vishvakrama, P. and S. Sharma, *Liposomes: An Overview.* International Journal of Research in Pharmaceutical and Biomedical Sciences, 2012. **3**: p. 1074-1084.
41. Xiong, X.B., et al., *Engineering of amphiphilic block copolymers for polymeric micellar drug and gene delivery.* Journal of Controlled Release, 2011. **155**(2): p. 248-261.
42. van Dongen, S.F.M., et al., *Biohybrid Polymer Capsules.* Chemical Reviews, 2009. **109**(11): p. 6212-6274.
43. Medina, S.H. and M.E.H. El-Sayed, *Dendrimers as Carriers for Delivery of Chemotherapeutic Agents.* Chemical Reviews, 2009. **109**(7): p. 3141-3157.
44. Hari, B.V., et al., *Dendrimer: Globular Nanostructured Materials for Drug Delivery.* International Journal OF PharmTech Research, 2012. **4**: p. 432-451.
45. Navath, R.S., et al., *Amino acid-functionalized dendrimers with heterobifunctional chemoselective peripheral groups for drug delivery applications.* Biomacromolecules, 2010. **11**(6): p. 1544-1563.
46. Elhissi, A.M., et al., *Carbon nanotubes in cancer therapy and drug delivery.* J Drug Deliv, 2012. **2012**: p. 837327.
47. Lay, C.L., J. Liu, and Y. Liu, *Functionalized carbon nanotubes for anticancer drug delivery.* Expert Rev Med Devices, 2011. **8**(5): p. 561-566.
48. Yih, T.C. and M. Al-Fandi, *Engineered nanoparticles as precise drug delivery systems.* Journal of Cellular Biochemistry, 2006. **97**(6): p. 1184-1190.
49. Madani, S.Y., et al., *A new era of cancer treatment: carbon nanotubes as drug delivery tools.* International Journal of Nanomedicine, 2011. **6**: p. 2963-2979.
50. Theisen, C., *Predicting the future: projections help researchers allocate*

resources. J Natl Cancer Inst, 2003. **95**(12): p. 846-848.
51. Matsumura, Y. and H. Maeda, *A new concept for macromolecular therapeutics in cancer-chemotherapy - mechanism of tumoritropic accumulation of proteins and the antitumor agent smancs.* Cancer Research, 1986. **46**(12): p. 6387-6392.
52. Allen, T.M., *Ligand-targeted therapeutics in anticancer therapy.* Nature Reviews Cancer, 2002. **2**(10): p. 750-763.
53. Carter, P., *Improving the efficacy of antibody-based cancer therapies.* Nature Reviews Cancer, 2001. **1**(2): p. 118-129.
54. Heath, T.D., R.T. Fraley, and D. Papahadjopoulos, *Antibody targeting of liposomes - cell specificity obtained by conjugation of f(ab')2 to vesicle surface.* Science, 1980. **210**(4469): p. 539-541.
55. Ferrari, M., *Cancer nanotechnology: opportunities and challenges.* Nat Rev Cancer, 2005. **5**(3): p. 161-171.
56. Langer, R. and D.A. Tirrell, *Designing materials for biology and medicine.* Nature, 2004. **428**(6982): p. 487-492.
57. Greenwald, R.B., et al., *Effective drug delivery by PEGylated drug conjugates.* Adv Drug Deliv Rev, 2003. **55**(2): p. 217-250.
58. Kumar, P.V., et al., *PEGylated dendritic architecture for development of a prolonged drug delivery system for an antitubercular drug.* Curr Drug Deliv, 2007. **4**(1): p. 11-29.
59. Calvo, P., et al., *PEGylated polycyanoacrylate nanoparticles as vector for drug delivery in prion diseases.* Journal of Neuroscience Methods, 2001. **111**(2): p. 151-155.
60. Choi, Y.H., et al., *Polyethylene glycol-grafted poly-L-lysine as polymeric gene carrier.* Journal of Controlled Release, 1998. **54**(1): p. 39-48.
61. Maruyama, K., *PEG-liposome in DDS and clinical studies.* Nippon Rinsho, 1998. **56**(3): p. 632-637.
62. Minato, S., et al., *Application of polyethyleneglycol (PEG)-modified liposomes for oral vaccine: effect of lipid dose on systemic and mucosal immunity.* J Control Release, 2003. **89**(2): p. 189-197.
63. Janssen, A.P., et al., *Peptide-targeted PEG-liposomes in anti-angiogenic therapy.* Int J Pharm, 2003. **254**(1): p. 55-58.
64. Abuchowski, A., et al., *Effect of Covalent Attachment of Polyethylene-Glycol on Immunogenicity and Circulating Life of Bovine Liver Catalase.* Journal of Biological Chemistry, 1977. **252**(11): p. 3582-3586.
65. Abuchowski, A., et al., *Alteration of immunological properties of bovine serum albumin by covalent attachment of polyethylene glycol.* Journal of Biological Chemistry, 1977. **252**(11): p. 3578-3581.
66. Abuchowski, A. and F.F. Davis, *Preparation and properties of polyethylene glycol-trypsin adducts.* Biochim Biophys Acta, 1979. **578**(1): p. 41-46.
67. Knop, K., et al., *Poly(ethylene glycol) in drug delivery: pros and cons as well as potential alternatives.* Angewandte Chemie-International Edition, 2010. **49**(36):

p. 6288-6308.
68. Ryan, S.M., et al., *Advances in PEGylation of important biotech molecules: delivery aspects.* Expert Opinion on Drug Delivery, 2008. **5**(4): p. 371-383.
69. Veronese, F.M. and G. Pasut, *PEGylation, successful approach to drug delivery.* Drug Discovery Today, 2005. **10**(21-24): p. 1451-1458.
70. Harris, J.M. and R.B. Chess, *Effect of pegylation on pharmaceuticals.* Nature Reviews Drug Discovery, 2003. **2**(3): p. 214-221.
71. Torchilin, V.P. and V.S. Trubetskoy, *Which Polymers Can Make Nanoparticulate Drug Carriers Long-Circulating.* Advanced Drug Delivery Reviews, 1995. **16**(2-3): p. 141-155.
72. Ahmad, M.Z., et al., *Metallic nanoparticles: technology overview & drug delivery applications in oncology.* Expert Opinion on Drug Delivery, 2010. **7**(8): p. 927-942.
73. Heneweer, C., S.E. Gendy, and O. Penate-Medina, *Liposomes and inorganic nanoparticles for drug delivery and cancer imaging.* Ther Deliv, 2012. **3**(5): p. 645-656.
74. Ojea-Jimenez, I., et al., *Engineered Inorganic Nanoparticles for Drug Delivery Applications.* Curr Drug Metab, 2012.
75. Brown, S.D., et al., *Gold Nanoparticles for the Improved Anticancer Drug Delivery of the Active Component of Oxaliplatin.* Journal of the American Chemical Society, 2010. **132**(13): p. 4678-4684.
76. Sun, C., J.S.H. Lee, and M.Q. Zhang, *Magnetic nanoparticles in MR imaging and drug delivery.* Advanced Drug Delivery Reviews, 2008. **60**(11): p. 1252-1265.
77. You, C.C., A. Chompoosor, and V.M. Rotello, *The biomacromolecule-nanoparticle interface.* Nano Today, 2007. **2**: p. 34-43.
78. Conde, J., G. Doria, and P. Baptista, *Noble metal nanoparticles applications in cancer.* J Drug Deliv, 2012. **2012**: p. 751075.
79. Bhattacharyya, S., et al., *Inorganic Nanoparticles in Cancer Therapy.* Pharmaceutical Research, 2011. **28**(2): p. 237-259.
80. Ghosh, P., et al., *Gold nanoparticles in delivery applications.* Advanced Drug Delivery Reviews, 2008. **60**(11): p. 1307-1315.
81. Nishiyama, N., *Nanomedicine - Nanocarriers shape up for long life.* Nature Nanotechnology, 2007. **2**(4): p. 203-204.
82. West, J.L. and N.J. Halas, *Engineered nanomaterials for biophotonics applications: Improving sensing, imaging, and therapeutics.* Annual Review of Biomedical Engineering, 2003. **5**: p. 285-292.
83. Mittal, A.K., Y. Chisti, and U.C. Banerjee, *Synthesis of metallic nanoparticles using plant extracts.* Biotechnology Advances, 2013. **31**(2): p. 346-356.
84. Liao, H.W., C.L. Nehl, and J.H. Hafner, *Biomedical applications of plasmon resonant metal nanoparticles.* Nanomedicine, 2006. **1**(2): p. 201-208.
85. Thanh, N.T.K. and L.A.W. Green, *Functionalisation of nanoparticles for biomedical applications.* Nano Today, 2010. **5**(3): p. 213-230.

86. Arvizo, R.R., et al., *Intrinsic therapeutic applications of noble metal nanoparticles: past, present and future.* Chemical Society Reviews, 2012. **41**(7): p. 2943-2970.
87. Cherukuri, P., E.S. Glazer, and S.A. Curleya, *Targeted hyperthermia using metal nanoparticles.* Advanced Drug Delivery Reviews, 2010. **62**(3): p. 339-345.
88. Hergt, R., et al., *Magnetic particle hyperthermia: nanoparticle magnetism and materials development for cancer therapy.* Journal of Physics-Condensed Matter, 2006. **18**(38): p. 2919-2934.
89. Yallapu, M.M., et al., *Multi-functional magnetic nanoparticles for magnetic resonance imaging and cancer therapy.* Biomaterials, 2011. **32**(7): p. 1890-1905.
90. Huang, X.H., et al., *Cancer cell imaging and photothermal therapy in the near-infrared region by using gold nanorods.* Journal of the American Chemical Society, 2006. **128**(6): p. 2115-2120.
91. Dickerson, E.B., et al., *Gold nanorod assisted near-infrared plasmonic photothermal therapy (PPTT) of squamous cell carcinoma in mice.* Cancer Lett, 2008. **269**(1): p. 57-66.
92. Huang, X.H., et al., *Plasmonic photothermal therapy (PPTT) using gold nanoparticles.* Lasers in Medical Science, 2008. **23**(3): p. 217-228.
93. Jain, P.K., et al., *Noble Metals on the Nanoscale: Optical and Photothermal Properties and Some Applications in Imaging, Sensing, Biology, and Medicine.* Accounts of Chemical Research, 2008. **41**(12): p. 1578-1586.
94. Dickerson, E.B., et al., *Gold nanorod assisted near-infrared plasmonic photothermal therapy (PPTT) of squamous cell carcinoma in mice.* Cancer Letters, 2008. **269**(1): p. 57-66.
95. Daniel, M.C. and D. Astruc, *Gold nanoparticles: Assembly, supramolecular chemistry, quantum-size-related properties, and applications toward biology, catalysis, and nanotechnology.* Chemical Reviews, 2004. **104**: p. 293-346.
96. Dreaden, E.C., et al., *The golden age: gold nanoparticles for biomedicine.* Chem. Soc. Rev., 2011. **41**: p. 2740-2749.
97. Turkevich, J., P.C. Stevenson, and J. Hillier, *A study of the nucleation and growth processes in the synthesis of colloidal gold.* Discussions of the Faraday Society, 1951(11): p. 55.
98. Kimling, J., et al., *Turkevich method for gold nanoparticle synthesis revisited.* Journal of Physical Chemistry B, 2006. **110**(32): p. 15700-15707.
99. Frens, G., *Controlled nucleation for regulation of particle-size in monodisperse gold suspensions.* Nature-Physical Science, 1973. **241**(105): p. 20-22.
100. Frens, G., *Particle-size and sol stability in metal colloids.* Kolloid-Zeitschrift and Zeitschrift Fur Polymere, 1972. **250**(7): p. 736.
101. Brust, M., et al., *Synthesis of thiol-derivatized gold nanoparticles in a 2-phase liquid-liquid system.* Journal of the Chemical Society-Chemical Communications, 1994(7): p. 801-802.

102. Ingram, R.S., M.J. Hostetler, and R.W. Murray, *Poly-hetero-omega-functionalized alkanethiolate-stabilized gold cluster compounds.* Journal of the American Chemical Society, 1997. **119**(39): p. 9175-9178.
103. Hostetler, M.J., A.C. Templeton, and R.W. Murray, *Dynamics of place-exchange reactions on monolayer-protected gold cluster molecules.* Langmuir, 1999. **15**(11): p. 3782-3789.
104. Templeton, A.C., M.P. Wuelfing, and R.W. Murray, *Monolayer protected cluster molecules.* Accounts of Chemical Research, 2000. **33**(1): p. 27-36.
105. Xue, C.H., et al., *Construction of conjugated molecular structures on gold nanoparticles via the Sonogashira coupling reactions.* Chemical Communications, 2005(8): p. 1055-1057.
106. Rothrock, A.R., R.L. Donkers, and M.H. Schoenfisch, *Synthesis of nitric oxide-releasing gold nanoparticles.* Journal of the American Chemical Society, 2005. **127**(26): p. 9362-9363.
107. Fan, H.Y., et al., *Surfactant-assisted synthesis of water-soluble and biocompatible semiconductor quantum dot micelles.* Nano Letters, 2005. **5**(4): p. 645-648.
108. Fan, H.Y., et al., *Synthesis of organo-silane functionalized nanocrystal micelles and their self-assembly.* Journal of the American Chemical Society, 2005. **127**(40): p. 13746-13747.
109. Perez-Juste, J., et al., *Gold nanorods: Synthesis, characterization and applications.* Coordination Chemistry Reviews, 2005. **249**(17-18): p. 1870-1901.
110. Chen, H., et al., *Gold nanorods and their plasmonic properties.* Chemical Society Reviews, 2013. **42**: p. 2679-2724.
111. Paciotti, G.F., et al., *Colloidal gold: A novel nanoparticle vector for tumor directed drug delivery.* Drug Delivery, 2004. **11**(3): p. 169-183.
112. Paciotti, G.F., et al., *Colloidal gold: A novel colloidal nanoparticle vector for tumor-directed drug delivery.* Clinical Cancer Research, 2001. **7**(11): p. 104.
113. Liu, J. and Y. Lu, *Preparation of aptamer-linked gold nanoparticle purple aggregates for colorimetric sensing of analytes.* Nature Protocols, 2006. **1**(1): p. 246-252.
114. Liu, H., et al., *Multifunctional gold nanoshells on silica nanorattles: a platform for the combination of photothermal therapy and chemotherapy with low systemic toxicity.* Angew Chem Int Ed Engl, 2011. **50**(4): p. 891-895.
115. Huschka, R., et al., *Gene Silencing by Gold Nanoshell-Mediated Delivery and Laser-Triggered Release of Antisense Oligonucleotide and siRNA.* Acs Nano, 2012. **6**(9): p. 7681-7691.
116. Cole, J.R., et al., *Photothermal Efficiencies of Nanoshells and Nanorods for Clinical Therapeutic Applications.* Journal of Physical Chemistry C, 2009. **113**(28): p. 12090-12094.
117. Cheng, F.Y., C.T. Chen, and C.S. Yeh, *Comparative efficiencies of photothermal*

destruction of malignant cells using antibody-coated silica@Au nanoshells, hollow Au/Ag nanospheres and Au nanorods. Nanotechnology, 2009. **20**(42).

118. Bardhan, R., et al., *Nanoshells with Targeted Simultaneous Enhancement of Magnetic and Optical Imaging and Photothermal Therapeutic Response.* Advanced Functional Materials, 2009. **19**(24): p. 3901-3909.
119. Levin, C.S., et al., *Magnetic-Plasmonic Core-Shell Nanoparticles.* Acs Nano, 2009. **3**(6): p. 1379-1388.
120. Loo, C., et al., *Gold nanoshell bioconjugates for molecular imaging in living cells.* Opt Lett, 2005. **30**(9): p. 1012-1014.
121. Erickson, T.A. and J.W. Tunnell, *Gold nanoshells in biomedical applications.* Nanotechnologies for the Life Sciences, 2009. **3**: p. 1-43.
122. Loo, C., et al., *Nanoshell-enabled photonics-based imaging and therapy of cancer.* Technology in Cancer Research & Treatment, 2004. **3**(1): p. 33-40.
123. Bawa, R., *Nanoparticle-based therapeutics in humans: a survey.* Nanotech. L. & Bus., 2008. **5**: p. 135-155.
124. Gobin, A.M., J.J. Moon, and J.L. West, *EphrinA I-targeted nanoshells for photothermal ablation of prostate cancer cells.* Int J Nanomedicine, 2008. **3**(3): p. 351-358.
125. Hirsch, L.R., et al., *Nanoshell-mediated near-infrared thermal therapy of tumors under magnetic resonance guidance.* Proc Natl Acad Sci U S A, 2003. **100**(23): p. 13549-13554.
126. Liong, M., et al., *Multifunctional inorganic nanoparticles for imaging, targeting, and drug delivery.* ACS Nano, 2008. **2**(5): p. 889-896.
127. Wang, F., B. Willner, and I. Willner, *DNA nanotechnology with one-dimensional self-assembled nanostructures.* Curr Opin Biotechnol, 2013.
128. Campolongo, M.J., et al., *DNA nanomedicine: Engineering DNA as a polymer for therapeutic and diagnostic applications.* Advanced Drug Delivery Reviews. **62**(6): p. 606-616.
129. Chhabra, R., et al., *DNA Self-assembly for Nanomedicine.* Advanced Drug Delivery Reviews, 2010. **62**(6): p. 617-625.
130. Nishikawa, M., S. Rattanakiat, and Y. Takakura, *DNA-based nano-sized systems for pharmaceutical and biomedical applications.* Advanced Drug Delivery Reviews. **62**(6): p. 626-632.
131. Alahari, S.K., et al., *Inhibition of expression of the multidrug resistance-associated P-glycoprotein by phosphorothioate and 5' cholesterol-conjugated phosphorothioate antisense oligonucleotides.* Molecular Pharmacology, 1996. **50**(4): p. 808-819.
132. Manoharan, M., *Oligonucleotide conjugates as potential antisense drugs with improved uptake, biodistribution, targeted delivery, and mechanism of action.* Antisense & Nucleic Acid Drug Development, 2002. **12**(2): p. 103-128.
133. Rosi, N.L., et al., *Oligonucleotide-modified gold nanoparticles for intracellular gene regulation.* Science, 2006. **312**(5776): p. 1027-1030.

134. Giljohann, D.A., et al., *Oligonucleotide loading determines cellular uptake of DNA-modified gold nanoparticles.* Nano Letters, 2007. **7**(12): p. 3818-3821.
135. Bagalkot, V., et al., *An aptamer-doxorubicin physical conjugate as a novel targeted drug-delivery platform.* Angewandte Chemie-International Edition, 2006. **45**(48): p. 8149-8152.
136. Bagalkot, V., et al., *Quantum dot-aptamer conjugates for synchronous cancer imaging, therapy, and sensing of drug delivery based on bi-fluorescence resonance energy transfer.* Nano Lett, 2007. **7**(10): p. 3065-3070.
137. La, T.H., et al., *Using DNA nanotechnology to produce a drug delivery system.* Advances in Natural Sciences: Nanoscience and Nanotechnology, 2013. **4**(1): p. 015002.
138. Lee, J.H., et al., *Molecular diagnostic and drug delivery agents based on aptamer-nanomaterial conjugates.* Adv Drug Deliv Rev. **62**(6): p. 592-605.
139. Chen, J.H. and N.C. Seeman, *Synthesis from DNA of a Molecule with the Connectivity of a Cube.* Nature, 1991. **350**(6319): p. 631-633.
140. Seeman, N.C., *DNA in a material world.* Nature, 2003. **421**(6921): p. 427-431.
141. Rothemund, P.W.K., *Folding DNA to create nanoscale shapes and patterns.* Nature, 2006. **440**(7082): p. 297-302.
142. Ke, Y.G., et al., *Self-assembled water-soluble nucleic acid probe tiles for label-free RNA hybridization assays.* Science, 2008. **319**(5860): p. 180-183.
143. He, Y., et al., *Hierarchical self-assembly of DNA into symmetric supramolecular polyhedra.* Nature, 2008. **452**(7184): p. 198-202.
144. Yurke, B., et al., *A DNA-fuelled molecular machine made of DNA.* Nature, 2000. **406**(6796): p. 605-608.
145. Gehring, K., J.L. Leroy, and M. Gueron, *A tetrameric DNA structure with protonated cytosine.cytosine base pairs.* Nature, 1993. **363**(6429): p. 561-565.
146. Marsh, R., R. Bierstedt, and E. Eichhorn, *The crystal structure of cytosine-5-acetic acid.* Acta Crystallographica, 1962. **15**(4): p. 310-316.
147. Inman, R.B., *Transitions of DNA homopolymers.* Journal of molecular biology, 1964. **9**(3): p. 624-637.
148. Akinrimisi, E.O., C. Sander, and P. Ts'o, *Properties of Helical Polycytidylic Acid*.* Biochemistry, 1963. **2**(2): p. 340-344.
149. Hartman Jr, K.A. and A. Rich, *The tautomeric form of helical polyribocytidylic acid.* Journal of the American Chemical Society, 1965. **87**(9): p. 2033-2039.
150. Gueron, M. and J.L. Leroy, *The i-motif in nucleic acids.* Current Opinion in Structural Biology, 2000. **10**(3): p. 326-331.
151. Gallego, J., et al., *The folding of centromeric DNA strands into intercalated structures: A physicochemical and computational study.* Journal of Molecular Biology, 1999. **285**(3): p. 1039-1052.
152. Liu, D. and S. Balasubramanian, *A proton-fuelled DNA nanomachine.* Angew Chem Int Ed Engl, 2003. **42**(46): p. 5734-5736.
153. Alberti, P., et al., *DNA nanomachines and nanostructures involving*

quadruplexes. Organic & Biomolecular Chemistry, 2006. **4**(18): p. 3383-3391.
154. Wang, W.X., et al., *A pH-driven, reconfigurable DNA nanotriangle.* Chemical Communications, 2009(7): p. 824-826.
155. Liu, H. and D.S. Liu, *DNA nanomachines and their functional evolution.* Chemical Communications, 2009(19): p. 2625-2636.
156. Liu, D.S., E.J. Cheng, and Z.Q. Yang, *DNA-based switchable devices and materials.* Npg Asia Materials, 2011. **3**: p. 109-114.
157. Liu, D.S. and S. Balasubramanian, *A proton-fuelled DNA nanomachine.* Angewandte Chemie-International Edition, 2003. **42**(46): p. 5734-5736.
158. Liedl, T. and F.C. Simmel, *Switching the conformation of a DNA molecule with a chemical oscillator.* Nano Lett, 2005. **5**(10): p. 1894-1898.
159. Liu, H., et al., *Light-driven conformational switch of i-motif DNA.* Angew Chem Int Ed Eng, 2007. **46**(14): p. 2515-2517.
160. Liu, D.S., et al., *A reversible pH-driven DNA nanoswitch array.* Journal of the American Chemical Society, 2006. **128**(6): p. 2067-2071.
161. Wang, S.T., et al., *Enthalpy-driven three-state switching of a superhydrophilic/superhydrophobic surface.* Angewandte Chemie-International Edition, 2007. **46**(21): p. 3915-3917.
162. Wang, W.X., et al., *Use of the interparticle i-motif for the controlled assembly of gold nanoparticles.* Langmuir, 2007. **23**(24): p. 11956-11959.
163. Shu, W.M., et al., *DNA molecular motor driven micromechanical cantilever arrays.* Journal of the American Chemical Society, 2005. **127**(48): p. 17054-17060.
164. Chen, C., et al., *A simple and sensitive colorimetric pH meter based on DNA conformational switch and gold nanoparticle aggregation.* Chemical Communications, 2008(46): p. 6149-6151.
165. Xu, X.D., et al., *An i-DNA based electrochemical sensor for proton detection.* Talanta, 2010. **82**(4): p. 1122-1125.
166. Xia, F., et al., *Gating of single synthetic nanopores by proton-driven DNA molecular motors.* Journal of the American Chemical Society, 2008. **130**(26): p. 8345-8350.
167. Mukherjee, S., R.N. Ghosh, and F.R. Maxfield, *Endocytosis.* Physiol Rev, 1997. **77**(3): p. 759-803.
168. Huotari, J. and A. Helenius, *Endosome maturation.* EMBO J, 2011. **30**(17): p. 3481-3500.
169. Lee, R.J., S. Wang, and P.S. Low, *Measurement of endosome pH following folate receptor-mediated endocytosis.* Biochimica Et Biophysica Acta-Molecular Cell Research, 1996. **1312**(3): p. 237-242.
170. Grant, B.D. and M. Sato, *Intracellular trafficking.* 2006.
171. Modi, S., et al., *A DNA nanomachine that maps spatial and temporal pH changes inside living cells.* Nature Nanotechnology, 2009. **4**(5): p. 325-330.
172. Cheng, E.J., et al., *A pH-Triggered, Fast-Responding DNA Hydrogel.* Angewandte

Chemie-International Edition, 2009. **48**(41): p. 7660-7663.
173. Mao, Y.D., et al., *Alternating-electric-field-enhanced reversible switching of DNA nanocontainers with pH.* Nucleic Acids Research, 2007. **35**(5).
174. Gerweck, L.E. and K. Seetharaman, *Cellular pH gradient in tumor versus normal tissue: Potential exploitation for the treatment of cancer.* Cancer Research, 1996. **56**(6): p. 1194-1198.
175. Weiss, R.B., *The Anthracyclines - Will We Ever Find a Better Doxorubicin.* Seminars in Oncology, 1992. **19**(6): p. 670-686.
176. Ayhan, S.S., et al., *The evaluation of doxorubicin-induced cardiotoxicity: Comparison of Doppler and tissue Doppler-derived myocardial performance index.* Cardiology Journal, 2012. **19**(4): p. 363-368.
177. Gupta, P.K., F.C. Lam, and C.T. Hung, *Investigation of the Stability of Doxorubicin Hydrochloride Using Factorial Design.* Drug Development and Industrial Pharmacy, 1988. **14**(12): p. 1657-1671.
178. Gewirtz, D.A., *A critical evaluation of the mechanisms of action proposed for the antitumor effects of the anthracycline antibiotics Adriamycin and daunorubicin.* Biochemical Pharmacology, 1999. **57**(7): p. 727-741.
179. Minotti, G., et al., *Anthracyclines: Molecular advances and pharmacologic developments in antitumor activity and cardiotoxicity.* Pharmacological Reviews, 2004. **56**(2): p. 185-229.
180. Nadas, J. and D.X. Sun, *Anthracyclines as effective anticancer drugs.* Expert Opinion on Drug Discovery, 2006. **1**(6): p. 549-568.
181. Chatterjee, K., et al., *Doxorubicin cardiomyopathy.* Cardiology, 2010. **115**(2): p. 155-162.
182. Susa, M., et al., *Doxorubicin loaded Polymeric Nanoparticulate Delivery System to overcome drug resistance in osteosarcoma.* BMC Cancer, 2009. **9**: p. 399-411.
183. Pramanik, D., et al., *A composite polymer nanoparticle overcomes multidrug resistance and ameliorates doxorubicin-associated cardiomyopathy.* Oncotarget, 2012. **3**(6): p. 640-650.
184. Shroff, K. and E. Kokkoli, *PEGylated liposomal doxorubicin targeted to alpha5beta1-expressing MDA-MB-231 breast cancer cells.* Langmuir, 2012. **28**(10): p. 4729-4736.
185. Shmeeda, H., et al., *Her2-targeted pegylated liposomal doxorubicin: retention of target-specific binding and cytotoxicity after in vivo passage.* J Control Release, 2009. **136**(2): p. 155-160.
186. Meng, H., et al., *Engineered design of mesoporous silica nanoparticles to deliver doxorubicin and P-glycoprotein siRNA to overcome drug resistance in a cancer cell line.* ACS Nano, 2010. **4**(8): p. 4539-4550.
187. Mirza, A.Z. and H. Shamshad, *Preparation and characterization of doxorubicin functionalized gold nanoparticles.* Eur J Med Chem, 2011. **46**(5): p. 1857-1860.
188. Shen, J., et al., *Mesoporous silica nanoparticles loading doxorubicin reverse*

multidrug resistance: performance and mechanism. Nanoscale, 2011. **3**(10): p. 4314-4322.

189. Wang, F., et al., *Doxorubicin-tethered responsive gold nanoparticles facilitate intracellular drug delivery for overcoming multidrug resistance in cancer cells.* ACS Nano, 2011. **5**(5): p. 3679-3692.
190. Gu, Y.J., et al., *Gold-doxorubicin nanoconjugates for overcoming multidrug resistance.* Nanomedicine, 2012. **8**(2): p. 204-211.
191. Frederick, C.A., et al., *Structural Comparison of Anticancer Drug DNA Complexes - Adriamycin and Daunomycin.* Biochemistry, 1990. **29**(10): p. 2538-2549.
192. Trouet, A., Deprezde.D, and C. Deduve, *Chemotherapy through Lysosomes with a DNA-Daunorubicin Complex.* Nature-New Biology, 1972. **239**(91): p. 110.
193. Cornu, G., et al., *Daunorubicin-DNA - Further Clinical Trials in Acute Non-Lymphoblastic Leukemia.* European Journal of Cancer, 1974. **10**(11): p. 695-700.
194. Trouet, A., et al., *Experimental Leukemia Chemotherapy with a Lysosomotropic Adriamycin-DNA Complex.* European Journal of Cancer, 1974. **10**(7): p. 405-411.
195. Wang, A.Z., et al., *Superparamagnetic iron oxide nanoparticle-aptamer bioconjugates for combined prostate cancer imaging and therapy.* ChemMedChem, 2008. **3**(9): p. 1311-1315.
196. Bagalkot, V., et al., *Quantum dot - Aptamer conjugates for synchronous cancer imaging, therapy, and sensing of drug delivery based on Bi-fluorescence resonance energy transfer.* Nano Letters, 2007. **7**(10): p. 3065-3070.
197. Zhang, L., et al., *Co-delivery of hydrophobic and hydrophilic drugs from nanoparticle-aptamer bioconjugates.* ChemMedChem, 2007. **2**(9): p. 1268-1271.
198. Alexander, C.M., M.M. Maye, and J.C. Dabrowiak, *DNA-capped nanoparticles designed for doxorubicin drug delivery.* Chem Commun (Camb), 2011. **47**(12): p. 3418-3420.
199. Alexander, C.M., J.C. Dabrowiak, and M.M. Maye, *Investigation of the drug binding properties and cytotoxicity of DNA-capped nanoparticles designed as delivery vehicles for the anticancer agents doxorubicin and actinomycin D.* Bioconjug Chem, 2012. **23**(10): p. 2061-2070.
200. Kim, D., Y.Y. Jeong, and S. Jon, *A drug-loaded aptamer-gold nanoparticle bioconjugate for combined CT imaging and therapy of prostate cancer.* ACS Nano, 2010. **4**(7): p. 3689-3696.
201. Alexander, C.M., M.M. Maye, and J.C. Dabrowiak, *DNA-capped nanoparticles designed for doxorubicin drug delivery.* Chemical Communications, 2011. **47**(12): p. 3418-3420.
202. Haj, H.T.B., et al., *New findings in the study on the intercalation of bisdaunorubicin and its monomeric analogues with naked and nucleus DNA.* Chemico-Biological Interactions, 2003. **145**(3): p. 349-358.

203. Lane, A.N., et al., *Stability and kinetics of G-quadruplex structures.* Nucleic Acids Research, 2008. **36**(17): p. 5482-5515.
204. Maeda, H., et al., *Tumor vascular permeability and the EPR effect in macromolecular therapeutics: a review.* Journal of Controlled Release, 2000. **65**(1-2): p. 271-284.
205. Choi, H.S., et al., *Renal clearance of quantum dots.* Nat Biotechnol, 2007. **25**(10): p. 1165-1170.
206. Seferos, D.S., et al., *Polyvalent DNA nanoparticle conjugates stabilize nucleic acids.* Nano Lett, 2009. **9**(1): p. 308-311.
207. Ji, X.H., et al., *Size control of gold nanocrystals in citrate reduction: The third role of citrate.* Journal of the American Chemical Society, 2007. **129**(45): p. 13939-13948.
208. Hill, H.D., et al., *The Role Radius of Curvature Plays in Thiolated Oligonucleotide Loading on Gold Nanoparticles.* Acs Nano, 2009. **3**(2): p. 418-424.
209. Chen, R.J., et al., *Modulation of cell membrane disruption by pH-responsive pseudo-peptides through grafting with hydrophilic side chains.* Journal of Controlled Release, 2005. **108**(1): p. 63-72.
210. Liu, X., et al., *Extinction coefficient of gold nanoparticles with different sizes and different capping ligands.* Colloids Surf B Biointerfaces, 2007. **58**(1): p. 3-7.
211. Hurst, S.J., A.K.R. Lytton-Jean, and C.A. Mirkin, *Maximizing DNA loading on a range of gold nanoparticle sizes.* Analytical Chemistry, 2006. **78**(24): p. 8313-8318.
212. Dhar, S., et al., *Polyvalent Oligonucleotide Gold Nanoparticle Conjugates as Delivery Vehicles for Platinum(IV) Warheads.* Journal of the American Chemical Society, 2009. **131**(41): p. 14652-14653.
213. Zhang, X.Q., et al., *Strategy for Increasing Drug Solubility and Efficacy through Covalent Attachment to Polyvalent DNA - Nanoparticle Conjugates.* Acs Nano, 2011. **5**(9): p. 6962-6970.
214. Levicky, R., et al., *Using self-assembly to control the structure of DNA monolayers on gold: A neutron reflectivity study.* Journal of the American Chemical Society, 1998. **120**(38): p. 9787-9792.
215. Demers, L.M., et al., *A fluorescence-based method for determining the surface coverage and hybridization efficiency of thiol-capped oligonucleotides bound to gold thin films and nanoparticles.* Analytical Chemistry, 2000. **72**(22): p. 5535-5541.
216. Patel, P.C., et al., *Scavenger receptors mediate cellular uptake of polyvalent oligonucleotide-functionalized gold nanoparticles.* Bioconjug Chem, 2010. **21**(12): p. 2250-2256.
217. Bajaj, S., D. Singla, and N. Sakhuja, *Stability Testing of Pharmaceutical Products.* Journal of Applied Pharmaceutical Science, 2012. **2**(03): p. 129-138.
218. Sarkar, S., et al., *Polymer-supported metals and metal oxide nanoparticles: synthesis, characterization, and applications.* Journal of Nanoparticle Research,

2012. **14**(2).
219. Tyurin, A., et al., *Particle size tuning in silver-polyacrylonitrile nanocomposites.* Express Polymer Letters, 2010. **4**(2): p. 71-78.
220. Hui, L., et al., *Quantification of Particulate Mixing in Nanocomposites.* 2008 Ieee Conference on Electrical Insulation and Dielectric Phenomena, 2008: p. 272-275.
221. Abdelwahed, W., et al., *Freeze-drying of nanoparticles: Formulation, process and storage considerations.* Advanced Drug Delivery Reviews, 2006. **58**(15): p. 1688-1713.
222. Verma, A., et al., *Surface-structure-regulated cell-membrane penetration by monolayer-protected nanoparticles.* Nat Mater, 2008. **7**(7): p. 588-595.
223. Shukla, R., et al., *Biocompatibility of gold nanoparticles and their endocytotic fate inside the cellular compartment: a microscopic overview.* Langmuir, 2005. **21**(23): p. 10644-10654.
224. Nativo, P., I.A. Prior, and M. Brust, *Uptake and intracellular fate of surface-modified gold nanoparticles.* ACS Nano, 2008. **2**(8): p. 1639-1644.
225. Saha, K., et al., *Surface Functionality of Nanoparticles Determines Cellular Uptake Mechanisms in Mammalian Cells.* Small, 2012. **9**(2): p. 300-305.
226. Giljohann, D.A., et al., *Gold nanoparticles for biology and medicine.* Angew Chem Int Ed Engl, 2010. **49**(19): p. 3280-3294.
227. See, V., et al., *Cathepsin L digestion of nanobioconjugates upon endocytosis.* ACS Nano, 2009. **3**(9): p. 2461-2468.
228. Gill, M.R., et al., *A ruthenium(II) polypyridyl complex for direct imaging of DNA structure in living cells.* Nat Chem, 2009. **1**(8): p. 662-667.
229. Tian, X.H., et al., *Live Cell Luminescence Imaging As a Function of Delivery Mechanism.* Chembiochem, 2011. **12**(4): p. 548-551.
230. Rosi, N.L., et al., *Oligonucleotide-modified gold nanoparticles for intracellular gene regulation.* Science, 2006. **312**(5776): p. 1027-1030.
231. Davis, F.F., *The origin of pegnology.* Adv Drug Deliv Rev, 2002. **54**(4): p. 457-458.
232. Abuchowski, A., et al., *Alteration of immunological properties of bovine serum albumin by covalent attachment of polyethylene glycol.* J Biol Chem, 1977. **252**(11): p. 3578-3581.
233. Abuchowski, A., et al., *Effect of covalent attachment of polyethylene glycol on immunogenicity and circulating life of bovine liver catalase.* J Biol Chem, 1977. **252**(11): p. 3582-3586.
234. Harris, J.M. and R.B. Chess, *Effect of pegylation on pharmaceuticals.* Nat Rev Drug Discov, 2003. **2**(3): p. 214-221.
235. Veronese, F.M. and G. Pasut, *PEGylation, successful approach to drug delivery.* Drug Discov Today, 2005. **10**(21): p. 1451-1458.
236. Wattendorf, U. and H.P. Merkle, *PEGylation as a tool for the biomedical engineering of surface modified microparticles.* J Pharm Sci, 2008. **97**(11): p. 4655-4669.

237. Herve, K., et al., *The development of stable aqueous suspensions of PEGylated SPIONs for biomedical applications.* Nanotechnology, 2008. **19**(46): p. 465608.
238. Milla, P., F. Dosio, and L. Cattel, *PEGylation of proteins and liposomes: a powerful and flexible strategy to improve the drug delivery.* Curr Drug Metab, 2012. **13**(1): p. 105-119.
239. Lu, Y.A. and A.M. Felix, *Pegylated Peptides - Solid-Phase Synthesis of N(Alpha)-Pegylated Peptides Using Fmoc Strategy.* Peptide Research, 1993. **6**(3): p. 140-146.
240. Lu, Y.A. and A.M. Felix, *Pegylated Peptides .3. Solid-Phase Synthesis with Pegylating Reagents of Varying Molecular-Weight - Synthesis of Multiply Pegylated Peptides.* Reactive Polymers, 1994. **22**(3): p. 221-229.
241. Boytos, C.M., et al., *PEGylated thrombopoietin-mimetic peptides elevate blood platelets and ablate the chemotherapy-induced platelet nadir in mice.* Blood, 1998. **92**(10): p. 377-377.
242. Noberini, R., et al., *PEGylation Potentiates the Effectiveness of an Antagonistic Peptide That Targets the EphB4 Receptor with Nanomolar Affinity.* Plos One, 2011. **6**(12) : p.28611-28623.
243. Veronese, F.M., *Peptide and protein PEGylation: a review of problems and solutions.* Biomaterials, 2001. **22**(5): p. 405-417.
244. Veronese, F.M. and J.M. Harris, *Peptide and protein PEGylation III: advances in chemistry and clinical applications.* Advanced Drug Delivery Reviews, 2008. **60**(1): p. 1-2.
245. Roberts, M.J., M.D. Bentley, and J.M. Harris, *Chemistry for peptide and protein PEGylation.* Advanced Drug Delivery Reviews, 2002. **54**(4): p. 459-476.
246. Balan, S., et al., *Site-specific PEGylation of protein disulfide bonds using a three-carbon bridge.* Bioconjugate Chemistry, 2007. **18**(1): p. 61-76.
247. Monfardini, C., et al., *A Branched Monomethoxypoly(Ethylene Glycol) for Protein Modification.* Bioconjugate Chemistry, 1995. **6**(1): p. 62-69.
248. Federico, R., et al., *Histaminase PEGylation: Preparation and characterization of a new bioconjugate for therapeutic application.* Journal of Controlled Release, 2006. **115**(2): p. 168-174.
249. Zhao, H., et al., *Linear and branched bicin linkers for releasable PEGylation of macromolecules: controlled release in vivo and in vitro from mono- and multi-PEGylated proteins.* Bioconjug Chem, 2006. **17**(2): p. 341-351.
250. Chapman, A.P., *PEGylated antibodies and antibody fragments for improved therapy: a review.* Adv Drug Deliv Rev, 2002. **54**(4): p. 531-545.
251. Kubetzko, S., et al., *PEGylation and multimerization of the anti-p185HER-2 single chain Fv fragment 4D5: effects on tumor targeting.* J Biol Chem, 2006. **281**(46): p. 35186-35201.
252. Humphreys, D.P., et al., *Alternative antibody Fab' fragment PEGylation strategies: combination of strong reducing agents, disruption of the interchain disulphide bond and disulphide engineering.* Protein Eng Des Sel, 2007. **20**(5): p.

227-234.
253. Ducreux, J., et al., *PEGylation of anti-sialoadhesin monoclonal antibodies enhances their inhibitory potencies without impairing endocytosis in mouse peritoneal macrophages.* Bioconjug Chem, 2009. **20**(2): p. 295-303.
254. Ryan, S.M., et al., *Advances in PEGylation of important biotech molecules: delivery aspects.* Expert Opin Drug Deliv, 2008. **5**(4): p. 371-383.
255. Knop, K., et al., *Poly(ethylene glycol) in drug delivery: pros and cons as well as potential alternatives.* Angew Chem Int Ed Engl, 2010. **49**(36): p. 6288-6308.
256. Chang, L.C., et al., *PEG-modified protamine with improved pharmacological/pharmaceutical properties as a potential protamine substitute: synthesis and in vitro evaluation.* Bioconjug Chem, 2005. **16**(1): p. 147-155.
257. Chakravarti, V.S., et al., *Chondroosseous dysplasia in severe combined immunodeficiency due to adenosine deaminase deficiency (chondroosseous dysplasia in ADA deficiency SCID).* Pediatr Radiol, 1991. **21**(6): p. 447-448.
258. Graham, M.L., *Pegaspargase: a review of clinical studies.* Adv Drug Deliv Rev, 2003. **55**(10): p. 1293-1302.
259. Bukowski, R.M., et al., *Treating cancer with PEG Intron: pharmacokinetic profile and dosing guidelines for an improved interferon-alpha-2b formulation.* Cancer, 2002. **95**(2): p. 389-396.
260. Reddy, K.R., *Development and pharmacokinetics and pharmacodynamics of pegylated interferon alfa-2a (40 kD).* Semin Liver Dis, 2004. **24** (2): p. 33-38.
261. Gabizon, A. and F. Martin, *Polyethylene glycol-coated (pegylated) liposomal doxorubicin. Rationale for use in solid tumours.* Drugs, 1997. **54 Suppl 4**: p. 15-21.
262. Gabizon, A.A., *Pegylated liposomal doxorubicin: metamorphosis of an old drug into a new form of chemotherapy.* Cancer Invest, 2001. **19**(4): p. 424-436.
263. Soares, A.L., et al., *Effects of polyethylene glycol attachment on physicochemical and biological stability of E. coli L-asparaginase.* Int J Pharm, 2002. **237**(1-2): p. 163-170.
264. Luangtana-Anan, M., et al., *Polyethylene glycol on stability of chitosan microparticulate carrier for protein.* AAPS PharmSciTech, 2010. **11**(3): p. 1376-1382.
265. Immordino, M.L., F. Dosio, and L. Cattel, *Stealth liposomes: review of the basic science, rationale, and clinical applications, existing and potential.* Int J Nanomedicine, 2006. **1**(3): p. 297-315.
266. Needham, D., T.J. McIntosh, and D.D. Lasic, *Repulsive interactions and mechanical stability of polymer-grafted lipid membranes.* Biochim Biophys Acta, 1992. **1108**(1): p. 40-48.
267. Allen, C., et al., *Controlling the physical behavior and biological performance of liposome formulations through use of surface grafted poly(ethylene glycol).* Biosci Rep, 2002. **22**(2): p. 225-250.

268. Alexis, F., et al., *Factors affecting the clearance and biodistribution of polymeric nanoparticles.* Mol Pharm, 2008. **5**(4): p. 505-515.
269. Davis, M.E., Z.G. Chen, and D.M. Shin, *Nanoparticle therapeutics: an emerging treatment modality for cancer.* Nat Rev Drug Discov, 2008. **7**(9): p. 771-782.
270. Cho, K., et al., *Therapeutic nanoparticles for drug delivery in cancer.* Clin Cancer Res, 2008. **14**(5): p. 1310-1316.
271. Dobrovolskaia, M.A., et al., *Preclinical studies to understand nanoparticle interaction with the immune system and its potential effects on nanoparticle biodistribution.* Mol Pharm, 2008. **5**(4): p. 487-495.
272. Karmali, P.P. and D. Simberg, *Interactions of nanoparticles with plasma proteins: implication on clearance and toxicity of drug delivery systems.* Expert Opin Drug Deliv, 2011. **8**(3): p. 343-357.
273. Giljohann, D.A., et al., *Oligonucleotide loading determines cellular uptake of DNA-modified gold nanoparticles.* Nano Lett, 2007. **7**(12): p. 3818-3821.
274. Massich, M.D., et al., *Cellular response of polyvalent oligonucleotide-gold nanoparticle conjugates.* ACS Nano, 2010. **4**(10): p. 5641-5646.
275. Gessner, A., et al., *Protein rejecting properties of PEG-grafted nanoparticles: Influence of PEG-chain length and surface density evaluated by two-dimensional electrophoresis and bicinchoninic acid (BCA)-proteinassay.* Pharmazie, 2006. **61**(4): p. 293-297.
276. Torchilin, V.P., et al., *Poly(Ethylene Glycol) on the Liposome Surface - on the Mechanism of Polymer-Coated Liposome Longevity.* Biochimica Et Biophysica Acta-Biomembranes, 1994. **1195**(1): p. 11-20.
277. Erbacher, P., et al., *Transfection and physical properties of various saccharide, poly(ethylene glycol), and antibody-derivatized polyethylenimines (PEI).* J Gene Med, 1999. **1**(3): p. 210-222.
278. Caliceti, P. and F.M. Veronese, *Pharmacokinetic and biodistribution properties of poly(ethylene glycol)-protein conjugates.* Adv Drug Deliv Rev, 2003. **55**(10): p. 1261-1277.
279. Ayen, W.Y., et al., *Effect of PEG chain length and hydrophilic weight fraction on polymersomes prepared from branched (PEG)(3)-PLA co-polymers.* Polymers for Advanced Technologies, 2011. **22**(1): p. 158-165.
280. Gref, R., et al., *'Stealth' corona-core nanoparticles surface modified by polyethylene glycol (PEG): influences of the corona (PEG chain length and surface density) and of the core composition on phagocytic uptake and plasma protein adsorption.* Colloids Surf B Biointerfaces, 2000. **18**(3-4): p. 301-313.
281. Pasut, G., A. Guiotto, and F. Veronese, *Protein, peptide and non-peptide drug PEGylation for therapeutic application.* Expert Opinion on Therapeutic Patents, 2004. **14**(6): p. 859-894.
282. Perry, J.L., et al., *PEGylated PRINT Nanoparticles: The Impact of PEG Density on Protein Binding, Macrophage Association, Biodistribution, and Pharmacokinetics.* Nano Lett, 2012. **12**(10): p. 5304-5310.

283. Marie, D., D. Vaulot, and F. Partensky, *Application of the novel nucleic acid dyes YOYO-1, YO-PRO-1, and PicoGreen for flow cytometric analysis of marine prokaryotes.* Applied and Environmental Microbiology, 1996. **62**(5): p. 1649-1655.
284. Fee, C.J., *Size comparison between proteins PEGylated with branched and linear poly(ethylene glycol) molecules.* Biotechnol Bioeng, 2007. **98**(4): p. 725-731.
285. Thigpen, J.T., *Innovations in anthracycline therapy: overview.* Community Oncol, 2005. **2**(Suppl 1): p. 3-7.
286. Preobrazhenskaya, M.N., et al., *Second generation drugs-derivatives of natural antitumor anthracycline antibiotics daunorubicin, doxorubicin and carminomycin.* Journal Of Medical Sciences-Taipei, 2006. **26**(4): p. 119.
287. Tong, G.L., et al., *Adriamycin analogues. 3. Synthesis of N-alkylated anthracyclines with enhanced efficacy and reduced cardiotoxicity.* J Med Chem, 1979. **22**(8): p. 912-918.
288. Mosher, C.W., et al., *Enhanced antitumor properties of 3'-(4-morpholinyl) and 3'-(4-methoxy-1-piperidinyl) derivatives of 3'-deaminodaunorubicin.* J Med Chem, 1982. **25**(1): p. 18-24.
289. Ryberg, M., et al., *New insight into epirubicin cardiac toxicity: Competing risks analysis of 1097 breast cancer patients.* Journal of the National Cancer Institute, 2008. **100**(15): p. 1058-1067.
290. Tevyashova, A., et al., *Formation of squaric acid amides of anthracycline antibiotics. Synthesis and cytotoxic properties.* Bioorg Med Chem Lett, 2004. **14**(18): p. 4783-4789.
291. Lewis, W., et al., *Doxorubicin and covalently crosslinked doxorubicin derivatives binding to purified cardiac thin-filament proteins in vitro.* Exp Mol Pathol, 1985. **43**(1): p. 64-73.
292. Fenick, D.J., D.J. Taatjes, and T.H. Koch, *Doxoform and daunoform: Anthracycline-formaldehyde conjugates toxic to resistant tumor cells.* Journal of Medicinal Chemistry, 1997. **40**(16): p. 2452-2461.
293. Minotti, G., et al., *Anthracyclines: molecular advances and pharmacologic developments in antitumor activity and cardiotoxicity.* Pharmacol Rev, 2004. **56**(2): p. 185-229.
294. Yu, S.W., et al., *Synthesis and Biological Activities of a 3 '-Azido Analogue of Doxorubicin Against Drug-Resistant Cancer Cells.* International Journal of Molecular Sciences, 2012. **13**(3): p. 3671-3684.
295. Torti, F.M., et al., *Cardiotoxicity of epirubicin and doxorubicin: assessment by endomyocardial biopsy.* Cancer Res, 1986. **46**(7): p. 3722-3727.
296. Ozkan, A. and K. Fiskin, *Epirubicin HCl toxicity in human liver-derived hepatoma G2 cells.* Polish Journal of Pharmacology, 2004. **56**(4): p. 435-444.
297. Mero, A., et al., *Synthesis and characterization of poly(2-ethyl 2-oxazoline)-conjugates with proteins and drugs: Suitable alternatives to*

PEG-conjugates? Journal of Controlled Release, 2008. **125**(2): p. 87-95.
298. Adalsteinsson, O., et al., *Preparation and Magnetic Filtration of Polyacrylamide Gels Containing Covalently Immobilized Proteins and a Ferrofluid.* Journal of Molecular Catalysis, 1979. **6**(3): p. 199-225.
299. Mitra, S., et al., *Novel fluorescent matrix embedded carbon quantum dots for the production of stable gold and silver hydrosols.* Journal of Materials Chemistry, 2011. **21**(44): p. 17638-17641.
300. Cheng, T.L., et al., *Analytical Measurement of PEGylated Molecules.* Bioconjugate Chemistry, 2012. **23**(5): p. 881-899.
301. Zeman, S.M., D.R. Phillips, and D.M. Crothers, *Characterization of covalent adriamycin-DNA adducts.* Proc Natl Acad Sci U S A, 1998. **95**(20): p. 11561-11565.
302. Lee, C.C., et al., *A single dose of doxorubicin-functionalized bow-tie dendrimer cures mice bearing C-26 colon carcinomas.* Proc Natl Acad Sci U S A, 2006. **103**(45): p. 16649-16654.
303. Momparler, R.L., et al., *Effect of adriamycin on DNA, RNA, and protein synthesis in cell-free systems and intact cells.* Cancer Res, 1976. **36**(8): p. 2891-2895.
304. Taatjes, D.J., et al., *Redox pathway leading to the alkylation of DNA by the anthracycline, antitumor drugs adriamycin and daunomycin.* Journal of Medicinal Chemistry, 1997. **40**(8): p. 1276-1286.
305. Frederick, C.A., et al., *Structural comparison of anticancer drug-DNA complexes: adriamycin and daunomycin.* Biochemistry, 1990. **29**(10): p. 2538-2549.
306. McBain, S.C., H.H.P. Yiu, and J. Dobson, *Magnetic nanoparticles for gene and drug delivery.* International Journal of Nanomedicine, 2008. **3**(2): p. 169-180.
307. Yoon, T.J., et al., *Multifunctional nanoparticles possessing a "magnetic motor effect" for drug or gene delivery.* Angewandte Chemie-International Edition, 2005. **44**(7): p. 1068-1071.
308. Lu, A.H., E.L. Salabas, and F. Schuth, *Magnetic nanoparticles: Synthesis, protection, functionalization, and application.* Angewandte Chemie-International Edition, 2007. **46**(8): p. 1222-1244.
309. Banerjee, R., et al., *Nanomedicine: Magnetic Nanoparticles and their Biomedical Applications.* Current Medicinal Chemistry, 2010. **17**(27): p. 3120-3141.
310. Jayalekshmi, A.C., S.P. Victor, and C.P. Sharma, *Magnetic and degradable polymer/bioactive glass composite nanoparticles for biomedical applications.* Colloids Surf B Biointerfaces, 2013. **101**: p. 196-204.
311. Chertok, B., et al., *Iron oxide nanoparticles as a drug delivery vehicle for MRI monitored magnetic targeting of brain tumors.* Biomaterials, 2008. **29**(4): p. 487-496.
312. Mahmoudi, M., et al., *Superparamagnetic iron oxide nanoparticles (SPIONs): Development, surface modification and applications in chemotherapy.* Advanced Drug Delivery Reviews, 2011. **63**(1-2): p. 24-46.

313. Alkilany, A.M., et al., *Gold nanorods: Their potential for photothermal therapeutics and drug delivery, tempered by the complexity of their biological interactions.* Advanced Drug Delivery Reviews, 2012. **64**(2): p. 190-199.
314. Xiao, Y.L., et al., *Co-delivery of doxorubicin and siRNA using octreotide-conjugated gold nanorods for targeted neuroendocrine cancer therapy.* Nanoscale, 2012. **4**(22): p. 7185-7193.
315. Xiao, Y.L., et al., *Gold Nanorods Conjugated with Doxorubicin and cRGD for Combined Anticancer Drug Delivery and PET Imaging.* Theranostics, 2012. **2**(8): p. 757-768.
316. Wijaya, A., et al., *Selective Release of Multiple DNA Oligonucleotides from Gold Nanorods.* Acs Nano, 2009. **3**(1): p. 80-86.
317. van Vlerken, L.E. and M.M. Amiji, *Multi-functional polymeric nanoparticles for tumour-targeted drug delivery.* Expert Opin Drug Deliv, 2006. **3**(2): p. 205-216.
318. Hoskins, C., et al., *Hybrid gold-iron oxide nanoparticles as a multifunctional platform for biomedical application.* Journal of Nanobiotechnology, 2012. **10**.
319. Tartaj, P., et al., *The preparation of magnetic nanoparticles for applications in biomedicine.* Journal of Physics D-Applied Physics, 2003. **36**(13): p. 182-197.
320. Roca, A.G., et al., *Progress in the preparation of magnetic nanoparticles for applications in biomedicine.* Journal of Physics D-Applied Physics, 2009. **42**(22).
321. Sajja, H.K., et al., *Development of multifunctional nanoparticles for targeted drug delivery and noninvasive imaging of therapeutic effect.* Curr Drug Discov Technol, 2009. **6**(1): p. 43-51.
322. Quarta, A., et al., *Multifunctional nanostructures based on inorganic nanoparticles and oligothiophenes and their exploitation for cellular studies.* J Am Chem Soc, 2008. **130**(32): p. 10545-10555.
323. Wei, A., A.P. Leonov, and Q. Wei, *Gold nanorods: multifunctional agents for cancer imaging and therapy.* Methods Mol Biol, 2010. **624**: p. 119-130.
324. von Maltzahn, G., et al., *SERS-Coded Gold Nanorods as a Multifunctional Platform for Densely Multiplexed Near-infrared Imaging and Photothermal Heating.* Advanced Materials, 2009. **21**(31): p. 3175-3180.
325. Na, H.B., I.C. Song, and T. Hyeon, *Inorganic Nanoparticles for MRI Contrast Agents.* Advanced Materials, 2009. **21**(21): p. 2133-2148.
326. Wang, Y.X.J., S.M. Hussain, and G.P. Krestin, *Superparamagnetic iron oxide contrast agents: physicochemical characteristics and applications in MR imaging.* European Radiology, 2001. **11**(11): p. 2319-2331.
327. Qiao, R.R., C.H. Yang, and M.Y. Gao, *Superparamagnetic iron oxide nanoparticles: from preparations to in vivo MRI applications.* Journal of Materials Chemistry, 2009. **19**(35): p. 6274-6293.
328. Liao, Z.Y., et al., *Polymeric Liposomes-Coated Superparamagnetic Iron Oxide Nanoparticles as Contrast Agent for Targeted Magnetic Resonance Imaging of Cancer Cells.* Langmuir, 2011. **27**(6): p. 3100-3105.
329. Thorek, D.L.J., et al., *Superparamagnetic iron oxide nanoparticle probes for*

molecular imaging. Annals of Biomedical Engineering, 2006. **34**(1): p. 23-38.

330. Su, H.Y., et al., *Amphiphilic starlike dextran wrapped superparamagnetic iron oxide nanoparticle clsuters as effective magnetic resonance imaging probes.* Biomaterials, 2013. **34**(4): p. 1193-1203.
331. Wang, J.X., et al., *Magnetic Nanoparticles for MRI of Brain Tumors.* Current Pharmaceutical Biotechnology, 2012. **13**(12): p. 2403-2416.
332. Berry, C.C. and A.S.G. Curtis, *Functionalisation of magnetic nanoparticles for applications in biomedicine.* Journal of Physics D-Applied Physics, 2003. **36**(13): p. 198-206.
333. Huff, T.B., et al., *Hyperthermic effects of gold nanorods on tumor cells.* Nanomedicine, 2007. **2**(1): p. 125-132.
334. Huang, X., I.H. El-Sayed, and M.A. El-Sayed, *Applications of gold nanorods for cancer imaging and photothermal therapy.* Methods Mol Biol, 2010. **624**: p. 343-357.
335. Lei, Z.L., et al., *A novel two-step modifying process for preparation of chitosan-coated Fe3O4/SiO2 microspheres.* Journal of Materials Processing Technology, 2009. **209**(7): p. 3218-3225.
336. Sauzedde, F., A. Elaissari, and C. Pichot, *Hydrophilic magnetic polymer latexes. 1. Adsorption of magnetic iron oxide nanoparticles onto various cationic latexes.* Colloid and Polymer Science, 1999. **277**(9): p. 846-855.
337. Nigam, S., K.C. Barick, and D. Bahadur, *Development of citrate-stabilized Fe3O4 nanoparticles: Conjugation and release of doxorubicin for therapeutic applications.* Journal of Magnetism and Magnetic Materials, 2011. **323**(2): p. 237-243.
338. Garcia, J., et al., *Multilayer enzyme-coupled magnetic nanoparticles as efficient, reusable biocatalysts and biosensors.* Nanoscale, 2011. **3**(9): p. 3721-3730.
339. Lim, J., et al., *Synthesis and single-particle optical detection of low-polydispersity plasmonic-superparamagnetic nanoparticles.* Advanced Materials, 2008. **20**(9): p. 1721-1726.
340. Pham, T., et al., *Preparation and characterization of gold nanoshells coated with self-assembled monolayers.* Langmuir, 2002. **18**(12): p. 4915-4920.
341. Goon, I.Y., et al., *Fabrication and Dispersion of Gold-Shell-Protected Magnetite Nanoparticles: Systematic Control Using Polyethyleneimine.* Chemistry of Materials, 2009. **21**(4): p. 673-681.
342. Lyon, J.L., et al., *Synthesis of Fe oxide core/Au shell nanoparticles by iterative hydroxylamine seeding.* Nano Letters, 2004. **4**(4): p. 719-723.
343. Lo, C.K., D. Xiao, and M.M.F. Choi, *Homocysteine-protected gold-coated magnetic nanoparticles: synthesis and characterisationt.* Journal of Materials Chemistry, 2007. **17**(23): p. 2418-2427.
344. Lu, Q.H., et al., *Synthesis and characterization of composite nanoparticles comprised of gold shell and magnetic core/cores.* Journal of Magnetism and Magnetic Materials, 2006. **301**(1): p. 44-49.

345. Pham, T.T.H., C. Cao, and J. Sim, *Application of citrate-stabilized gold-coated ferric oxide composite nanoparticles for biological separations.* Journal of Magnetism and Magnetic Materials, 2008. **320**(15): p. 2049-2055.
346. Deng, H., et al., *Monodisperse magnetic single-crystal ferrite microspheres.* Angewandte Chemie-International Edition, 2005. **44**(18): p. 2782-2785.
347. Liu, J., et al., *Highly Water-Dispersible Biocompatible Magnetite Particles with Low Cytotoxicity Stabilized by Citrate Groups.* Angewandte Chemie-International Edition, 2009. **48**(32): p. 5875-5879.
348. Robinson, I., et al., *Synthesis of core-shell gold coated magnetic nanoparticles and their interaction with thiolated DNA.* Nanoscale, 2010. **2**(12): p. 2624-2630.
349. Cheng, G.J. and A.R.H. Walker, *Synthesis and characterization of cobalt/gold bimetallic nanoparticles.* Journal of Magnetism and Magnetic Materials, 2007. **311**(1): p. 31-35.
350. Yong, K.T., et al., *Synthesis and plasmonic properties of silver and gold nanoshells on polystyrene cores of different size and of gold-silver core-shell nanostructures.* Colloids and Surfaces a-Physicochemical and Engineering Aspects, 2006. **290**(1-3): p. 89-105.
351. Shi, W.L., et al., *Gold nanoshells on polystyrene cores for control of surface plasmon resonance.* Langmuir, 2005. **21**(4): p. 1610-1617.
352. Lin, J., et al., *Gold-coated iron (Fe@Au) nanoparticles: Synthesis, characterization, and magnetic field-induced self-assembly.* Journal of Solid State Chemistry, 2001. **159**(1): p. 26-31.
353. Zhou, W.L., et al., *Nanostructures of gold coated iron core-shell nanoparticles and the nanobands assembled under magnetic field.* European Physical Journal D, 2001. **16**(1-3): p. 289-292.
354. Carpenter, E.E., C. Sangregorio, and C.J. O'Connor, *Effects of shell thickness on blocking temperature of nanocomposites of metal particles with gold shells.* Ieee Transactions on Magnetics, 1999. **35**(5): p. 3496-3498.
355. Carpenter, E.E., *Iron nanoparticles as potential magnetic carriers.* Journal of Magnetism and Magnetic Materials, 2001. **225**(1-2): p. 17-20.
356. Pham, T.A., N.A. Kumar, and Y.T. Jeong, *Facile preparation of boronic acid functionalized Fe-core/Au-shell magnetic nanoparticles for covalent immobilization of adenosine.* Colloids and Surfaces a-Physicochemical and Engineering Aspects, 2010. **370**(1-3): p. 95-101.
357. Kayal, S. and R.V. Ramanujan, *Anti-Cancer Drug Loaded Iron-Gold Core-Shell Nanoparticles (Fe@Au) for Magnetic Drug Targeting.* Journal of Nanoscience and Nanotechnology, 2010. **10**(9): p. 5527-5539.
358. Ban, Z.H., et al., *The synthesis of core-shell iron@gold nanoparticles and their characterization.* Journal of Materials Chemistry, 2005. **15**(43): p. 4660-4662.
359. Jana, N.R., L. Gearheart, and C.J. Murphy, *Seed-mediated growth approach for shape-controlled synthesis of spheroidal and rod-like gold nanoparticles using a surfactant template.* Advanced Materials, 2001. **13**(18): p. 1389-1393.

360. Nikoobakht, B. and M.A. El-Sayed, *Preparation and growth mechanism of gold nanorods (NRs) using seed-mediated growth method.* Chemistry of Materials, 2003. **15**(10): p. 1957-1962.
361. Sau, T.K. and C.J. Murphy, *Seeded high yield synthesis of short Au nanorods in aqueous solution.* Langmuir, 2004. **20**(15): p. 6414-6420.
362. Schrama, D., R.A. Reisfeld, and J.C. Becker, *Antibody targeted drugs as cancer therapeutics.* Nature Reviews Drug Discovery, 2006. **5**(2): p. 147-159.
363. Goldenberg, D.M. and R.M. Sharkey, *Using antibodies to target cancer therapeutics.* Expert Opinion on Biological Therapy, 2012. **12**(9): p. 1173-1190.
364. Farokhzad, O.C., et al., *Nanoparticle-aptamer bioconjugates: a new approach for targeting prostate cancer cells.* Cancer Res, 2004. **64**(21): p. 7668-7672.
365. Shieh, Y.A., et al., *Aptamer-based tumor-targeted drug delivery for photodynamic therapy.* ACS Nano, 2010. **4**(3): p. 1433-1442.
366. Zhang, Y., H. Hong, and W. Cai, *Tumor-targeted drug delivery with aptamers.* Curr Med Chem, 2011. **18**(27): p. 4185-94.
367. Pan, J. and S.S. Feng, *Targeted delivery of paclitaxel using folate-decorated poly(lactide) - vitamin E TPGS nanoparticles.* Biomaterials, 2008. **29**(17): p. 2663-2672.
368. Sudimack, J. and R.J. Lee, *Targeted drug delivery via the folate receptor.* Advanced Drug Delivery Reviews, 2000. **41**(2): p. 147-162.
369. Gupta, Y., D.V. Kohli, and S.K. Jain, *Vitamin B12-mediated transport: a potential tool for tumor targeting of antineoplastic drugs and imaging agents.* Crit Rev Ther Drug Carrier Syst, 2008. **25**(4): p. 347-79.
370. Nagpal, S., S. Na, and R. Rathnachalam, *Noncalcemic actions of vitamin D receptor ligands.* Endocr Rev, 2005. **26**(5): p. 662-687.
371. Zhang, H., Y. Ma, and X.L. Sun, *Recent developments in carbohydrate-decorated targeted drug/gene delivery.* Med Res Rev, 2010. **30**(2): p. 270-289.
372. Davis, B.G. and M.A. Robinson, *Drug delivery systems based on sugar-macromolecule conjugates.* Curr Opin Drug Discov Devel, 2002. **5**(2): p. 279-288.
373. Sinha, R., et al., *Nanotechnology in cancer therapeutics: bioconjugated nanoparticles for drug delivery.* Molecular Cancer Therapeutics, 2006. **5**(8): p. 1909-1917.
374. Choi, C.H., et al., *Mechanism of active targeting in solid tumors with transferrin-containing gold nanoparticles.* Proc Natl Acad Sci U S A, 2010. **107**(3): p. 1235-1240.
375. Kirpotin, D.B., et al., *Antibody targeting of long-circulating lipidic nanoparticles does not increase tumor localization but does increase internalization in animal models.* Cancer Res, 2006. **66**(13): p. 6732-6740.
376. Bartlett, D.W., et al., *Impact of tumor-specific targeting on the biodistribution and efficacy of siRNA nanoparticles measured by multimodality in vivo imaging.* Proc Natl Acad Sci U S A, 2007. **104**(39): p. 15549-15554.

377. Schmidt, M.M. and K.D. Wittrup, *A modeling analysis of the effects of molecular size and binding affinity on tumor targeting.* Mol Cancer Ther, 2009. **8**(10): p. 2861-2871.
378. van Vlerken, L.E., T.K. Vyas, and M.M. Amiji, *Poly(ethylene glycol)-modified nanocarriers for tumor-targeted and intracellular delivery.* Pharm Res, 2007. **24**(8): p. 1405-1414.
379. Hirsjarvi, S., C. Passirani, and J.P. Benoit, *Passive and active tumour targeting with nanocarriers.* Curr Drug Discov Technol, 2011. **8**(3): p. 188-196.
380. Park, J.W., et al., *Anti-HER2 immunoliposomes: enhanced efficacy attributable to targeted delivery.* Clin Cancer Res, 2002. **8**(4): p. 1172-1181.
381. Zhang, C., et al., *Targeted minicircle DNA delivery using folate-poly(ethylene glycol)-polyethylenimine as non-viral carrier.* Biomaterials, 2010. **31**(23): p. 6075-6086.
382. Zhang, P.C., et al., *Folate-PEG modified poly(2-(2-aminoethoxy)ethoxy) phosphazene/DNA nanoparticles for gene delivery: Synthesis, preparation and in vitro transfection efficiency.* International Journal of Pharmaceutics, 2010. **392**(1-2): p. 241-248.
383. Zhang, T., et al., *A new strategy improves assembly efficiency of DNA mono-modified gold nanoparticles.* Chemical Communications, 2011. **47**(20): p. 5774-5776.
384. Sudimack, J. and R.J. Lee, *Targeted drug delivery via the folate receptor.* Adv Drug Deliv Rev, 2000. **41**(2): p. 147-162.
385. Zhao, X., H. Li, and R.J. Lee, *Targeted drug delivery via folate receptors.* Expert Opin Drug Deliv, 2008. **5**(3): p. 309-319.
386. Mathias, C.J., et al., *Tumor-selective radiopharmaceutical targeting via receptor-mediated endocytosis of gallium-67-deferoxamine-folate.* J Nucl Med, 1996. **37**(6): p. 1003-1008.
387. Ke, C.Y., C.J. Mathias, and M.A. Green, *Folate-receptor-targeted radionuclide imaging agents.* Adv Drug Deliv Rev, 2004. **56**(8): p. 1143-1160.
388. Liu, J.Q., et al., *Targeted drug delivery to chemoresistant cells: Folic acid derivatization of FdUMP[10] enhances cytotoxicity toward 5-FU-resistant human colorectal tumor cells.* Journal of Organic Chemistry, 2001. **66**(17): p. 5655-5663.
389. Ladino, C.A., et al., *Folate-maytansinoids: Target-selective drugs of low molecular weight.* International Journal of Cancer, 1997. **73**(6): p. 859-864.
390. Reddy, J.A., et al., *Preclinical evaluation of EC145, a folate-vinca alkaloid conjugate.* Cancer Res, 2007. **67**(9): p. 4434-4442.
391. Pan, X. and R.J. Lee, *Tumour-selective drug delivery via folate receptor-targeted liposomes.* Expert Opin Drug Deliv, 2004. **1**(1): p. 7-17.
392. Stella, B., et al., *Design of folic acid-conjugated nanoparticles for drug targeting.* J Pharm Sci, 2000. **89**(11): p. 1452-1464.
393. Jeong, J.H., et al., *In vivo tumor targeting of ODN-PEG-folic acid/PEI*

polyelectrolyte complex micelles. J Biomater Sci Polym Ed, 2005. **16**(11): p. 1409-1419.

394. Sharma, M., et al., *Folic acid conjugated guar gum nanoparticles for targeting methotrexate to colon cancer.* J Biomed Nanotechnol, 2013. **9**(1): p. 96-106.
395. Lorusso, P.M., et al., *Phase I Study of Folate Conjugate EC145 (Vintafolide) in Patients With Refractory Solid Tumors.* J Clin Oncol, 2012. **30**(32): p. 4011-4016.
396. Leamon, C.P., et al., *Preclinical antitumor activity of a novel folate-targeted dual drug conjugate.* Mol Pharm, 2007. **4**(5): p. 659-667.
397. Low, P.S., W.A. Henne, and D.D. Doorneweerd, *Discovery and development of folic-acid-based receptor targeting for imaging and therapy of cancer and inflammatory diseases.* Acc Chem Res, 2008. **41**(1): p. 120-129.
398. Leamon, C.P. and P.S. Low, *Delivery of Macromolecules into Living Cells - a Method That Exploits Folate Receptor Endocytosis.* Proceedings of the National Academy of Sciences of the United States of America, 1991. **88**(13): p. 5572-5576.
399. Wang, S., et al., *Synthesis, purification, and tumor cell uptake of Ga-67-deferoxamine-folate, a potential radiopharmaceutical for tumor imaging.* Bioconjugate Chemistry, 1996. **7**(1): p. 56-62.
400. Nam, J.M., C.S. Thaxton, and C.A. Mirkin, *Nanoparticle-based bio-bar codes for the ultrasensitive detection of proteins.* Science, 2003. **301**(5641): p. 1884-1886.
401. Pierschbacher, M.D. and E. Ruoslahti, *Cell Attachment Activity of Fibronectin Can Be Duplicated by Small Synthetic Fragments of the Molecule.* Nature, 1984. **309**(5963): p. 30-33.
402. Ruoslahti, E., *RGD and other recognition sequences for integrins.* Annual Review of Cell and Developmental Biology, 1996. **12**: p. 697-715.
403. Zhang, C.F., et al., *Specific targeting of tumor angiogenesis by RGD-conjugated ultrasmall superparamagnetic iron oxide particles using a clinical 1.5-T magnetic resonance scanner.* Cancer Research, 2007. **67**(4): p. 1555-1562.
404. Temming, K., et al., *RGD-based strategies for selective delivery of therapeutics and imaging agents to the tumour vasculature.* Drug Resistance Updates, 2005. **8**(6): p. 381-402.
405. Bogdanowich-Knipp, S.J., et al., *Solution stability of linear vs. cyclic RGD peptides.* J Pept Res, 1999. **53**(5): p. 530-541.
406. Danhier, F., A.L. Breton, and V. Preat, *RGD-Based Strategies To Target Alpha(v) Beta(3) Integrin in Cancer Therapy and Diagnosis.* Mol Pharm, 2012. **9**(11): p. 2961-2973.
407. Arap, W., R. Pasqualini, and E. Ruoslahti, *Cancer treatment by targeted drug delivery to tumor vasculature in a mouse model.* Science, 1998. **279**(5349): p. 377-380.
408. Chen, K. and X. Chen, *Integrin targeted delivery of chemotherapeutics.* Theranostics, 2011. **1**: p. 189-200.

409. Beer, A.J. and M. Schwaiger, *Imaging of integrin alphavbeta3 expression.* Cancer Metastasis Rev, 2008. **27**(4): p. 631-644.
410. Decristoforo, C., et al., *68Ga- and 111In-labelled DOTA-RGD peptides for imaging of alphavbeta3 integrin expression.* Eur J Nucl Med Mol Imaging, 2008. **35**(8): p. 1507-1515.
411. Burtea, C., et al., *Molecular imaging of alpha v beta3 integrin expression in atherosclerotic plaques with a mimetic of RGD peptide grafted to Gd-DTPA.* Cardiovasc Res, 2008. **78**(1): p. 148-157.
412. Schnell, O., et al., *Imaging of integrin alpha(v)beta(3) expression in patients with malignant glioma by [18F] Galacto-RGD positron emission tomography.* Neuro Oncol, 2009. **11**(6): p. 861-870.
413. Ye, Y. and X. Chen, *Integrin targeting for tumor optical imaging.* Theranostics, 2011. **1**: p. 102-126.
414. Zhang, C., et al., *Specific targeting of tumor angiogenesis by RGD-conjugated ultrasmall superparamagnetic iron oxide particles using a clinical 1.5-T magnetic resonance scanner.* Cancer Res, 2007. **67**(4): p. 1555-1562.
415. Lin, R.Y., et al., *Targeted RGD nanoparticles for highly sensitive in vivo integrin receptor imaging.* Contrast Media Mol Imaging, 2012. **7**(1): p. 7-18.
416. Liu, X.Y., et al., *Preparation of RGD-modified long circulating liposome loading matrine, and its in vitro anti-cancer effects.* Int J Med Sci, 2010. **7**(4): p. 197-208.
417. Lestini, B.J., et al., *Surface modification of liposomes for selective cell targeting in cardiovascular drug delivery.* J Control Release, 2002. **78**(1-3): p. 235-247.
418. Danhier, F., et al., *Targeting of tumor endothelium by RGD-grafted PLGA-nanoparticles loaded with paclitaxel.* J Control Release, 2009. **140**(2): p. 166-173.
419. Han, H.D., et al., *Targeted Gene Silencing Using RGD-Labeled Chitosan Nanoparticles.* Clinical Cancer Research, 2010. **16**(15): p. 3910-3922.
420. Jeong, J.H., et al., *In vivo tumor targeting of ODN-PEG-folic acid/PEI polyelectrolyte complex micelles.* Journal of Biomaterials Science-Polymer Edition, 2005. **16**(11): p. 1409-1419.